



HAL
open science

Modification of Carbon Felt for Contruction of Air-Breathing Cathode and Its Application in Microbial Fuel Cell

Widya Ernayati Kosimaningrum

► **To cite this version:**

Widya Ernayati Kosimaningrum. Modification of Carbon Felt for Contruction of Air-Breathing Cathode and Its Application in Microbial Fuel Cell. Material chemistry. Université Montpellier; Institut teknologi Bandung, 2018. English. NNT : 2018MONTTS110 . tel-02152383

HAL Id: tel-02152383

<https://theses.hal.science/tel-02152383>

Submitted on 11 Jun 2019

HAL is a multi-disciplinary open access archive for the deposit and dissemination of scientific research documents, whether they are published or not. The documents may come from teaching and research institutions in France or abroad, or from public or private research centers.

L'archive ouverte pluridisciplinaire **HAL**, est destinée au dépôt et à la diffusion de documents scientifiques de niveau recherche, publiés ou non, émanant des établissements d'enseignement et de recherche français ou étrangers, des laboratoires publics ou privés.

THÈSE POUR OBTENIR LE GRADE DE DOCTEUR DE L'UNIVERSITÉ DE MONTPELLIER

En Chimie et Physico-Chimie de Matériaux

École doctorale Sciences Chimiques Balard (ED 459)

Unité de recherche Institut Européen des Membranes

En partenariat international avec

INSTITUT TEKNOLOGI BANDUNG, Indonésie

Modification of Carbon Felt for Construction of Air-Breathing Cathode and Its Application in Microbial Fuel Cell

Présentée par

Widya Ernayati KOSIMANINGRUM

Le 13 Novembre 2018

Sous la direction de

Dr. Christophe INNOCENT et Pr. Buchari BUCHARI

Devant le jury composé de

Mme. Eniya Listiani DEWI, Professeur Agency for The Assesment and Application of Technology, BPPT, Indonésie	President du Jury
M. Maxime PONTIE, Professeur Université de Angers, Angers	Rapporteur
M. Mathieu ETIENNE, Directeur de Recherche CNRS Université de Lorraine, Villers-les-Nancy	Examineur
Mme. Laurence SOUSSAN, Maitré de Conference Ecole Nationale Supérieure de Chimie de Montpellier, ENSCM, Montpellier	Examinatrice
M. Henry SETIYANTO, Assistant Professeur Institut Teknologi Bandung, Indonésie	Examineur
M. Marc CRETIN, Professeur (Co-Directeur de These) Université de Montpellier, Montpellier	Invité
M. Indra NOVIANDRI, Associate Professeur (Co-Directeur de These) Institut Teknologi Bandung, Indonésie	Invité



UNIVERSITÉ
DE MONTPELLIER



RÉSUMÉ GENERAL

Les préoccupations environnementales actuelles obligent à revoir les modes de production d'énergie basés sur la combustion d'énergie fossile. L'augmentation des gaz à effet de serre et le souhait de limiter l'impact des activités humaines sur l'environnement ont initié de nombreuses recherches en faveur du développement durable. L'énergie est un enjeu majeur dans nos sociétés. Produire cette énergie de manière durable, sans effet néfaste sur l'environnement devient un souci permanent. Le développement de l'énergie électrique en alternative aux procédés thermiques pose le problème de sa production. Les piles à combustible, dispositifs électrochimiques capable de produire de l'électricité sans production de gaz à effet de serre sont considérées comme des systèmes séduisants. Toutefois, la nécessité de catalyser les réactions électrochimiques avec des catalyseurs de type métallique comme le platine, augmente à la fois les coûts économiques de ces dispositifs et les rend captifs des matières premières dont l'extraction n'est pas sans conséquence sur l'environnement. La substitution de ces catalyseurs synthétiques par des systèmes biologiques s'avère une alternative particulièrement intéressante. L'utilisation de micro-organismes spécifiques capable de catalyser des transferts électroniques a permis ainsi le développement des piles à combustible microbiennes (Microbial fuel cell- MFC). Même si la production d'électricité par ces dispositifs reste modeste, leur faible impact environnemental et leur parfaite intégration écologique constitue des avantages notables.

L'objectif du travail développé dans cette thèse est de contribuer à l'amélioration des performances de ces piles microbiennes par la préparation de matériaux d'électrode performants pouvant assurer une bonne connexion électronique entre les micro-organismes et l'électrode et notamment la construction d'une cathode à air permettant d'utiliser l'air comme comburant.

Le manuscrit est divisé en trois parties : une première partie bibliographique résume l'état de l'art sur les piles microbiennes avec leur fonctionnement, leur caractérisation et les différentes méthodes pour assurer une modification des matériaux d'électrode dans l'objectif d'améliorer les performances

électrochimiques. Le deuxième chapitre expose la partie expérimentale et la méthodologie. La troisième partie présente les résultats de ce travail.

Afin de réduire l'impact de l'utilisation d'énergies fossiles fortes contributrices à l'effet de serre, les recherches s'orientent vers des sources renouvelables d'énergie. Les piles à combustible, capable de convertir une énergie chimique en énergie électrique sans combustion s'avère une solution crédible. L'oxydation de l'hydrogène et la réduction de l'oxygène dans une pile à combustible génèrent de l'électricité et de l'eau comme produit de la réaction. La capacité de composés naturels à catalyser des réactions d'oxydo-réduction peut être mise à profit pour la construction d'une biopile. Des enzymes peuvent ainsi catalyser les réactions redox pour générer de l'électricité par exemple dans le cas de l'oxydation du glucose par l'enzyme glucose oxydase et la réduction de l'oxygène par l'enzyme laccase ou la bilirubine oxydase. Il est possible de s'affranchir de l'utilisation d'enzymes qui nécessitent souvent de longues étapes d'extraction et de purification, et d'utiliser directement des micro-organismes capables de se connecter à l'électrode. La catalyse électrochimique est alors assurée par la cellule vivante via l'électrode. Le métabolisme interne associe le cycle de Krebs qui assure le transfert d'électron de la chaîne respiratoire. Dans les phases de respiration classique des êtres vivants, les électrons terminent leur cheminement en réduisant l'oxygène. Le principe des piles microbiennes est de modifier cette phase terminale : l'oxygène n'est plus l'accepteur ultime d'électron, mais l'électrode assure ce rôle. Les capacités électrogéniques des cellules sont liées à deux types de mécanisme : le transfert direct d'électrons entre la cellule et l'électrode via les protéines membranaires cellulaires et le transfert médié d'électrons via des médiateurs électrochimiques. Ceux-ci peuvent être externes (ajouter au milieu cellulaire) ou interne car excrétés par la cellule. Les électrons sont ainsi conduits par l'électrode qui constitue une anode et migrent vers la cathode.

Pour obtenir une biopile efficace, il est nécessaire d'associer à l'anode microbienne une cathode. Différents dispositifs existent, faisant appel à des accepteurs d'électrons spécifiques. L'oxygène, bien sûr, est le plus connu et

utilisé. La réaction de réduction de l'oxygène conduit à la production d'eau. D'autres composés peuvent être utilisés comme le ferricyanure de potassium $K_3Fe(CN)_6$ ou des oxydes de manganèse. Ces différentes voies ont été testées dans ce travail.

L'association d'une anode microbienne et d'une cathode conduit à la formation d'une pile capable de générer du courant électrique. Les performances de ces piles sont liées aux caractéristiques thermodynamiques des réactions électrochimiques mises en jeu ainsi qu'aux cinétiques de réactions aux électrodes. De plus, le design du système est important pour l'optimisation des performances. Des systèmes rustiques ont été développés initialement (simple jonction de deux flacons de verre renfermant les électrodes) mais les recherches s'orientent sur des systèmes plus sophistiqués. L'utilisation de cathode à air permet ainsi le design de piles à un seul compartiment liquide. Le choix des matériaux d'électrode est aussi crucial dans l'amélioration des performances de ces biopiles. Essentiellement centré autour de l'utilisation du carbone comme matériaux de base des électrodes, sa mise en forme, sa structure et sa morphologie (fibre, feutre, feuillet, tube, etc.) ainsi que sa modification avec des composés comme des polymères conducteurs ou des particules métalliques ou d'oxydes métalliques permettent d'améliorer les performances. En particulier, la catalyse de la réaction de réduction de l'oxygène (ORR) est un point majeur pour augmenter la production d'électricité par la pile microbienne. La cathode reste souvent l'élément limitant du dispositif en raison d'une cinétique faible de la réduction de l'oxygène.

Compte tenu de l'état de l'art, deux types de dispositif expérimental ont été utilisés dans ce travail. Il s'agit d'un réacteur à deux compartiments, présenté sur la Figure-A et d'un réacteur à compartiment unique (Figure-B), utilisant une cathode à air. Les deux compartiments de la cellule de la Figure-A sont séparés par une membrane échangeuse d'ions de type Nafion.

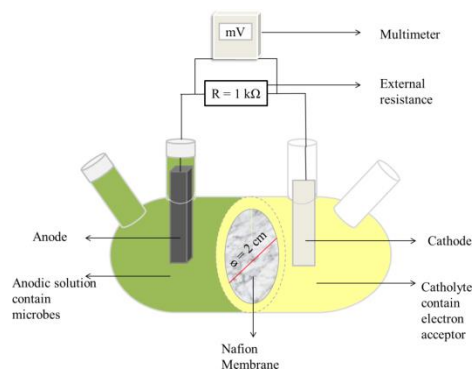


Figure-A : Réacteur à deux compartiments associant une anode bactérienne et une cathode fonctionnant en catalyse homogène en solution

La seconde configuration étudiée utilise une cathode à air capable de réduire l’oxygène de l’air. Ce design à un seul compartiment permet de simplifier le dispositif tout en améliorant les performances (Figure-B).

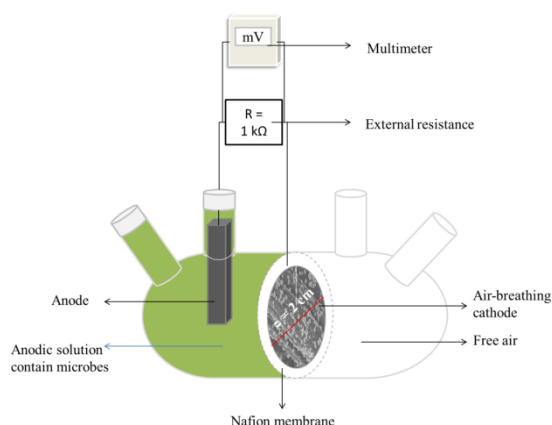


Figure-B: Réacteur à compartiment unique associant une anode bactérienne et une cathode à air.

L’inoculum choisi pour les piles microbiennes préparées dans ce travail est le terreau de jardin commercial. L’anode en feutre de carbone est plongée dans un lixiviat de terreau et d’électrolyte afin d’assurer la conductivité de la solution. Le biofilm anodique a été formé soit par croissance naturelle dans ce milieu soit sous polarisation (-0.16 V/Ag/AgCl). Les performances des deux systèmes ont été enregistrées et sont présentées sur la Figure-C. Nous avons montré que la polarisation améliore la cinétique de formation du biofilm à l’électrode dans les premiers jours, mais de meilleures performances électriques ont été enregistrées pour le système non polarisé comme le prouvent les résultats présentés sur la Figure-C.

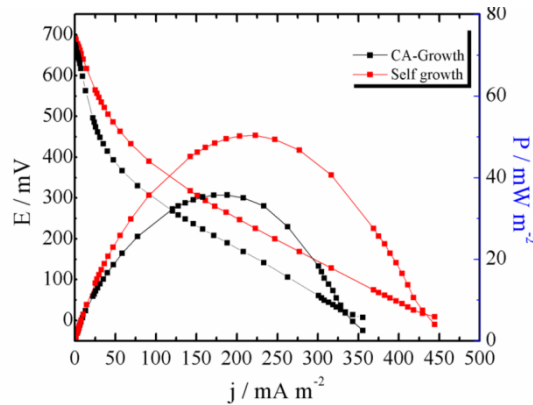


Figure-C : Evolution de la tension et de la puissance d'une biopile obtenue sous polarisation (**CA growth**) à -0.16 V/Ag/AgCl et sans polarisation externe (**self growth**).

Par ailleurs, différents types de matériaux ont été testés afin de déterminer le meilleur choix pour l'anode. Des essais de modifications du carbone, notamment avec des nanoparticules de platine, initialement étudiées pour les réactions cathodiques, se sont avérés particulièrement intéressants en terme de performances comme le montrent les résultats présentés Figure-D.

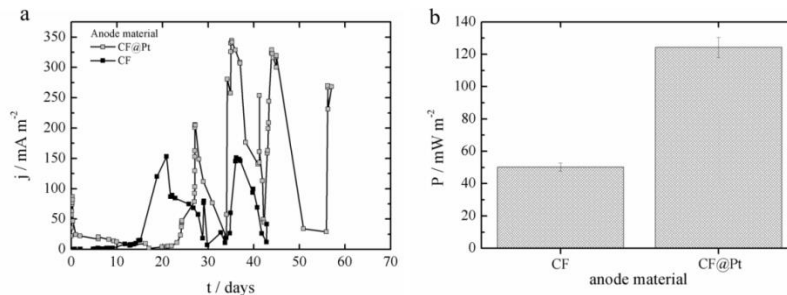


Figure-D : Densité de courant (a) et puissance (b) de la biopile avec différentes anodes : CF : feutre de carbone et CF@Pt: feutre de carbone modifié avec des nanoparticules de platine.

L'objectif de ce travail a été aussi de se concentrer sur l'élément cathodique de la pile qui constitue très souvent une limitation sévère au système. Notamment dans le cas de la réduction de l'oxygène en solution, la faible concentration d' O_2 dissous et les cinétiques électrochimiques lentes limitent la réaction cathodique. Dans ce contexte, le développement de cathodes à air, capables d'utiliser directement l'oxygène de l'air constitue une avancée intéressante. L'utilisation de biopiles à compartiment unique associées à une cathode à air a été étudiée en détail dans ce travail. Les cathodes sont construites par électrodéposition de platine sur carbone puis traitées thermiquement. L'influence d'un dépôt de

polymère conducteur de type polypyrrole afin de renforcer les caractéristiques mécaniques et la conductivité du matériau a été étudiée. Les performances des électrodes ont été déterminées comme précédemment et sont comparées à celles obtenues dans le cas de l'utilisation d'une cellule à deux compartiments (Figure-E).

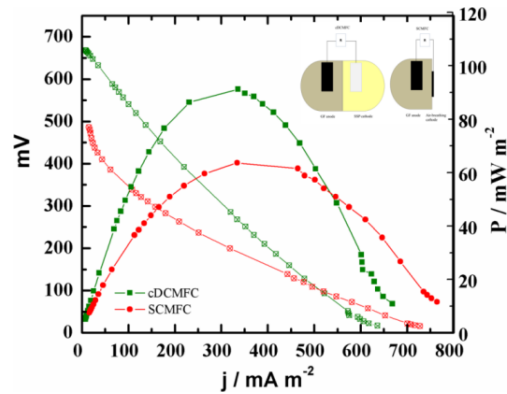


Figure-E : Comparaison des performances (tension et puissance) des piles microbiennes à deux compartiments et compartiment unique avec cathode à air.

Afin de trouver une alternative au platine, moins coûteuse, une étude a été engagée sur la modification du carbone par l'oxyde de manganèse, connu pour former des films par électrodéposition et qui présente des propriétés catalytiques pour la réduction de l'oxygène. L'analyse des électrodes modifiées a permis de montrer une bonne stabilité de la modification ainsi que de bonnes performances électrochimiques. L'application de ces électrodes dans des piles microbiennes a conclu ce travail.

Enfin, quelques applications originales de ces électrodes modifiées ont été envisagées. L'utilisation de l'électrode carbone modifiée par des nanoparticules de platine a été caractérisée pour la production d'hydrogène. Les résultats sont encourageants et permettent de réfléchir à de potentielles applications en électrolyse microbienne de ces matériaux. L'utilisation de l'électrode de carbone modifiée par de l'oxyde de manganèse a été appliquée à la dégradation de colorants par procédé électro-Fenton, le manganèse, en présence de peroxyde d'hydrogène, formé par la réduction à deux électrons de l'oxygène, étant capable de générer des radicaux.



Ces radicaux peuvent alors réagir sur des composés organiques, par analogie avec le procédé Fenton classique mettant en jeu du peroxyde d'hydrogène et des ions ferriques.

Les résultats préliminaires obtenus sont très prometteurs, que ce soit en termes d'efficacité de la dégradation des polluants organiques que de la stabilité du système, comme le représente la Figure-F.

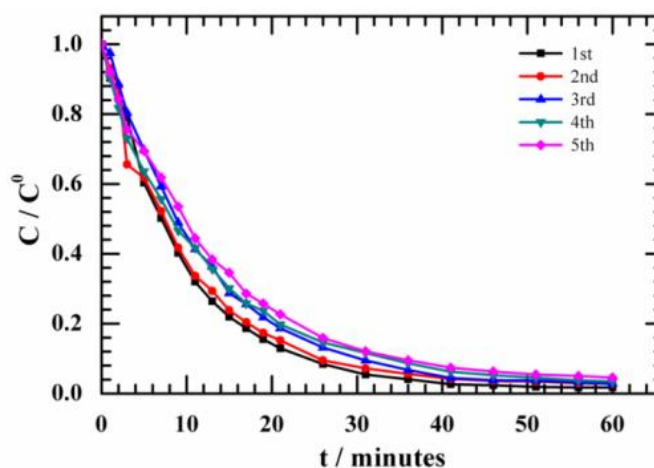


Figure-F : Cinétique de dégradation du colorant Acid Orange 7, sur une cathode en carbone modifiée par du dioxyde de manganèse, en fonction du nombre de cycle de fonctionnement.

En conclusion, ce travail a permis de montrer l'intérêt de la modification de matériaux carbonés d'électrode pour la mise en œuvre de cathodes à air performantes et leur application aux piles microbiennes. L'utilisation d'un design de cellule plus simple comme le compartiment unique constitue une avancée intéressante. La stabilité de ces systèmes a aussi été démontrée avec des piles qui fonctionnent ainsi sur plusieurs mois sans nécessité d'intervention sur la partie cathodique, contrairement au cas de l'utilisation d'un système à deux compartiments, qu'il convient de changer régulièrement du fait de la consommation du comburant principalement.

Des expériences préliminaires ont montré la possibilité d'utiliser ces électrodes dans d'autres procédés, comme l'électrolyse microbienne pour la génération d'hydrogène ou les procédés dérivés de la dégradation Fenton. Cela ouvre la voie au couplage de ces électrodes avec des systèmes microbiens, pour permettre à la fois la dégradation de polluants ou la production de composés spécifiques associés à la production d'énergie électrique de la biopile.

ACKNOWLEDGMENT

This thesis has been conducted under the scheme of International Joint Doctoral Convention (*Convention de Cotutelle Internationale de Thèse*) between Institut Teknologi Bandung, ITB, Indonesia and Université de Montpellier, France. The experimental research has been fully conducted in Institut Européen des Membranes (IEM), Université de Montpellier, specifically in the laboratory group of Design des Matériaux Membranaires et Systèmes Multifonctionnels (DM3) as well as Interface, Physicochimie, Polymères (IP2), and partially in Analytical Chemistry Laboratory of ITB. This program has been succeeded under financial support from Indonesian Government through Ministry of Research, Technology and Higher Education of the Republic of Indonesia (RISTEKDIKTI), Institut Européen des Membranes, Université de Montpellier, and partially from the *Bourse de Gouvernement Français*, (BGF), Campus France.

I would like to thank Prof. Philippe MIELE (Director) for having accepted me in Institut Européen des Membranes and his administrative team M. Philippe FALQUE and Mme. Dominique DIAMANTE, Mme. Fabienne BIONDI, Mme. Christelle FLOUTIER, Mme. Florence LEROY, and Mme. Cathy SCOGNAMIGLIO.

I would like to thank Prof. Philippe AUGÉ (Président de L'Université de Montpellier), Prof Dr. Kadarsah SURYADI (Rector of ITB), Prof. Jean-Jacques VASSEUR (Directeur de L'Ecole Doctorale Sciences Chimiques Balard), Mme. Pascale DECOMBLE, Prof. Dr. Pudji Astuti WALUYO (Dean of Graduate School of ITB), Prof. Ir. Bermawi Priyatna ISKANDAR, M.Sc., Ph.D., Prof Dr. Fida Madayanti WARGANEGARA, Prof. Dr. Abdul WARIS and his secretary for administrative Mrs. Ani HAMIDAH. Thank for either arranging or facilitating The International Joint Ph.D. scheme or your valuable support to follow this program. I would also thank Prof. Dr. H. Sholeh HIDAYAT (Rector of University of Sultan Ageng Tirtayasa) for his permit to follow Ph.D. program. I would like to thank Campus France team: Mme. Ratri WULANDARI, Mme. Arini

SATYANDITA, M. Anton HILMAN, and Mme. Arielle MICHEL for bridging Indonesia-to-France student.

I would like to thank for all juries both French and Indonesian: Pr. Maxime PONTIE, Prof. DR. Eng. Eniya Listiani DEWI, B.Eng. M.Eng, Dr. Mathieu ETIENNE, Dr. Laurence SOUSSAN, Dr. Henry SETIYANTO, Dr. Bunbun BUNJALI and the ITB's graduate school representatives Prof. Dr. Yana Maolana SYAH. I would also thank Prof. Ir. Iwan Kridasantausa HADIHARDAJA, M.Sc. Ph.D. for the Ph.D. thesis writing guidelines.

I would like to express my sincere thank PhD thesis supervisors: Dr. Christophe INNOCENT, Prof. Buchari BUCHARI, Prof. Marc CRETIN, Dr. Indra NOVIANDRI, and Dr. Yaovi HOLADE. Thank you very much for your acceptance, your teaching, your support, your guidance, your patience, your precious help and all of your kindness. It is an honor of being your student. I have learned so much from your advice with so many precious experiences.

I would like to thank Department of Graduate School of Chemistry, ITB especially Prof. Dr. Djulia ONGGO, Dr. Lia Dewi JULIAWATI Dr. Deana WAHYUNINGRUM, and the administrative team Mr. Handi, Mrs. Dessy and Mrs. Tini for facilitating all academic activities.

I would like to thank Dr. Sophie TINGRY and Dr. Michael BECHELANY for so many precious helps and advices. It was an honor for being your team work part. I would also thank Dr. Laurence SOUSSAN for training electron transfer mechanism, Dr. Stéphanie ROUALDES for annual Committee de These arrangement, Dr. Vincent ROUESSAC for contact angle training, Dr. Sophie CERNEAUX for safety laboratory advice, Dr. Martha BOEGLIN for writing clinic.

I would like to thank M. Abdeslam EL MANSSOURI, M. Christophe CHARMETTE, M. Jim CARTIER, Mme. Valérie BONNIOL, M. Bruno NAVARRA for a lot of helps. I would like to thank M. Didier COT for SEM analysis, M. Bertrand REBIERE for SEM-EDX analysis, M. Nathalie

MASQUELEZ for TGA, M. Eddy PETIT for some help with FTIR analysis operation, M. Arie VAN DER LI for XRD Analysis.

I would like to thank my friends: Dr. Thi Xuan Huong Le, Dr. Duy Linh Nguyen, Dr. Benoit Guenot, Dr. Roseline Esmilaire, Dr. Joffrey Champavert, Dr. Adriana Both Engel, Dr. Umyy Mardiana, Pr. Mostefa Kameche, Dr. Yassin Ouarda, Dr. Clément Trelu, Dr. Marleny, Dr. Chantal Karam, Dr. Thi Bich Hue Tran, Dr. Shaktivel Nagarajan, Houssin Makhlof, Rossa Rouche, Dr. Mekhaissia Ouis, Chahinez Yahiaoui, Hakima Kebaili, Dr. Zaineb Bouaziz, Sara Kawrani, Dr. Arnoud Joel Kinack Leoga, Dr. Laurene Youssef, Houda El Ghadary, Dr. Heba El Maghribi, Dr. Amr Ahmad Neda, Azariel Ruiz Valencia, Maya Abdhahah, Thomas Babut, Habib Belaid, Maria Di Vincenzo, Meryem Jerroudi, Meryem, Octavio Graniel Tamayo, Dr. Danae Gonzalez-Ortiz, Dr. Niccoleta, Ai Jing Lu, Luci Ries, Tian Ji Ma.

Thanks for “Persatuan Pelajar Indonesia (PPI)” France especially PPI Montpellier: Yogi Wilia Susanto and Ratna Dewanda, Dr. Rinny Rahmania, Mas Adi, Dr. Andes H. Rozak, Ika Sari Rahadiani, Andriyadi Mardin, Nafasya Aldilla, Anastasia Bella Adiwijaya, Ivana Wijaya, Rhesa Ananta, Moch. Raffi, Wirya M. Muhammad, Dr. Anita Thea Saraswati, Dr. Pria Sembada, Dr. Ellen Bless, Melania Seta Dhesti W., Nuna Nafikoh, Victorya Devie, Kezia Celine, Seraphina, Dr. Erlia Narulita. Thanks and love PPI Montpellier juniors: Annisa, Shaquille, Sharia, Crystal, Andra, and Edwige.

Many thanks for my whole ITB Friends Ervin Tri Suryandari, Enung Siti Nurhidayah, Intan Windyasari, Dikdik Mulyadi, Sony Widiarto, Nur Umriani Permatasari, Popy Asri Kurniatin, Dr. Nurochma Juliasih, Ivon Telussa, I Putu Parwata, Neena Zakia, Herlina Lubis, Lasmaryna Sirumapea, Dr. M. Yudhistira Aziz, Dr. Herlinawati, Dr. Hussain Sosidi, Dr. Siti Aminah, Dr. Herawati, Dr. Ana Hidayati, Dr. Yulia Sukmawardani, Dr. Fitri Dara, Djabal Nur Bashir, Widyo Wartono. I also thank DDIP 2015 team Apriliani Suryaningtyas, Ibnu Nurul Huda, Indah Rosidah Maemunah, Saadah Sajjana Carita, I Made Adiyatmika, and Dimas Prananta Simatupang.

I would like to thank my whole colleagues of University of Sultan Ageng Tirtayasa: Kurnia Nugraha, ST., MT., Ali Alhamidi, ST., MT. (Dean of Faculty Engineering), Endang Suhendi, ST., MT (Head of Chemical Engineering Department), Dr. Ing. Anton Irawan, Dr. Fatah Sulaeman, Prof. Yeyen Maryani, Dr. Teguh Kurniawan, Dr. Nuryoto, Dr. Endarto Yudo Wardhono, Dr. Indar Kustiningsih, Dr. Ekasari, Dr. Rahmayetty, Dr. Alia Badra Pitaloka, Rudi Hartono, ST., MT., Marta Pramudita, ST., MT., Meri Yulvianti, S.Pd., M.Si., Dhen Ria Barleany, ST. M.Eng., Sri Agustina, ST., MT., Heri Heriyanto, ST., M. Eng., Jayanudin, ST., M. Eng., Rusdi, ST., MT., Nufus Kanani, ST., M.Eng., Harly Demustila, ST., MT., Agus Rohmat, S.Si. M.Pharm, Iqbal Syaichurrozi, ST., MT., Denni Kartikasari, ST.M.Eng, Retno S.D. Lestari, ST., M.Eng, Wardalia, ST., MT, Elvi Nur Rochmah, ST., MT., Winny Muliadini, ST., MT., and Hafid Alwan, ST. MT.

Finally this big work is dedicated to my beloved big family: Bapa (H.N. Sunardi), Mamah (Rd. Hj. Lia Kartadibrata), Ibu (Hj. Yayat Sidik), Mame (H. Asmawi), my heart (Ir. Didi Agustiadi, IPM), my super sisters (DR Tety Suratika, Tita Khosima, Apt), my super stars (Amanda, Azarine, Zaidan, Abdul, Khansa), my super brothers (DR Diono Purwanto, Briptu Imam A. Munandar), my super soul mates (Eha Roseha, M.Pd., Astuningsih, M.Pd).

TABLE OF CONTENTS

RÉSUMÉ GENERAL.....	i
ACKNOWLEDGMENT.....	ix
TABLE OF CONTENTS.....	xiii
LIST OF FIGURES.....	xix
LIST OF TABLES.....	xxix
ABBREVIATIONS AND SYMBOLS.....	xxxix
General Introduction.....	3
Chapter 1 Bibliographic Study.....	11
1.1 Fuel cells.....	13
1.2 Photoelectrochemical fuel cell (PEFC).....	14
1.3 Biological fuel cells (BFCs).....	15
1.4 Microbial fuel cells (MFCs).....	16
1.4.1 Electrogeneration.....	18
1.4.2 Principle of voltage generation in MFCs.....	20
1.4.3 Electroactive microorganism/biocatalyst.....	21
1.4.4 Electroactive biofilm.....	21
1.4.5 Mechanism of electron transfer.....	23
1.4.6 Electron acceptor in MFC.....	25
1.4.7 Thermodynamics overview.....	28
1.4.8 Standard electrode potential.....	30
1.4.9 MFC performance parameters.....	31
1.4.10 MFC reactor design.....	37
1.4.12 Air-breathing cathode system.....	47
1.4.13 Oxygen reduction reaction catalysis.....	51
1.5 Electrodeposition.....	57
1.5.1 Electrodeposition of Pt.....	58
1.5.2 Electrodeposition of MnO ₂	59
1.5.3 Electrodeposition of conductive polymer.....	60
Chapter 2 Experimental Methodology.....	65
2.1 Chemicals and materials.....	65
2.2 Preliminary experiment.....	65
2.2.1 Cleaning glassware equipment.....	65
2.2.2 Cleaning raw material.....	66
2.3 Electrochemical method.....	66

2.3.1 The principle of electrochemical method	66
2.3.2 Electrochemical cell	71
2.3.3 Electrochemical synthesis	72
2.3.4 Electrochemical characterization.....	75
2.4 Microbial fuel cell experiment	78
2.4.1 Performance of MFC	78
2.5 Study the feasibility of garden compost in classical double chamber microbial fuel cell (DCMFC)	79
2.5.1 DCMFC reactor	79
2.5.2 Microbial source preparation (Lixiviation)	80
2.5.3 General DCMFC operation	81
2.5.4 Growing the biofilm	81
2.5.5 DCMFC experiment at various anodes	82
2.5.6 Stability test of the bioanode	82
2.5.7 Buffered system of the anodic solution	82
2.5.8 DCMFC experiment to study various electron acceptor in the cathodic chamber	83
2.6 Single chamber microbial fuel cell (SCMFC) with air-breathing cathode system	83
2.6.1 Electrochemical characterization of CF	83
2.6.2 Preliminary test of CF as air-breathing cathode	84
2.6.3 Preliminary test of CF as air-breathing cathode in microbial fuel cell... 84	
2.6.4 Modification of CF by Polypyrrole/Platinum (PPy/Pt) and its preliminary application as air-breathing cathode in the SCMFC	85
2.6.5 Glass tube-shaped SCMFC reactor.....	86
2.6.6 Application of the tube-shaped glass SCMFC reactor with CF@PPy@Pt air-breathing cathode	87
2.6.7 Electrochemical characterization of CF, CF@PPy, and CF@PPy@Pt.. 87	
2.7 SCMFC with ACF@Pt-based and ACF@MnOx-based air-breathing cathode	88
2.7.1 Fabrication of air-breathing cathode: ACF@Pt based air-breathing cathode.....	88
2.7.2 Fabricating of air-breathing cathode: ACF@MnOx based air-breathing cathode.....	88
2.7.3 General SCMFC operation	88
2.7 Single chamber microbial cell with air-breathing cathode to study electron transfer mechanism.....	88
2.9 Electrochemical characterization in the MFC cell	90

2.10 Other application of the developed material	90
2.10.1 ACF@Pt electrode for hydrogen evolution reaction (HER).....	90
2.10.2 Application of ACF@MnOx in electro-Fenton-like (EF-like) experiment.....	90
2.11 Physicochemical characterization	91
2.11.1 Fundamental.....	91
2.11.2 Experimental	97
 Chapter 3 Result and Discussion.....	 103
3.1 Study of double chamber microbial fuel cell (DCMFC) powered by garden compost	103
3.1.1 Garden compost microbial source.....	103
3.1.2 Growing the bioanode	104
3.1.3 Effect of structure of anode material.....	111
3.1.4 Modification of the anode	114
3.1.5 Stability of the bioanode	117
3.1.6 Biocompatibility of the garden compost leachate toward phosphate buffer in MFC	118
3.1.7 Cathodic compartment of the DCMFC	119
3.1.8 Consumption of the catholyte	121
3.1.9 Effect of the cathode	121
3.1.10 Microbial fuel cell-vanadium redox flow battery (MFC-VRFB) system	123
3.1.11 Effect of acidic catholyte solution.....	125
3.2 Air-breathing cathode for SCMFC: preliminary experiment.....	127
3.3 Polypyrrole-platinum modified carbon felt (CF@PPy@Pt) air-breathing cathode: preparation, characterization, and application.....	131
3.3.1 Preparation of air-breathing cathode.....	131
3.3.2 Electrochemical characterization	131
3.3.3 Air-breathing cathode for SCMFC: application of CF@PPy@Pt	134
3.4 Platinum-modified carbon felt (ACF@Pt): material development and characterization	139
3.4.1 Pre-synthesis of material	139
3.4.2 Electrodeposition of Pt on ACF	142
3.4.3 Electrochemical performance.....	143
3.4.4 Effect of electrodeposition method	145
3.4.5. Effect of nitrogen atmosphere saturation	146
3.4.6 Effect of time.....	147

3.4.7 Effect of concentration	148
3.4.8 Effect of thermal treatment.....	150
3.4.9 Platinum mass loading quantification.....	150
3.4.10 Morphological structure of the material	154
3.4.11 Structure of the materials.....	156
3.4.12 Surface analysis	158
3.4.13 Electrochemical impedance spectroscopy (EIS)	160
3.4.14 Fourier Transform Infra Red (FTIR) Spectroscopy	161
3.4.15 Electrochemical performance toward ORR following 4-electron transfer mechanism.....	161
3.5 Air-breathing cathode for SCMFC: application of platinum modified carbon felt (ACF@Pt)	164
3.5.1 Application of ACF@Pt as air-breathing cathode in SCMFC and its comparison to DCMFC	164
3.5.2 Elaboration of Pt modified carbon felt (ACF@Pt) as anode in SCMFC	168
3.5.3 SCMFC for the study of the electron transfer mechanism	170
3.6 Manganese oxide modified carbon felt (ACF@MnOx): material development and characterization.....	174
3.6.1 Electrodeposition of manganese oxide (MnOx)	174
a. Effect of electrodeposition potential.....	178
b. Effect of electrodeposition time.....	178
c. Effect of precursor concentration.....	180
3.6.2 MnOx mass loading.....	180
3.6.3 Physico-chemical characterization	184
3.6.4 Determination of H ₂ O ₂ production.....	189
3.6.5 Degradation of H ₂ O ₂	191
3.7 Air-breathing cathode for SCMFC: application of manganese oxide modified carbon felt (ACF@MnOx)	192
3.8 Other applications of the developed material	195
3.8.1 ACF@Pt electrode for hydrogen evolution reaction (HER) electrocatalysis.....	195
3.8.2 ACF@MnOx electrode for electro-Fenton-like (EF-like) process.....	196

General Conclusion and Perspective.....	205
REFERENCES.....	211
ANNEXES	231
Abstract	239
Résumé.....	240

LIST OF FIGURES

Figure 1 Domination of fossil fuel energy resources in meeting world energy needs [25].....	11
Figure 2 The classical hydrogen-oxygen fuel cell [5].....	13
Figure 3 Schematic diagram of PEFC [35]	14
Figure 4 Schematic diagram of a concentric glucose/O ₂ BFC prototype using enzyme-based biocatalyst [43]	16
Figure 5 Schematic diagram of conventional two-chamber microbial fuel cell separated by a membrane. On the left is the anodic compartment, where microbes produce electrons by degrading organic substrate, and on the right is the cathodic compartment, which contains the terminal electron acceptor (TEA) [47].	17
Figure 6 Generation of electron carriers, NAD and FADH ₂ , through the Krebs cycle [52]	19
Figure 7 Schematic diagram of bacterial membrane respiration [48].....	20
Figure 8 Schematic representation of voltage generation in an MFC [10]	20
Figure 9 Schematic representation of biofilm formation steps [58].....	22
Figure 10 Schematic representation of DET through (a) cell membrane and (b) cell appendage (nanowire)[44]	23
Figure 11 Schematic illustration of MET through secondary metabolites, wherein shuttling occurs via the outer cell membrane cytochrome and via periplasmic or cytoplasmic redox couple [44].	24
Figure 12 Molecular mediator compounds (a) phenazine, (b) phenothiazines, (c) phenoxazines, and (d) quinones.	25
Figure 13 System configuration of vanadium redox flow battery (VRFB) [73].....	28
Figure 14 Polarization curve of anode and cathode [76]	32
Figure 15 The polarization curve of MFC [68].....	32
Figure 16 (a) Measured voltage at each resistance, (b) polarization (current density vs. cell voltage) and power density (current density vs. power density) curves [68].	34
Figure 17 (a) H-type and (b) flat-type double chamber MFC [95]	38
Figure 18 Various tubular type of double chamber MFCs (a) packed bead anode inside and cathode outside, separated by a membrane [97], (b) interior cathode immersed in the packed bead of the anode[98], (c) up-flow system with packed reticulated vitreous carbon (RVC) both in the anode (bottom) and the cathode (top) [96].	39
Figure 19 Schematic diagram (a), prototype (b), and separated components (c) of a cube shaped of single chamber MFC [99]	40
Figure 20 Bottle shaped MFC with air-breathing cathode [100].	41
Figure 21 Tubular single chamber MFC [101]	41

Figure 22 Schematic diagram (a) and prototype (b) of a flat-plate type single chamber MFC [68,102].	42
Figure 23 Chemical structure of Nafion membrane [76].	42
Figure 24 Various types of anode materials applied in MFC: (a) carbon paper, (b) graphite plate, (c) carbon cloth, (d) carbon mesh, (e) granular graphite, (f) granular activated carbon, (g) carbon felt, (h) reticulated vitreous carbon, (i) carbon brush, and (j) stainless steel mesh [103].	45
Figure 25 Schematic diagram of a single chamber MFC with air-breathing cathode system [113].	48
Figure 26 Schematic diagram of a gas- or air-diffusion layer on the air-breathing cathode of a fuel cell [76].	50
Figure 27 ORR catalytic mechanism over a Pt catalyst [123].	52
Figure 28 ORR mechanism that shows the catalytic active site of a carbonaceous catalyst [125].	56
Figure 29 The bridge model of oxygen adsorption on polyaniline (PANI) [133].	57
Figure 30 Schematic representation of potential-controlled reduction and oxidation processes on the electrode [135].	58
Figure 31 Reduction mechanism of metal electrodeposition [136].	59
Figure 32 Pourbaix diagram of manganese [138].	60
Figure 33 The mechanism of electropolymerization of pyrrole [140].	61
Figure 34 (a) Potential-time (wave form) (b) current-potential curve (CV voltammogram) obtained by sweeping potential at scan rate 0.1 V s^{-1} as a function of time during CV measurement [143].	67
Figure 35 LSV curve expressed as (a) potential vs. time (E-t) (b) current vs. potential (i-E) and (c) concentration vs. distance from the electrode [135].	68
Figure 36 Current-time curve of chronoamperometry.	69
Figure 37 (a) Randles cell circuit and its (b) Nyquist plot (c) Warburg circuit cell and its (d) Nyquist plot.	70
Figure 38 (a) Schematic diagram and (b) prototype of conventional three-electrode arrangement electrochemical cell either for electrosynthesis (electrodeposition) and electrochemical characterization of the synthesized material.	71
Figure 39 Schematic cell diagram for H_2O_2 degradation test.	77
Figure 40 Customized reactor for running DCMFC experiment.	80
Figure 41 Air-breathing electrode configuration for electrochemical measurement.	84
Figure 42 Schematic diagram of electropolymerization of polypyrrole and consecutive electrodeposition of platinum onto carbon felt.	85
Figure 43 Customized SCMFC reactor with air-breathing cathode system.	86

Figure 44	Three-electrode configuration in (a) DCMFC and (b) SCMFC during electrochemical characterization of bioanode.....	90
Figure 45	(a) Schematic and (b) electrolysis cell for EF-like process in demineralization of AO7 at ACF@MnO _x electrode.....	91
Figure 46	(a) Bragg's Diffraction, (b) Debye-Scherrer powder camera and (c) its typical developed film [154].....	92
Figure 47	(a) Illustration of interaction between photon and electron in the inner shell of an atom and (b) schematic diagram of electron energy analyzer in XPS [154].....	93
Figure 48	Schematic diagram of FTIR instrument [154].....	94
Figure 49	Schematic diagram of SEM-EDX instrument [154].....	96
Figure 50	Schematic diagram of TGA instrument [154].....	96
Figure 51	Plasma generation [156].....	97
Figure 52	DCMFC operation (a) during the beginning period, before and (b) after biofilm growth on the anode after around 15 days. Close up of (c) bare anode and (d) anode covered by biofilm under SEM examination.....	104
Figure 53	Voltage evolution of the garden compost DCMFC showing the self growth of biofilm (<20 days) and the performance of the DCMFC after growing biofilm (>20 days). The blue solid arrows show the addition of acetate, the yellow dash arrows show refreshing ferricyanide solution, and the green short dash show refreshing the anodic solution.....	105
Figure 54	Electron hopping, the molecular mechanism of extracellular electron transfer through EPS, as a natural pathway of microbial extracellular electron transfer [165].....	106
Figure 55	Electrochemical behavior of the anode before and after biofilm formation: (a) by LSV, as recorded at scan rate of 5 mV s ⁻¹ , and (b) by CV as measured in the anodic solution (garden compost leachate containing acetate) at scan rate of 10 mV s ⁻¹	108
Figure 56	CA at -0.16 V vs. Ag/AgCl in the DCMFC reactor grows the biofilm on the CF anode for 21 days. The anodic compartment contained garden compost leachate and acetate, while the cathodic part contained 0.1 M KCl solution. The red arrows indicate the addition of acetate.....	108
Figure 57	CV measurement at scan rate 10 mV s ⁻¹ to observe electrochemical biofilm formation. CV measurements were conducted on day 0, 7, 16, and 21.	109
Figure 58	The comparison of voltage evolution of the DCMFC with CA- (black line) and self-growth (red line) bioanode. The negative x- and y-axis mean the period during the potential is applied for growing biofilm (-0.16 V vs. Ag/AgCl) prior to its application in DCMFC.....	110

Figure 59	The polarization and power density curve of the DCMFC with self- and CA-growth bioanode.	110
Figure 60	(a) Current density generation of the DCMFC with carbon felt (CF) and graphite bar (GB) anode (note: acetate addition was done for every four days) (b) power density and polarization curve of the MFC with CF and GB anode. Normalization of the current is toward the geometric surface area of the anode.	112
Figure 61	Morphology of the clean unmodified GB (a) and CF (c) and biofilm covering GB (b) and CF (d) observed under SEM.	112
Figure 62	CV behavior of the clean anode and the bioanode based on CF (a) and GB (b) respectively, recorded at scan rate of 10 mV s^{-1}	114
Figure 63	LSV curves, recorded at scan rate of 5 mV s^{-1} , for the polarization of the anodes based on CF and GB, respectively, before and after biofilm formation.	114
Figure 64	(a) Current density and (b) power density resulted from the DCMFC with different anodes: carbon felt (CF) and platinum NPs-modified carbon felt (CF@Pt) respectively.	115
Figure 65	SEM overview of (a,b) clean anode of unmodified CF and Pt nanoparticles modified carbon felt (CF@Pt), and (c) biofilm covered CF@Pt, CF@Pt@Biofilm, (bioanode).	116
Figure 66	LSV curves indicating the polarization of the clean anode and the bioanodes based on CF and CF@Pt substrate respectively.	116
Figure 67	Voltage generation indicating the performance of old bioanodes i.e. the CF@Pt@biofilm and the CF@Biofilm respectively in the DCMFC. The anodic solution contained only 60 mM KCl contain 20 mM acetate whereas cathodic solution was a ferricyanide solution.	117
Figure 68	Voltage generation profile of the three independent DCMFC experiments before and after switching to buffer system of the anodic solution. Each experiment was starting from a different old running DCMFC i.e. (a) 42 days old (b) a 56 days old and (c) 64 days old.	119
Figure 69	The ferricyanide solution in the cathodic part: its initial color (a) and turned colorless (b) indicating the consumption of ferricyanide upon the DCMFC operation.	120
Figure 70	Histogram giving the life-time of ferricyanide solution in hours as a function of the average potential of the cell.	121
Figure 71	Voltage evolution of the two independent DCMFC experiments corresponding to the cathode material change. (a) from SSP to ACF cathode, (b) from SSP to ACF@Pt cathode.	122
Figure 72	Histogram of the power density of the DCMFC as a function of the cathodic material.	122
Figure 73	Progressive vanadium solution color change at (a) 1 st day (b) 3 rd day and (c) 7 th day of DCMFC operation.	123

Figure 74 Comparison of ferricyanide and vanadium solution, at the same concentration, as electron acceptor in the DCMFC, toward its voltage evolution. Anode was carbon felt based bioanode (CF@Biofilm) and cathode was electroactivated carbon felt (ACF). Yellow arrows shows the refreshing ferricyanide solution and green arrows imply refreshing of vanadium solution.	125
Figure 75 The voltage evolution of the DCMFC with ferricyanide solution in cathodic part with ACF@Pt cathode (< 0 hour). Fluctuating voltage evolution is corresponding to pH instability in the cathodic part (of batch system) with the ACF@Pt cathode in 0.1 M KNO ₃ solution at pH 2 (from 0 – 200 hours). The green arrows indicate to the refreshed cathodic solution with fresh pH 2 electrolyte.	126
Figure 76 Stability of the voltage evolution corresponding to the pH of the cathodic solution.....	126
Figure 77 Chemical structure of graphite [176]	128
Figure 78 (a) CV of CF in 10 mM of ferricyanide solution that containing 0.1 M KNO ₃ at various scan-rates and (b) plot of anodic and cathodic peak current vs. the square root of scan rate.....	128
Figure 79 The CV voltammogram show oxygen reduction peak at region -0.6 V vs. Ag/AgCl (black arrow) (a) and plot of cathodic wave current versus square root of scan rate (b) for CF in air-breathing configuration in 50 mM PBS solution. As described in the experimental part, one side of the electrode is in contact with oxygen whereas the other side is in contact with PBS solution.	129
Figure 80 Chronoamperometric characterization of CF air-breathing electrode as recorded in PBS solution under respectively nitrogen, free-air, and oxygen exterior atmospheres respectively.....	130
Figure 81 CV in PBS solution (anodic) at scan rate 20 mV s ⁻¹ in air-breathing cathode configuration (a) under exterior atmosphere influence (nitrogen, air, and oxygen atmosphere) (b) as comparison between under exterior free-air containing gaseous oxygen and dissolved oxygen (by filling the free air space with oxygen-saturated water).	130
Figure 82 CV voltammogram of pyrrole electropolymerization on the CF surface (in aqueous phase side) at 20 mV s ⁻¹ for 30 cycles, and (a) CV voltammogram of electroreduction of Pt on previous resulted CF@PPy surface from 2 mM H ₂ PtCl ₆ solution at 20 mV s ⁻¹ for 20 cycles. SEM image of resulted (c) CF@PPy and CF@PPy@Pt(d). ...	132
Figure 83 In situ CV of CF and CF@PPy (a) and CF@PPy@Pt (b) air-breathing electrode at scan rate of 20 mV s ⁻¹ in PBS solution under nitrogen atmosphere.	133
Figure 84 LSV at scan rate 20 mV s ⁻¹ (a) and CA at -0.6 V vs. Ag/AgCl of (b) the CF, CF@PPy, and CF@PPy@Pt air-breathing electrodes	

	respectively, under oxygen atmosphere. The LSV curve (c) and CA at -0.6 V vs. Ag/AgCl (d) of CF@PPy@Pt air-breathing electrode under nitrogen, free air, and oxygen atmosphere.	134
Figure 85	Various MFC performances depicted as daily generated current density (a) and power density (b) curves. Either current density or power density were normalized toward the exposed surface area of air-breathing cathode.....	135
Figure 86	SCMFC experiment with CF@PPy@Pt air-breathing cathode in different reactor: (a) square-shaped acrylic with its wide top opening, which allow partially anaerob condition in anodic chamber, and (b) tube-shaped glass reactor with narrower top opening, which keeps better anaerobic condition in anodic chamber	136
Figure 87	Comparison of MFC performance between classical double chamber and single chamber MFC with air-breathing cathode system, as expressed in power density and polarization curve.	138
Figure 88	Survey scan of XPS spectrum of raw carbon felt (RCF) and activated carbon felt (ACF).....	140
Figure 89	Deconvolution of C1s peak at 284 eV of (a) RCF and (b) ACF.....	141
Figure 90	Water droplet test on (a) RCF and (b) ACF surface. Both photos were taken immediately after water was dropped.....	141
Figure 91	Voltammograms obtained on RCF and ACF under nitrogen atmosphere and 10 mM K ₃ Fe(CN) ₆ (in 1 M KNO ₃) at 10 mV s ⁻¹	142
Figure 92	LSV curve in 0.1 M KOH solution at scan rate 5 mV s ⁻¹ of (a) RCF, ACF and ACF@Pt under saturated oxygen atmosphere and (b) ACF@Pt electrode under saturated nitrogen and oxygen atmosphere. .	144
Figure 93	CV voltammogram of ACF@Pt electrode in 0.1 M KOH solution at 5 mV s ⁻¹ under nitrogen atmosphere showing the PtH desorption region (green raster) used to determine the electrochemical surface active area (ECSA).....	145
Figure 94	(a) CV under nitrogen atmosphere and (b) LSV under oxygen atmosphere at 5 mV s ⁻¹ in 0.1 M KOH solution of the as-synthesized ACF@Pt_CV and ACF@Pt_CA.	146
Figure 95	Cyclic voltammograms of the ACF@Pt in 0.1 M KOH solution at scan rate of 5 mV s ⁻¹ under unflow and flow of nitrogen	146
Figure 96	Electrochemical characterization of the ACF@Pt electrode by (a,b) CV at scan rate 5 mV s ⁻¹ under nitrogen atmosphere at pH 13 (0.1 M KOH) and (b) pH 7 (50 mM PBS (50 mM KCl), (c,d) LSV) at scan rate 5 mV s ⁻¹ under oxygen atmosphere at pH 13 (c) and 7 (d).....	147
Figure 97	CV voltammogram under nitrogen atmosphere at scan rate 5 mV s ⁻¹ (a,b) and LSV curve under oxygen atmosphere at scan rate 5 mV s ⁻¹ (c,d) in 0.1 M KOH pH 13 for (a,c) and in 50 PBS (50 mM KCl) pH 7 for (b,d).	149

Figure 98	Electrochemical characterization after thermal treatment for ACF@Pt electrodes recorded (a,b) at 5 mV s ⁻¹ in 0.1 M KOH and 50 mM PBS (in 50 mM KCl) solution respectively (d) at 10 mV s ⁻¹ in 10 mM K ₃ Fe(CN) ₆ (in 1 M KNO ₃) under nitrogen atmosphere and (c) LSV curve at 5 mV s ⁻¹ under oxygen atmosphere.....	151
Figure 99	Thermogravimetric analysis curves of RCF, ACF and ACF@Pt representatives (inset shows the weight loss between 480 and 600 °C)	153
Figure 100	SEM image of the Pt particles grown on ACF from 5 mM of precursor with reaction times 1 hour: (a) overview at 50 μm (b) 5 μm, and (c) zoomed single particle at 500 nm magnification.....	154
Figure 101	SEM images of the Pt particles growth on ACF for reaction time (a,d) 0.5 hour, (b,e) 1 hour and (c,f) 2 hours.	155
Figure 102	SEM image of the Pt particles grown on ACF for a reaction time of 1 hour from concentration of precursor (a) 1 mM, (b) 3 mM and (c) 5 mM.	155
Figure 103	SEM image of ACF@Pt without (a) and with heat treatment at (b) 400 °C and (b) 1000 °C.....	156
Figure 104	XRD patterns of CF, ACF, and selected ACF@Pt samples.....	157
Figure 105	XPS survey spectrum of RCF, ACF and ACF@Pt	159
Figure 106	High resolution XPS spectra of (a) C1s and (b)O1s of the RCF, ACF and ACF@Pt (c) Pt4f core level of ACF@Pt sample (d) surface atomic composition.....	159
Figure 107	Complex-plane Nyquist impedance plots for RCF, ACF and ACF@Pt electrodes recorded at the open circuit potential (i.e. 0.35, 0.42 and 0.41 V vs. RHE for RCF, ACF and ACF@Pt, respectively) in 10 mM K ₃ [Fe(CN) ₆] + 1 M KNO ₃ aqueous solution. The normalization is based on an estimated geometric surface area of 3.9 cm ² for the working electrode.	160
Figure 108	FTIR spectra of the ACF@Pt, ACF, and RCF	161
Figure 109	(a) Behavior of I and (b) Q during one hour CA in 0.1 M KOH aqueous solution under oxygen atmosphere on the RCF, ACF and ACF@Pt electrodes at various electrode potentials	162
Figure 110	Potential-dependent production of H ₂ O ₂ from ORR as quantified from UV-Vis assay	163
Figure 111	(a) Performance of SCMFC and DCMFC exhibited by current generation at a load resistance of 1 kΩ connected to the MFC (b) MFC polarization curve (iR-uncorrected). Nafion 115 PEM separated both side: anodic chamber contains garden compost leachate while the cathodic chamber (in DCMFC) contain ferricyanide solution. The addition of acetate is indicated by solid blue arrows for DCMFC and blue dash arrows for SCMFC. The refreshing anodic solution is noted	

	by green solid (DCMFC) and dash (SCMFC) arrows. The yellow arrows show the refreshing of ferricyanide solution in DCMFC.....	165
Figure 112	LSV measurement of air-breathing cathode (ACF@Pt) and ACF as blank control (scan rate of 5 mV s^{-1}) in SCMFC containing garden compost leachate.	167
Figure 113	SCMFC performance with various anode expressed by daily current generated (a) and polarization and power density (b) curves. ...	168
Figure 114	Current generation of DCMFC and SCMFC system with platinum based bioanode.	169
Figure 115	SCMFC operation with anodic compartment contain garden compost leachate (a)before and (b) after separation	171
Figure 116	The evolution of voltage before (minus x axis) and after separation	171
Figure 117	The optical density of compost garden leachate at 600 nm determined for different cases.....	172
Figure 118	Anodic compartment at 0 h (a), 24 h (b) and 48 h (c).....	173
Figure 119	Voltammograms of ACF electrode at scan rate 5 mV s^{-1} in manganese precursor (2.5 mM MnCl_2 in 200 mM NaNO_3) and only electrolyte (200 mM NaNO_3) solution under nitrogen and oxygen atmosphere.	175
Figure 120	(a,c) Voltammogram at scan rate 10 mV s^{-1} under nitrogen atmosphere and (b,d) LSV curve at scan rate 5 mV s^{-1} under oxygen atmosphere of the ACF@MnOx electrodes resulted by CV electrodeposition at various potential ranges (two experimental sets). .	176
Figure 121	(a) Voltammogram under nitrogen atmosphere at scan rate 10 mV s^{-1} and (b) LSV curve under oxygen atmosphere at scan rate 5 mV s^{-1} , in 50 mM PBS solution of the developed ACF@MnOx electrodes resulted through CV electrodeposition at potential range $0.8 - 1.4 \text{ V}$ vs. Ag/AgCl at various numbers of cycles.....	177
Figure 122	(a) Voltammogram under nitrogen atmosphere at scan rate 10 mV s^{-1} and (b) LSV curve under oxygen atmosphere at scan rate 5 mV s^{-1} , in 50 mM PBS solution of the developed ACF@MnOx electrodes resulted through CV electrodeposition at potential range $0.8 - 1.4 \text{ V}$ vs. Ag/AgCl at various scan rates.	178
Figure 123	(a) Voltammogram under nitrogen atmosphere at scan rate 10 mV s^{-1} and (b) LSV curve under oxygen atmosphere at scan rate 5 mV s^{-1} , in 50 mM PBS solution of the developed ACF@MnOx electrodes resulted through one hour CA electrodeposition at various electrodeposition potentials.....	179
Figure 124	(a) Voltammogram under nitrogen atmosphere at scan rate 10 mV s^{-1} , and (b) LSV curve under oxygen atmosphere at scan rate 5 mV s^{-1} , in 50 mM PBS solution of the developed ACF@MnOx	

	electrodes resulted through CA electrodeposition at 1.3 V vs. Ag/AgCl at various time periods of electrodeposition.	179
Figure 125	(a) Voltammogram under nitrogen atmosphere at scan rate 10 mV s ⁻¹ and (b) LSV curve under oxygen atmosphere at scan rate 5 mV s ⁻¹ , in 50 mM PBS solution of the developed ACF@MnOx electrodes resulted through CA electrodeposition at 1.3 V vs. Ag/AgCl for 4 hours at various precursor concentrations.	180
Figure 126	Correlation of MnOx mass loading with (a) potential range, and (b) number of cycles.	181
Figure 127	Behavior of developed CA curve and the correlation of MnOx mass loading (theoretical, experimentally weighed, and Faradic) of the ACF@MnOx material as resulted at various (a,b) potentials (c,d) reaction time and (e,f) precursor concentration dependence.	183
Figure 128	EDX spectrum of (a) ACF and (b) ACF@MnOx resulted after one hour of CA electrodeposition at 1.3 V vs. Ag/AgCl from 25 mM of precursor	184
Figure 129	Predicted manganese oxide composition of the resulted ACF@MnOx at various electrodeposition potentials as calculated based on EDX spectra.....	185
Figure 130	(a) Survey scan XRD spectra of the developed ACF@MnOx electrode at various electrodeposition potentials and (b) XRD spectra of ACF@MnOx resulted from electrodeposition for 1 and 4 hours respectively.....	187
Figure 131	Overview (a,b,c) and closed-up view (d,e,f) of the morphological structure of ACF@MnOx material resulted from electrodeposition potentials respectively of 1.25, 1.3 and 1.4 V vs. Ag/AgCl	188
Figure 132	SEM images of as resulted ACF@MnOx from electrodeposition at 1.3 V vs. Ag/AgCl (a,c) for one hour and (b,c) four hours	188
Figure 133	SEM images of ACF@MnOx at higher magnification resulted from electrodeposition at 1.3 V vs. Ag/AgCl (a,c) for one hour and (b,c) four hours.	189
Figure 134	CA curves of oxygen reduction for various ACF@MnOx electrodes at various applied potentials.	190
Figure 135	As quantified H ₂ O ₂ after one hour of CA for various electrodes at various applied potentials.	190
Figure 136	Degradation of H ₂ O ₂ at the ACF and the ACF@MnOx electrodes.	191
Figure 137	(a) SCMFC operation and (b) its daily-monitored voltage evolution using the ACF@MnOx_C180, ACF@MnOx_C90, and ACF@MnOx_C25 air-breathing cathode respectively.	192
Figure 138	The illustration of ORR catalysis on the air-breathing cathode which contain manganese oxide catalyst [124]	193

Figure 139 EIS of various ACF@MnOx air-breathing cathodes in single chamber microbial fuel cell.....	194
Figure 140 Power density of single chamber MFC with various ACF@MnOx air-breathing cathodes.	195
Figure 141 (a) HER polarization curves as recorded at 5 mV s ⁻¹ on ACF and ACF@Pt in N ₂ -saturated 0.1 M KOH solution (b) durability of ACF@Pt at at -0.98 vs. Ag/AgCl (-0.12 V vs. RHE)	196
Figure 142 The molecular structure of acid orange 7, AO7	196
Figure 143 Kinetic degradation of AO7 at Pt, ACF, and ACF@MnOx cathode by applying a 18 mA current (a) at normal pH (b) for comparison with the presence of common Fenton catalyst FeSO ₄	198
Figure 144 Kinetic degradation of AO7 at normal pH: (a) at various applied currents, and (b) at different electrodes.	199
Figure 145 Demineralization over the two electrodes (a) at total 4 hours of EF treatment and (b) at 5 consecutives cycles.....	200
Figure 146 Kinetic degradation of AO7 over five consecutives cycles, revealing the stabilization of the developed electrode	200

LIST OF TABLES

Table 1	Standard electrode potential of ORR at 25 °C [67].....	26
Table 2	Standard potential (E^0) and calculated half-cell potential of anode and cathode (E_{MFC}) under various MFC conditions. All potentials are versus SHE [68].	30
Table 3	Maximum generated power density of various double chamber MFCs .	36
Table 4	The maximum generated power density of various single chamber MFCs with air-breathing cathode system	37
Table 5	The comparison of carbon-based MFC's anode characteristics.....	44
Table 6	Modification of carbon felt for MFC's anode application	47
Table 7	Various carbon-felt based air-breathing cathodes and their performances in MFC application.....	51
Table 8	Various MFC with air-breathing cathode, which use manganese oxide based catalyst	55
Table 9	Various parameter for electrodeposition MnOx by CV method	74
Table 10	Various parameter for electrodeposition MnOx by CA method	75
Table 11	The initial condition of three independent DCMFC experiments before switching to buffered anodic solution.....	82
Table 12	Various treatment during the DCMFC operation.....	83
Table 13	The SCMFC experiments with various air-breathing cathode system..	89
Table 14	Composition and basic characterization of garden compost [163]	103
Table 15	Anodic solution pH as recorded at the beginning and the end of DCMFC operation.....	119
Table 16	OCV determined from the polarization curve.....	136
Table 17	Electrochemical active surface area (ECSA) and specific electrochemical active surface area (SECSA) derived from voltammogram in alkaline and neutral solution.....	148
Table 18	Electrochemical active surface area (ECSA) and specific electrochemical active surface area (SECSA) of electrodes as concentration dependent derived from voltammogram in alkaline and neutral solution.....	150
Table 19	Summarized Pt mass loading from theoretical calculation, Faradic mass, TGA, and ICP	152
Table 20	Calculated crystallite size derived from the Debye-Scherrer equation	157
Table 21	Data obtained from electroanalytical study of O ₂ reduction.	162
Table 22	Performances comparison of the MFC system	170
Table 23	The consumption of acetate.....	173
Table 24	Prediction of developed manganese oxide (MnOx) based on chemical composition as roughly calculated from EDX spectra.	185
Table 25	Demineralization through EF and EF-like treatment of AO7 at various electrodes.....	199

ABBREVIATIONS AND SYMBOLS

Abbreviation	Name	Firstly used on page
ACF	electroactivated carbon felt	72
ADP	adenosine diphosphate	19
AO7	acid orange 7	91
ATP	adenosine triphosphate	19
AQDS	anthraquinone-1,6-disulfonic acid	24
BE	binding energy	94
BFC	biological fuel cell	15
CA	chronoamperometry	66
CE	coulombic efficiency	35
CF	carbon felt	66
CNT	carbon nano tube	37
CV	cyclic voltammetry	59
DCMFC	double chamber microbial fuel cell	3
DET	direct electron transfer	23
DFT	density functional theory	52
DNA	deoxyribonucleic acid	22
EAB	electroactive bacteria	21
ECSA	electrochemical surface area	143
EDTA	ethylenediaminetetracetic	24
EET	extracelullar electron transfer	106
EF-like	electro-Fenton-like	90
EIS	electrochemical Impedance spectroscopy	66
FTIRS	fourier-transform infra red spectroscopy	95
FADH, FADH ₂	flavin adenine dinucleotide	19
GHG	green house gas	11
GDL	gas-diffusion layer	50
GB	graphite bar	102
HER	hydrogen evolution reaction	7
HNQ	2-hydroxy-1,4,-naphtoquinone	24
ICP-MS	inductively coupled plasma mass spectrometer	97
IHME	institute for health metrics and evaluation	11
IUPAC	International Union of Pure and Applied Chemistry	30
LSV	linear sweep voltammetry	66
MET	mediated electron transfer	23
MB	methylene blue	24
MelB	meldola blue	24
MEC	microbial electrolysis cell	125
MFC	microbial fuel cell	3
NAD, NADH	nicotinamide adenine dinucleotide	19
NDC	nationally determined contribution	12

NR	neutral red	24
NRE	new and renewable energy	12
OCP	open circuit potential	76
OCV	open circuit voltage	16
ORR	oxygen reduction reaction	5
PANI	polyaniline	57
PBS	phosphate-buffered solution	75
PEDOT	poly (3,4-ethylenedioxythiophene)	60
PEFC	photoelectrocatalytic fuel cell	14
PEM	proton exchange membrane	37
PPy	polypyrrole	8
RCF	raw carbon felt	66
RHE	reversible hydrogen electrode	52
RVC	reticulated vitreous carbon	39
SCMFC	single chamber microbial fuel cell	4
SECSA	specific electrochemical surface area	145
SEM-EDX	Scanning Electron Microscopy-Energy Dispersive X-ray	95
SHE	standard hydrogen electrode	15
SSP	stainless steel plate	81
TEA	terminal electron acceptor	17
TGA	thermogravimetric analysis	95
TOC	total organic carbon	91
VRFB	vanadium redox flow battery	27
XRD	X-Ray Diffraction	91
XPS	X-ray photoelectron spectroscopy	93
Symbols	Name	
A	the electroactive area	141
ACF@Pt	Platinum-modified electroactivated carbon felt	7
ACF@MnOx	Manganese-oxide-modified electroactivated carbon felt	7
A_x	A_{an} for anode geometric surface area, A_{cat} for cathode geometric surface area	34
b_{es}	total of released electrons	35
β	is the half-peak width for Pt in radian	157
CF@PPy	Polypyrrole modified carbon felt	85
CF@PPy@Pt	Polypyrrole/Pt-modified carbon felt	8
C	concentration of electroactive molecule	141
C_{dl}	the double layer capacitance at this interface	70
D	the diffusion coefficient	141
Δc	substrate's concentration change, also usually assumed as c^0	35
ΔE	the width of the potential window	67
E_{emf}	electromotive force	20
E_{cat}	cathode potential	20
E_{an}	anode potential	20
E_{MFC}	generated voltage	33

$E(t)$	potential at time t	69
E_0	the amplitude of the signal	69
F	Faraday's constant (96485 C mol^{-1})	29
ΔG_r	Gibbs free energy for specific conditions	28
ΔG_r^0	Gibbs free energy under standard conditions	28
I	current	33
I_p	peak current	141
$I dv$	represents the area under either the cathodic or the anodic voltammogram	60
$I(t)$	is current after shifting in phase ϕ and which has different amplitude with I_0	69
j	current density	78
K	a constant, based on the assumption of uniform size small cubic crystals, $K= 0.93944$	157
L_v	crystallite size	157
λ	the X-ray wavelength	157
M_s	molecular weight of the substrate	35
m_e	the active electrode weight	59
n	number of electrons per reaction mol	29
P_{MFC}	output power	33
Q	the charge transferred in the reaction, expressed in Coulomb	29
R	universal gas constant ($8.31447 \text{ J mol}^{-1} \text{ K}^{-1}$)	29
R_{ext}	external load	33
R_s	the solution-phase resistance	70
R_{ct}	the charge-transfer resistance at the electrode/solution interface	70
S_r or v	scan rate	141
T	absolute temperature	29
Θ	the Bragg's angle.	157
V_{an}	volume of liquid in the anodic compartment	35
ω	the radial frequency (rad/s) that 2π times of the conventional frequency in hertz ($\omega=2\pi f$)	69
Π	reaction quotient calculated as the activities of the products divided by those of the reactants according to: $\Pi = \Pi a_i^{v_i}$ with v_i (stoichiometric coefficient) of the reactants < 0 and v_i of the products > 0	28

General Introduction

General Introduction

The research fields of energy sustainability and water sanitation are part of a challenging worldwide strategy to achieve two global goals i.e. social prosperity and economic development. Until now, world energy consumption is mostly satisfied by fossil fuels (oil, coal, and natural gas). Reservoir depletion and greenhouse gas issues are threatening world energy security, thus encouraging the development of clean and cost-competitive renewable energy sources [1]. An example is electrochemical technology has gave birth of a clean and noiseless energy generator. Electrochemical energy systems promise energy sustainability, effective energy conversion and storage, environmental friendliness, less greenhouse gas emission, and economical reasonableness [2]. Electrochemical energy systems provide energy conversion and energy storage and are mostly available as portable units that can power small devices such as watches or huge transportation systems such as space shuttles [3]. Fuel cells (energy generator) and batteries (energy storage) are the most popular representatives of electrochemical energy systems. Since Alessandro Volta pioneered this field in the 19th century [4], its development has continuously increased, leading to low carbon emissions and low electricity costs.

Biofuel cells, i.e. biologically catalyzed electrochemical energy systems, in particular microbial fuel cells (MFCs), enable the extraction energy from diverse and abundant organic materials, which are in principal more sustainable than conventional fuel cells [5]. The power generated by MFCs still lower than other conventional fuel cells. However, they have a wide variety of advantageous applications. Among them, the most recent interesting application is its feasibility to achieve zero energy depollution [6]. MFCs can degenerate organic waste and/or wastewater simultanesously, using them to generate electricity [7,8].

There are two general type of MFC reactor configuration, double and single chamber [9,10]. The classical type of MFC is double chamber (DCMFC), each chamber correspond to anodic and cathodic which are separated by a membran. In

this system, both chamber involve an aqueous phase. Anodic chamber contains inoculum source and organic substrate as fuel, whereas the cathodic chamber contains electron acceptor specieses in electrolyte solution. Anode and cathode are dipped inside in each part and connected externally by a conductive wire through a resistor. The single chamber MFC (SCMFC) consists of anodic chamber and air-breathing cathode system, in which the aqueous cathodic system is substituted by the gaseous phase [10].

The MFC performances involve a sustain generated voltage, current and power density, which tightly correlates to many factors i.e. the kind of bacteria and its source, substrate, medium condition (pH, temperature), electrode (anode, cathode) material, electron acceptor in cathodic part, reactor configuration, and so on [10,11]. The match integration of these factors can lead to high performance MFC.

Herein, our research intention is in the cathodic part. The classical DCMFC can use various redox active electron acceptors solution in the cathodic part such as ferricyanide and permanganate [8], to facilitate a better cathodic reaction even on an only bare cathode. The use of these redox active electron acceptor promises high voltage output [12,13]. However, once they are being reduced, such electron acceptors hardly to regenerate chemically [14]. Thus, the voltages are going to decline. The only way to recover and/or maintain the voltage is by reload a fresh electron acceptor solution continuously [9,13,14]. Indeed, this necessity leads to an impractical operation [8], additional costs and lowering net energy, which generate the common limitation in a DCMFC system. The use of oxygen can be an alternative to substitute such of redox active electron acceptor, unless it needs an effective catalyst on the cathode for being reduced [8]. Moreover, the oxygen is introduced into DCMFC system by sparging air continuously [8,15], which needs more effort to operate. Owing to these limitations, the application of DCMFC for power generation in large scale is inefficient. However, DCMFC systems still can be routed for attractive application such as wastewater remediation by which the pollutant can be involved as electron acceptor in the cathodic solution for being reduced which subsequently lowers their toxicity [8].

Different with DCMFC, SCMFC with air-breathing cathode system uses the oxygen from free air rather than a dissolved form. The air-breathing cathode that designed to be exposed toward free air provides unlimited passively oxygen supply, which ensures the sustainability of the MFC's operation [15]. Moreover, the single configuration of the reactor is more practicable and more feasible in large-scale application. Since the final product from the cathodic part is water and no pollutants are released during operation [9], this MFC system is also eco-friendly. Therefore, the SCMFC is more attracting for the power source development. The main obstacle of the single chamber MFC is its limited power production due to the sluggish kinetic of the oxygen reduction reaction (ORR) in the cathodic part [16,17]. Using an effective ORR catalyst is essential to improve the effectiveness of air-breathing cathode system which then enhances the SCMFC performances.

The application of garden compost leachate has been shown in our group as an effective electroactive bacterial source for MFC power generation [18,19]. We hypothesized that; 1) by taking part in the cathodic part, garden compost MFC performance can be improved, 2) the air-breathing cathode system can be applied for the garden compost MFC to substitute the aqueous phase cathode, which turns the system into single chamber, which has more advantages, 3) an effective air-breathing cathode can be developed by incorporating an excellent ORR catalyst such as platinum (Pt) and manganese oxide (MnOx).

In this research we have drawn the goal to study the improvement of the MFC performance using garden compost leachate as the bacterial source and the transformation of the classical DCMFC into the SCMFC by replacing a conventional aqueous phase cathode system with a home made air-breathing cathode one. In order to maximize its performance, the garden compost DCMFC was operated using effective electron acceptor, such as ferricyanide and vanadium solution, in the cathodic part. For the SCMFC operation, we fabricated an effective air-breathing cathode by developing material based on carbon felt to contain ORR catalyst i.e. platinum nanoparticles and manganese oxide

nanostructure. Furthermore, the as-developed material was integrated as air-breathing cathode in a reactor that as the same as for the DCMFC operation unless the cathodic chamber was emptied to contain only air, which accomplished the transformation of DCMFC system into an SCMFC. This integration of our homemade air-breathing cathode in our customized reactor to run garden compost SCMFC is being the novelty of our research.

In our work, we firstly selected garden compost as bacterial source to empower an MFC. The application of garden compost, a soil-based rich electroactive bacterial source, promises sustainable MFC system everywhere. Other major considerations are it is cheap, easy to handle, and non-harmful. We applied the garden compost both in a DCMFC and an SCMFC.

The material development for air-breathing cathode in this research consisted of three steps. The first was the selection of the support electrode material and its pretreatment. We selected commercial carbon felt as supporting material because it meets the basic requirements for an electrode. Carbon felt is electrically conductive, has a high surface area, and is mechanically strong. Moreover, it is chemically and electrochemically stable over a long period of time [20–22]. The second step was the catalyst loading onto the support material. On this carbon felt electrode, we layered platinum nanoparticles (standard ORR catalyst) and manganese oxide (second class of ORR catalyst) respectively, by electrodeposition method over various optimization steps. The advantages of electrosynthesis are it is simple, rapid, and works under mild conditions compared to common chemical synthesis. The last part was characterization of the resulted materials from the second step by electrochemical and physicochemical techniques. The electrochemical characterization evaluated the electrocatalytic performance of the materials toward ORR. The physicochemical characterization investigated the morphological structure, atomic composition, and nanoscale structure of the resulted materials. After carefully conducting and interpreting this analysis, we determined the optimum synthesis conditions for fabricating the air-breathing cathode.

In this research, we have successfully grown Pt and MnOx on carbon felt (CF), which resulted in a modified form of CF respectively named as ACF@Pt and ACF@MnOx. The very well-defined Pt nanoparticles have been found to spread up throughout the support material. The catalytic activity of the ACF@Pt toward ORR was found five times higher than that of its raw material. The MnOx also has been grown on the carbon felt surface thoroughly, which showed a nanostructure morphology on the deposited MnOx outer surface. Moreover, the catalytic activity of the ACF@MnOx toward ORR also has been shown better than its pristine.

The application of our home-made air-breathing cathode using both Pt- and MnOx-based catalyst in an SCMFC, powered by garden compost, revealed its feasibility in power generation. It is worth noting that the performance of the MFC is affected by various factors such as anodic conditions, reactor configuration, electrode space, and so on. Therefore, the performance of the MFC still can be improved by optimizing these contributing factors.

We also reported here the other promising application of our developed materials. For example ACF@Pt has been applied as an electrode in a hydrogen evolution reaction, HER. H₂ is a critical chemical feed stock in the modern industries such as ammonia synthesis for fertilizer and petroleum refining [23]. Whereas, ACF@MnOx has shown its feasibility as a promising catalyst in the electro-Fenton-like process for mineralization of azo dye at relatively low current and natural pH condition. Moreover, our preliminary experiment has opened the path for further elaborating the garden compost MFC in an electro-Fenton-like system using our developed ACF@MnOx electrode for wastewater treatment.

This manuscript is organized into three chapters. Chapter 1 presents our bibliographic study, which comprised the fundamental aspects of general fuel cell systems and comprehensive microbial fuel cell system (include electron-generation, electroactive bacterial, thermodynamic overview, power generation, configuration, application and so on). Herein, we also present the principle of electrochemical deposition as the primary method for developing air-breathing

cathode material. Chapter 2 describes all materials used and their specification, the primary equipment used, and experimental procedures used for material synthesis, characterization and application. Chapter 3 presents the results and discussion comprising three major subjects: 1) The study of feasibility of using garden compost in a conventional DCMFC, 2) Air-breathing cathode MFC: material development, construction, and application. The developed material are including polypyrrole/Pt modified carbon felt (CF@PPy@Pt), Pt nanoparticles modified carbon felt (ACF@Pt), and MnO_x modified carbon felt (ACF@MnO_x) 3) Other promising applications of the developed material i.e. ACF@Pt in hydrogen evolution reaction electrocatalysis and ACF@MnO_x in the electro-Fenton-like process for the degradation of azo dye compound.

Chapter 1:
Bibliographic Study

Chapter 1 Bibliographic Study

Fossil fuels, including oil, gas, and coal, are the energy resources most consumed for the world vital needs. Primarily, they are either burns to produce electricity or refine for both heating and transportation fuel [24]. **Figure 1** shows that world consumption of fossil fuel energy resources is almost constant. Only a decrease of 2 % from 1993 to 2011 was observed. By 2020, fossil fuel will still dominate up to 76 % in line with the beginning of renewable era.

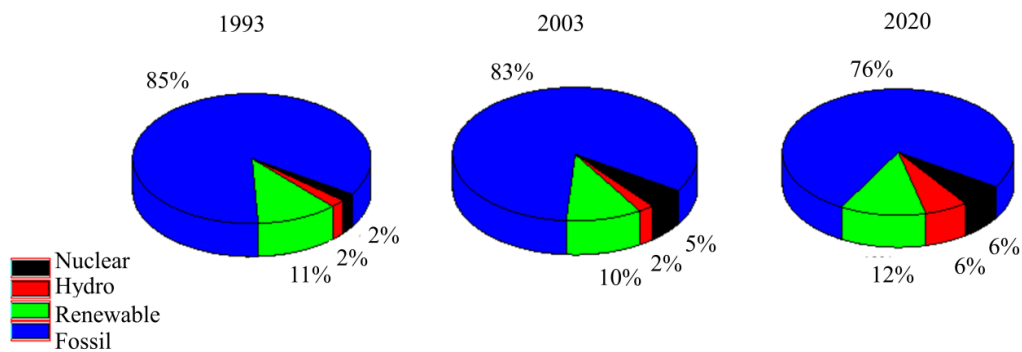


Figure 1 Domination of fossil fuel energy resources in meeting world energy needs[25]

Over the 20 past years, about 75 % of human-caused emissions were related to the burning of fossil fuels [24]. The emission of greenhouse gases (GHGs) such CO₂, NO_x, and SO_x deteriorates the environmental conditions, leading to global warming, ozone layer depletion, acid rain and many other serious environmental problems [1]. The Institute for Health Metrics and Evaluation (IHME) has reported that air pollution was responsible for 5.5 million deaths in 2013 [26].

These severe environmental impacts bring the urgency of a global shift toward cleaner and more efficient energy systems as stated in *World Energy Outlook 2017* [27]. Previously, the Kyoto Protocol and the Paris Agreement were also bringing the same mission for settling internationally binding emission reduction targets. These world energy conventions force the intensification of the use of renewable energy resources [1]. According to the Energy International Association's *World Energy Outlook 2017*, renewables increase 2.8 % per year and by 2040 will provide 31 % of electricity generation i.e. equal to coal [27].

Indonesian government fully supports the Paris Agreement, as committed in the Nationally Determined Contribution (NDC), by improving the utilization of low-carbon energy technology, so-called clean energy technology. In line with this commitment, Indonesian government already has a National Action Plan (RAN-GRK) as stipulated in presidential regulation 61/2011. In addition to RAN-GRK, the government also has issued a National Energy Policy (KEN) in Government Regulation 79/ 2014, which set the new target of new and renewable energy (NRE) at 23 % in 2025 and 31% in 2050, as stated in Indonesia Energy Outlook 2017 [28]. Indonesia has a great potential of NRE but has not been well-developed. Many obstacles, concerning the geographical gap between location of energy supply and high technology demand and investment to develop NRE-based technology, are the main reason for this stagnant NRE development. Realizing this fact, the achieved target of NRE, as calculated in Indonesia Energy Outlook 2018, is only 14.6 % in 2024 and 15.2 % in 2050 [29]. This outlining the importance of NRE-based development breakthrough to reach the national target, as set in Indonesia Energy Outlook 2017. The portable energy generator systems, such as fuel cell, can be one of the reasonable strategies to accelerate the NRE's target achievement. Herein, the fuel cells are especially empowered by biomass-based or biomass-derivative-based fuel. Accordingly, Indonesia has an abundance source of biomass, which can be routed toward the development of a sustainable and renewable fuel.

Renewable energy is produced through on-going natural processes such as sunshine, flowing water, wind, biological processes, and geometrical heat flows. These energy flows can be used directly or indirectly by transforming them into other convenient forms of energy [30]. Renewable energy resources are inexhaustible, cleaner, and have a much lower environmental impact than conventional fossil resources.

The integration of renewable fuel in a fuel cell system realizes an efficient, sustainable, and cleaner energy generator system which concerns to the requirement for the future energy provision as stated in the energy convention. Fuel cells convert chemical energy into electrical energy directly in a one-step

process [2] with a little greenhouse gases (GHGs) emission [31]. This clearly differs from combustion-based heat engines, which involve multi-step processes (from chemical to thermal to mechanical to electrical) [2]. Fuel cells seem to be one of the appropriate candidates to play an important role in reducing GHGs emission [31].

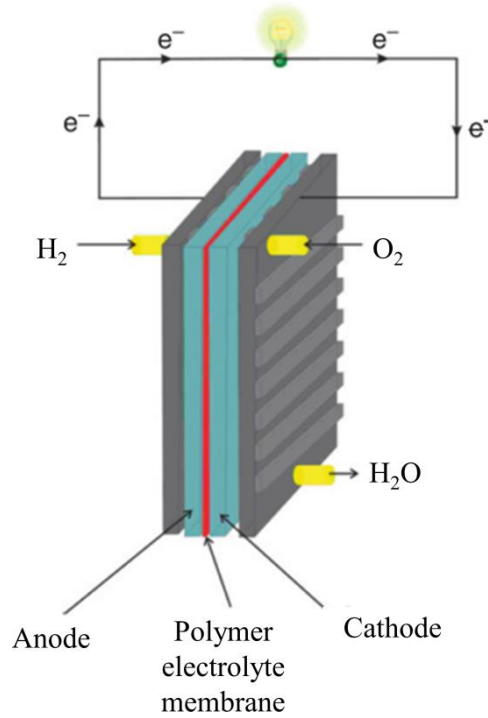


Figure 2 The classical hydrogen-oxygen fuel cell [5]

1.1 Fuel cells

Fuel cells (FC) are electrochemical devices that convert the stored chemical energy in fuels into electrical energy directly [2,5]. The classical fuel cell, the so-called hydrogen-oxygen fuel cell, uses hydrogen (H_2) as fuel and oxygen (O_2) as oxidant. A schematic hydrogen-oxygen fuel cell is presented in **Figure 2**. Principally, the fuel cell contains two main compartments which are connected by an electrolyte membrane. The anode and cathode, externally connected by a conductive wire, are placed in each compartment to which hydrogen and oxygen are supplied respectively. At the anode, the hydrogen gas ionizes to proton (H^+) and releases electrons according to **Eq. 1**. The protons traverse the electrolyte toward the cathode compartment, in which oxygen is present. Subsequently, the generated electrons flow to the cathode through an external circuit. Protons and

electrons are combined at the cathode to reduce the oxygen (**Eq. 2**). The electrons flowing from the anode to the cathode are harvested as electricity. Fuel cells need a continuous supply of both the fuel and the oxidant for sustained power generation [5].



1.2 Photoelectrochemical fuel cell (PEFC)

Photoelectrochemical fuel cell (PEFC) is a special fuel cell, which consume organic fuel and use solar radiation to generate useful forms of energy such as electricity and hydrogen [32,33]. A PEFC contains semiconductor photoanode, metal cathode, and electrolyte. The principle of PEFCs is light-induced electron excitation at photoanode, which resulted in electron (e^-) and holes (h^+). The created holes (h^+) stimulate the oxidation of water on the anode to produce oxygen and proton. On the opposite, proton is reduced to produce hydrogen. The principle reactions of the PEFCs are expressed in **Eqs. 3-6** [33,34].

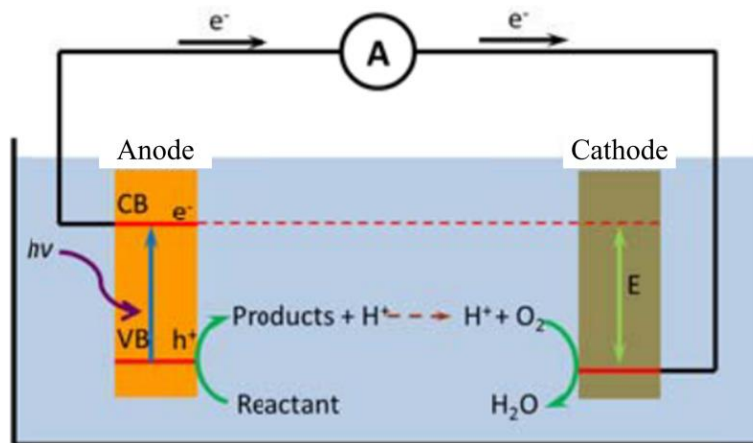
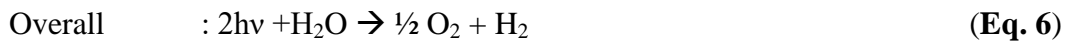


Figure 3 Schematic diagram of PEFC [35]

The schematic diagram of PEFC is presented in **Figure 3**. Photoanode contains semiconductor photocatalyst [32] such as TiO_2 (n-type), InP (p-type), and n-

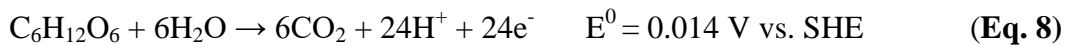
GaAs/p-Inp (n-p type) [33]. The cathode also contains electrocatalyst especially for hydrogen reduction such as Pt [33]. Anode and cathode are connected externally by a conductive wire through a load.

TiO₂ is an effective photocatalyst, which is also commonly used in PEFC [36]. The reaction of TiO₂ under UV lighting is expressed in **Eq. 7** [37]. The oxide absorbs photon from the light sources, which generate electron-hole pairs. These created holes react with the fuel to produce energy. The fuels of PEFC include pure water, alcohols (methanol, ethanol, propanol, etc.), polyols (glycerol, glucose, sorbitol, etc.) and various organic pollutants [33,38].



1.3 Biological fuel cells (BFCs)

Biological fuel cells (BFC) are bio-electrochemical devices that convert chemical energy into electricity through biochemical pathways [5,39] using enzyme catalysis [40]. The enzyme could either as a pure protein or naturally present in living microorganism [5,40]. Based on these biocatalyst, BFCs can be classified as enzymatic fuel cells and microbial fuel cells [5,39]. The principle of the biological fuel cell is the same as that of the conventional chemical fuel cell. Wherein, the bio-fuel and oxidant need to be supplied continuously into the anodic and the cathodic part respectively [5]. A wide variety of bio-fuels [41] and diverse biocatalysts in BFCs have been reported [42]. **Figure 4** shows a schematic diagram of an enzymatic fuel cell prototype working with glucose and oxygen as bio-fuel and oxidant respectively [43]. The enzymatic-catalyzed oxidation of glucose on the anode is according to **Eq. 8** with its potential (E) vs. standard hydrogen electrode (SHE) [5].



Therefore, the complete reduction of the oxidant in the cathodic part proceeds according to **Eq. 9**.



BFCs have many advantages over conventional chemical FCs for example: 1) they are more sustainable due to the abundant availability of diverse organic-based fuels [39]; 2) they are more economically advantageous by applying cost-effective biocatalysts [39]; and 3) they require milder operation conditions i.e. room temperature and neutral pH [5,44]. Nevertheless, the BFCs suffer several drawbacks i.e. low open circuit voltage (E_{OCV}) [45], low stability [45], and low power density, which limit their application [5]. In spite of these limitations, the BFC has shown a promising application as an interesting power source for small electronic devices such as implantable medical biosensor [45].

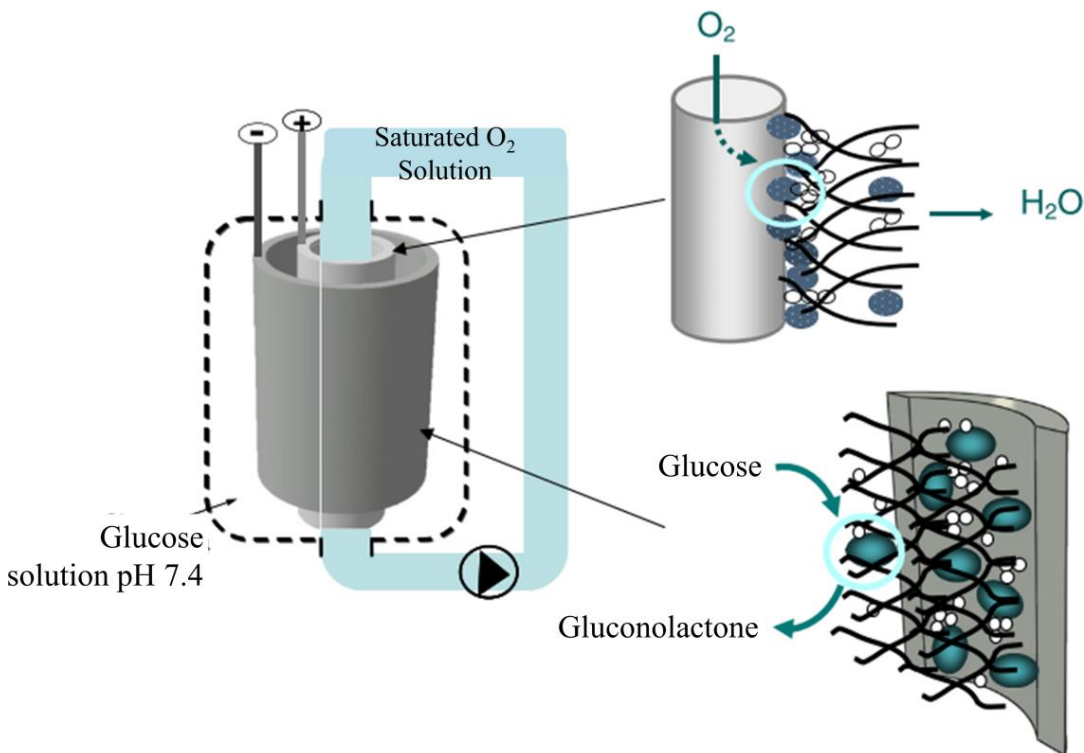


Figure 4 Schematic diagram of a concentric glucose/O₂ BFC prototype using enzyme-based biocatalyst [43]

1.4 Microbial fuel cells (MFCs)

The microbial fuel cell, MFC, is a type of BFC using whole living microorganisms as multi-enzyme biocatalyst system to convert organic-based fuel directly to electricity [5,39,41]. Potter (1911) was the first to propose the idea that microbes are able to generate electricity [20,41]. However, high interest in MFCs started to appear only around 1980s, after power output enhancement due to redox mediator addition was discovered [11]. In the two last decades, the MFCs have

attracted great attention due to its capability of transformation organic waste into electricity [20]. The number of articles published on MFC have increased dramatically since 2003 [10,41]. To date, the MFC researches are intensively conducted, resulting in significant progress in many aspects: 1) the understanding of the electro-generation mechanism [20]; 2) the advancement of materials, operating conditions, reactor designs and configurations [46]; and 3) its various possible applications. However, several important challenges remain, especially power enhancement and the feasibility of the MFC application in real environments [20,46].

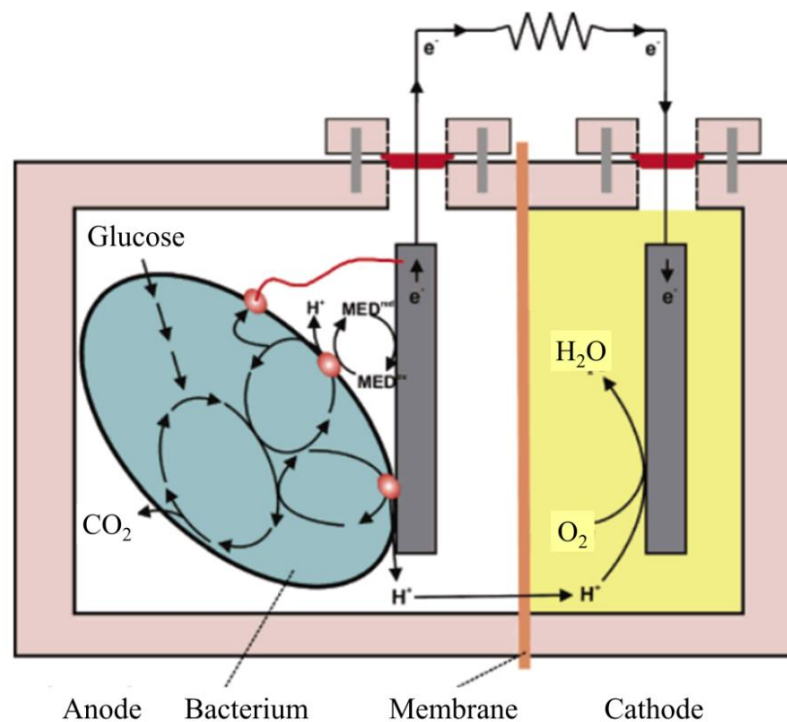


Figure 5 Schematic diagram of conventional two-chamber microbial fuel cell separated by a membrane. On the left is the anodic compartment, where microbes produce electrons by degrading organic substrate, and on the right is the cathodic compartment, which contains the terminal electron acceptor (TEA) [47].

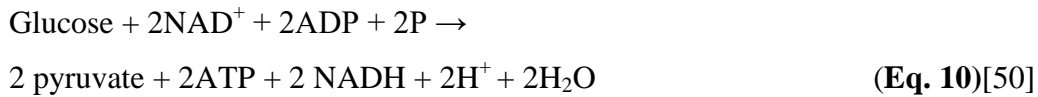
The principle of the MFC is coupling the oxidation of organic materials catalyzed by microorganisms in the anodic part with reduction of terminal electron acceptor (TEA) species in the cathodic part [47]. **Figure 5** shows a schematic of the general principle of the MFC. Microbial-catalyzed oxidation of organic materials produces electrons and protons. The released electrons flow toward the cathodic part through the external circuit. The produced protons are transported to the

cathodic part, pass through the membrane to maintain charge balance and complete the electrical circuit. Finally, the continuous flow of electrons from the anode to the cathode can be harvested as electricity [10,47].

1.4.1 Electrogeneration

In an MFC, microbes use the whole cell to biocatalyze oxidation of the fuel which allows multiple enzymes to cooperate [39]. Electrons are generated through microbial catabolism [44] by which the organic molecules are broken down through sequences of enzyme-catalyzed reactions, with the release of energy in the form of ATP (adenosine triphosphate) [44,48].

Catabolism, or cellular respiration, involves three main stages: 1) glycolysis; 2) citric acid cycles, or Krebs cycles (**Figure 6**); and 3) extracellular electron transfer [49]. Glycolysis breaks down glucose (fatty acids or amino acids in a different way) into two pyruvates (3-membered carbon compounds). This process involves a ten-step biochemical pathway, which is expressed in simplified form as shown in **Eq.10** [49].



The pyruvates are further oxidized (catalyze by pyruvate oxidase) into acetyl units of acetyl CoA prior to entering the Krebs cycle. Pyruvate oxidation leads to the reduction of nicotinamide adenine dinucleotide, NAD^+ to NADH (**Eq.11**) [48].



The Krebs cycle is a nine-step metabolic process that completes the decarboxylation of acetyl CoA into carbon dioxide [49]. The entering acetyl CoA initially merges with oxaloacetate (four-membered carbon compound) to form citrate (six-membered carbon compound). The next two reaction steps are oxidative decarboxylation of isomerized citrate-to- α -ketoglutarate (five-membered carbon compound) and α -ketoglutarate-to-succinate (four-membered carbon compound) respectively, by each release of one molecule of carbon dioxide. Thereafter, the succinate is converted back to oxaloacetate (through

three-step reaction) to complete the whole citric acid cycle or Krebs cycle[51]. One cycle results in electron carriers in the form of NADH and flavin adenine dinucleotide, FADH₂ [48].

NADH and FADH₂ are electron carriers that enable the transfer of electrons from the cytoplasm, where the citric acid cycle occurs, as shown in **Figure 6**, to the cell membrane [48]. The electrons are transferred through several membrane intermediaries which pump protons out of the cell as they are reduced (**Figure 7**). The generated proton gradient, mediated through the ATP synthase transmembranar protein, is used by the cell to phosphorylate adenosine diphosphate, ADP and produce ATP [48].

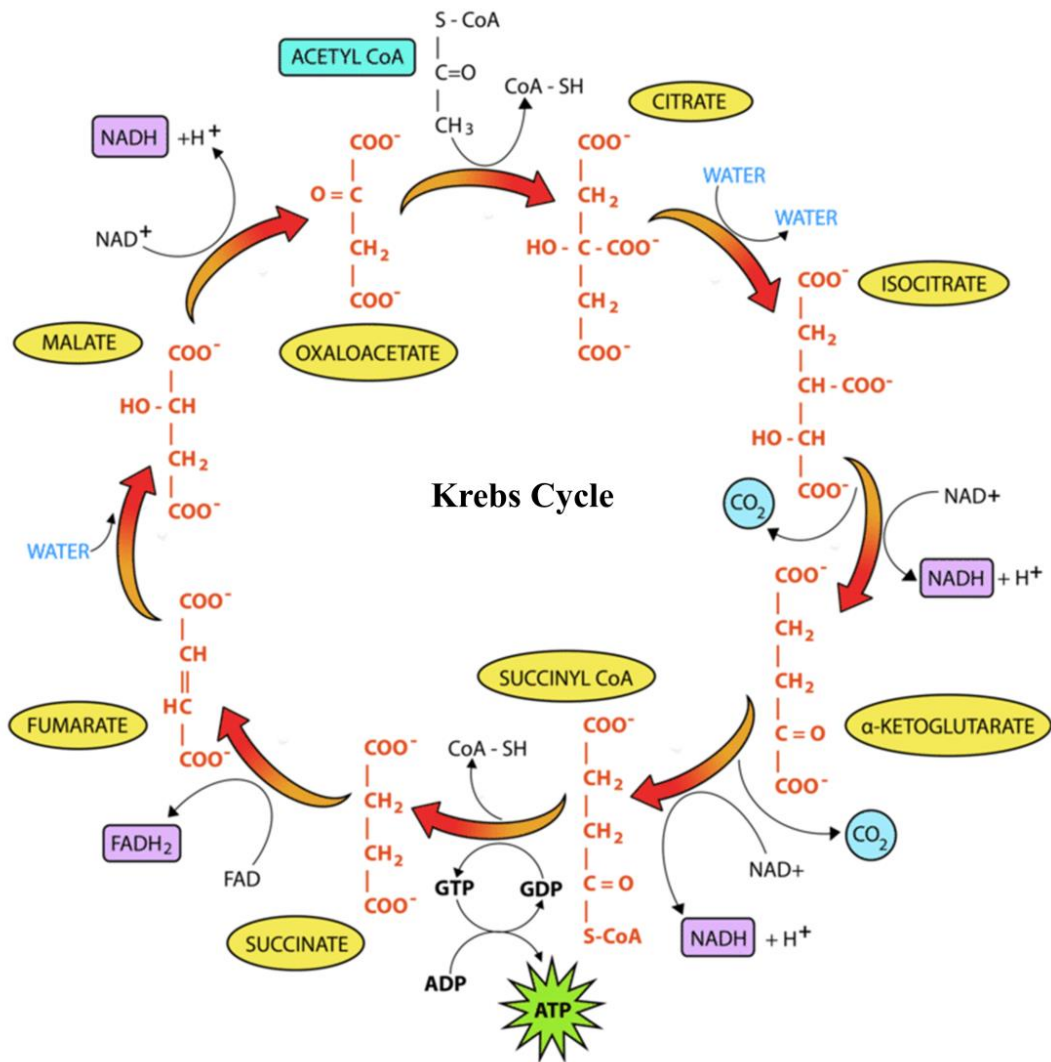


Figure 6 Generation of electron carriers, NAD and FADH₂, through the Krebs cycle [52]

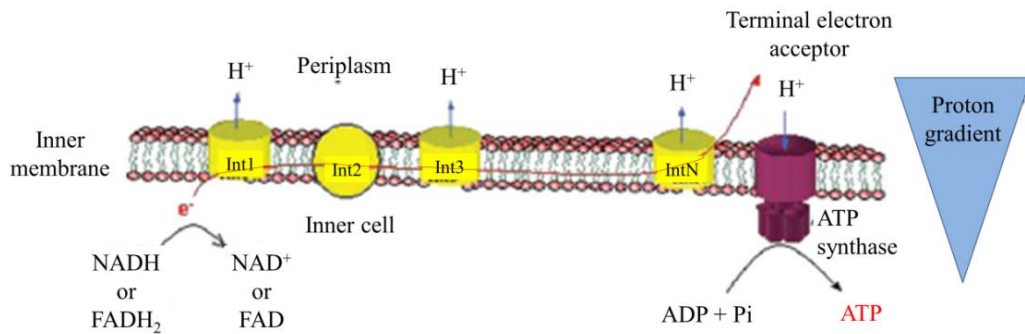


Figure 7 Schematic diagram of bacterial membrane respiration [48].

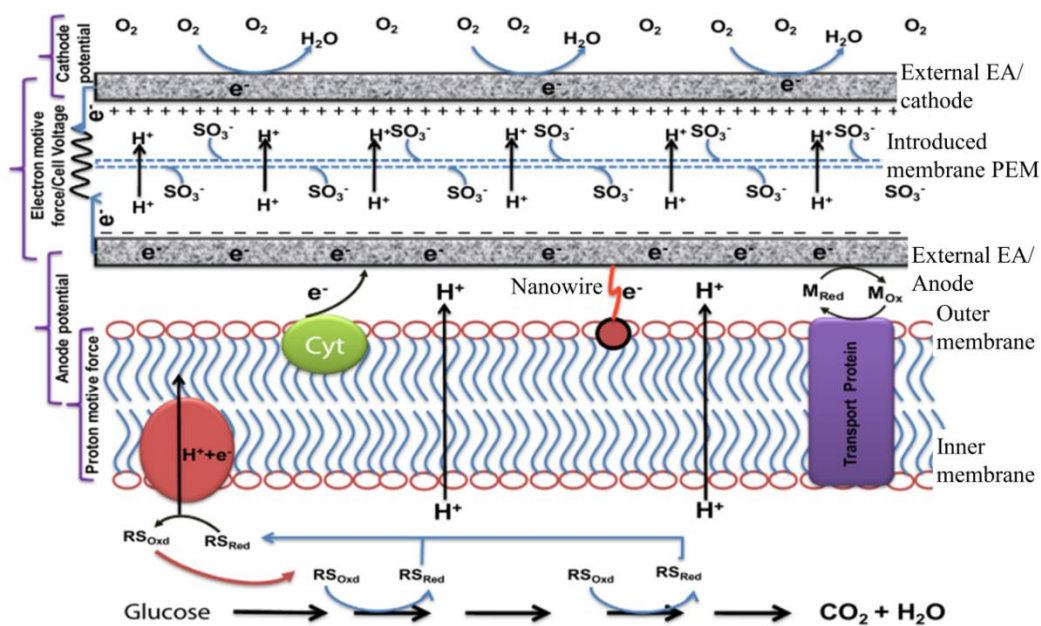


Figure 8 Schematic representation of voltage generation in an MFC [10]

1.4.2 Principle of voltage generation in MFCs

The microbial generated electron can be harnessed by artificially introducing an electrode (solid electron acceptor) into the MFC anodic compartment. This stimulates the development of the potential difference between the bacterial membrane and the anode, which contributes to the anode potential that helps in the electron delivery. The electrons that are drawn to the anode induce negative potential, while the migrating protons develop the positive potential of the cathode. The potential difference between anode and cathode is referred to as the electromotive force (E_{emf}) or cell voltage (**Eq. 12**). This potential drives the

mobility of electrons from anode to cathode through external circuits across the load, which can be harvested as electricity [10]. The history of voltage generation in an MFC is schematically presented in **Figure 8**.

$$E_{\text{emf}} = E_{\text{cat}} - E_{\text{an}} \quad (\text{Eq. 12})$$

Where,

E_{emf} : electromotive force (V)

E_{cat} : cathode potential (V)

E_{an} : anode potential (V)

1.4.3 Electroactive microorganism/biocatalyst

MFCs use microorganisms that are capable of exocellular electron transfer, and are called exoelectrogens [53], electricigens [54] or defined here as electrochemically active or electroactive bacteria (EAB) [10]. EABs are mostly species from the Proteobacteria class [53] such as *Aeromonas*, *Desulfuromonas*, *Escherichia coli*, *Shewanella*, *Geobacter*, and *Pseudomonas* species [48].

Geobacter and *Shewanella* are the most studied EABs for mono-strain MFC purposes [10]. The use of single culture bacteria in an MFC could have the benefit with high power generation. However, a pure culture has special requirements for both the strain's growth and metabolic activities, and strictly sterile and aseptic conditions to operate [10]. Therefore, the use of a pure culture in an MFC is usually intended only to study a specific organism and its electro-activity [39] at laboratory scale rather than being applied in industrial applications [10].

The application of mixed-culture microbes as biocatalyst to empower an MFC has been studied widely [10]. Mixed-cultured bacteria abundantly present in wastewater [55], marine and river water, sediment [56] and soil [57]. They also can be collected from anaerobic or aerobic bioreactors [10]. These unlimited resources promote the mixed-culture bacteria as promising MFC power generators with many attractive potential applications such as wastewater remediation.

1.4.4 Electroactive biofilm

Bacteria, both pure and mixed culture, always tend to form a biofilm. In which communities of microbes (bacteria, algae, and fungi) stick together and colonize

the surface. The cells are bonded together by a self-produced polymeric matrix, which consists of proteins, deoxyribonucleic acid (DNA), and polysaccharides, i.e. so-called extracellular polymeric substances (EPS) [58]. The development of biofilm is important for the survival [59] and reproductive success of the microorganisms [60].

Biofilm formation involves five consecutive steps (**Figure 9**): 1) reversible attachment 2) irreversible attachment 3) micro-colony development 4) maturation and 5) biofilm dispersal. The planktonic bacteria initially start a weak and reversible adherence on the surface through the cell appendages. This stage can lead to stable attachment or the bacteria can return to their planktonic state. In the irreversible stage, the cells start to settle on the surface by producing an extracellular matrix to assist cell-to-surface adhesion. The attached cells gather together to form a micro-colony, which continues to grow by proliferation. Mature biofilm mostly contains EPS that consists of polysaccharide, nucleic acid, proteins, lipids, and other biopolymers. EPS facilitate the adhesion, scaffolding, and 3D architecture of the cell. Besides, it also gives the cell protection toward various stresses. Dispersion is a final step, in which some bacterial cells are dispersed out and revert to planktonic growth. Dispersion can be triggered by many factors, such as temperature change, starvation, oxygen deficiency, and metabolite accumulation [58].



Figure 9 Schematic representation of biofilm formation steps [58]

The growing biofilm can be electroactive, non-electroactive, or a mixture of both depending on the type of bacterial source. In MFC application, electroactive biofilm is more interesting because of its biocatalytic role in hydrolyzing the

substrate for proton and electron production. In theory, more electro-active biofilm leads to more electricity production.

1.4.5 Mechanism of electron transfer

The anode chamber of MFC contains bacterial consortia which either lead to biofilm formation or stay in their planktonic state [10]. Considering these two bacterial states, the electron transfer from cell-to-anode can be classified into two mechanisms: direct electron transfer (DET) and mediated electron transfer (MET) [10,44].

1.4.5.1 Direct electron transfer (DET)

Biofilm-forming microorganisms can transfer electrons directly from the cell membrane to the electrode due to physical contact [44] either through the outer surface of the microbial cells (**Figure 10a**) or cell appendages (**Figure 10b**) [61]. The direct electron transfer (DET) mechanism occurs in the bacteria that have redox protein in its outer membrane (OM). The redox protein, such as c-type cytochrome (a multi-heme protein), allows electron transfer to an external solid acceptor (MFC anode). This protein is obviously present in the sediment inhabiting metal reduction microorganisms such as *Geobacter*, *Rhodospirillum rubrum* and *Shewanella* [10]. Both *Geobacter sulfurreducens* [62] and *Shewanella oneidensis* [63] can produce conductive pilus-type appendages or nanowire that allow the better electron delivery process [44].

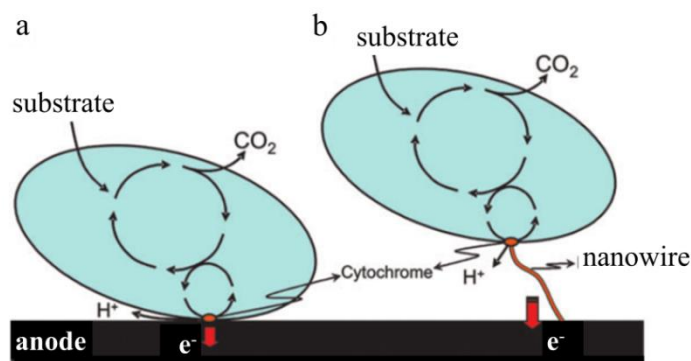


Figure 10 Schematic representation of DET through (a) cell membrane and (b) cell appendage (nanowire) [44]

1.4.5.2 Mediated electron transfer (MET)

Planktonic microorganisms rely on a mediator as electron shuttle to perform the electron transfer from cell-to-anode [10]. The mediator can be either an organic or an inorganic compound that serves as a reversible terminal electron acceptor. It can be artificially added or secreted through the bacterial metabolism [61]. The mediator in oxidized state enables to move across the membrane, grabs the electrons from the electron transport chain, and releases them either to a solid oxidant (anode) or into the aerobic layers of the biofilm. The mediator is readily re-oxidized and be available for the subsequent redox processes. For this purpose, the mediator should: 1) possess enough positive potential to allow a high electrode reaction rate [64]; 2) move easily across the cell membrane [64]; 3) possess good solubility in the anolyte for a long MFC run time [10,64]; 4) be non-biodegradable [10]; and 5) be non-toxic or non-interfering toward microbial metabolism processes [10,64]. The MET mechanism, as shown in **Figure 11**, represents an effective means to link the bacterial metabolism to the anode. However, the mechanism varies depending on the nature of the redox species [44].

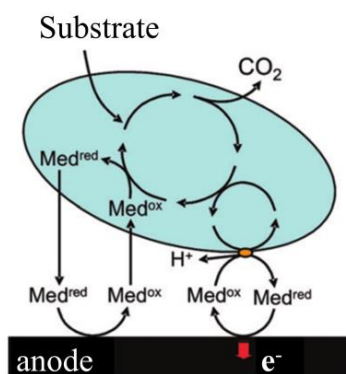


Figure 11 Schematic illustration of MET through secondary metabolites, wherein shuttling occurs via the outer cell membrane cytochrome and via periplasmic or cytoplasmic redox couple [44].

An artificial mediator is usually added to the anodic solution or immobilized on the anode [39,64]. Typical synthetic exogenous mediators include dyes and metal-organics such as anthraquinone-1,6-disulfonic acid (AQDS) [64], neutral red (NR) [65], methylene blue (MB), thionine, meldola blue (MeIb), 2-hydroxy-1,4-naphthoquinone (HNQ) and iron(III) ethylenediaminetetraacetic (FE(III)EDTA) [10]. However, artificial mediators are potentially toxic and can harm microbial

life as well as the environment [44]. Moreover, the application of this exogenous mediators in MFC is also technologically impractical because of the necessity of their regular addition [44].

Some bacteria can release electron shuttling molecules through their secondary metabolism pathway which is stimulated by a lack both of soluble and solid electron acceptors [10,44]. Some naturally secreted mediators are pycocyanin, phenazines, phenoxazines, and quinone (**Figure 12**) [10]. Pycocyanin and phenazines, produced by *Pseudomonas aeruginosa*, reveal an efficient electron transfer [10,44]. The presence of this self-produced mediator should have further advantages in MFC application since it eliminates the need of artificial mediator. One molecule of a self-secreted mediator is enough to serve thousands of redox cycles [44]. Only a small amount of this mediator directly produced in the anodic biofilm, allows the microbe to pull electrons out at a sufficiently high rate [44].

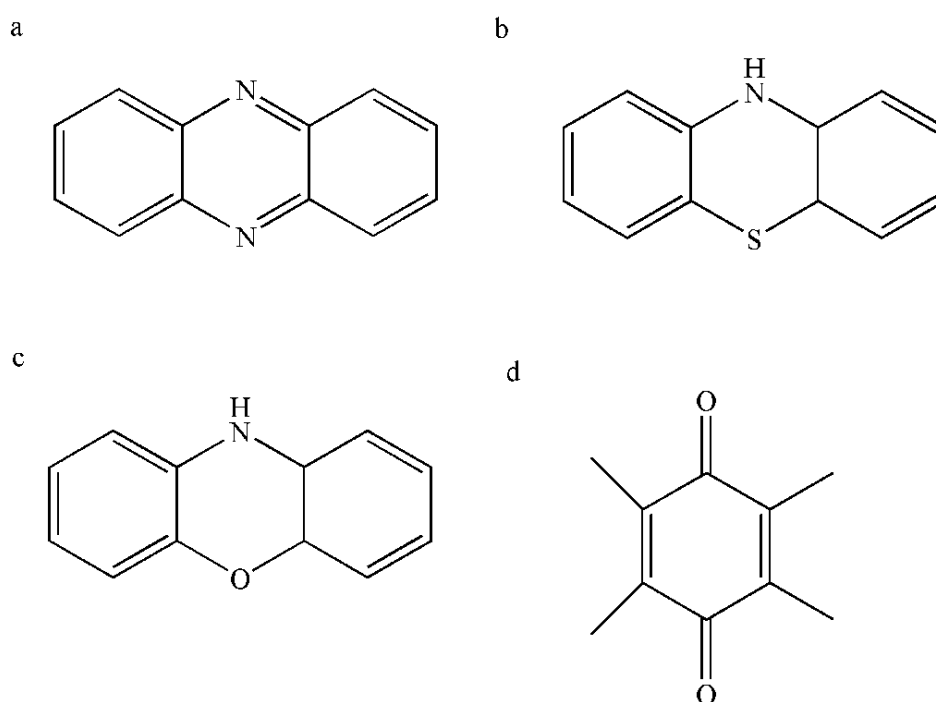


Figure 12 Molecular mediator compounds (a) phenazine, (b) phenothiazines, (c) phenoxazines, and (d) quinones.

1.4.6 Electron acceptor in MFC

As the electrons and protons arrive at the cathode, the existing electron acceptors are readily reduced. The reduction rate of the electron acceptors contributes to the

efficiency of power generation in the MFC [10]. Electron acceptors have specific physical and chemical properties which lead to a certain oxidation potential and finally affect the efficiency of electricity production [8]. Dissolved oxygen, ferricyanide, or manganese oxide have been used as aqueous electron acceptors in a double chamber MFC [12].

1.4.6.1 Oxygen

Oxygen is considered the most suitable electron acceptor for MFC due to its high redox potential and its unlimited availability in the atmosphere [66]. Oxygen can be provided in the cathodic compartment by sparging air into the water or by using an air-breathing cathode [8]. The oxygen reduction reaction in an aqueous solution can follow two pathways: 1) a 4-electron transfer mechanism, by which the oxygen is reduced directly into water; and 2) a 2-electron transfer mechanism, which involves hydrogen peroxide formation. The standard electrode potentials of the ORR vs. standard hydrogen electrode (SHE) are listed in **Table 1**. A limitation of oxygen is its slow kinetics, which results in poor contact with the normal carbon electrode [8].

Table 1 Standard electrode potential of ORR at 25 °C [67]

Aqueous solution	ORR reaction	Standard electrode potential, V vs. SHE
Acidic solution at pH 0	$O_2 + 4H^+ + 4e^- \rightarrow 2H_2O$	1.229
	$O_2 + 2H^+ + 2e^- \rightarrow H_2O_2$	0.695
	$H_2O_2 + 2H^+ + 2e^- \rightarrow 2H_2O$	1.76
Alkaline solution at pH 14	$O_2 + 2H_2O + 4e^- \rightarrow 4OH^-$	0.401
	$O_2 + H_2O + 2e^- \rightarrow HO_2^- + OH^-$	-0.065
	$HO_2^- + H_2O + 2e^- \rightarrow 3 OH^-$	0.867

1.4.6.2 Ferricyanide

Ferricyanide ($Fe(CN)_6^{3-}$) is an excellent cathodic electron acceptor for the double chamber MFCs, which generates more power than oxygen with a Pt-carbon

cathode [8,12]. It facilitates efficient electron transfer on the cathode [68]. Ferricyanide has a low overpotential and also a low internal resistance, which allows a higher reaction rate and higher power output respectively [8,68]. Owing to its excellent natural electrochemical performance, no additional cathode catalyst is needed [68].



The adjusted value for ferricyanide according to **Eq. 14** is 0.361 V vs. SHE at T 298 K [12].

$$E = E^0 - \frac{RT}{F} \ln \left(\frac{[\text{Fe(CN)}_6]^{4-}}{[\text{Fe(CN)}_6]^{3-}} \right) \quad (\text{Eq. 14})$$

1.4.6.3 Manganese dioxide

Manganese oxide is a good cathode material and catalyst for batteries and alkaline fuel cells [8]. MnO₂ has also been shown to be an electron acceptor or electron mediator that facilitates electron transfer from the cathode to the electron acceptor [8]. Rhoads et al. have revealed this possibility by growing biomineralized MnO₂ on the cathode to accept electrons from the anode and then be firstly reduced (**Eq. 15**). The subsequent reduction results in the manganese ions, Mn²⁺, which being released into the solution (**Eq. 16**). Thereafter, Mn²⁺ is oxidized back to MnO₂ by manganese-oxidizing bacteria (**Eq.17**) [69].



1.4.6.4 Vanadium

Vanadium (V) has a high redox potential in acidic conditions and its application as electron acceptor in MFC has been reported [70–72]. Vanadium could be a pollutant that found in wastewater of vanadium mines [8]. Therefore, by applying it as electron acceptor in the cathodic part of an MFC can provide a route to treat wastewater that contains vanadium.

The application of vanadium acceptor electrons in MFC's cathodic part mimics a vanadium redox flow battery (VRFB), as schematically shown in **Figure 13**. In the VRFB system, the VO₂⁺/VO²⁺ in the cathodic part is coupled to the V³⁺/V²⁺ in

the anodic part. The main advantage of the VRFB system is its feasibility to recharge both catholyte and anolyte solution to their initial fresh condition. The reaction, in each part during discharge, is according to **Eqs. 18** and **19** respectively [73].

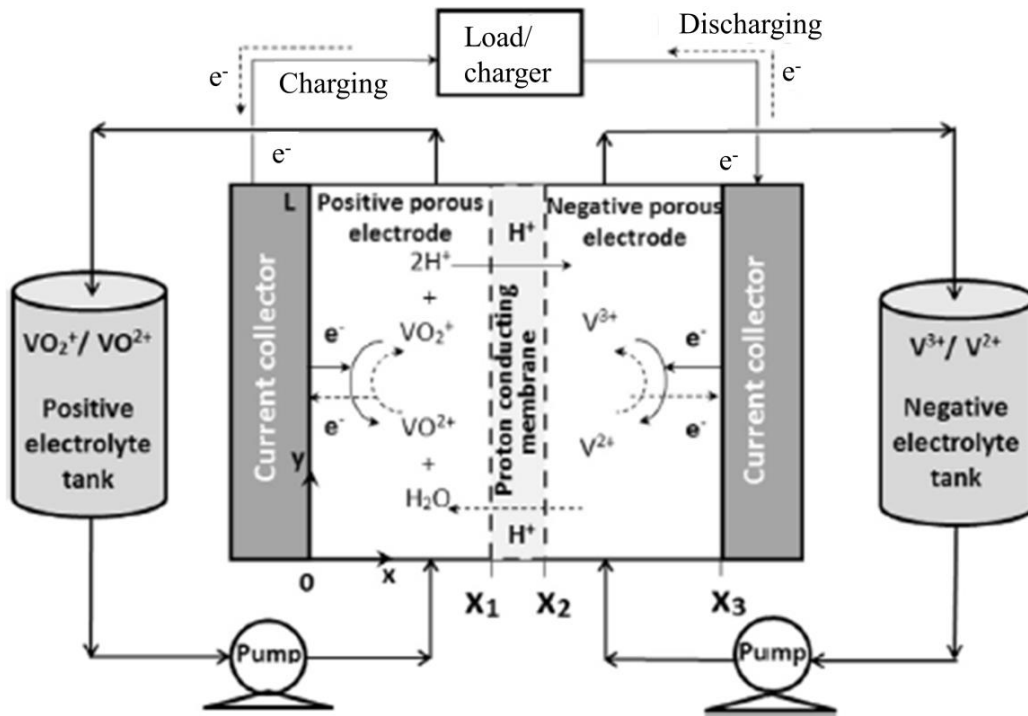
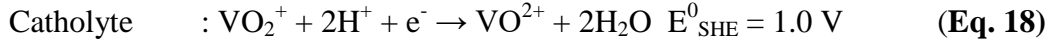


Figure 13 System configuration of vanadium redox flow battery (VRFB) [73].

1.4.7 Thermodynamics overview

The reaction can be evaluated in terms of Gibbs free energy, which is a measure of the maximal work that can be derived from a reaction, calculated as follows (Eq.20):

$$\Delta G_r = \Delta G_r^0 + RT \ln(\Pi) \quad (\text{Eq. 20})$$

where

ΔG_r : Gibbs free energy for specific conditions (J mol^{-1})

ΔG_r^0 : Gibbs free energy under standard conditions (J mol^{-1}), $T = 298.15 \text{ K}$, 1 bar pressure, activity = 1 for all species

R : universal gas constant ($8.311447 \text{ J mol}^{-1} \text{ K}^{-1}$)

T : absolute temperature (K)

Π : reaction quotient calculated as the activities of the products divided by those of the reactants according to: $\Pi = \Pi a_i^{v_i}$ with v_i (stoichiometric coefficient) of the reactants < 0 and v_i of the products > 0

The reaction is thermodynamically favorable when $\Delta G_r < 0$. For MFC calculations, we prefer the term of the overall cell electromotive force (E_{emf}) to evaluate the reaction. Herein, we can relate E_{emf} of the MFC to work, W (J), produced by the cell, or:

$$W = E_{emf} \cdot Q = -\Delta G_r \quad (\text{Eq. 21})$$

Where,

$$Q = nF \quad (\text{Eq. 22})$$

Q : the charge transferred in the reaction, expressed in Coulomb (C)

n : number of electrons per reaction mol

F : Faraday's constant (96485 C mol⁻¹)

Combining **Eq. 21** and **Eq. 22**, we have:

$$E_{emf} = -\frac{\Delta G_r}{nF} \quad (\text{Eq. 23})$$

If all reactions are evaluated at standard condition, $\Pi = 1$, then:

$$E_{emf}^0 = -\frac{\Delta G_r^0}{nF} \quad (\text{Eq. 24})$$

Where,

E_{emf}^0 : standard cell electromotive force (V)

The overall reaction in terms of potential can be expressed as:

$$E_{emf} = E_{emf}^0 - \frac{RT}{nF} \ln(\Pi) \quad (\text{Eq. 25})$$

The calculated E_{emf} through **Eq. 25** provides the upper limit of the cell voltage. However, the measured potential generated from the MFC is usually lower due to various potential losses [47].

1.4.8 Standard electrode potential

By International Union of Pure and Applied Chemistry, IUPAC, convention, standard potential is written as a reduction potential, i.e. the reaction is written as the consumption of electrons [68]. Thus the oxidation of acetate at the anode is written according to **Eq. 26**.

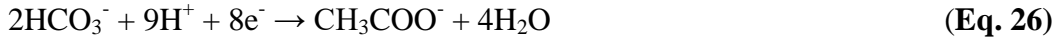


Table 2 Standard potential (E^0) and calculated half-cell potential of anode and cathode (E_{MFC}) under various MFC conditions. All potentials are versus SHE [68].

Electrode	Half cell reaction	E^0 / V	Condition	$E_{\text{MFC}} / \text{V}$	Ref
Anode	$2\text{HCO}_3^- + 9\text{H}^+ + 8\text{e}^- \rightarrow \text{CH}_3\text{COO}^- + 4\text{H}_2\text{O}$	0.187	$[\text{HCO}_3^-] = 5 \text{ mM}$, $[\text{CH}_3\text{COO}^-] = 5 \text{ mM}$, pH = 7	-0.298	[47]
	$2\text{HCO}_3^- + 9\text{H}^+ + 8\text{e}^- \rightarrow \text{CH}_3\text{COO}^- + 4\text{H}_2\text{O}$	0.187	$[\text{HCO}_3^-] = 5 \text{ mM}$, $[\text{CH}_3\text{COO}^-] = 16.9 \text{ mM}$, pH = 7	-0.300	[47]
	$2\text{HCO}_3^- + 9\text{H}^+ + 8\text{e}^- \rightarrow \text{CH}_3\text{COO}^- + 4\text{H}_2\text{O}$	0.187	$[\text{HCO}_3^-] = 35 \text{ mM}$, $[\text{CH}_3\text{COO}^-] = 5 \text{ mM}$, pH = 8.6	-0.418	[74]
	$\text{CO}_2 + \text{HCO}_3^- + 8\text{H}^+ + 8\text{e}^- \rightarrow \text{CH}_3\text{COO}^- + 3\text{H}_2\text{O}$	0.130	pH = 7	-0.284	[68]
	$6\text{CO}_2 + 24\text{H}^+ + 24\text{e}^- \rightarrow \text{C}_6\text{H}_{12}\text{O}_6 + 6\text{H}_2\text{O}$	0.014	pH = 7	-0.428	[68]
Cathode	$\text{O}_2 + 4\text{H}^+ + 4\text{e}^- \rightarrow 2\text{H}_2\text{O}$	1.229	pO ₂ = 0.2 pH = 7	0.805	[47]
	$\text{O}_2 + 4\text{H}^+ + 4\text{e}^- \rightarrow 2\text{H}_2\text{O}$	1.229	pO ₂ = 0.2 pH = 10	0.627	[47]
	$\text{O}_2 + 2\text{H}^+ + 2\text{e}^- \rightarrow \text{H}_2\text{O}_2$	0.695	pO ₂ = 0.2, [H ₂ O ₂] = 5 mM, pH = 7	0.328	[47]
	$\text{Fe}(\text{CN})_6^{3-} + \text{e}^- \rightarrow \text{Fe}(\text{CN})_6^{4-}$	0.361	$[\text{Fe}(\text{CN})_6^{3-}] = [\text{Fe}(\text{CN})_6^{4-}]$	0.361	[47]
	$\text{MnO}_2(\text{s}) + 4\text{H}^+ + 2\text{e}^- \rightarrow \text{Mn}^{2+} + 2\text{H}_2\text{O}$	1.23	$[\text{Mn}^{2+}] = 5 \text{ mM}$, pH = 7	0.470	[47]

The theoretical anode potential, E_{an} , can be calculated using **Eq. 27**. Herein, we assume the activities of the different species equal to their concentration. For the oxidation of acetate, as an example, we have:

$$E_{an} = E_{an}^0 - \frac{RT}{8F} \ln \left(\frac{[CH_3COO^-]}{[HCO_3^-]^2 [H^+]^9} \right) \quad (\text{Eq. 27})$$

Thus, for the theoretical cathode potential, E_{cat} , by considering oxygen as terminal electron acceptor in the cathodic part, we can write:



and

$$E_{cat} = E_{cat}^0 - \frac{RT}{4F} \ln \left(\frac{1}{pO_2 [H^+]^4} \right) \quad (\text{Eq. 29})$$

The calculated theoretical anode and cathode potentials for typical conditions of an MFC are also presented in **Table 2**.

1.4.9 MFC performance parameters

1.4.9.1 Polarization

The open circuit voltage (OCV) is the voltage across the terminal of the cell when no external current flows (unlimited external resistance) [75]. It is usually close to the thermodynamic voltage for the system and is theoretically calculated according to **Eq. 7**. Considering an MFC with acetate as fuel and oxygen as oxidant, the potential anode and cathode can be expressed as in **Eq. 27** and **Eq. 29**, respectively.

A polarization curve, shown in **Figure 14**, is a plot of cell potential against current density under a set of constant operating conditions. It is the standard electrochemical technique to characterize the MFC's performance [76] in terms of how well the MFC maintains the voltage as a function of current production [68]. It also gives information on performance loss during operation [76].

To obtain the polarization curve, the MFC voltage is measured through a series of different resistances in the circuit. Then, the measured voltage of each resistance can be plotted as shown in **Figure 15**. The current is obtained by calculation using Ohm's law and subsequently normalizing it to the geometric surface area of the limiting electrode (anode or cathode, depending on the case).

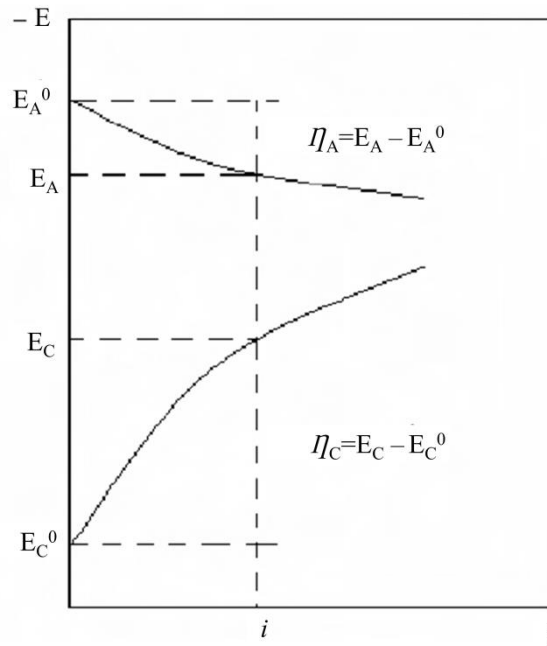


Figure 14 Polarization curve of anode and cathode [76]

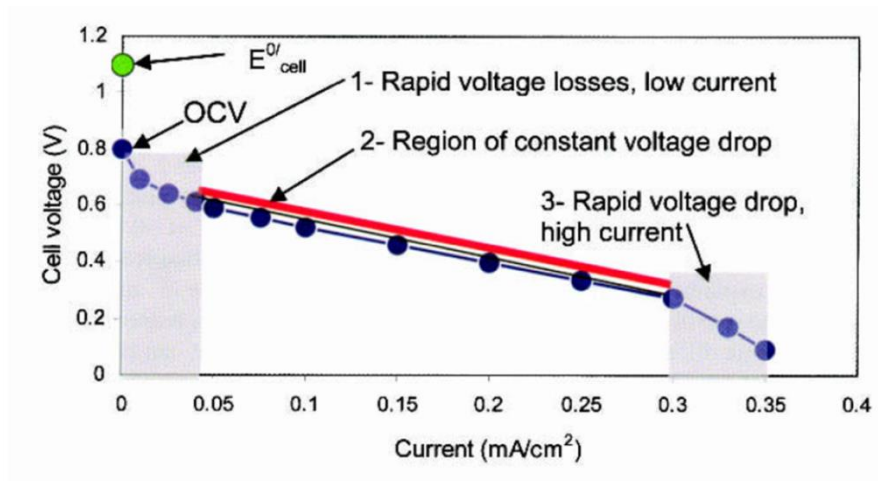


Figure 15 The polarization curve of MFC [68]

1.4.9.2 Voltage loss

Voltage loss can be classified into three categories: 1) activation loss (activation polarization); 2) ohmic loss (ohmic polarization); and 3) concentration loss. At low current density, the cell's potential drops sharply mostly due to energy loss as heat for oxidation initiation in the anode or reduction in the cathode and energy loss during electron transfer from the cell membrane to the anode surface. Several ways to reduce activation loss are by improving the cathode kinetics, selecting bacteria, and improving the membrane-to-anode electron transfer. At intermediate

current density, the ohmic resistance mainly originates from the resistance of ions (solution conductivity), membrane (if present) and the electrical wiring. Many efforts to limit ohmic loss rely on the reduction of the electrodes spacing, selection of a low resistance electrode and coating, or increasing the ionic conductivity of the electrolyte. At high current density, the cell performance drops drastically due to the mass transport limit of the reactant(s) to the electrode and subsequently, the product(s) out of the electrode [68,76].

1.4.9.3 Power generation

Power production is one of the key parameters of MFC performance [68]. Typically, the output power is determined from the cell voltage and the delivered current (**Eq. 30**). The generated MFC voltage is routinely measured across the fixed load by a multimeter of high impedance in order to minimize any current flow in the voltmeter, whereas the current can be calculated using Ohm's law (**Eq. 31**) or directly measured using a multimeter [47,77,78]. During our thesis work, a polarization function (E_{cell} vs I) was obtained when the cell was connected to an external variable resistance load R_{ext} (R_{ext} varied from 1 M Ω to 10 Ω) and the voltage/current produced on the load was measured with a high impedance multimeter.

$$P_{\text{MFC}} = E_{\text{MFC}} \times I \quad (\text{Eq. 30})$$

$$E_{\text{MFC}} = U = R_{\text{ext}} \times I \Rightarrow I = \frac{E_{\text{MFC}}}{R_{\text{ext}}} \quad (\text{Eq. 31})$$

By combining **Eqs. 30** and **31**, the output power can be calculated by using either **Eq. 32** or **Eq. 33** [47,77,78].

$$P = \frac{E_{\text{MFC}}^2}{R_{\text{ext}}} \quad (\text{Eq. 32})$$

or

$$P = R_{\text{ext}} \times I^2 \quad (\text{Eq. 33})$$

where

P_{MFC} : output power (W)

I : current (A)

E_{MFC} : generated voltage (V)

R_{ext} : external load (Ω)

It is obvious that the current produced by a cell depends on the size of the electrodes. Thus, the current density (j) and power densities (P) should be given as a function of the geometric surface area of the current-limiting electrode (**Eq. 34**), which can be the cathode or the anode and in the particular case of an MFC, normalization volume can be considered (**Eq. 35**) [68]. Usually, the data are normalized by the geometrical surface area of the exposed to the solution (accounting for either single or both sides of the modified electrodes, but not taking into account the internal surface of the 3D-electrodes) that is determined to be the current-limiting electrode [47,77,79].

$$P = \frac{E_{MFC}^2}{A_x R_{ext}} \quad (\text{Eq. 34})$$

Where,

A_x : A_{an} for anode geometric surface area, A_{cat} for cathode geometric surface area (m^2)

or

$$P = \frac{E_{MFC}^2}{V.R_{ext}} \quad (\text{Eq. 35})$$

Where V is the total reactor volume (m^3)

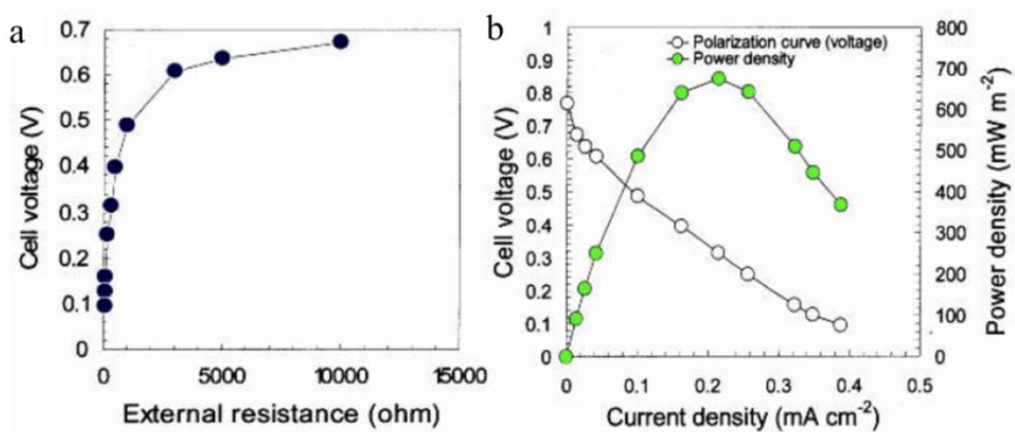


Figure 16 (a) Measured voltage at each resistance, (b) polarization (current density vs. cell voltage) and power density (current density vs. power density) curves [68].

1.4.9.4 Power density curves

Power density and current are plotted to form the power curve (**Figure 16b**). The power density maximum is obviously determined from the top of the power curve

[68]. The power density of various double chamber and single chamber MFCs is listed in the **Tables 3** and **4**, respectively.

1.4.9.5 Coulombic efficiency

Coulombic efficiency (CE) is defined as fraction (or percentage) of electrons recovered as current versus that in the starting organic matter [68](**Eq.36**). CE is another important MFC parameter, which implies the capability of the system to extract as much electrons stored in the biomass as possible [68]. CE calculation is according to **Eq.37**.

$$CE = \frac{\text{Coulomb recovered}}{\text{total Coulomb in the substrate}} \quad (\text{Eq. 36})$$

$$CE = \frac{M_s \int_0^{tb} I dt}{F b_{es} v_{an} \Delta c} \quad (\text{Eq. 37})$$

Where,

CE : Coulombic efficiency

M_s : molecular weight of the substrate (g mol^{-1})

I : generated current (A)

F : Faraday's constant ($96,485 \text{ C mol}^{-1}$)

b_{es} : total of released electrons

v_{an} : volume of liquid in the anodic compartment (L)

Δc : substrate's concentration change, also usually assumed as c^0 (mol L^{-1})

Table 3 Maximum generated power density of various double chamber MFCs

Anode	Cathode	Electron acceptor	Microorganism source/substrate	Power density	Ref
Stainless steel foam/Poly ethylene imine/reduced graphene oxide (SSF/PEI/rGO)	Carbon felt/Poly-NiTSPc	Dissolved O ₂ in KNO ₃ 0.1 M	Garden compost/ acetate	24.8 mW m ⁻²	[18]
Carbon felt/Poly Neutral Red	Nickel plate	Ferricyanide 20 mM	Yeast /glucose	6.1 mW m ⁻²	[65]
Graphite bar/Polypyrrole	Platinized Titanium Sheet	Dissolved O ₂ HCl 0.1 M	Garden compost/acetate	25 mW m ⁻²	[19]
Reticulated vitreous carbon vs. Graphite felt	Reticulated vitreous carbon vs. graphite felt	Buffered ferricyanide 50 mM	<i>Shewanella oneidensis</i> / lactate	24 mW m ⁻² vs. 10 mW m ⁻²	[80]
Graphite brush	Activated carbon bcloth	Sodium percarbonate vs. ferricyanide	Activated sludge/ acetate	9.6 W m ⁻³ vs. 14 W m ⁻³	[81]
Carbon fiber felt	Carbon fiber felt	Vanadium (V) pH 2	Sludge/ glucose	419 mW m ⁻²	[72]
Carbon cloth/Bio-Paladium	Carbon paper / Pt	Phosphate buffer solution	Anaerobic sludge/ acetate	605 mW m ⁻²	[82]
Carbon Nano Tube/Polyaniline/Graphite felt	Plain carbon cloth	Ferricyanide 50 mM	<i>Shewanella putrefaciens</i> / acetate	257 mW m ⁻²	[83]
Alumina/nickel nanoparticles-dispersed carbon nanofiber (AA:Ni-ACF/CNF)	Alumina/nickel nanoparticles-dispersed carbon nanofiber (AA:Ni-ACF/CNF)	K ₂ Cr ₂ O ₇ 200 ppm	<i>Eschechrichia coli</i> / sucrose-acetate	1530 mW m ⁻²	[84]

Table 4 The maximum generated power density of various single chamber MFCs with air-breathing cathode system

Anode	Air-breathing cathode	Bacterial source/substrate	Power density	Ref
Carbon cloth	carbon/ poly tetrafluoroethylene, PTFE/Pt	Domestic wastewater/ glucose	766 mW m ⁻²	[85]
Heat treated carbon cloth	carbon/PTFE/Fe-pthalocyanine	Domestic wastewater/glucose	634 mW m ⁻²	[86]
Carbon cloth	carbon cloth/PTFE/Pt	Domestic wastewater/ polyalcohol: galacticol	2650 mW m ⁻²	[87]
Graphite granules	carbon cloth/ PVDA/ β -MnO ₂	<i>Klebsiella pneumoniae</i> strain L17/glucose	3773 mW m ⁻³	[88]
Carbon cloth	Carbon cloth/polypyrrole/ carbon black	Activated sludge/glucose	401.8 mW m ⁻²	[89]
Carbon brush	carbon cloth/PTFE/Pt	Domestic wastewater/ acetate	1370 mW m ⁻²	[90]
Graphite fiber brush	carbon/PTFE/meso porous nitrogen rich carbon (MNC)	Domestic wastewater/acetate	979 mW m ⁻²	[91]
Carbon cloth	carbon cloth/PTFE/cobalt oxide nanocarbon (CoO-NCNT)	Anaerobic sludge/acetate	469 mW m ⁻²	[92]
Carbon felt	Electrodeposited Pt nano particles, Pt NPs, on activated carbon felt	Garden compost leachate / acetate	140 mW m ⁻²	[93]

1.4.10 MFC reactor design

1.4.10.1 Double chamber MFC (DCMFC)

An MFC reactor is typically designed in a double chamber configuration, as previously shown in **Figure 5**. The anodic chamber contains bacteria solution and is separated by a membrane from cathodic chamber, which contains aqueous electron acceptor. There are several types of DCMFC reactor designs such as H-type, flat-plate, and tubular designs [68,94].

An H-shaped MFC (**Figure 17a**) constructed by connecting two bottles with a tube containing a proton exchange membrane (PEM) or salt bridge. This configuration leads to high internal resistance. Therefore, H-type MFCs obviously produce a low power density [68]. Flat-plate type MFCs (**Figure 17b**) are

typically two square-shaped reactors joined by placing a membrane in the middle [94]. This design is able to reduce the internal resistance since the anode and cathode can be adjusted closer to each other [68]. Hence, flat-plate MFCs types are mostly preferred up to now due to their better performance. Moreover, they can be also stacked together to achieve higher voltage (in series) and/or current (in parallel) [94].

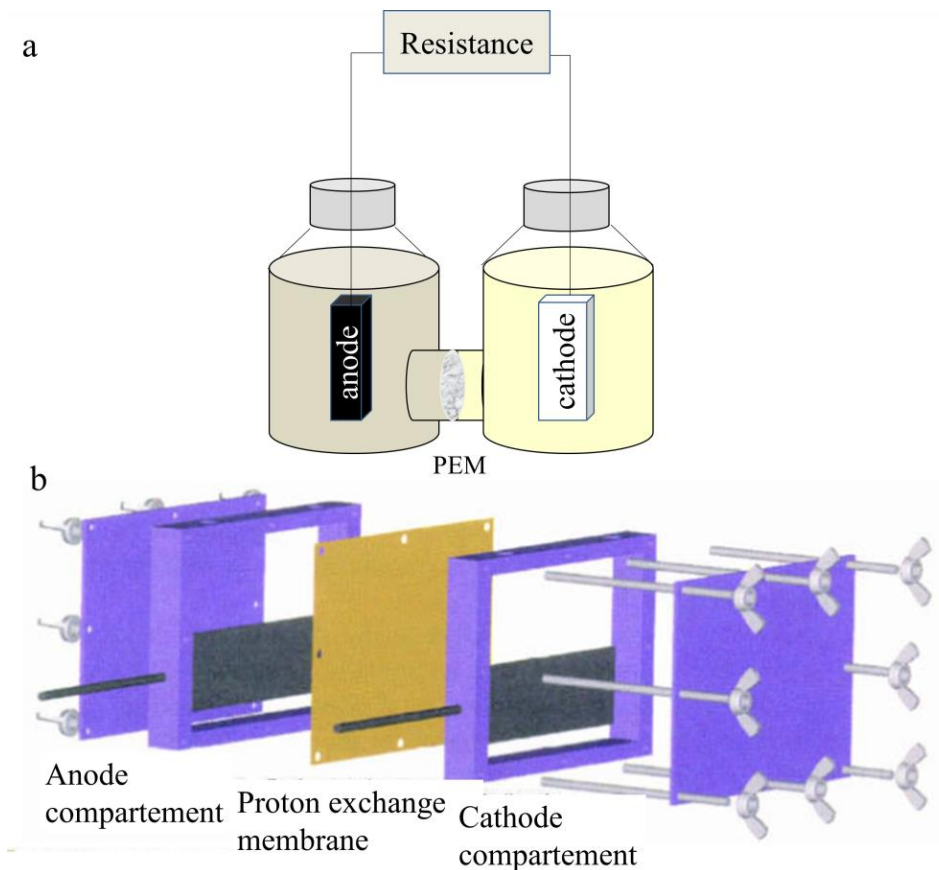


Figure 17 (a) H-type and (b) flat-type double chamber MFC [95]

Double chamber MFCs in various tubular shapes are schematically presented in **Figure 18**. The first type (**Figure 18a**) is a tube that has an inner compartment and an outer compartment, separated by a PEM. The inner side of the tube, acting as an anodic chamber, is filled with packed granulated anode material and bacterial solution. The outer compartment is the cathodic chamber, which contains the catholyte as well as the electron acceptor. The second type of tubular shaped MFC (**Figure 18b**) is only slightly different with the first one in the arrangement of the cathodic chamber. It has a U-shaped tube that is placed in the tube core along with

the packed anode. The tubular shape MFCs are designed to operate in a flowing system, wherein the anolyte and catholyte are recirculated [68]. Another tubular configuration for MFCs (**Figure 18c**), developed by He, et al. 2005, is constructed by positioning a packed of reticulated vitreous carbon (RVC) as the cathode above and the anode below, and placing a PEM in between them [96].

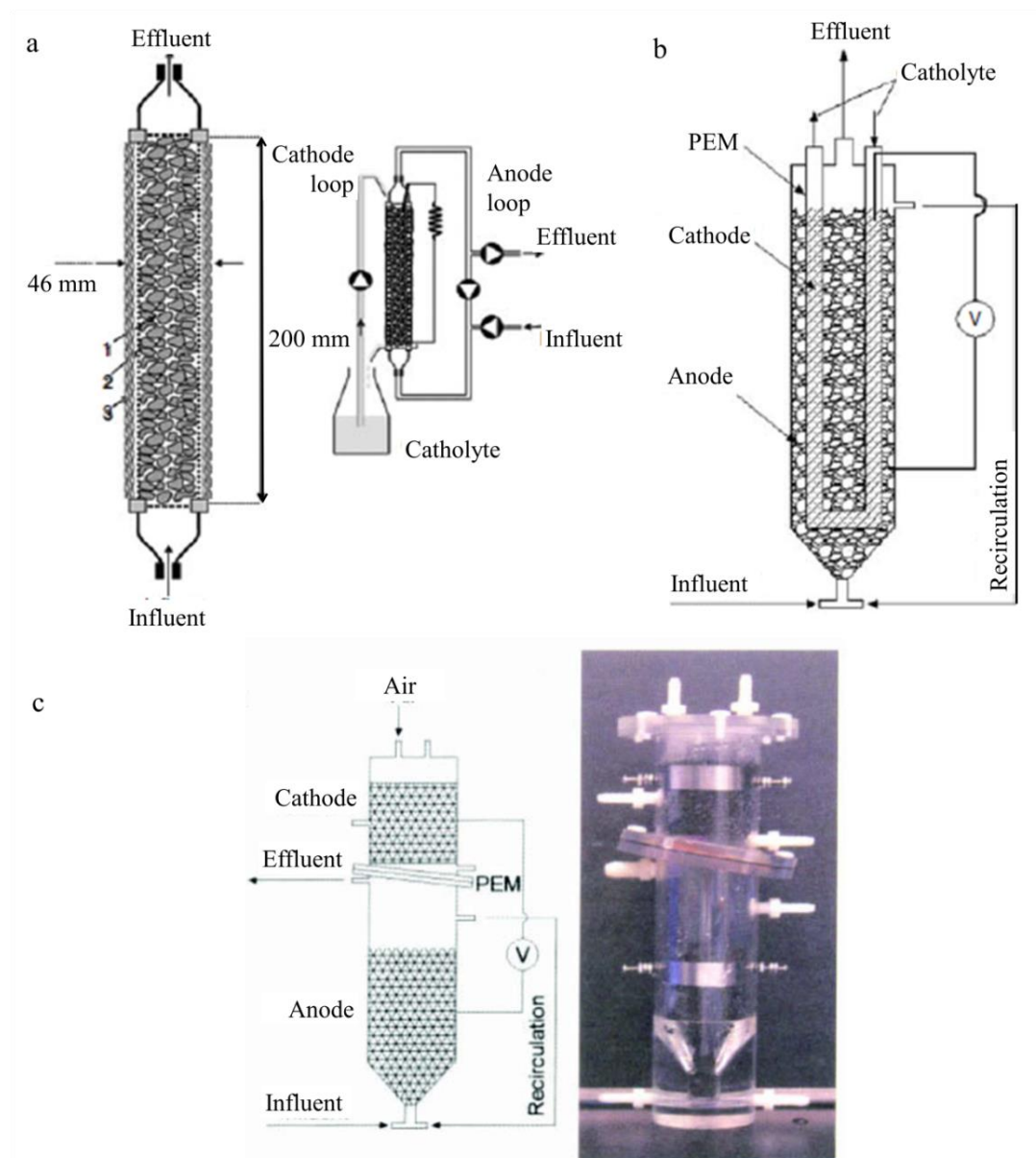


Figure 18 Various tubular type of double chamber MFCs (a) packed bead anode inside and cathode outside, separated by a membrane [97], (b) interior cathode immersed in the packed bead of the anode [98], (c) up-flow system with packed reticulated vitreous carbon (RVC) both in the anode (bottom) and the cathode (top) [96].

1.4.10.2 Single chamber MFC (SCMFC)

a. Cube reactor SCMFC

The cube reactor MFC (**Figure 19**), first developed by Liu and Logan 2004, is a simple design that is frequently used and has been widely reported. The reactor is square-shaped and has an inner tube with a diameter of around 3 cm. It is commonly made of acrylic (poly(methyl methacrylate), PMMA) or lexan™ (polycarbonate). The two electrodes are fixed on opposite ends. The two openings are prepared on top so the reactor to be easily drained and filled. All components are installed in a very well-sealed condition to avoid leakage and keep maintain the anaerobic environment [68,99].

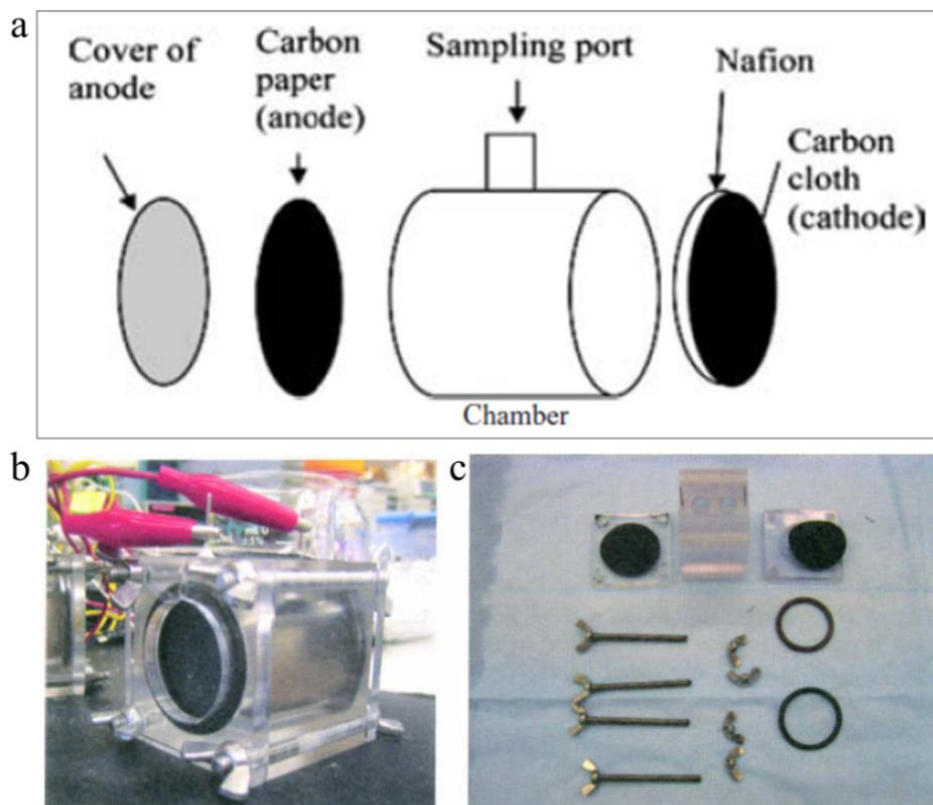


Figure 19 Schematic diagram (a), prototype (b), and separated components (c) of a cube shaped of single chamber MFC [99]

b. Bottle type SCMFC

Figure 20 shows the bottle type SCMFC prototype. In this case, the reactor is constructed by modifying a standard media laboratory bottle to contain a side arm with a large diameter. The cathode is placed at the opening end of the side arm

and held tightly by a short side arm extension. Beforehand, on the cathode, for example made of carbon cloth, a diffusion layer was made at the air-side to prevent leakage and evaporation [68,100].



Figure 20 Bottle shaped MFC with air-breathing cathode [100]

c. Tubular type SCMFC

The tubular type SCMFC was first developed by Liu et al. in 2004, as shown in **Figure 21**. In this design, the air cathode is positioned in an acrylic core tube which surrounded by eight graphite rod anodes. The cathode is made by hot-pressing Nafion onto carbon cloth and then wrapped inside the acrylic tube. All eight graphite rods are connected to the cathode with a wire. Air is flowed into the cathodic tube hole to allow air-cathode-oxygen contact [68,101].

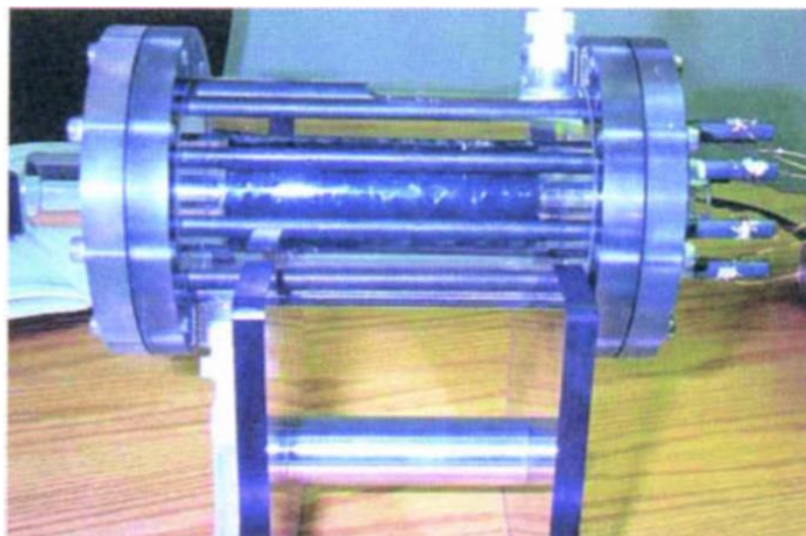


Figure 21 Tubular single chamber MFC [101]

d. Flat-plate SCMFC

The development of a flat-plate SCMFC (**Figure 22**), first done by Min and Logan in 2004, was initially motivated by the hydrogen fuel cell. It is well known that hydrogen fuel cells produce higher power due to their low ohmic resistance, as the electrodes are arranged closer to each other. Two plates (each 15 x 15 x 2 cm) are cut to form a serpentine flow path through the system, which mimics a plug-flow type reactor. The Nafion, as PEM, was sandwiched between the two plates. The bacterial solution and air are flowed through the anodic and cathodic flow path respectively [102].

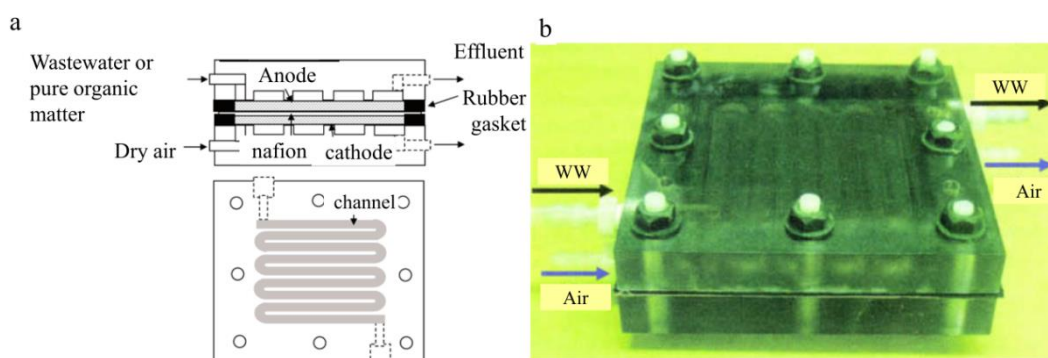


Figure 22 Schematic diagram (a) and prototype (b) of a flat-plate type single chamber MFC [68,102]

Nafion, a polymer created by DuPont Company, is the most widely used for PEMs in fuel cells. The structure of Nafion contains an aliphatic perfluorinated backbone with ether-like side chains ending in sulfonate cation exchange sites (**Figure 23**). Owing to its structure, which mimics Teflon, Nafion shows long-term stability under oxidative and reductive conditions. In a dry state, the ionic clusters are dispersed in a continuous tetrafluoroethylene phase. When the membrane adsorbs water, the ionic domain swells and forms proton-conducting channels above a critical water content [76].

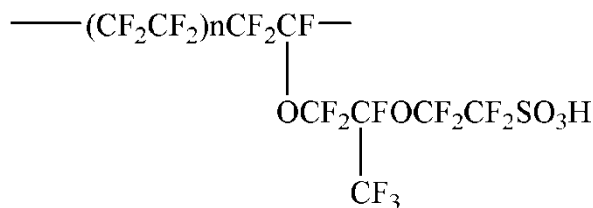


Figure 23 Chemical structure of Nafion membrane [76]

1.4.11.2 Electrode material

The electrode is an essential part of the MFC, which determines its performance in power generation and operating cost [103]. Some requirements of basic electrode are conductiveness, chemical stability, high mechanical strength, and low cost [103]. A bare, unmodified electrode, are usually used as supporting material and current collector. The application of a bare electrode in an MFC usually results in poor performance. Therefore, it is obvious to modify the bare electrode to obtain a more appropriate electrode for MFC application purposes.

According to its modification, the electrode in an MFC can be classified as a bioelectrode and a chemical electrode. A bioelectrode, bioanode or biocathode, is a modified electrode that contains immobilized biocatalyst. Chemical electrodes are obtained through a wide variety of chemical modifications and are mainly used for air-breathing cathodes and air-aqueous cathodes [103].

a. Anode for MFC

The anode is the place where microorganisms can grow to catalyze the oxidation of organic substrates [64]. The growth of electroactive bacteria is greatly affected by the nature of the anode surface, which accepts the electrons from bacterial metabolism [10]. The anode material must also provide a conducive environment for bacterial growth and electrical connections [68]. The suitability of the anode material is essential to minimize electron loss and to increase power generation [10]. The basic electrode for bioanode development purposes should be biocompatible, have high surface roughness, facilitate efficient electron transfer between bacteria and the anode surface [103], and have a large surface area for their feasibility in large scale application [10]. The microbial generated electrons will travel from its generation point on the electrode surface to the collection point (anode-wire connection point). Therefore, electrode materials with low internal resistance are required in order to minimize the ohmic loss, which leads to low power production. Moreover, the anode material should be highly conductive but also non-corrosive as well [68].

i. Carbon-based material

Carbon-based materials are the most common anode materials in MFCs that meet electrode requirements such as biocompatibility, good chemical stability, highly conductivity and low cost. Carbon-based anodes are used in various configurations such as plane, packed and brush structures [103]. Carbon electrodes with a thin plane structure are carbon cloth, carbon paper, and graphite planes or sheets. Carbon felt and graphite felt have a thicker plane structure composed of fibrous structure. A carbon electrode with a brush configuration, such as a graphite brush, is an ideal current collector due to its large surface area, high porosity and efficiency. The brush is made of carbon fibers that are cut, wound, and then twisted around a core of a conductive and non-corrosive titanium wire. In other cases, the anode has a conductive granular packing form, for example, graphite granular packing that fills the anodic chamber in such a biological filter way [103]. Various carbon-based anodes are presented in **Figure 24a-i**. The comparison of carbon-based anode characteristics in MFC application has been resumed [104] as shown in **Table 5**.

Table 5 The comparison of carbon-based MFC's anode characteristics

Anode	Advantages	Disadvantages	Ref.
Graphite rod	Good electrical conductivity, chemical stability, economist, and availability	Low surface area	[101,105]
Graphite fiber brush	Higher specific surface area and easy to produce	Clogging, expensive	[100,106]
Carbon cloth	High surface area, large porosity, high electrical conductivity, flexibility, mechanical strength	Expensive	[20,106]
Carbon paper	Easy to connect wiring	Expensive, Fragile	[107]
Carbon felt	High electrical conductivity, fibrous structure, large surface area, large porosity, mechanical strength, cheap	Large resistance	[20–22]
Reticulated vitreous carbon (RVC)	Good electrical conductivity and plasticity, great porosity	Large resistance and fragile	[20,98]

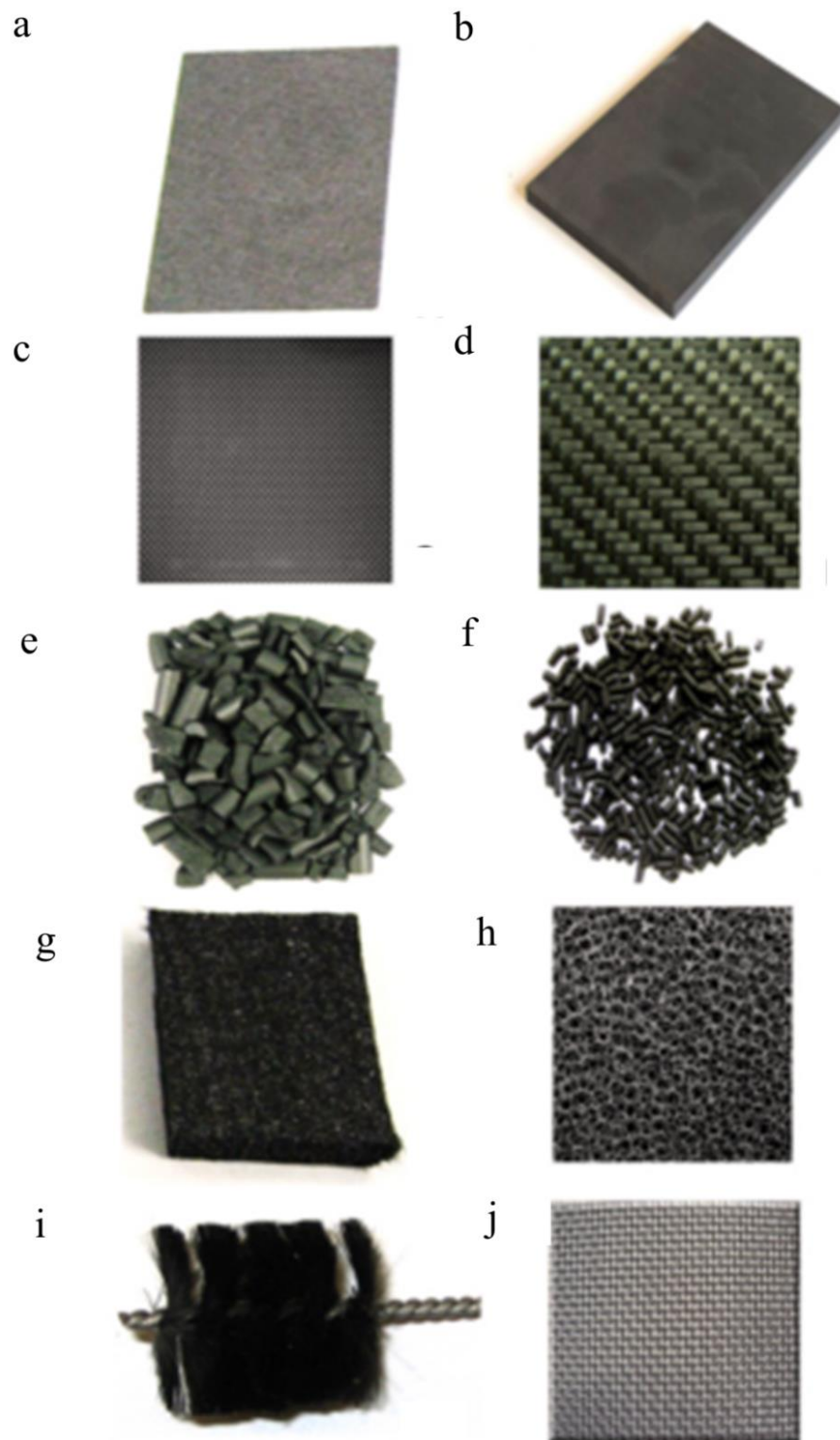


Figure 24 Various types of anode materials applied in MFC: (a) carbon paper, (b) graphite plate, (c) carbon cloth, (d) carbon mesh, (e) granular graphite, (f) granular activated carbon, (g) carbon felt, (h) reticulated vitreous carbon, (i) carbon brush, and (j) stainless steel mesh [103].

ii. Metal and metal oxide materials

Metals are more conductive than carbon, however, only non-corrosive metals can be used for MFC anode application. Moreover, metals have a smooth surface, which seems unfit for bacterial adhesion. So far, only stainless steel (**Figure 24j**) and titanium are commonly used for anode application purposes, but both metals show lower results than graphite electrodes. Although a gold electrode has been used as an anode in MFC with *Geobacter sulfureducens*, it only produces a current that was close to the current produced by a graphite electrode [103].

iii. Modified anode

Modification of anode material can be done as a strategy to facilitate bacterial adhesion and electron transfer to the anode surface. Some methods of anode modification are: surface treatment by chemical [108] or physical methods, addition of a highly conductive or electroactive coating [19] and metal-graphite composite [103]. **Table 6** listed some modifications of carbon felt anode in MFC application, which show significant performance improvement as compared to pristine carbon felt.

b. Cathode for MFC

The MFC cathode is an electrode where the electron acceptors are reduced [109]. The cathode is also developed from the substrate materials, which have a plane structure form as described above. Modification of these substrate materials is usually conducted by loading or adding a catalyst for enhancing the cathodic reaction, which commonly is oxygen reduction reaction (ORR). Various materials have been explored to find cost-effective ORR catalysts for MFC cathodes. Oxygen, the electron acceptor in cathodic part, is obtained from free air by sparging it continuously into the cathodic solution in a double chamber MFC, or by only exposing it directly to the cathode of single chamber MFC. Accordingly, the cathode can be termed as air-aqueous cathode and air-breathing cathode system respectively [103].

Air-aqueous cathodes are used in conventional double chamber MFCs. It consists of a conductive substrate, a catalyst and a binder. The solubility of O₂ in

water is only 4.6×10^{-6} (mole fraction basis) compared to 0.21 in air [68]. Indeed, the low concentration of dissolved oxygen limits the cathode's performance [103].

Table 6 Modification of carbon felt for MFC's anode application

Modified anode	MFC system	Cathode	Bacterial source/ substrate	Performance (mW m ⁻²)/ improvement	Ref.
Graphene oxide-zeolite modified carbon felt	Single chamber	Air-breathing cathode stainless steel mesh coated Pt/C	Anaerobic sludge/ acetate	280.56 / 17 times	[110]
Nitric acid - treated carbon felt	Single chamber	Air-breathing cathode carbon paper Pt/C	Pond sediment	2066 / 1.5 times	[111]
Polyaniline modified carbon felt	Double chamber	Carbon cloth / ferricyanide solution	Baker yeast (<i>Sacharomices cereviseae</i>) /glucose	450 / 3 times	[22]
Ruthenium oxide-coated carbon felt	Double chamber	Carbon felt/ferricyanide solution	<i>Shewanella decolorientis</i> S12/lactate	3080 / 17 times	[112]
Polyneutral red - modified carbon felt	Double chamber	Nickel plate / ferricyanide	Baker yeast (<i>Sacharomices cereviseae</i>) /glucose	6.1 / 2 times	[65]

1.4.12 Air-breathing cathode system

The development of the air-breathing cathode was motivated by the hydrogen fuel cell where the cathode is bonded directly to a PEM, which lets the oxygen in the air reacts directly on its surface [99]. Therefore, the air-breathing cathode is designed to be exposed to the free air. It replaces the conventional aqueous phase of the cathodic system. With this system, the oxygen is provided passively, thus no intensive energy is needed for aeration, which leads to lower operation costs [99].

Air-breathing cathode systems usually have three main parts, as illustrated in **Figure 25**: 1) the electrode substrate; 2) the catalyst layer; and 3) the air-diffusion layer [113].

1) The electrode substrate

The electrode substrate is a support material that is the backbone of the air-breathing cathode as well as current collector. Some requirements for the electrode substrate are that it should be non-corrosive, porous, and conductive. Owing to its conductivity and stability, carbon based materials are the most commonly used as electrode substrate for fabricating air-breathing cathode. Air-breathing cathodes, with carbon cloth, carbon felt, carbon mesh, have been reported. The use of metal-based materials for the air-breathing cathode substrate has also been evaluated, for example, nickel mesh and foam, stainless steel mesh, and copper mesh. However, the application of metal-based electrode substrate may lead to corrosion because of the presence of water and oxygen [113].

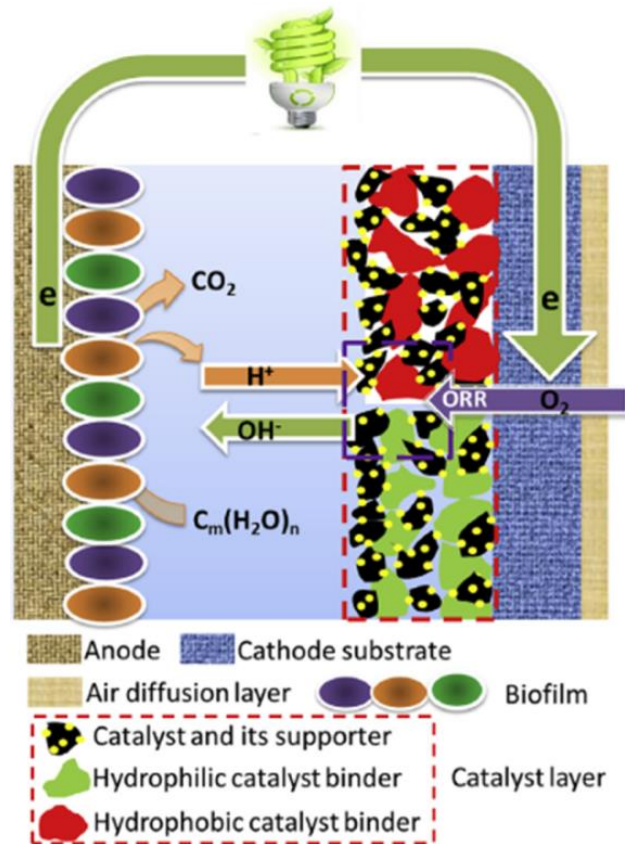


Figure 25 Schematic diagram of a single chamber MFC with air-breathing cathode system [113]

2) Catalyst Layer

The presence of an ORR catalyst is essential for air-breathing cathode performance. The use of a bare electrode may not be good enough to perform an efficient ORR. Therefore, the ORR catalyst is obviously layered onto the substrate [113]. The catalyst is typically applied to the electrode substrate using a polymeric binder such as perfluorosulfonic acid (liquid Nafion) and poly(tetrafluoroethylene) (PTFE suspension) [103]. Methods to layer catalyst onto the substrate using a binder are [114]:

1. Spreading. In this method, PTFE and catalyst are mixed to form catalyst ink, which is spread out over the substrate followed by heat treatment.
2. Spraying. Herein, the catalyst ink is repetitively sprayed onto the substrate, where every single spraying step is followed by solvent evaporation to prevent catalyst dissolution in the next spraying step.
3. Ionomer impregnation. In this method, the catalyst and binder suspension are first mixed in alcohol and water and then applied on the electrode surface.
4. Dry spraying. In this method, the components are mixed in a knife mill. The mixture is then atomized and sprayed in a nitrogen stream through a slit nozzle onto the substrate surface. This method enables the development of a catalyst layer with 5 μm thickness.
5. Painting. The catalyst ink is painted directly onto the substrate surface.

The use of a binder can be eliminated, when the catalyst is directly deposited on the electrode substrate. Deposition of catalyst can be conducted through physical, chemical, and electrochemical methods. An example of physical deposition is catalyst powder deposition, where the powdered-form catalyst mixture is mixed in a fast-running knife mill and subsequently applied onto a substrate [76]. Chemical deposition is conducted by addition of chemical reductant/oxidant onto the substrate, which contains the desired species to be deposited [115]. Meanwhile, electrodeposition is a technique by which catalyst coating is performed through an electrolysis process [115]. Further explanation of electrodeposition is presented in the next section.

3) Gas-diffusion layer

An air- or gas-diffusion layer (GDL) is a hydrophobic polymeric coating that allows air diffusion and prevents water leakage. The GDL also provides mechanical support for the catalyst layer, an electronic pathway for electrons, and a flow channel for the reacting gas and product. An appropriate GDL should meet some requirements, such as being porous, hydrophobic, non-corrosive, mechanically strong and flexible, and conductive [113]. A GDL is usually a carbon-based porous substrates such as carbon cloth or carbon paper [76]. It is also possible to coat the hydrophobic material such as PTFE onto one side of the GDL. A schematic of the GDL [76] is presented in **Figure 26**.

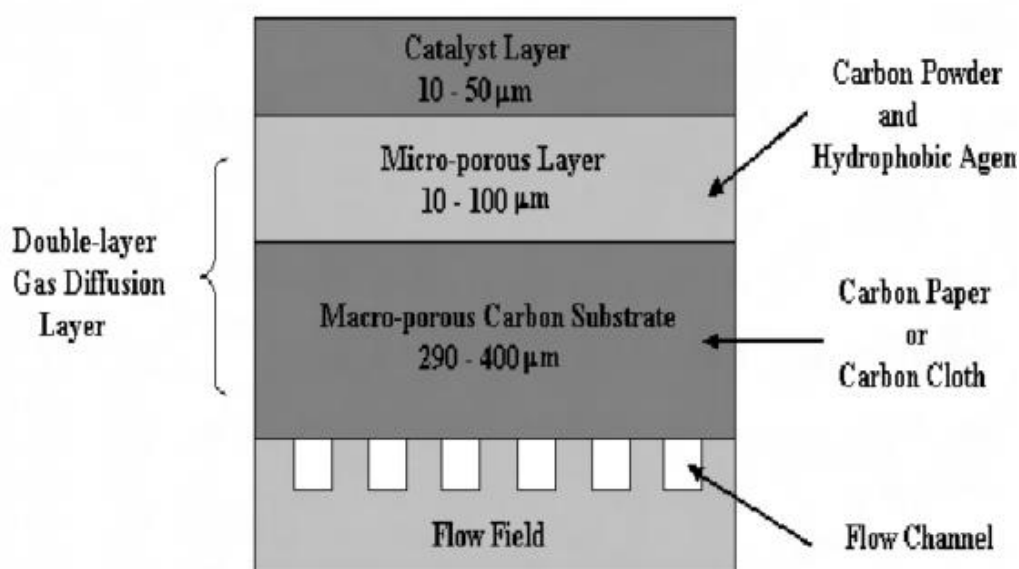


Figure 26 Schematic diagram of a gas- or air-diffusion layer on the air-breathing cathode of a fuel cell [76]

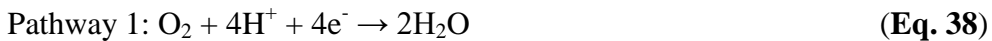
In this research, we selected carbon felt as a support for air-breathing cathode fabrication. Only few studies of carbon felt – based MFCs air-breathing cathode are found, which listed in **Table 7**. Thus, further study of carbon felt utilization as cost-effective material for air-breathing cathode application needs to be extended. Herein, we preferred binder-free loading catalyst layer i.e. by electrochemical deposition method.

Table 7 Various carbon-felt based air-breathing cathodes and their performances in MFC application

Air-breathing cathode	Anode	Bacterial source	MFC's performance	Ref
Carbon based microporous layer modified carbon felt	Carbon fiber veil sheet	Activated sludge/urine	28.2 mW m ⁻²	[116]
Activated carbon modified carbon felt	Carbon fiber veil sheet	Activated sludge/urine	42.7 mW m ⁻²	[116]
Activated Carbon Fiber Felt	Carbon felt	Anaerobic wastewater sludge/glucose	2023 – 4653 mW m ⁻³	[117]
Conductive carbon ink(Vulcan XC72R carbon-MnO ₂)-modified Carbon felt	Carbon felt	Anaerobic sludge /sucrose	600 mW m ⁻³	[118]
Pt NPs modified activated carbon felt	Carbon felt	Garden compost leachate/acetate	140 mW m ⁻²	[93]

1.4.13 Oxygen reduction reaction catalysis

The electroreduction of oxygen is a key reaction in the cathodic part of an energy conversion system such as a fuel cell or a metal-air battery [115]. Oxygen is widely applied as an electron acceptor for both its high standard potential and unlimited availability. However, the kinetic rate of the ORR is low because of the high required activation energy to break the O=O bonds (498 kJ mol⁻¹). Oxygen is reduced through the following two pathways, i.e. 4-electron transfer and 2-electron transfer mechanism (**Eqs. 38-40**) [119].



A 4-electron transfer pathway is always preferred for air-breathing cathode purposes because it enables to maximize the Faradic efficiency and avoids the energy losses as in a 2-electron transfer pathway. Indeed, an incomplete ORR results in energy loss and, most importantly, the intermediate H₂O₂ production and accumulation may denature the (bio)catalyst and destroy the membrane [120].

To drive the ORR toward a 4-electron pathway, great attention has been paid to developing catalysts that can effectively decrease the energy needed to break O=O bonds. To date, ORR catalysts based on metals, carbon, conductive polymers and microbes have been tested in MFCs. Their application greatly enhances the ORR kinetics and promotes the power generation [119].

1.4.13.1 Platinum (Pt)

Platinum is the traditional and state-of-the-art catalyst for the ORR in the cathodic part. The ORR over a Pt catalyst occurs at very low overpotential, i.e. at 1.05 V vs. RHE (reversible hydrogen electrode) at pH 7 [121]. The activity of metal catalysts toward the ORR relies on their d-band center vacancies. Among metals, Pt has the strongest ORR catalyst activity based on calculation of O₂, O, and OH binding energies [119].

The catalytic mechanism for Pt is simplified in **Figure 27**. This mechanism implies that O₂ can be reduced either completely to H₂O at rate k₁ or incompletely to adsorbed H₂O₂ at rate k₂. The H₂O₂ can be reduced further to H₂O at rate k₃, chemically decomposed on the surface, and/or released to the electrolyte solution at rate k₅ [122].

Theoretical calculations on the electronic structure based on density functional density (DFT) have been used to determine the ORR mechanism. Herein, there are two proposed mechanisms, namely dissociative and associative mechanisms for low current density and high density range, respectively [122].

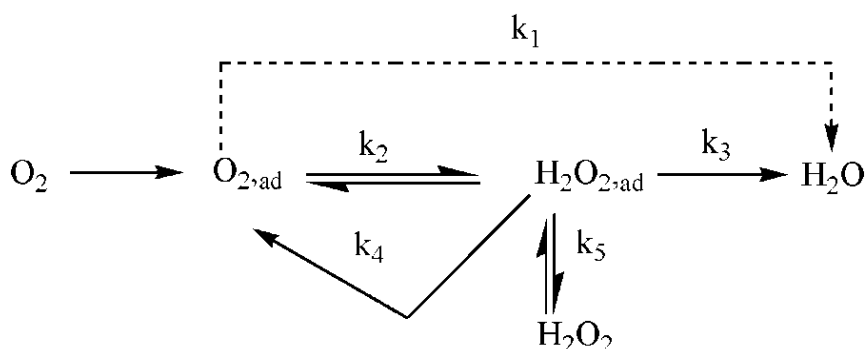


Figure 27 ORR catalytic mechanism over a Pt catalyst [123]

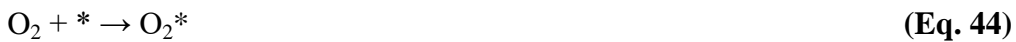
a. Dissociative Mechanism

The adsorbed O₂, parallel to the electrode surface (needing 2 side-by-side active sites), is readily broken into adsorbed O* atoms (Eq. 41), which is followed by two consecutive reduction reactions to form water (Eqs. 42 and 43). In this adsorption mode, which promotes direct O=O bond cleavage, no production of H₂O₂ is possible. This pathway thus involves 4e⁻ transfer, which enables conversion of O₂ to H₂O [122].



b. Associative Mechanism

The associative mechanism proposed in Eqs. 44-48, also follows a 4-electron transfer pathway. However, in this mechanism, O₂ is adsorbed perpendicular to the electrode surface by a single oxygen atom, which stays in O-O* state (Eq. 44). Owing to this unbroken O₂, the product of the subsequent step (HO₂*) might be H₂O₂* (HO₂* + H⁺ + e⁻ → H₂O₂*), which can be reduced further or present as product [122].

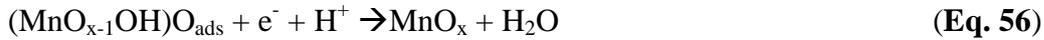
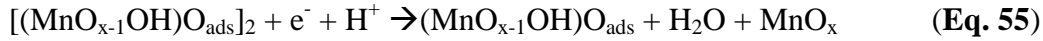
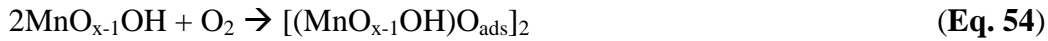
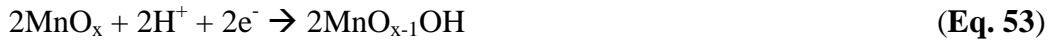


1.4.13.2 Manganese oxide (MnO₂)

The application of a cheaper transition metal oxide, such as manganese oxide, has attracted much attention. A catalytic mechanism of ORR over manganese oxide in alkaline solutions has been proposed as shown in Eqs. 49-52 [119]. The electrocatalytic activity of MnO₂ is strongly dependent on the surface concentration of Mn^{III} ions, in which the oxygen is reduced.



The mechanism of oxygen reduction reaction catalyzed by manganese oxide in neutral solution has been proposed [124] as shown in **Eqs. 53 – 56**. The reaction is started by the entering of electrons and protons to the MnO_x to form $\text{MnO}_{x-1}\text{OH}$ which contains Mn(III) active site (**Eq. 53**). Then, the O_2 is being adsorbed onto the two neighboring $\text{MnO}_{x-1}\text{OH}$ sites (bridged adsorption site) as shown in **Eq. 54**. The **Eq. 55** is the rate determining step i.e. the second electron transfer step. Finally, the $\text{O}_{2,\text{ads}}$ species is being reduced to yield final product of 4-e transfer ORR i.e. H_2O (**Eq. 56**)



Many applications of manganese oxide based catalyst on air-breathing cathode have been reported, as listed in the **Table 8**.

1.4.13.3 Carbon-based materials

Carbon-based materials facilitate the ORR through a 2-electron transfer mechanism at large overpotential that produces H_2O_2 [121]. The ORR mechanism on a glassy carbon surface is proposed in **Eqs. 57-62**. Oxygen initially is adsorbed onto the carbon surface. The $\text{O}_{2(\text{ads})}$ receives an electron and forms superoxide $[\text{O}_{2(\text{ads})}]^-$ which further migrates to more reactive species $\text{O}_{2(\text{ads})}^-$. This step is considered as a rate-determining step (rds) for the reaction at $\text{pH} > 10$. Further reaction leads to the formation of ionic hydrogen peroxide (HO_2^-). It is implied that the ORR on the carbon surface follows a 2-electron transfer pathway that produces H_2O_2 [122].





The catalytic activity of carbon-based materials is mainly attributed to the quinone group. The mechanism of ORR on a carbon surface, proposed by Garten and Weiss [125], is shown in **Figure 28**.

Table 8 Various MFC with air-breathing cathode, which use manganese oxide based catalyst

Cathodic catalyst	Cathode support	Anode	Bacterial source/ substrate	MFC's Performance	Ref.
Sprayed MnO ₂ /Graphene Oxide	Carbon cloth	Carbon cloth	Anaerobic sludge/ glucose	3359 mW m ⁻²	[126]
β-MnO ₂ /carbon nano tube (CNT)	Carbon cloth	Carbon cloth	Mixed culture/ domestic waste water	97.8 mW m ⁻²	[127]
Multivalent MnO _x supported on nitrogen-doped carbon	Carbon cloth	Graphite brush	acetate	467 mW m ⁻²	[128]
α-MnO _x nanowire supported on carbon vulcan	Carbon cloth	Graphite brush	Mixed culture/ acetate	180 mW m ⁻²	[129]
Mesoporous layer α-MnO ₂	Stainless steel mesh	Carbon felt	Acetate	1671 mW m ⁻²	[130]
MnO ₂ /CNT and polymethyl siloxane	Stainless steel mesh	PPy/ AQDS modified carbon felt	<i>Shewanella decolorationis</i> S12/lactate	2676 mW m ⁻²	[131]
Electrodeposited MnO _x nanostructure	Carbon paper	Activated carbon fiber	Anaerobic sludge/ acetate - wastewater	777.8 mW m ⁻³	[124]
Electrodeposited MnO ₂	Activated carbon	Carbon felt	Acetate	1554 mW m ⁻²	[132]

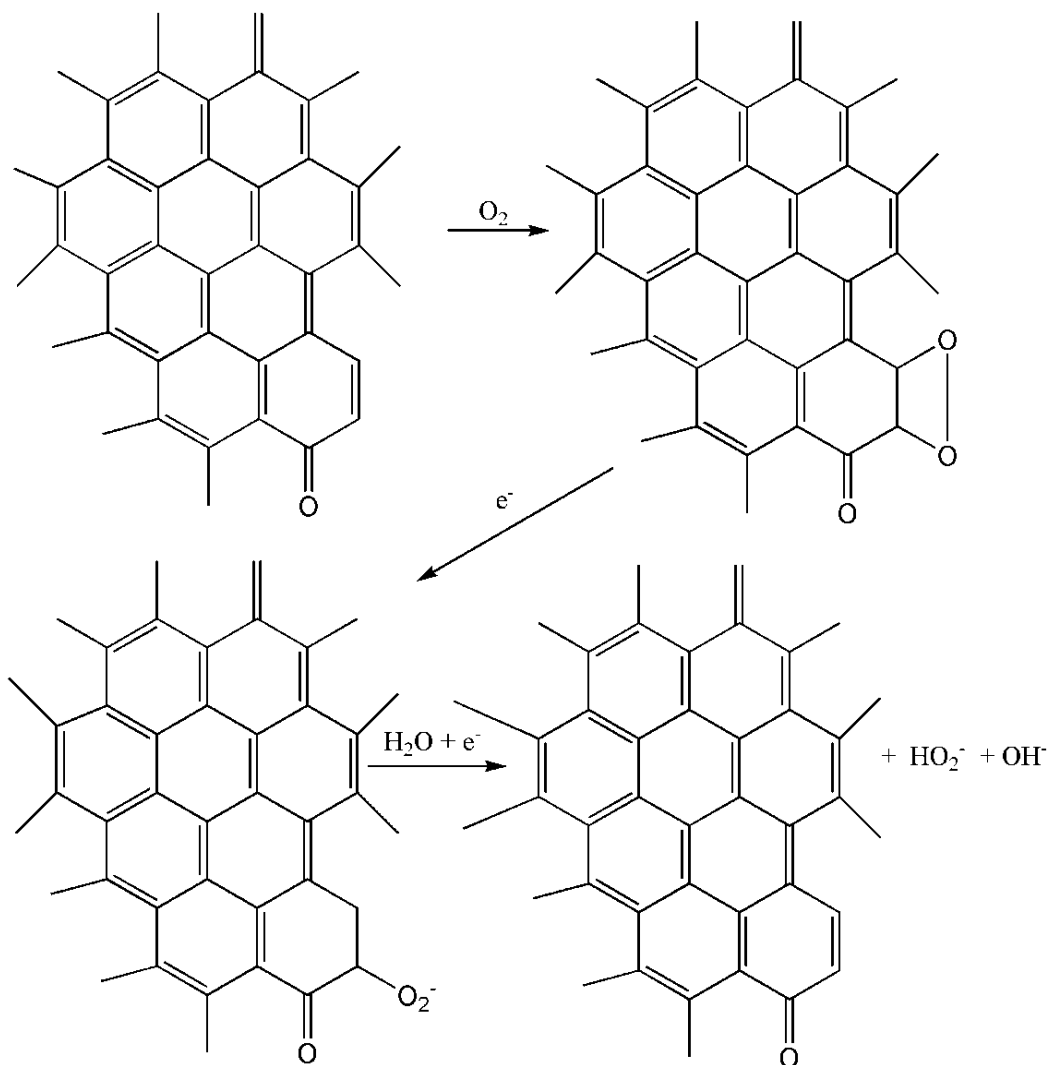


Figure 28 ORR mechanism that shows the catalytic active site of a carbonaceous catalyst [125]

1.4.13.4 Conducting polymers

Conducting polymers have a specific electronic structure that enables the chemisorption of oxygen reversibly through a bridge adsorption model at some active carbon centers that donate electron density. The bond order of the chemisorbed oxygen molecule decreases, whereas the bond length increases, resulting in a high degree of activation and thus the chemisorbed oxygen molecules can be easily reduced [119]. The oxygen adsorption on the conductive polymer has been bridge modeled, as shown in **Figure 29**, according to electronic structure calculation [133].

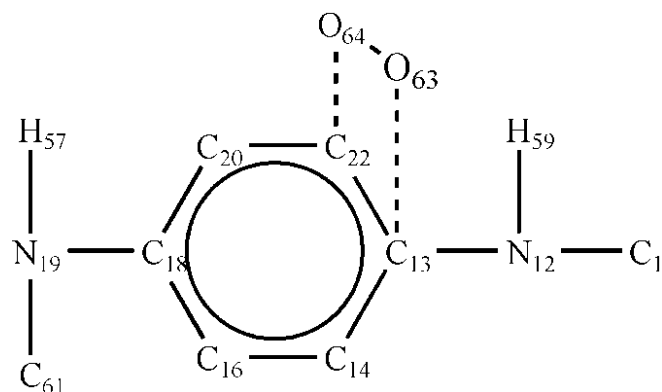


Figure 29 The bridge model of oxygen adsorption on polyaniline (PANI) [133]

1.5 Electrodeposition

Electrodeposition is considered as a simple and versatile technique to develop unique nanoscale architectures of electrocatalysts in low temperature fuel cells and to fabricate electrodes with distinctive morphology and exceptional specific properties [134]. In this method, reduction or oxidation takes place by supplying external power toward the electrodes in a electrolytic solution that contains the desired precursor [115]. Metals, metal oxides, and conductive polymers are commonly loaded by this technique for the development of electrochemical energy devices such as fuel cells, batteries and supercapacitors [134].

The basic concept of the reduction and oxidation processes on the electrode is explained through the schematic diagram in **Figure 30**. The reduction of the species on the electrode surface occurs due to electrons at high energy level flowing into vacant electronic states on neighboring species in the solution. High energy level electrons can be generated by adjusting the applied potential to more negative potential to the working electrode (**Figure 30a**). Oppositely, applying positive potential lowers the energy of the electrons and favors the extraction of electrons from the species into the electrode (**Figure 30b**). In this case, the species are oxidized [135].

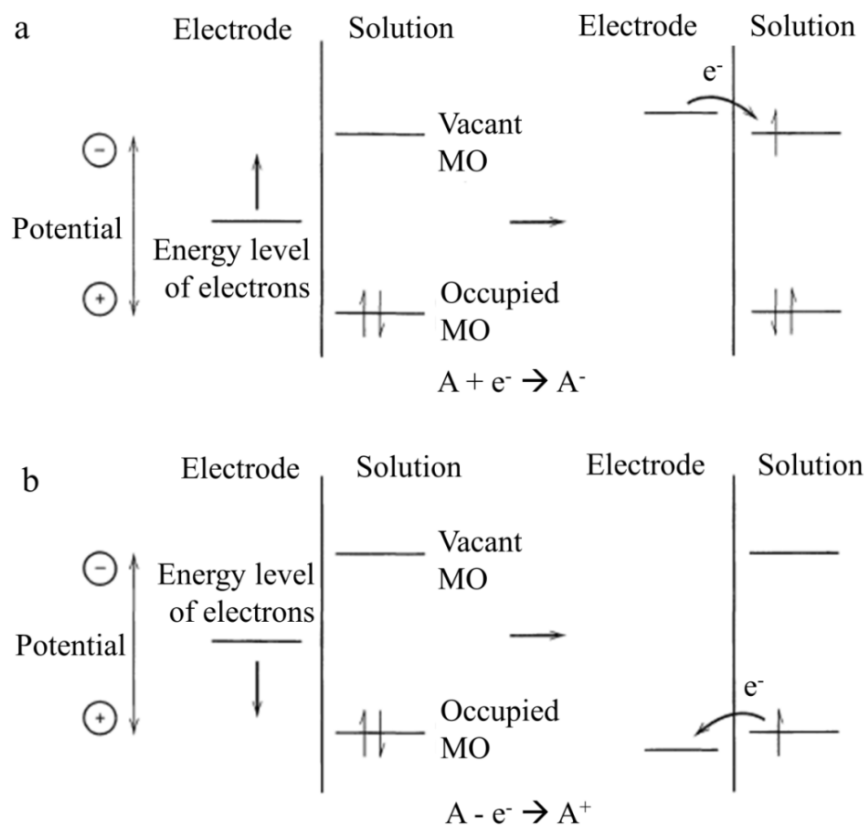


Figure 30 Schematic representation of potential-controlled reduction and oxidation processes on the electrode [135]

1.5.1 Electrodeposition of Pt

Electrodeposition of Pt is typically conducted from a chloride, amine, sulfate-nitrite, and hydroxyl complexes in aqueous media. The reduction mechanism of Pt electrodeposition, modeled in **Figure 31**, involves three main steps: 1) the solvated Pt ion that present in the electrolyte goes to the cathode due to the influence of the imposed electrical field as well as by diffusion and convection; 2) the solvated Pt ion entering the diffusion layer at the cathode, the field strength only enables aligning the solvated water molecules but not sufficiently to liberate the Pt ion; 3) the solvated Pt ion liberates free ionic Pt due to the electrical field strength is high (of the order 10^7 V cm^{-1}) at the double layer since it is close to the electrode surface; finally the free ionic Pt species is then being reduced and deposited onto the electrode [136].

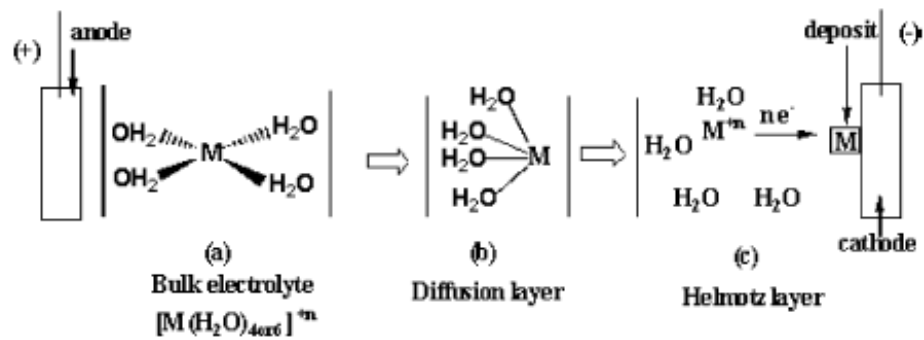


Figure 31 Reduction mechanism of metal electrodeposition [136]

1.5.2 Electrodeposition of MnO_2

Electrodeposition of MnO_2 is a promising technique that enables us to grow MnO_2 directly on a conductive substrate's surface in the development of MnO_2 -based electrodes. MnO_2 is anodically deposited from aqueous solution of chelated- and/or non-chelated- Mn salts with or without buffers and surfactants. Anodic potential hydrolyzes manganese ions and subsequently deposits MnO_2 according to **Eq. 63**. Various deposition parameters influence several important properties of manganese oxides, such as morphology, electronic conductivity, exposed specific surface area, crystal structure and defect chemistry (cation distribution and oxidation states). All these features considerably determine its performance [134].



The Pourbaix diagram of manganese in **Figure 32** can be used to determine, theoretically, the electrodeposition parameter. The diagram shows which form of manganese is most prevalent given a certain pH and applied potential. As pH increases the redox potential drops and forms manganese dioxide. The manganese ion, Mn^{2+} , predominates in acidic conditions ($\text{pH} < 7.0$) [137].

The specific capacitance of the deposited films can be analyzed by means of cyclic voltammetry (CV). The following equation (**Eq. 64**) can be used to calculate the specific capacitance from voltammogram [134].

$$C_{sp} = \frac{Q}{m_e \times \Delta E} = \frac{\int I dt}{m_e \times \Delta E} = \frac{\int I dv}{m_e \times \Delta E \times S_r} (F g^{-1}) \quad (\text{Eq. 64})$$

where Q is the total charge (F), m_e the active electrode weight (g), ΔE the width of the potential window (V), I the current (A), v the potential (V), S_r the scan rate, and $\int I dv$ represents the area under either the cathodic or the anodic voltammogram.

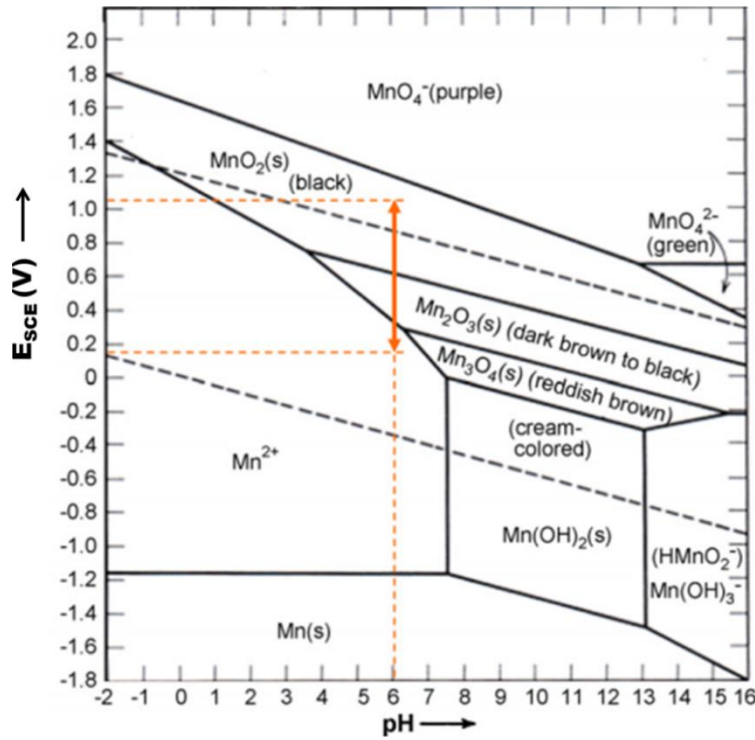


Figure 32 Pourbaix diagram of manganese [138]

1.5.3 Electrodeposition of conductive polymer

Conductive polymers have special properties such as electrical conductivity, electroactivity, and ion exchange ability. The high electronic conductivity of the conductive polymer is due to its delocalized electrons in a π -conjugated system along the polymer chains. Conductive polymers are also capable of undergoing reversible redox reactions upon application of an external potential. Ions diffuse in and out of the conductive polymer, which results in doping and undoping states to allow a redox reaction that maintains electroneutrality. Owing to these special properties, conductive polymers are often used for fabrication of systems such as sensors, energy storage devices, diodes, transistors, display devices, ion exchange membranes and catalyzing electrodes. Some of the popular conductive polymers are such as polyaniline (PANI), polypyrrole (PPy), and poly (3,4-ethylenedioxythiophene) (PEDOT) [139].

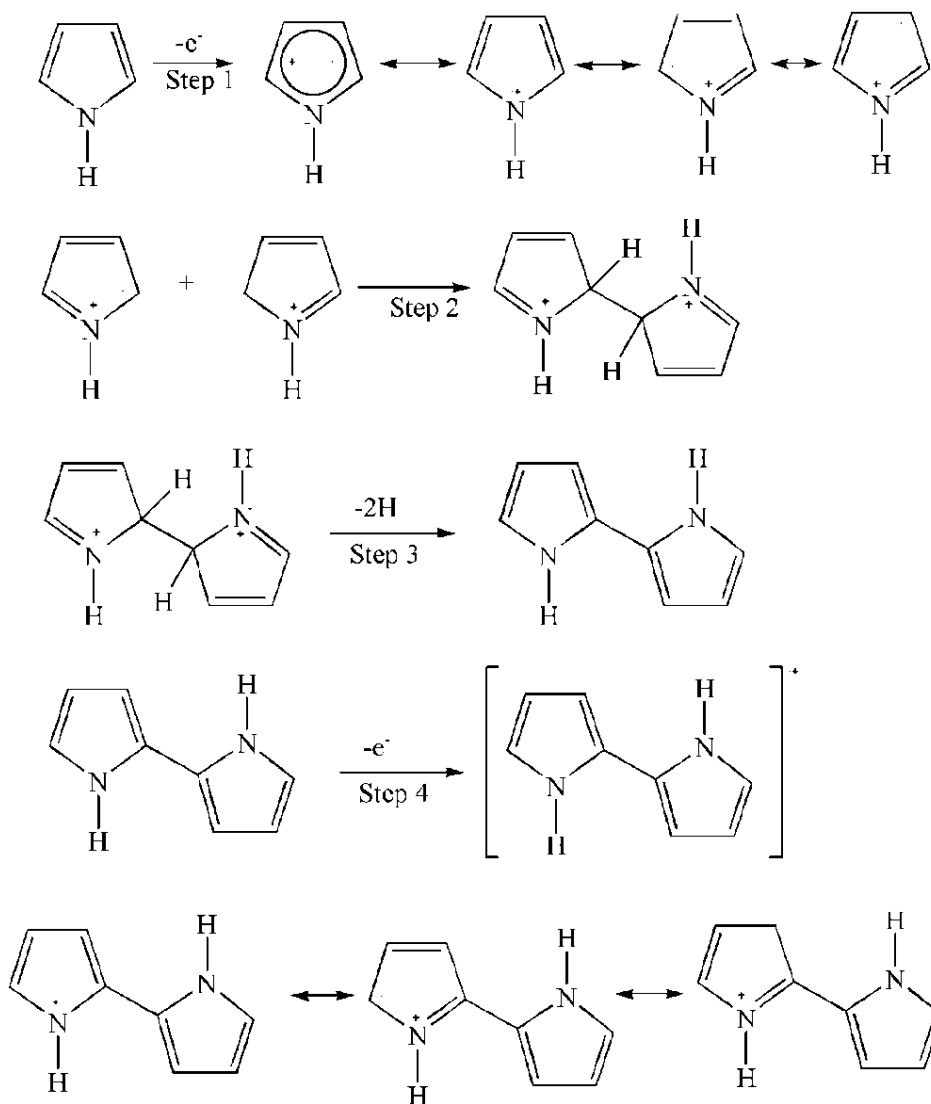


Figure 33 The mechanism of electropolymerization of pyrrole [140]

Conductive polymers can be synthesized via chemical and electrochemical polymerization methods. Conductive polymers are prepared from the electrolytes containing monomers via either electrooxidation or electroreduction, depending on the used of monomer type. The electrodeposition of polymers includes nucleation and growth. The deposition mechanism involves a number of steps: 1) oxidation of monomers adsorbed onto the electrode surface; 2) diffusion of the oxidized monomers and oligomerization; 3) formation of clusters; and 4) film growth. Pyrrole in aqueous electrolyte can be electropolymerized by electrooxidation to deposit PPy. **Figure 33** shows the mechanism of pyrrole electropolymerization. Advanced electropolymerization using a template is also possible, which leads to great improvement [141].

Chapter 2:
Experimental Methodology

Chapter 2 Experimental Methodology

2.1 Chemicals and materials

During this research, we used the chemicals of analytical grade without any purification before their utilization. All used chemicals and materials are listed below:

Carbon felt (CF, 6.35 mm thick, 99%) from Alfa Aesar, garden compost (Neuhaus, France), potassium chloride (KCl, 99%, Sigma Aldrich), sodium acetate (CH_3COONa , 99%, Carlo Erba), potassium ferricyanide ($\text{K}_3\text{Fe}(\text{CN})_6$, 99% Sigma Aldrich), sodium metavanadate (Na_2VO_3 , Sigma Aldrich), sulfuric acid (H_2SO_4 , 97%, Sigma Aldrich), potassium nitrate (KNO_3 , 99%, Sigma Aldrich), sodium phosphate monobasic monohydrate ($\text{NaH}_2\text{PO}_4 \cdot \text{H}_2\text{O}$, 99%, sigma Aldrich), sodium diphosphate dibasic dihydrate, $\text{Na}_2\text{HPO}_4 \cdot 2\text{H}_2\text{O}$, 98%, Fluka Analytical sodium hydroxide (NaOH, 85%, Prolabo), hexahydrate hexachloroplatinic (IV) acid ($\text{H}_2\text{PtCl}_6 \cdot 6\text{H}_2\text{O}$, 99%, Sigma Aldrich), manganese (II) chlorid tetrahydrate ($\text{MnCl}_2 \cdot 4\text{H}_2\text{O}$, p.a, Merck), sodium nitrate (NaNO_3 , 99%, Fluka Chemika), pyrrole (Aldrich), sodium perchlorate ($\text{NaClO}_4 \cdot \text{H}_2\text{O}$, 98%, Fluka), ethanol (96%, VWR), glutaraldehyde (25 wt. %, Merck), potassium titanium oxide oxalate (>90% Ti basis, Sigma Aldrich), hydrogen peroxide (30 wt. % in H_2O , Sigma Aldrich), sodium sulphate (> 99%, Sigma Aldrich), poly(ethyleneimine) 50% (w/v) in H_2O (contain aziridine, homopolymer, Sigma Aldrich), potassium bromide (Sigma Aldrich), Orange II sodium salt (dye content > 85%, Aldrich), potassium permanganate, ultrapure water (produced by a Milli-Q Millipore source, 18.2 M Ω cm at 293 K)), nitrogen (N_2 , Air Liquide, ultra-pure) and oxygen (O_2 , Air Liquide, ultra-pure) gases.

2.2 Preliminary experiment

2.2.1 Cleaning glassware equipment

All glasswares were cleaned very well before every experiment conducted. The glasswares were firstly soaked in acidified potassium permanganate solution overnight to oxidize all organic stains on the glass surface. Then, the glasswares were rinsed with hydrogen peroxide contain sulfuric acid (25 wt. % H_2SO_4 and 10

wt. % H₂O₂). The glasswares were then rinsed thoroughly with ultra-pure water and dried.

2.2.2 Cleaning raw material

The as-received carbon felt (CF) material was cut into certain size and cleaned ultrasonically using ethanol for 2 hours. Every 30 minutes, the ethanol was replaced. Then, the CF was rinsed with water to remove the ethanol. Finally, the CF is dried in oven at 70° C for 24 hours and is further referred as raw carbon felt (RCF).

2.3 Electrochemical method

2.3.1 The principle of electrochemical method

There are four electrochemical methods were involved in this research namely cyclic voltammetry (CV), chronoamperometry (CA), linear sweep voltammetry (LSV), and electrochemical impedance spectroscopy (EIS). All electrochemical measurements of CV, CA, and LSV were performed using Potentiostat Biologic SP 50. Whereas, EIS measurements were conducted using Potentiostat Biologic SP 150.

2.3.1.1 Cyclic voltammetry (CV)

CV is an electrochemical method which conducted by sweeping potential linearly at a certain range as a function of time (**Figure 34a**). Potential sweep forward then turn backward to form one cycle of CV voltammogram. The cycle can be repeated infinitely by sweeping potential continuously.

The current is generated along with the potential sweeping. Then, the recorded currents are plotted toward potential, which results in a current-potential curve so called CV voltammogram (**Figure 34b**). The current peaks reveal the oxydation and reduction reactions on the electrode surface. These two peaks are usefull to determine redox potential ($E_{1/2}$). Ideally, CV voltammogram for a reversible redox couple shows an equal oxydation and reduction peak and the ratio should be negative one, as expressed in **Eq. 65** [142].

$$(I_{pc}/I_{pa} = -1) \tag{Eq. 65}$$

with peak separation, ΔE_{peak} , closes to 60 mV. Herein, ΔE_{peak} is:

$$|E_{\text{pc}} - E_{\text{pa}}| = 2.3 RT/nF \quad (\text{Eq. 66})$$

Where R is gas constant, T is temperature, n is number of electron involved in the electrochemical process, and F is Faraday's constant. At 298 K, $2.3RT/nF = 0.059$ V for $n = 1$.

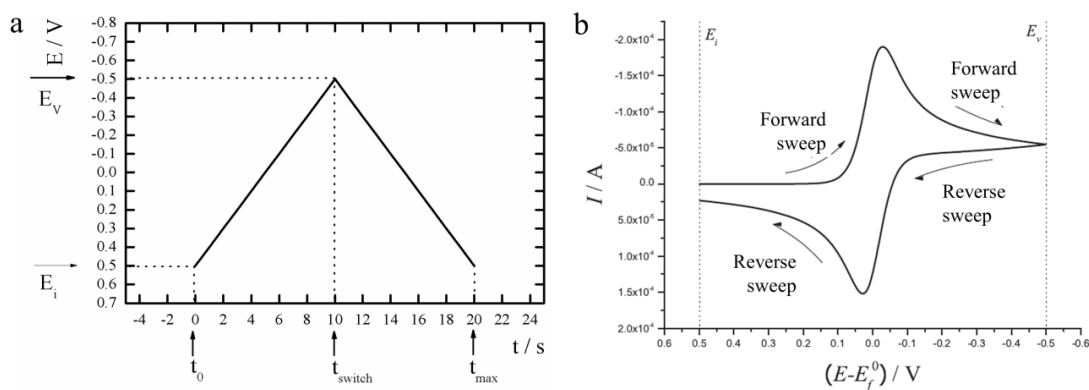


Figure 34 (a) Potential-time (wave form) (b) current-potential curve (CV voltammogram) obtained by sweeping potential at scan rate 0.1 V s^{-1} as a function of time during CV measurement [143].

In CV, an oxidation and a reduction reaction can be stimulated as the potential scanning is applied. Therefore this technique can be used for the electrosynthesis, which involves oxidation and/or reduction process. Some operating conditions of CV, such as potential sweep range, scan rate, and number of cycles, can be varied during the electrosynthesis to obtain an optimum condition.

2.3.1.2 Linear sweep voltammetry (LSV)

LSV is an electrochemical method by sweeping potential. The potentials are varied linearly with time at various scan rates. In this experiment, the current are plotted toward potential to form an i - E curve so-called LSV voltammogram. This curve allows us to characterize the presence of the different species [135]. This technique is similar with CV unless the potential sweep is nonreversal.

Figure 35a is an E - t curve that illustrate potential sweep in LSV experiment. The initial potential is marked as E_i in this figure, the potentials are swept by time from positive to negative direction. As potential shift, the reaction of species on the electrode is begun and gives a respond of increasing current. The non-faradic

current (often called the capacitive current) appear at potential range between E_i and E^0 , which emerges from the spontaneous reduction reaction (**Figure 35b**). When the E equal to E^0 , the current starts to flow and accelerates the reduction reaction, hence the concentration of A^+ and A at the electrode surface are equal [135,144]. The further potential sweep toward negative potential cause the increasing concentration of A which form a cathodic current peak ($I_{p,c}$). At this point, the increasing of A is originated from the bulk solution by diffusion process [144]. The next scanning is resulting in the decreasing of current due to the diffusion layer on the electrode surface grow thicker which may slower down the mass transport of A^+ to the electrode [144]. At this point, the profile of concentration of A^+ around the electrode surface is shown in **Figure 35c**.

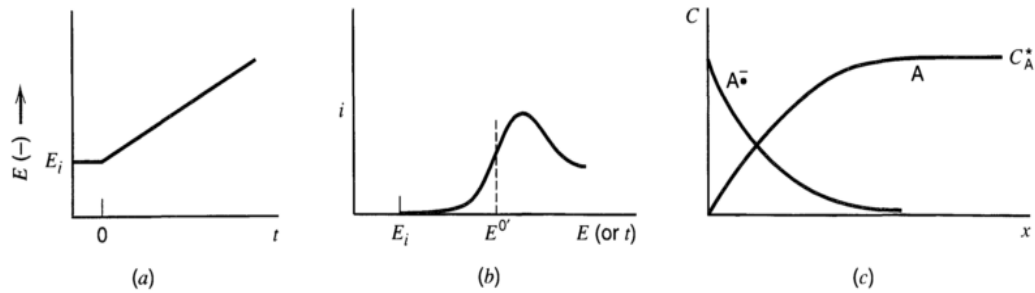


Figure 35 LSV curve expressed as (a) potential vs. time (E-t) (b) current vs. potential (i-E) and (c) concentration vs. distance from the electrode [135]

2.3.1.3 Chronoamperometry (CA)

CA is an electrochemical method by applying fixed-potential over a period of time. The resulted current was recorded and plotted in a current-time curve form (**Figure 36**). Different with CV, CA is intended to single reaction (oxidation or reduction) by selecting fixed-potential at controlled time. Since CA curve imply current vs. time, therefore the charge (Q) can be calculated by integration. This can be used to predict the electrodeposited mass by Faraday's Law (**Eq. 67**).

$$m = \frac{Q}{F} \times \frac{M}{Z} \quad (\text{Eq.67})$$

Where,

- m : loading mass (gram)
- Q : charge (Coulomb)
- M : molecular weight (gram mol⁻¹)

F : Faraday's constant (96485 C mol⁻¹)

Z : electron transferred

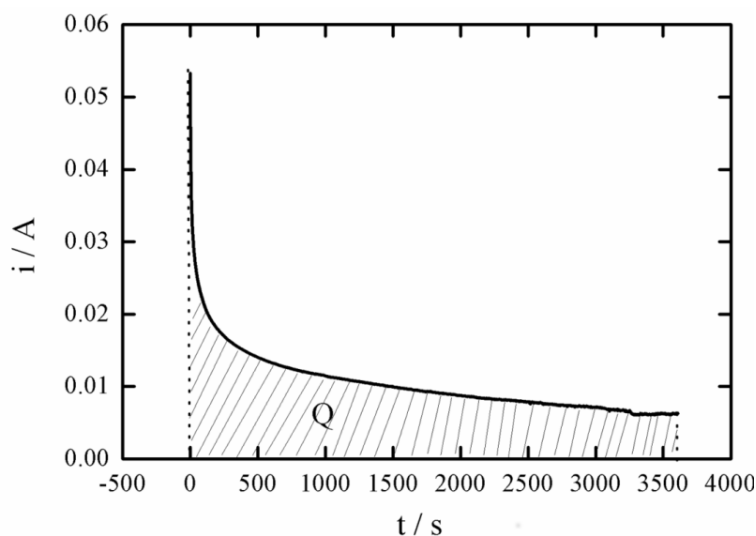


Figure 36 Current-time curve of chronoamperometry

2.3.1.4 Electrochemical impedance spectroscopy (EIS)

EIS is a powerful measurement technique to study the electrochemical phenomena such as charge transfer at the interfaces (solid-liquid, solid-solid) and solid phase. It is also useful to diagnose the electrode material properties, the state of charge batteries, and the state of health of fuel cells [145–147]. The impedance is measured by applying small alternating current (AC) to the electrochemical system (electrode or cell) of interest and subsequently measuring the resulted current response toward this stimulus. A sinusoidal potential and AC current can be expressed according to **Eqs. 68 and 69** [145] respectively.

$$E(t) = E_0 \sin(\omega t) \quad \text{(Eq. 68)}$$

$E(t)$ is potential at time t , E_0 is the amplitude of the signal, ω is the radial frequency (rad/s) that 2π times of the conventional frequency in hertz ($\omega=2\pi f$).

$$I(t) = I_0 \sin(\omega t + \phi) \quad \text{(Eq. 69)}$$

$I(t)$ is current after shifting in phase ϕ and which has different amplitude with I_0 .

Analogues to Ohm's law, thus the impedance can be expressed according to **Eq. 70** [145,148]. The common EIS graphic is a Nyquist curve that plots the $Z(\omega)$ real on the x-axis and its imaginary on the y-axis. Each point on the Nyquist plot

corresponds to the impedance at one frequency. The frequency are going lower from the left to the right of the X-axis Nyquist plot [148]. The Nyquist plot shows the electrical circuits of the resistance and capacitance in parallel. The perfect semicircular Nyquist plot, as shown in **Figure 37b**, corresponds to the Randles electrical circuits (**Figure 37a**), which fits to many half-cell electrochemical systems. The circuit components in the Randles electrical can be correlate to familiar physical phenomena, such as adsorption or film formation. The other type of Nyquist plot (**Figure 37d**) arising from Warburg circuits (**Figure 37c**), which implies the presence of the diffusion of reactant or product at the electrode surface that influence the electrochemical reaction [148].

$$\text{Impedance}(Z) = \frac{E(t)}{I(t)} = \frac{E_o \sin(\omega t)}{I_o \sin(\omega t + \phi)} = Z_o \frac{\sin(\omega t)}{\sin(\omega t - \phi)} \quad (\text{Eq. 70})$$

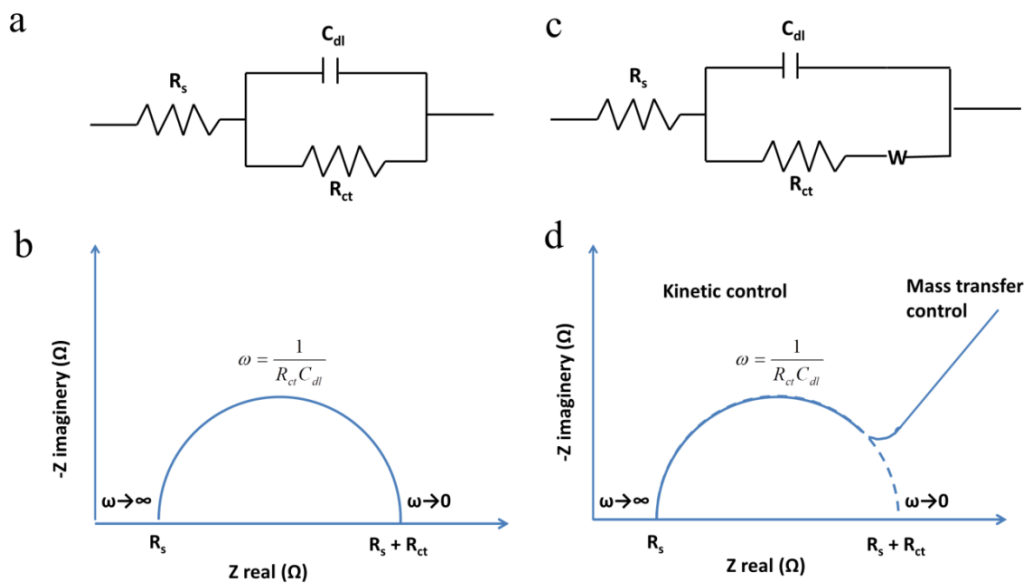


Figure 37 (a) Randles cell circuit and its (b) Nyquist plot (c) Warburg circuit cell and its (d) Nyquist plot

According to **Figure 37**, R_s is the solution-phase resistance, R_{ct} is the charge-transfer resistance at the electrode/solution interface that inversely proportional to the rate of electron transfer thus it possible to calculate the electrochemical reaction rates, C_{dl} is the double layer capacitance at this interface. The C_{dl} provide information on adsorption and desorption phenomena [149].

The polarization resistance is determined by extrapolating the Nyquist plot to the real axis x as the frequency approaching zero 0 Hz. The first intersection of the Nyquist plot with the real axis indicate charge transfer resistance. The accurate value can be obtained by subtracting the resistance with the solution resistance [149].

2.3.2 Electrochemical cell

Electrochemical experiments (CV, LSV, and CV) were conducted using Potentiostat Biologic SP-50. The electrochemical cell was a glass reactor which can contain up to 50 mL solution. The three electrodes namely working, counter, and reference electrode were arranged in the cell. Working electrode was the material of interest which are going to be modified or characterized, counter electrode was a platinum mesh, and reference electrode was silver-silver chloride (Ag/AgCl) purchased from Metrohm. The electrochemical cell was covered by a special cover contain five-fixed holes to keep the electrode at the same position for every experiment. The electrochemical cell arrangement is shown in **Figure 38**.

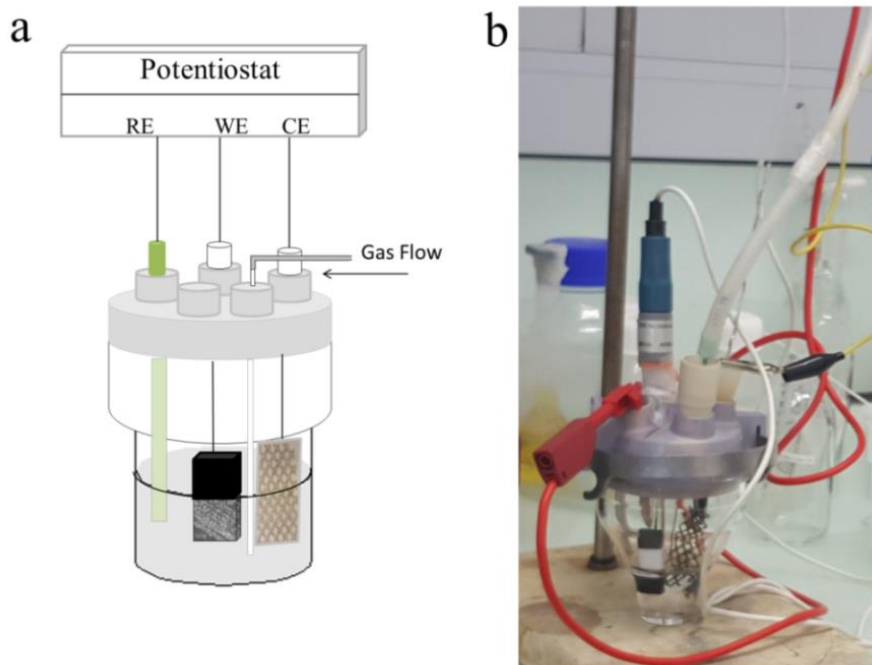


Figure 38 (a) Schematic diagram and (b) prototype of conventional three-electrode arrangement electrochemical cell either for electrosynthesis (electrodeposition) and electrochemical characterization of the as synthesized material.

2.3.3 Electrochemical synthesis

2.3.3.1 Preparation of Pt nanoparticles based electrode material

a. Electroactivation of CF

We observed that the previously cleaned CF samples are too hydrophobic to allow their efficient use for some of our planned applications; similar observations are available in literature for carbon felt electrodes of variable thickness [150,151]. Thus, we decided to adapt the procedure that has been established in the laboratory [150]. Herein, CF electrodes were electrochemically pretreated in 1 M H₂SO₄ solution by the method of CV from 0 to 1.5 V vs. Ag/AgCl for 30 cycles at a scan rate of 20 mV s⁻¹ (the counter electrode was platinum mesh). Then, the samples were thoroughly rinsed with distilled water until neutral pH and finally dried in oven at 70 °C. The cleaned and dried sample was then referred as electroactivated, ACF, (bulk density of 16 ± 1 mg cm⁻², accounting for both sides of the modified electrodes, but not taking into account the internal surface of the 3D-electrodes.)

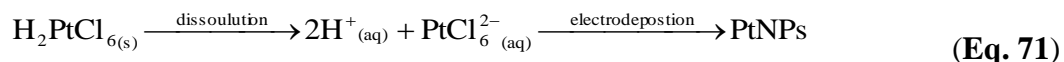
b. Electrodeposition of platinum (Pt) on ACF by cyclic voltammetry method

The Pt was electrodeposited on ACF (geometric surface area 3.9 cm²) by method of cyclic voltammetry at 20 mV·s⁻¹ from 0 to -1 V vs. Ag/AgCl for 30 cycles in 20 mL of 5 mM H₂PtCl₆ solution (pH adjusted to 9) under N₂ atmosphere. Synthesis was conducted in a three-electrode electrochemical cell where ACF acts as working electrode, saturated silver-silver chloride (Ag/AgCl) as reference electrode and platinum mesh as counter electrode. After electrodeposition, the sample was rinsed and dried at 70 °C. The sample fabricated by CV method is label as ACF@Pt_CV, meaning ACF decorated by PtNPs.

c. Electrodeposition of platinum (Pt) on ACF by chronoamperometry (CA) method

Pt electrodeposition was conducted by applying fixed potential -0.6 V vs. Ag/AgCl by varying experimental parameter such as the reaction time (0.5, 1, 2, and 4 hours) and the precursor concentrations (1, 2, 3, 5, and 7 mM). During the electrodeposition, the N₂ was flowed into the cell continuously to obtain saturated N₂ atmosphere. After electrodeposition, the sample was rinsed and dried at 70 °C.

It should be noted that the applied potential is significant lower than the standard redox potential of $\text{PtCl}_6^{2-}/\text{Pt}$ ($E^\circ = 0.7 \text{ V vs. SHE} = 0.5 \text{ V vs. Ag/AgCl}$), thus proving enough (**Eq. 71**) thermodynamic driving force for PtNPs deposition and growth (Pt^{+IV} reduction to Pt^0 reaction).



The resulting samples, labeled as ACF@Pt_CA-T0.5, ACF@Pt_CA-T1, ACF@Pt_CA-T2, and ACF@Pt_CA-T5, are resulted from electrodeposition for 0.5, 1, 2 and 5 hours respectively. The best compromise of 1 hour electrodeposition was used for different $[\text{PtCl}_6^{2-}]$ concentrations from 1 to 7 mM. The as-prepared samples are named as ACF@Pt_CA-C1, ACF@Pt_CA-C2, ACF@Pt_CA-C3, ACF@Pt_CA-C5, and ACF@Pt_CA-C7 for 1, 2, 3, 5 and 7 mM, respectively.

2.3.3.2 Preparation of MnOx based electrode material on ACF (ACF@MnOx)

a. Potential work finding

Preliminary experiments were conducted by performing CV of the ACF electrode in 25 mM MnCl_2 in 200 mM NaNO_3 at scanning the electrode potential from -1 to 1 V vs. Ag/AgCl at a scan rate 5 mV s^{-1} either under nitrogen or oxygen atmosphere. These experiments were performed in order to find the potential redox of the manganese species. From the obtained voltammogram, we designed the experiments to obtain the optimum synthesis condition of the material by electrochemical method of either CV or CA.

b. Electrodeposition of MnOx by CV method

A seri of CV electrodeposition parameters were designed to obtain the precise optimum condition for the synthesis of ACF@MnOx electrodes. Herein, MnOx were electrodeposited on the projected area of $2 \times 2 \times 0.635 \text{ cm}$ ACF's surface. The syntheses were conducted at room temperature and ambient air condition. The optimization parameters involve potential range (Entry 1 to 13), number of cycles (Entry 14 to 16), and scan rate dependence (Entry 17 to 19), as gathered in **Table 9**.

Table 9 Various parameter for electrodeposition MnOx by CV method

Entry	[MnCl ₂] / mM	[NaNO ₃] / mM	Number (cycles)	Scan rate (mV s ⁻¹)	Potential range (V vs. Ag/AgCl)
1	25	200	50	50	0 – 1.0
2	25	200	50	50	0 – 1.1
3	25	200	50	50	0 – 1.2
4	25	200	50	50	0 – 1.3
5	25	200	50	50	0 – 1.4
6	25	200	50	50	0 – 1.5
7	25	200	50	50	0 – 1.6
8	25	200	50	50	0.2 – 1.4
9	25	200	50	50	0.4 – 1.4
10	25	200	50	50	0.6 – 1.4
11	25	200	50	50	0.8 – 1.4
12	25	200	50	50	1.0 – 1.4
13	25	200	50	50	1.2 – 1.4
14	25	200	50	30	0.8 – 1.4
15	25	200	50	70	0.8 – 1.4
16	25	200	50	100	0.8 – 1.4
17	25	200	10	50	0.8 – 1.4
18	25	200	20	50	0.8 – 1.4
19	25	200	70	50	0.8 – 1.4

c. Electrodeposition of MnOx by CA method

Electrodeposition by applying fixed potential, i.e, CA has been conducted based on parameters listed in **Table 10**. Optimization parameters have involved potential electrodeposition (Entry 1 to 4), time reaction (Entry 5 to 8), and concentration of precursors (Entry 9 to 13).

Table 10 Various parameter for electrodeposition MnO_x by CA method

Entry	[MnCl ₂], [NaNO ₃] (mM)	Potential (V vs. Ag/AgCl)	Time (h)	Denoted
1	25 mM, 200 mM	1.1	1	ACF@MnO _x -E1.1
2	25 mM, 200 mM	1.2	1	ACF@MnO _x -E1.2
3	25 mM, 200 mM	1.3	1	ACF@MnO _x -E1.3
4	25 mM, 200 mM	1.4	1	ACF@MnO _x -E1.4
5	25 mM, 200 mM	1.3	0.5	ACF@MnO _x -T0.5
6	25 mM, 200 mM	1.3	2	ACF@MnO _x -T2
7	25 mM, 200 mM	1.3	4	ACF@MnO _x -T4
8	25 mM, 200 mM	1.3	6	ACF@MnO _x -T6
9	10 mM, 200 mM	1.3	4	ACF@MnO _x -C10
10	45 mM, 200 mM	1.3	4	ACF@MnO _x -C45
11	90 mM, 200 mM	1.3	4	ACF@MnO _x -C90
12	180 mM, 200 mM	1.3	4	ACF@MnO _x -C180
13	260 mM, 200 mM	1.3	4	ACF@MnO _x -C260

2.3.4 Electrochemical characterization

2.3.4.1 Electrochemical characterization of ACF@Pt based electrode

a. CV profile and LSV oxygen reduction reaction

CV profile and LSV ORR curve were recorded either in the electrolyte solution 0.1 M potassium hydroxide (KOH, pH 13) or 50 mM of phosphate-buffered solution (PBS, pH 7) under nitrogen and oxygen atmosphere respectively. The working electrode was the developed electrode with its projected geometric surface area was 3.9 cm². The reference electrode was saturated Ag/AgCl while the counter electrode was large Pt mesh. Herein, the potential were also scaled versus the reversible hydrogen electrode (RHE) according to **Eq. 72** with $E^{\circ}\text{Ag/AgCl} = 0.20 \text{ V vs. standard hydrogen electrode (SHE) at } 20\text{-}25^{\circ}\text{C}$.

$$E(\text{V vs. RHE}) = E(\text{V vs. Ag/AgCl}) + 0.06\text{pH} + E^{\circ}\text{Ag/AgCl} (\text{V vs. SHE}) \quad (\text{Eq.72})$$

b. Hydrogen peroxide quantification

The chronoamperometry experiments were performed in the 20 mL of 0.1 M KOH solution under saturated oxygen atmosphere at three electrodes: 1) RCF

($E_{\text{appl}} = 0.5$ V vs. RHE), 2) ACF ($E_{\text{appl}} = 0.5$ and 0.6 V vs. RHE), and 3) ACF@Pt ($E_{\text{appl}} = 0.5, 0.6$ and 0.8 V vs. RHE). According to **Eq. 73**, the produced hydrogen peroxide most probably in the HO_2^- form ($\text{pK}_a \text{H}_2\text{O}_2/\text{HO}_2^- = 11.75$). Then, the obtained sample was immediately acidified toward pH 3.5 to form H_2O_2 . The quantity of H_2O_2 in sample was determined by spectrophotometry using potassium titanium (IV) oxalate based on formation a clear yellow complex solution of $\text{H}_2\text{O}_2\text{-Ti(IV)}$. The absorbance of the complex solution was measured at $\lambda = 400$ nm through a 1 cm polystyrene cuvette by a Jenway 6300 spectrophotometer (Barioworld Scientific Ltd, Dunmow, UK).



c. Electrochemical impedance spectrometry (EIS)

The electrochemical impedance spectroscopy measurements were using Potentiostat Biologic SP 150. The EIS curve was recorded in 10 mM potassium ferricyanide in 1 M KNO_3 solution by scanning twenty-six frequencies from 20 KHz to 1 Hz with amplitude of 10 mV at the open circuit potential (OCP ca. 0.4 V vs. Ag/AgCl at pH 7). It should be noted that ORR starts roughly at this potential. Hence, it enables getting the real kinetic parameters. Zview Software was used to fit the EIS data with a representative equivalent electrical circuit (EEC).

2.3.4.2 Electrochemical characterization of ACF@MnOx based electrode

a. CV profile and ORR LSV curve

The CV profile and ORR LSV curve were recorded as the same procedure for ACF@Pt based electrode above. However, the measurements were only performed in 50 mM PBS solution, pH 7, under nitrogen and oxygen atmosphere respectively. The CV voltammogram was recorded at scan rate of 10 mV s^{-1} which covers from -1.0 to $+1.0$ V vs. Ag/AgCl. Whereas, the ORR LSV curve was recorded at scan rate of 5 mV s^{-1} from OCP to -0.1 V vs. Ag/AgCl. The working electrode was the developed ACF@MnOx material (the coated geometric surface area 7.175 cm^2).

b. H_2O_2 quantification

The chronoamperometry experiments were performed in 20 mL of 0.1 M Na_2SO_4 solution for 1 hour under saturated oxygen atmosphere at four electrodes i.e ACF,

ACF@MnO_x-C25, ACF@MnO_x-C90, and ACF@MnO_x-C180 respectively. The ACF was treated under applied potential -0.4 V vs. Ag/AgCl while the rest three electrodes were treated either at -0.4 or +0.1 V vs Ag/AgCl. The produced H₂O₂ was quantified spectrophotometrically in the same way as the ACF@Pt electrode, as explained above.

c. H₂O₂ degradation test

100 mL of 100 ppm H₂O₂ solution was filled into a beaker glass equipped with a stir bar inside (**Figure 39**). About 1 mL of solution was previously taken and counted as sample at t_0 . As the ACF@MnO_x electrode was dipped in the solution (projected area 7.175 cm²), the time start to count. 1 mL of aliquot was taken every 5 minutes reaction. The test was conducted for one hour. The each aliquot was reacted with 1 mL of H₂SO₄ and 1 mL of titanium oxalate solution (50 g/L) to form a yellow H₂O₂-Ti(IV) complex solution. Thereafter, the absorbance were measured spectrophotometrically as previously explained.

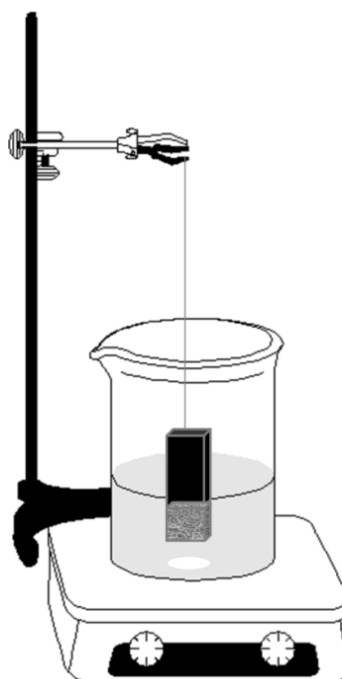


Figure 39 Schematic cell diagram for H₂O₂ degradation test

2.4 Microbial fuel cell experiment

2.4.1 Performance of MFC

Characterization of MFC performance both the double-chamber (DCMFC) and the single-chamber (SCMFC) were evaluated by several parameters: 1) open circuit voltage (OCV), 2) voltage generation, 3) power density, and 4) internal resistance.

2.4.1.1 OCV

Open circuit voltage (OCV) is the cell voltage at high external resistance where almost no current flow. The OCV means the highest voltage that can be reached by the cell. The OCV value can be seen from the polarization curve i.e. the intersection at y-axis.

2.4.1.2 Voltage generation

The voltage generation was measured daily using multimeter. The external resistance is fixed $R = 1 \text{ k}\Omega$. The generated current can be calculated by Ohm's Law according to **Eq. 74**. The current density, j , can be calculated by normalization toward the geometric surface area of the cathode or anode.

$$E_{\text{MFC}} = R_{\text{ext}} \times I_{\text{MFC}} \quad (\text{Eq.74})$$

where

E_{MFC} : generated voltage (V)

I_{MFC} : current (A)

R_{ext} : external resistance (Ohm)

2.4.1.3 Power density

The output power (mW) or power density maximum (mW m^{-2}) can be determined by conducting polarization i.e. measuring cell voltage at various resistances from $1 \text{ M}\Omega$ to $100 \text{ }\Omega$ using a resistor boat. We calculate the current using Ohm's Law as previously mention and the power using **Eq. 75**. Then, the calculated power densities were plotted toward the calculated current densities.

$$P_{\text{MFC}} = E_{\text{MFC}} \times I_{\text{MFC}} \quad (\text{Eq.75})$$

Where,

P_{MFC} : output power (W),

E_{MFC} : voltage (V), and

I_{MFC} : current (A).

Another way to measure the polarization is by LSV using potentiostat at scan rate 1 mV s^{-1} . The LSV measurement using two electrodes arrangement with working electrode connected to the cathode and counter electrode connected to the anode. The LSV start at the OCV (Its take around 30 minutes to 1 hour to reach stable OCV). The LSV was stopped at 0.01 V to prevent electrolysis in the cell. The LSV curve is current-voltage plot, by conversion we can re-plot to the power-current curve.

2.4.1.4 Internal resistance

Internal resistance of the MFC cell was measured by Electrochemical Impedance Spectroscopy (EIS) of Potentiostat Biologic-SP150. EIS measurement involves two-electrode arrangement. In this configuration, the cathode was connected as working electrode and the anode as counter electrode. The impedance spectrum was recorded at OCV with frequency range of 100 kHz to 100 Hz and voltage amplitude 10 mV. EIS also was used to identify the internal resistance of the anode and the cathode. For this purposes, impedance measurement conducted in a three-electrode arrangement using Ag/AgCl as reference electrode.

2.5 Study the feasibility of garden compost in classical double chamber microbial fuel cell (DCMFC)

2.5.1 DCMFC reactor

The microbial fuel cell was a customized tube-shaped glass reactor (**Figure 40**) which consists of two compartments with an equal volume. Both chambers were connected tightly and separated by a Nafion® 115 membrane which had previously soaked in water overnight. One chamber was oriented as anodic and another as cathodic one. In this research, we were using a tube-shaped glass reactor with narrow top opening for each compartment.

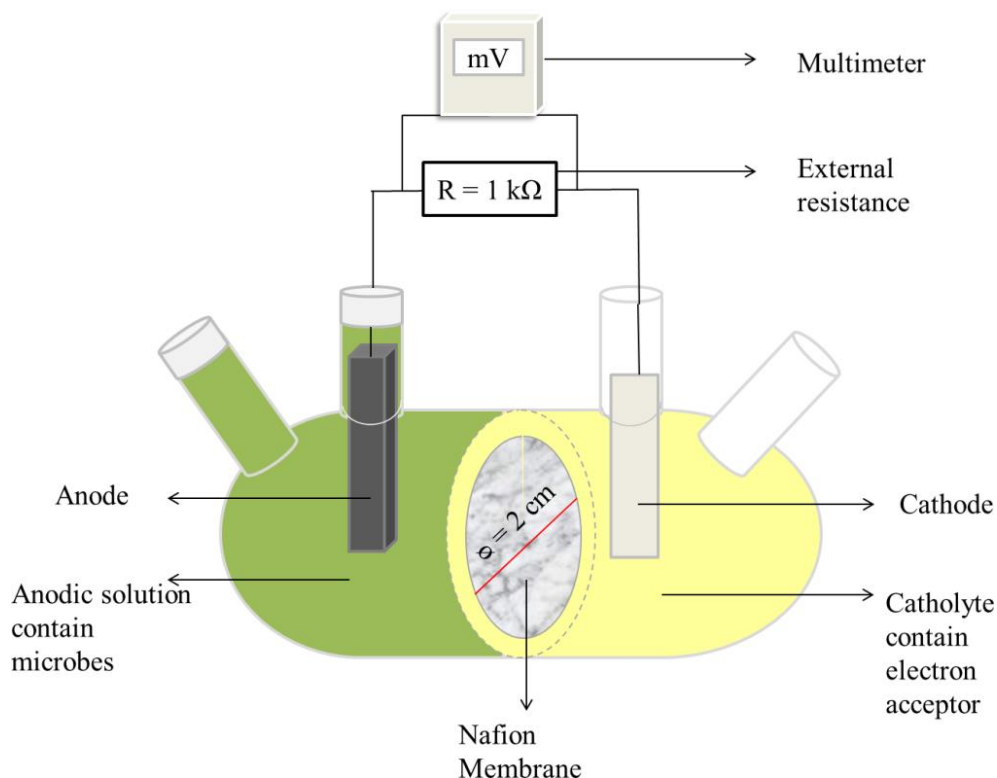


Figure 40 Customized reactor for running DCMFC experiment

In classical MFC experiment, called double chamber MFC (DCMFC), both anodic and cathodic compartments contain aqueous phase solution. The anodic solution was containing inoculum source, substrate, and electrolyte. The cathodic solution was the catholyte that composed of terminal electron acceptor species (such as ferricyanide solution). The anode and cathode were dipped inside their corresponding compartments and connected each other through external circuit with external resistance of $R_{\text{ex}} = 1 \text{ k}\Omega$. More detail of DCMFC operating condition will be provided later.

2.5.2 Microbial source preparation (Lixiviation)

Lixiviation is the process to prepare the inoculum source from garden compost leachate. About 1000 mL garden compost was mixed with 1000 mL of 60 mM KCl solution in a beaker glass. The mixture was gently stirred for 24 hours. The mixture then was filtered using gross filter 500 micrometer to separate solid part. The resulted leachate is then stored in closed container at room temperature.

2.5.3 General DCMFC operation

All MFC experiments in this research were using garden compost leachate as inoculum source. The DCMFC reactor was properly installed without leakage. Anodic part was fully filled by compost garden leachate in 60 mM potassium chloride solution that also contains 20 mM acetate. Anodic part was completely closed to maintain anaerobic atmosphere. The cathodic chamber was filled by 80 mL of 20 mM ferricyanide solution. The anode and cathode were connected through an external load $R_{ex} = 1 \text{ k}\Omega$. The generated voltage was measured daily using a high impedance multimeter (Voltcraft) to minimize current drop within R_{ex} .

2.5.4 Growing the biofilm

Self-growth method. In order to grow the biofilm on the anode surface, we run an experiment in a DCMFC reactor, as shown in **Figure 40**, according to general DCMFC operating condition, by dipped a carbon felt anode ($6 \times 1 \times 0.65 \text{ cm}$) in anodic chamber and stainless steel plate (SSP) cathode ($4 \times 1 \times 0.1 \text{ cm}$) in cathodic chamber.

Chronoamperometry method. The anodic chamber of the DCMFC, as shown in **Figure 40**, was fully filled by compost garden leachate that contains 20 mM acetate. Then, CF anode ($6 \times 1 \times 0.65 \text{ cm}$) was inserted inside. The anodic chamber was keep closed to maintain anaerobic atmosphere. The cathodic part was filled with 80 mL of 0.1 M KNO_3 solution and platinum disc was dipped inside as cathode. Chronoamperometry was running for 21 days at fixed potential of -0.16 V vs. Ag/AgCl reference electrode to develop biofilm on CF anode. The carbon felt anode was connected as working electrode and the Pt disc was connected to counter electrode. The growth of the biofilm was monitored by CV method at day 0, 7, 16, and 21.

After 21 days, the biofilm had formed and the operation was continued as general DCMFC operation by replacing the cathodic solution with 80 mL of 20 mM ferricyanide solution and the Pt disc cathode was changed with SSP ($4 \times 1 \times 0.1 \text{ cm}$).

2.5.5 DCMFC experiment at various anodes

Three DCMFC experiments, in the DCMFC reactor as shown in **Figure 40**, were conducted as general operation above by elaboration three kinds of anode i.e carbon felt (6 x 1 x 0.65 cm), carbon felt containing Pt NPs (4 x 1 x 0.65 cm) and graphite bar (4 x 1 x 0.5 cm). The cathode was SSP (4 x 1 x 0.5 cm) for each experiment.

2.5.6 Stability test of the bioanode

A cleaned DCMFC reactor was prepared. The anodic chamber was fully filled by 60 mM potassium chloride solution containing 20 mM sodium acetate solution, whereas the cathodic chamber was filled by 80 mL of 20 mM ferricyanide solution. The old bioanode (after stored for 1 month at 4°C) was placed as anode toward stainless steel plate cathode. The anode and cathode were connected through $R_{ex} = 1 \text{ k}\Omega$. The generated voltage was measured daily using multimeter (Voltcraft).

2.5.7 Buffered system of the anodic solution

Fresh garden compost leachate containing 50 mM phosphate buffer and 20 mM sodium acetate was replacing the anodic solution of a running MFC (listed in **Table 11**). The bioanode from this old MFC was kept inside. The cathodic solution was refreshed by a new solution of ferricyanide solution. The MFC was continued to operate. The generated voltage either before or after buffer addition were recorded. Three experiments were conducted as listed in the **Table 11**.

Table 11 The initial condition of three independent DCMFC experiments before switching to buffered anodic solution.

Entry	Running MFC age/ days old	anode	cathode
1	42	CF(6 x 1 x 0.65 cm)	CF@Pt (4 x 1 x 0.65 cm)
2	56	CF (6 x 1 x 0.65 cm)	SSP (4 x 1 x 0.1 cm)
3	64	CF(6 x 1 x 0.65 cm)	SSP (4 x 1 x 0.1 cm)

2.5.8 DCMFC experiment to study various electron acceptor in the cathodic chamber

The DCMFC, as shown in **Figure 40**, was initially operated for 42 days to grow the biofilm on the carbon felt anode surface as described in general operation above. The anodic solution was replaced by buffered system and the cathodic was refreshed. After 8 days run, the stainless steel cathode was replaced with the ACF cathode. The detailed experiment conditions are listed in **Table 12**.

2.6 Single chamber microbial fuel cell (SCMFC) with air-breathing cathode system

2.6.1 Electrochemical characterization of CF

Preliminary study of CF was conducted in 10 mM potassium ferricyanide (in 0.1 M KNO_3) in a common half-cell CV at various scan rates (30, 40, 50, 60, 70, 80, 90, 100 mV s^{-1})

Table 12 Various treatment during the DCMFC operation

Period / days	Anodic part		Cathodic part		The aim of experiment is in order to observe:
	Base	Anodic solution	cathode	Electron acceptor	
0-42	CF	Non-buffered	SSP	20 mM Fericyanide	Growing biofilm
42-48	CF	Buffered	SSP	20 mM Fericyanide	Effect of buffer
49-69	CF	Buffered	ACF	20 mM Fericyanide	Effect of cathode material
70-71	CF	Buffered	ACF	H_2SO_4 pH 2	Effect of acidic catholyte
72- 86	CF	Buffered	ACF	20 mM Vanadium in H_2SO_4 pH 2	Effect of electron acceptor
87- 93	CF	Buffered	ACF	20 mM Fericyanide	Effect of electron acceptor
94 - 101	CF	Buffered	ACF	100 mM Vanadium in H_2SO_4 pH 2	Effect of electron acceptor concentration
102 - 108	CF	Buffered	ACF	4 mM Vanadium in H_2SO_4 pH 2	Effect of electron acceptor concentration

2.6.2 Preliminary test of CF as air-breathing cathode

A clean CF (4 x 3 x 0.635 cm) was installed between two-square-shaped acrylic reactors, as shown in **Figure 41**, hence form two-chamber cell. Chamber 1 was filled by phosphate buffer solution pH 7. Then, a reference (Ag/AgCl) and a counter electrode (Pt disc) were arranged in this chamber and were connected to CF (as working electrode) in the middle of the reactor. Chamber 2 was a gaseous phase chamber, which filled by the studied atmosphere i.e. nitrogen, air, or oxygen during electrochemical measurement (CV, LSV, and CA).

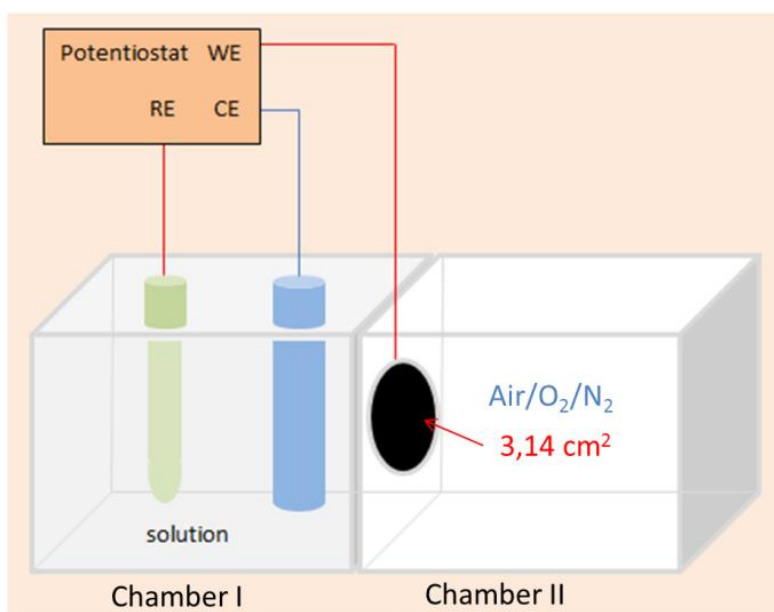


Figure 41 Air-breathing electrode configuration for electrochemical measurement

2.6.3 Preliminary test of CF as air-breathing cathode in microbial fuel cell

The twin square acrylic reactor (**Figure 41**) was tested for MFC operation. The CF air-breathing electrode was previously adhered with Nafion115 before installed in the reactor. The Nafion side was oriented to face the anodic chamber containing solution whereas the other side was facing empty chamber. The anodic chamber was filled with garden compost leachate as bacterial source. The graphite felt (GF) (3 x 1 x 0.65 cm) was inserted inside as anode and the system was closed by parafin film. The cathodic chamber was kept open to free air. The anode and air-breathing cathode were then connected through 1 k Ω resistance load. The generated voltage was monitored daily using high impedance multimeter (Voltcraft). The current and power were calculated by Ohmic Law and

normalized toward exposure surface area of air-breathing cathode. Herein, the daily generated voltages were very low due to no catalyst presented on the air-breathing cathode. Therefore, the modification of CF is important to obtain better performance of the MFC.

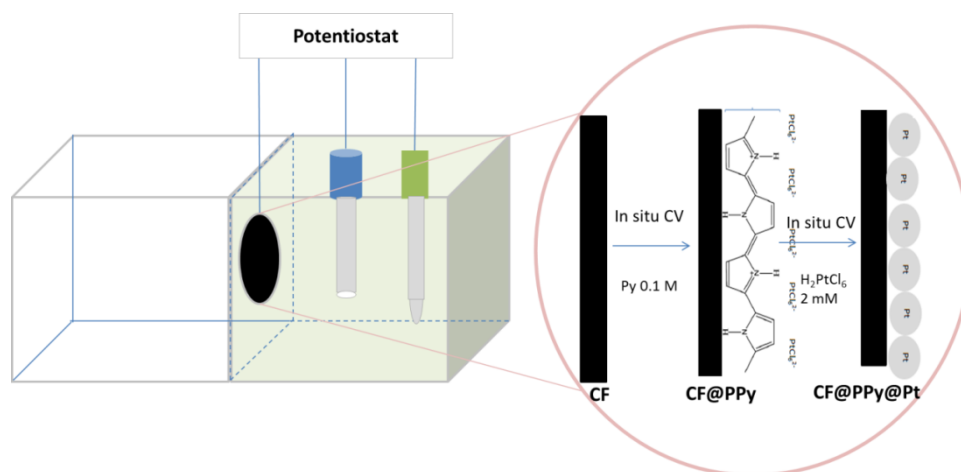


Figure 42 Schematic diagram of electropolymerization of polypyrrole and consecutive electrodeposition of platinum onto carbon felt

2.6.4 Modification of CF by Polypyrrole/Platinum (PPy/Pt) and its preliminary application as air-breathing cathode in the SCMFC

In the reactor (**Figure 41**), one side of CF was facing electrochemical solution chamber and another was facing empty chamber/free air with both exposure area were 3.14 cm^2 . The electrochemical solution, 0.1 M pyrrole in 0.02 M sodium perchlorate, was introduced into the reactor and the three-electrode were arranged. The CF was connected as working electrode, Ag/AgCl as reference electrode and platinum disc as counter electrode. Then, the reactor was covered by paraffin film immediately. The nitrogen gas was purged into the solution for 15-20 minutes before electropolymerization started. The electropolymerization was conducted by CV at potential range 0 – 1.0 V vs. Ag/AgCl for 30 cycles at 20 mV s^{-1} . The polypyrrole was only formed on certain localized area (3.14 cm^2) on the half side of CF that was exposed to the solution during electropolymerization. This resulted in the material, which referred as CF@PPy. Further modification was loading platinum on CF@PPy by electroreduction. For this, the electrochemical solution was changed by 2 mM chloroplatinic acid solution. Electroreduction was

conducted by CV from 0 to -0.5 V vs. Ag/AgCl for 20 cycles at scan rate of 20 mV s^{-1} . The electropolymerization of PPy and electroreduction Pt on the CF surface to yield CF@PPy@Pt is illustrated in **Figure 42**.

The resulted material, referred as CF@PPy@Pt, was used as air-breathing cathode in SCMFC following the same procedure, as described in **Section 2.6.3**. The polarization curve was plotted from a series of measured voltages over various external resistances (From $100 \text{ k}\Omega$ to 10Ω) using a resistor boat.

2.6.5 Glass tube-shaped SCMFC reactor

The utilization of the square-shaped SCMFC reactor (**Figure 41**) has resulted a poor MFC performance, although by using the PPy/Pt modified CF (CF@PPy@Pt) air-breathing cathode. The square-shaped SCMFC reactor has a wide top opening which allowed oxygen from air to enter the anodic chamber. This made a difficulty to keep anaerobic environment in anodic chamber which led to low MFC's performance. In order to overcome this problem, a tube-shaped glass reactor, as used in DCMFC, was modified into SCMFC reactor (**Figure 43**).

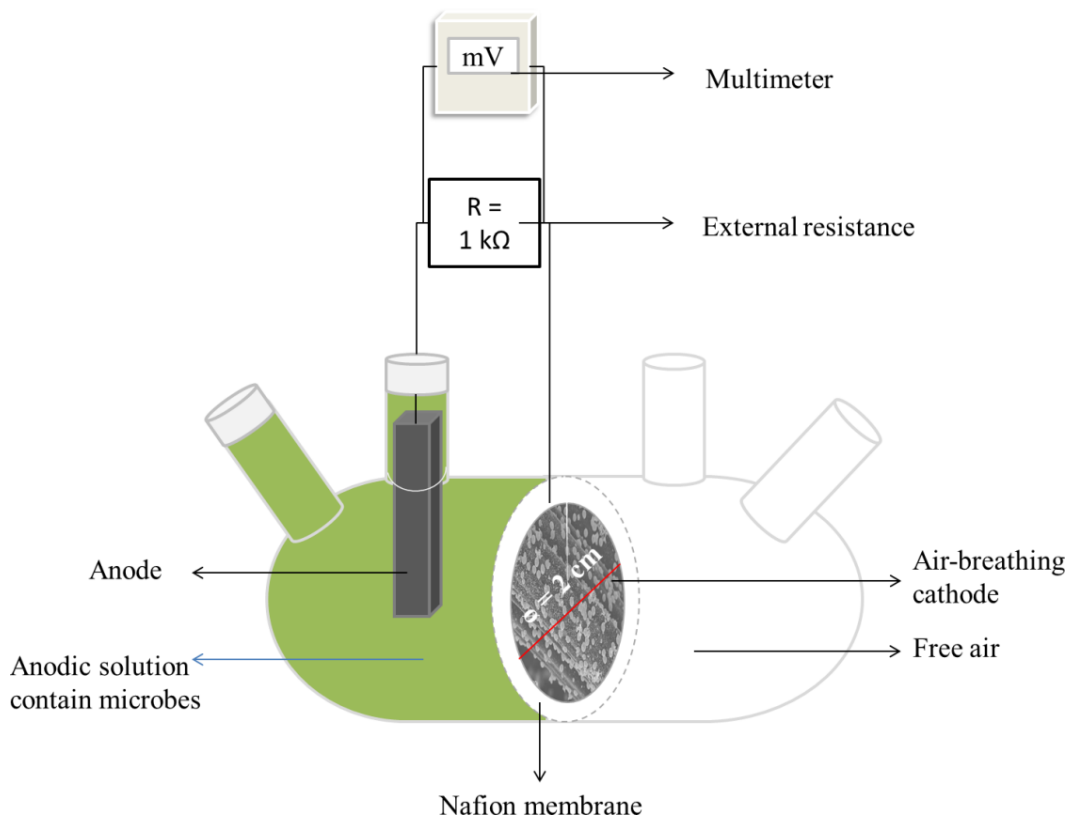


Figure 43 Customized SCMFC reactor with air-breathing cathode system

SCMFC operation was conducted in similar reactor as DCMFC with a slight modification. Herein, the aqueous phase of cathodic compartment suppressed. Hence, the cathode was air-breathing type which was adhered with Nafion®115 and positioned in the middle between anodic and cathodic compartment. The Nafion®115 side was faced the anodic solution and the air-breathing cathode was faced the free air in the cathodic compartment. The schematic diagram of the SCMFC reactor is shown in **Figure 43**.

2.6.6 Application of the tube-shaped glass SCMFC reactor with CF@PPy@Pt air-breathing cathode

The SCMFC procedure in **Section 2.6.3** was repeated in this reactor (**Figure 42**) by applying the CF@PPy@Pt air-breathing cathode. The PPy modified CF (CF@PPy), without Pt, was also tested as air-breathing cathode to run an equal SCMFC experiment as a control. Herein, we also tested the CF@PPy air-breathing cathode without Nafion 115 in equal SCMFC experiment. The classical double chamber MFC was also performed in tube-shaped glass reactor (**Figure 40**) with the same anodic part condition unless the cathodic part was filled by 20 mM potassium ferricyanide solution as terminal electron acceptor and commercial stainless steel plate as cathode.

2.6.7 Electrochemical characterization of CF, CF@PPy, and CF@PPy@Pt

All electrochemical measurements were carried out using Potentiostat Biologic SP-50. The study of oxygen reduction reaction (ORR) performance of CF, CF@PPy and CF@PPy@Pt were conducted in electrochemical cell, contains phosphate-buffered solution (PBS), as configured in **Figure 41**. In this configuration, the modified part, either CF@PPy or CF@PPy@Pt, was faced the solution whereas another was faced the free air space. The study of each air-breathing electrode toward nitrogen or oxygen atmosphere was being conducted by flow each gas into the free air space chamber during electrochemical measurement.

2.7 SCMFC with ACF@Pt-based and ACF@MnOx-based air-breathing cathode

2.7.1 Fabrication of air-breathing cathode: ACF@Pt based air-breathing cathode

ACF@Pt with dimensions of 3 cm high, 3 cm wide and 0.6 cm thickness (i.e. a geometric area of 23.7 cm² available for the entire 5 exposed rectangular surfaces) as air-cathode was prepared at optimum condition (1 hour, 5 mM) of Pt electrodeposition as described in **Section 2.3.3.1** above.

2.7.2 Fabricating of air-breathing cathode: ACF@MnOx based air-breathing cathode

Three air-breathing cathodes were constructed by electrodeposition of manganese oxide (MnOx) on ACF from MnCl₂ solution at various concentration i.e. 25, 90, and 180 mM at $E_{\text{appl}} = 1.3 \text{ V vs Ag/AgCl}$ for $t = 4$ hours.

2.7.3 General SCMFC operation

Air-breathing electrode was previously adhered with Nafion®115 before installed in the reactor. The Nafion®115 side was oriented to face the anodic chamber containing solution whereas the other side was facing free air (empty chamber). The anodic chamber was fully filled with garden compost leachate contain 20 mM sodium acetate. The anode was inserted inside as anode and the system was closed properly. The cathodic chamber was kept open to free air. The anode and air-breathing cathode were then connected through $R_{\text{ex}} = 1 \text{ k}\Omega$. The generated voltage was monitored daily using a high impedance multimeter. Some experiments of single chamber microbial fuel cell with air-breathing cathode are listed in the **Table 13**. The exposed electrode area is based of accounting for one sides of the cathode that faces the air (circle of 1 cm radii), but not taking into account the internal surface of the 3D-electrodes, which cannot evaluated easily.

2.7 Single chamber microbial cell with air-breathing cathode to study electron transfer mechanism

Garden compost leachate from the anodic compartment of running air-cathode microbial fuel cell (SCMFC) was pumped out using peristaltic pump (35 rpm, Masterflex I/P). The bioanode was kept inside the closed SCMFC reactor. The

voltage was noted before and after withdrawing leachate. The leachate was divided into two centrifuge tube of same weight and centrifuged at 4400 rpm for 10 min at room temperature. The obtained pellets were suspended in 60 mM KCl with the same volume solution as previously used to measure the initial absorbance at 600 nm. The two supernatant leachate solutions were mixed in a beaker glass and 2 mL was taken for acetate analysis (the sample was filtered using 0.2 μm filter before analysis) and absorbance measurement (at 600 nm). The remaining suspension was nitrogenized for 10 minutes and consecutively pumped back into the anodic compartment of SCMFC reactor while maintaining the nitrogen flow. The volume of the recovered solution was decreased due the separation by centrifugation (as the solid volume was lost) and the sampling processing. The contacted surface area of the anode was consequently decreased (by about 1/3 from the initial). The voltage was monitored periodically. After 24 and 48 hours, samples were taken (about 2 mL) i.e. 1 mL for absorbance measurement and 1 mL for acetate measurement by liquid chromatography.

Table 13 The SCMFC experiments with various air-breathing cathode system

Entry	Anode	Air-breathing cathode	Exposure area / cm^2
1	CF (10 x 1 x 0.65 cm)	ACF@Pt (3 x 3 x 0.65 cm)	3.14
2	ACF (4 x 1 x 0.65 cm)	ACF@Pt (3 x 3 x 0.65 cm)	3.14
3	ACF@Pt (4 x 1 x 0.65 cm)	ACF@Pt (3 x 3 x 0.65 cm)	3.14
4	CF (6 x 1 x 0.65 cm)	ACF (2.5 x 3 x 0.65 cm)	3.14
5	CF (6 x 1 x 0.65 cm)	ACF@MnOx-C180 (2.5 x 3 x 0.65 cm)	3.14
6	CF (6 x 1 x 0.65 cm)	ACF@MnOx-C90 (2.5 x 3 x 0.65 cm)	3.14
7	CF (6 x 1 x 0.65 cm)	ACF@MnOx-C25 (2.5 x 3 x 0.65 cm)	3.14

2.9 Electrochemical characterization in the MFC cell

The anodic part of the MFC was studied electrochemically in our customized MFC reactor configuration using three-electrode arrangement (**Figure 44**). The anode is connected to the working electrode, whereas the cathode as the counter electrode. The CV voltammetry is run at range -1 to 1 V at scan rate of 10 mV s^{-1} . This method is useful to see the difference between clean electrode and electrode with biofilm on it. The LSV of the anode also was measured before and after the biofilm formation to study the behavior of bioanode.

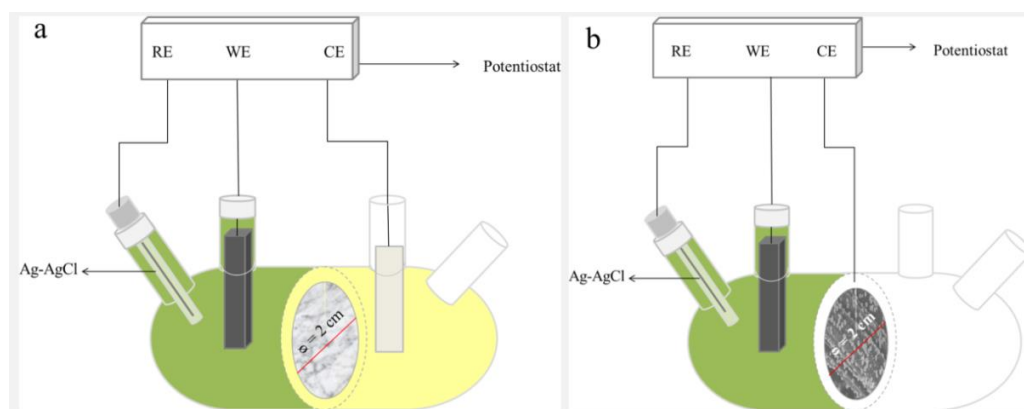


Figure 44 Three-electrode configuration in (a) DCMFC and (b) SCMFC during electrochemical characterization of bioanode

2.10 Other application of the developed material

2.10.1 ACF@Pt electrode for hydrogen evolution reaction (HER)

Electrocatalytic activity towards HER was evaluated by LSV at scan rate of 5 mV s^{-1} in N_2 -saturated 0.1 M KOH solution and stability was carried out at by CA at $E_{\text{appl}} = -0.22 \text{ V vs. RHE}$ for 10 hours. The above potentiostat was used and all the electrochemical measurements were conducted at room temperature.

2.10.2 Application of ACF@MnOx in electro-Fenton-like (EF-like) experiment

The electro-Fenton-like (EF-like) experiment was conducted at room temperature in 100 mL beaker glass with two electrode arrangement (**Figure 45**). The working electrode was the developed ACF@MnOx-C90 (gsa. 7.175 cm^2) and positioned as cathode whereas the counter electrode was platinum mesh. The distance of electrodes was kept 3 cm . The current was applied using power supply (CNB

Electronique). The electrofenton experiments were conducted to mineralization of 60 mL of 0.1 mM acid orange 7, AO7, solution containing 50 mM Na₂SO₄ as electrolyte. The solution was oxygenated for 15 minutes before applying current by sparging air continuously into the solution. The solution color fading was monitored every 5 minutes for 1 hour reaction by measuring its absorbance at 485 nm. Demineralization was conducted by measuring total organic carbon, TOC, using TOC Analyzer (TOC-L CSH/CSN Shimadzu, Japan) of the samples either fresh or after treated at 1, 2, 4, 6 and 8 hours of electrolysis. The stabilization of the electrodes was tested by reusing the electrode up to 5 consecutive cycles.

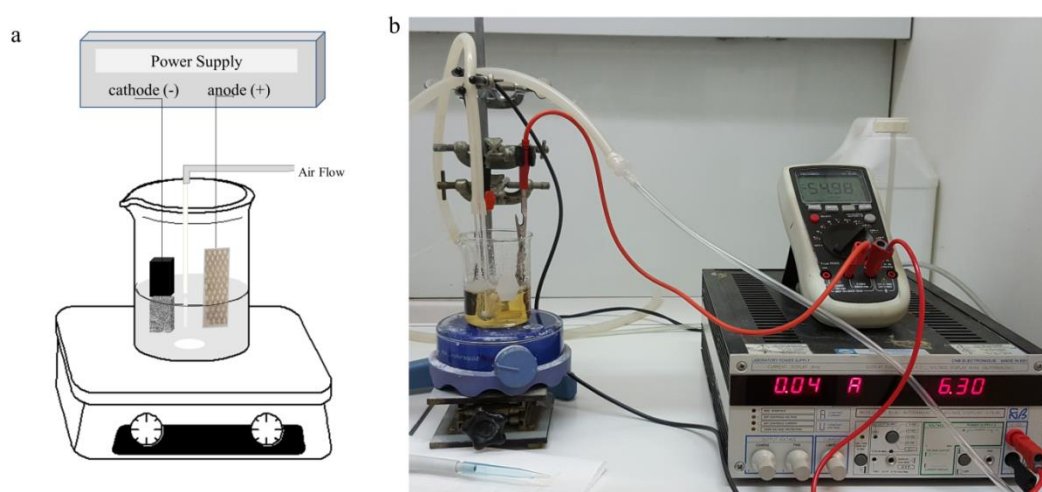


Figure 45 (a) Schematic and (b) electrolysis cell for EF-like process in demineralization of AO7 at ACF@MnO_x electrode

2.11 Physicochemical characterization

2.11.1 Fundamental

2.11.1.1 X-ray diffraction (XRD) analysis

X-Ray Diffraction is an analysis method to determine crystallographic properties and atomic spacing. The principles of the XRD is the interaction between monochromatic X-rays and crystalline that results in constructive interference and a diffracted ray [152,153]. The diffraction of X-rays by a crystal is presented in **Figure 46a**. From this diffraction path, the Bragg's Law correlates the wavelength of electromagnetic radiation to the diffraction angle and lattice spacing of crystalline sample. A monochromatic X-ray radiation strikes the crystal at angle θ

which leads to the scattering due to the interaction of the radiation with the atom located at O, P, and R [154].

If the distance,

$$AP + PC = n\lambda \quad (\text{Eq.76})$$

When n is an integer, the scattered radiation will be in phase at OCD, and the crystal will appear to reflect the X-radiation, but

$$AP = PC = d \sin \theta \quad (\text{Eq.77})$$

Where d is the interplanar distance of the crystal. Thus the conditions for constructive interference of the beam at angle θ are

$$n \lambda = 2d \sin \theta \quad (\text{Eq.78})$$

then,

$$\sin \theta = n \lambda / 2d \quad (\text{Eq.79})$$

Eq. 79 is the important Bragg's equation. Note that X-rays appear to be reflected from the crystal only if the angle of incidence satisfies the condition.

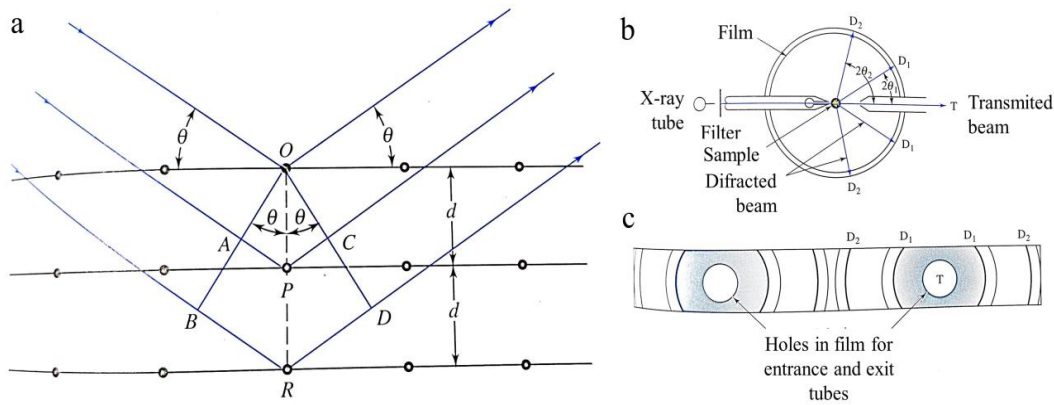


Figure 46 (a) Bragg's Diffraction, (b) Debye-Scherrer powder camera and (c) its typical developed film [154]

The diffraction pattern is recorded by Debye-Scherrer powder camera which shown schematically in **Figure 46b**. The non-diffracted radiation T passes out of the camera through a narrow exit tube. The cylindrical camera consists of an inside film strip covering. The sample is placed in the center of the beam. The typical exposed and developed film is shown in **Figure 46c**. The lines represent diffraction from one set of crystal planes. Then, the Bragg's angle for each line can be evaluated easily from the geometry of the camera [154].

2.11.1.2 X-ray photoelectron spectroscopy (XPS)

X-ray photoelectron spectroscopy is a useful technique for the elemental analysis of the surface [155]. XPS provides information either the atomic composition of the samples or the structure and oxidation state of the compound being examined. The XPS principle based on the interaction between the photon and the inner electron at shell K of the atom. XPS using a characteristic monochromatic X-ray radiation (with photon energy 200 – 2000 eV) to induces electron removal from an inner energy level that results in radiation out of the surface. **Figure 47a** is a schematic representation of the physical process involved in XPS.

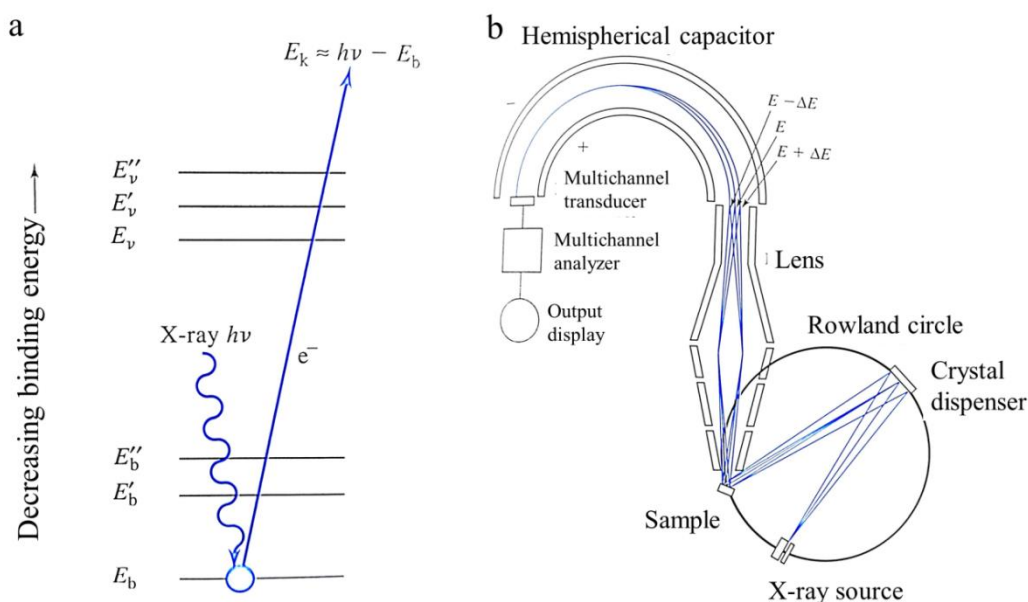


Figure 47 (a) Illustration of interaction between photon and electron in the inner shell of an atom and (b) schematic diagram of electron energy analyzer in XPS [154]

As shown in the illustration, one of the photons of a monochromatic X-ray beam of known energy, $h\nu$, displaces an electron, e^- , from a K orbital of energy E_b . The process can be represented as **Eq.80**.



For energy conservation, thus

$$E(A) + h\nu = E(A^{+*}) + E(e^-) \quad (\text{Eq.81})$$

The electron energy is present in the form of kinetic energy (KE) that can be expressed in **Eq. 82**.

$$KE = h \nu - BE \quad (\text{Eq.82})$$

Herein BE is binding energy i.e. the difference energy between neutral and ionized atom (**Eq. 83**)

$$BE = (E(A^{+*}) - E(A)) \quad (\text{Eq.83})$$

The kinetic energy of the released photoelectron can be measured using electron energy analyzer and recorded as photoelectron spectrum. Thus, the BE can be calculated according to the **Eq. 82**. The BE of an electron is characteristic of the atom and orbital which emits the electron [154].

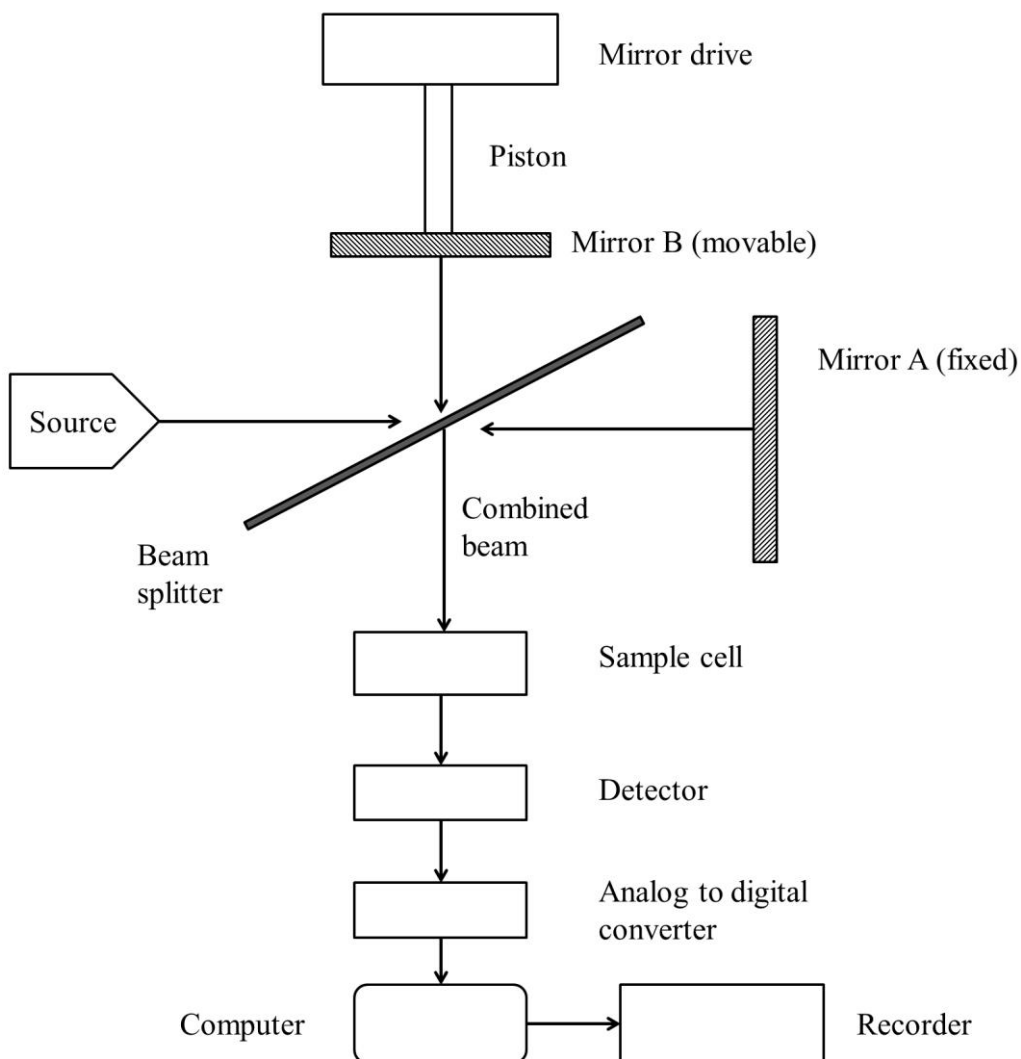


Figure 48 Schematic diagram of FTIR instrument [154]

2.11.1.3 Fourier-transform infra red spectroscopy (FTIRS)

Electromagnetic radiation of IR at 4000 cm^{-1} and 400 cm^{-1} is useful for spectroscopic analysis. IR in this range is absorbed and converted into energy of molecular vibration. The vibrational spectra appear as band that characteristic for every molecule. The analysis of one pass of radiation through the sample will give rise to complete IR spectrum [154]. The schematic diagram of FTIR is presented in **Figure 48**.

2.11.1.4 Scanning electron microscopy (SEM) - energy dispersive X-ray (EDX)

SEM is the important technique for obtaining detailed information about physical nature of surfaces with much higher-resolution. The finely focused beam of electron is struck on the solid sample surface to produce SEM image. The beam of electrons is scanning across the sample. The resulted signal is received above the surface (in z direction), stored in a computer, and converted to an image. The types of resulted signal for SEM instrument are a backscattered and secondary electron respectively. Many SEM modern are also equipped with X-ray detector, so-called scanning electron microscopy-energy dispersive X-Ray or SEM-EDX, are more advantage that allow qualitative and quantitative analysis by X-ray fluorescence aid [154]. The instrument of SEM-EDX is presented schematically in **Figure 49**.

2.11.1.5 Thermo gravimetric analysis (TGA)

Thermo gravimetric analysis (TGA) is one of the popular thermal analysis techniques in which physical properties of substance or its reaction products are measured as a function of temperature. In TGA, the mass of a sample under controlled atmosphere is recorded continuously as a function of temperature or time as the temperature of the sample is increased (usually linearly with time). A plot of mass or mass percentage as a function of time is called as thermogram or a thermal decomposition curve. Commercial TGA unit consist of a sensitive microbalance, furnace, pure-gas system or reactive atmosphere, computer. The schematic diagram of the TGA unit presented in **Figure 50** [154].

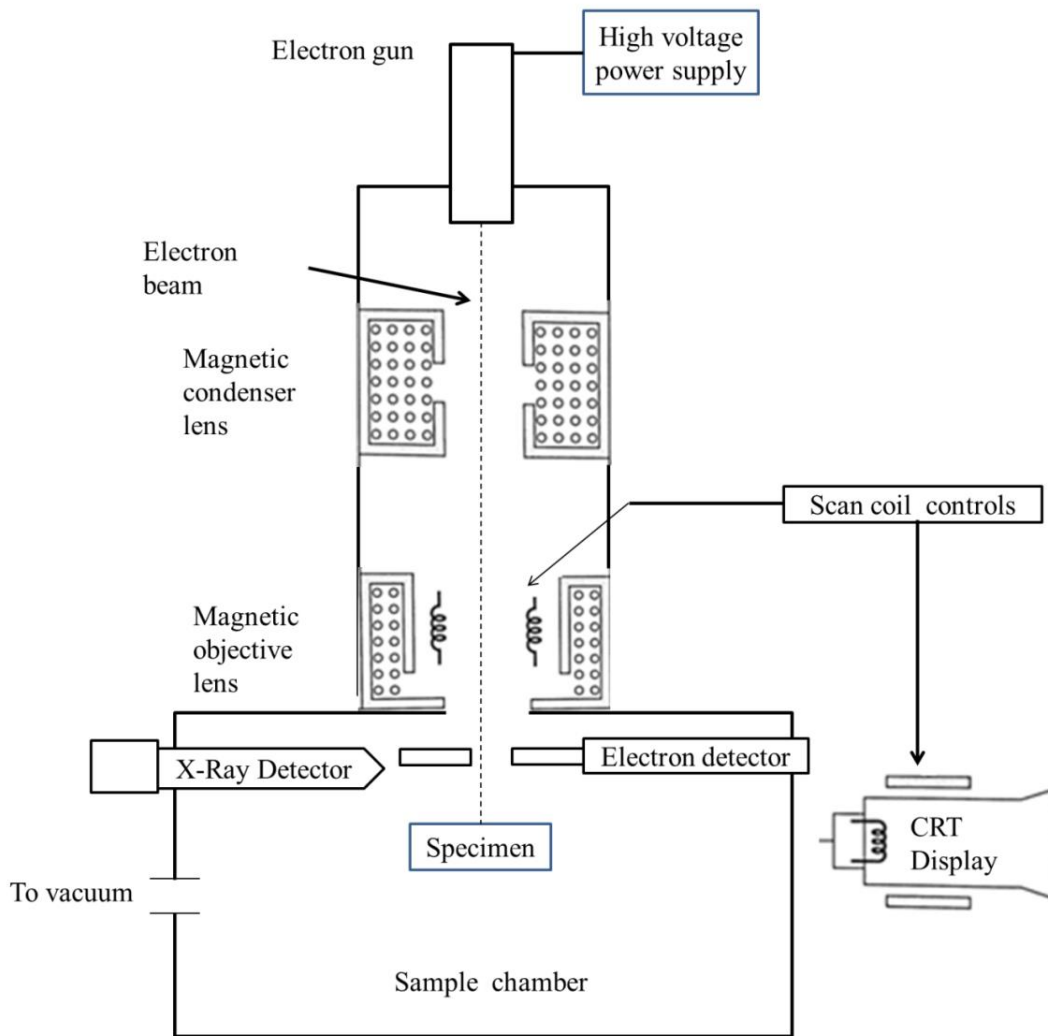


Figure 49 Schematic diagram of SEM-EDX instrument [154]

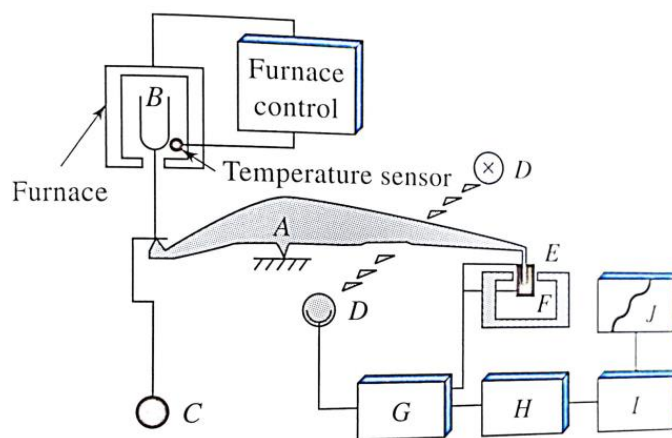


Figure 50 Schematic diagram of TGA instrument [154]

2.11.1.6 Inductively couple plasma-mass spectrometer (ICP-MS)

Inductively couple plasma mass spectrometry (ICP-MS) is an analytical technique for elemental determination. The ICP source converts the atom of element in the sample to gaseous ion. The ICP source is an ICP torch as shown schematically in **Figure 51**. Argon gas is located in the high frequency field to be ionized. The electrons are stripped off the argon atoms to form argon ions by applying a spark. These ions collide with other argon atoms under the oscillating fields and form argon discharge or plasma. The sample, usually in aerosol form, is fed to the ICP torch and completely be desolvated. The elements in the aerosol are converted first into gaseous atoms and then ionized towards the end of the plasma. Then, these resulted gaseous ion are then separated and detected by a mass spectrometer [156].

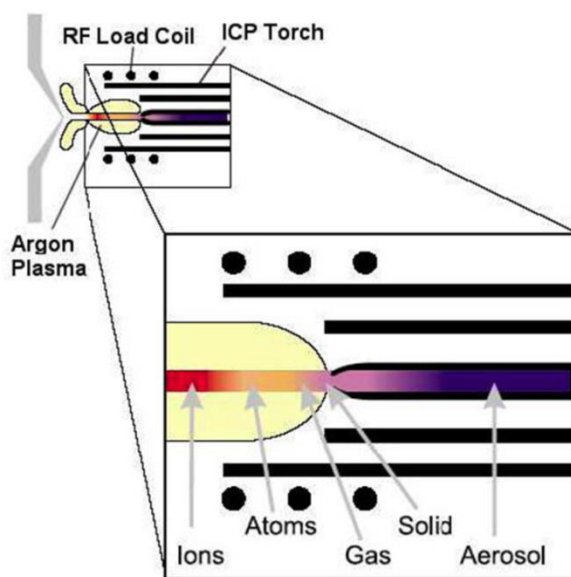


Figure 51 Plasma generation [156]

2.11.2 Experimental

2.11.2.1 XRD

X-Ray Diffraction analysis (XRD) was used to determine the crystallographic structure and the crystallite size of the as-synthesized nanostructures. The raw XRD pattern data were recorded using PANalytical Xpert-PRO diffractometer (equipped with an X'celerator detector employing nickel filter) in Bragg–Brentano (θ - θ) configuration with a copper tube powered at 40 kV and 20 mA

($\text{Cu}_{k\alpha 1} = 1.54060 \text{ \AA}$ and $\text{Cu}_{k\alpha 2} = 1.54443 \text{ \AA}$). The diffractogram acquisition was realized from 10 to 80° in diffraction angle (in 2θ) every 0.017° with respect to a time of 55.245 s/step . Finally, information on interest was extracted from the patterns by using the common pseudo-Voigt function on HighScorePlus software; however, XRD patterns shown herein are not fitted. Textural and morphological analyses of the materials were performed using scanning electron microscope (SEM) on a Hitachi S-4800 microscope.

XRD was used to determine the crystallographic structure and the crystallite size of the as-synthesized nanostructures. The raw XRD pattern data were recorded using PANalytical Xpert-PRO diffractometer (equipped with an X'celerator detector employing nickel filter) in Bragg–Brentano (θ - θ) configuration with a copper tube powered at 40 kV and 20 mA ($\text{Cu}_{k\alpha 1} = 1.54060 \text{ \AA}$ and $\text{Cu}_{k\alpha 2} = 1.54443 \text{ \AA}$). The diffractogram acquisition was realized from 10 to 80° in diffraction angle (in 2θ) every 0.017° with respect to a time of 55.245 s/step . Finally, information on interest was extracted from the patterns by using the common pseudo-Voigt function on HighScorePlus software; however, XRD patterns shown herein are not fitted.

2.11.2.2 XPS

X-ray Photoelectron Spectroscopy was used to characterize surface state. Three representative samples were selected i.e RCF, ACF and ACF@Pt as resulted from optimum condition and analyzed using XPS ESCALAB 250 spectrometer (Thermo Electron, monochromatic radiation source $\text{Al K}\alpha = 1486.6 \text{ eV}$). Survey spectra were recorded at a step of 1 eV (transition energy: 150 eV) and high-resolution spectra were recorded at a step of 0.1 eV (transition energy: 20 eV). The measurement of binding energy was corrected on the basis of the energy of $\text{C } 1s$ at 284.4 eV , and the quantification was carried out from the corresponding XPS peak area after correction with a suitable sensitivity factor.

2.11.2.3 FTIRS

Fourier-transform infrared spectroscopy (FTIRS) analysis was carried out on a Nicolet Nexus FTIR spectrometer (Thermo Electron Corporation). To perform

this analysis, the samples were prepared previously as potassium bromide pelleted. About 2 mg of each selected samples (CF, ACF, and ACF@Pt) is crushed and mixed with 100 mg of mg potassium bromide.

2.11.2.4 SEM

Scanning Electron Microscopy (SEM) was used to analyze texture and morphology of the resulted materials. Those were performed on Hitachi S-4800 microscope.

SEM of biofilm

Before analysis, the bioanode samples were pretreated to strengthen biofilm attachment and to remove water content. To this end, a piece of bioanode (0.5 cm x 0.5 cm x 0.635 cm) was immersed in 4 wt. % of glutaraldehyde solution for 4 hours. Then, the samples were copiously rinsed by water. Dehydration process was carried out by maceration of the samples in a series of graded concentration ethanol solution (20 wt. %, 40 wt. %, 60 wt. %, 80 wt. %, and 98 wt. %) for 10 minutes in each concentration. The samples were then dried in desiccator at room temperature for 24 hour.

2.11.2.5 SEM-EDX

Scanning Electron Microscopy (SEM) with energy dispersive X-ray (EDX) spectroscopy was used to analyze either texture and morphology or chemical composition of the resulted materials. Those were performed on SEM Zeis EVO HD15 and EDX analyzer Oxford Instruments X-max^N SDD (Institut Europeen des Membranes, France).

2.11.2.6 TGA

Thermo gravimetric analysis (TGA) was used to determine the metal loading. Both analyses were conducted on TA Instrument SDT 2960 apparatus equipped with TA Universal Analysis software. In standard test, a representative sample of 15-20 mg was put in a platinum crucible, thermally heated under air flow of 60 mL min⁻¹ at a heating rate of 10 °C min⁻¹ to 600°C followed by an isothermal 60 min at 600 °C and finally heating rate at 10 °C min⁻¹ to 800°C. A second empty crucible was used as reference.

2.11.2.7 ICP-MS

Inductively couple plasma (ICP) was performed to additional quantitative analysis of the Pt content on the resulted material. Herein, we used ICP-MS, iCAP Q (Thermo Scientific) on the AETE-ISO platform (OSU-OREME/Universite de Montpellier).

2.11.2.8 Wetability test

Wetability tests were performed by water droplet method as usually being conducted for contact angle measurement. Herein, ultrapure water aliquot of 6 μL is dropped on the electrode. The drop shape was analyzed using a low-bond axis symmetric technique.

Chapter 3:

Result and Discussion

Chapter 3 Result and Discussion

3.1 Study of double chamber microbial fuel cell (DCMFC) powered by garden compost

3.1.1 Garden compost microbial source

In an MFC, the microorganism used as the source for electricity generation are bacteria that are capable of transferring electrons outside their cells, so-called exoelectrogenic or electroactive bacteria (EAB) [68]. Various interesting electroactive inoculum sources such as wastewater [55], activated and anaerobic sludge [157], sediment [56], soil [57], compost [18], manure [158], rumen [159], and agro-industrial wastes have been reported [160].

Garden compost contains a very wide microbial diversity, among which electroactive bacteria. Some reports have shown the possibility of harnessing electroactive bacteria from this source and apply it in an MFC for generating power [18,74,161,162] In this research, we selected garden compost as microbial source referring to our previous work [163] for its basic characterization, as listed in **Table 14**.

Table 14 Composition and basic characterization of garden compost [163]

Composition	Characteristic	
Black soil mainly containing vegetal based compost	Dry material	30 wt. %
	Organic material	60 wt. %
	Water retention capacity	680 mL L ⁻¹
	Conductivity	0.5 mS cm ⁻¹
	pH	6.5

Preparation of garden compost as inoculum source was done by lixiviation in 60 mM KCl solution to produce leachate. The role of the KCl solution is to obtain a medium with proper conductivity to support the electrochemical process [161]. The garden compost leachate had conductivity of 7.5 mS cm⁻¹ after lixiviation [163].

In this research, we added acetate to the medium in the anodic part of the MFC to feed the electroactive microbes. Acetate is a common substrate for growing anaerobic consortia in MFC that produces higher power and current density than other substrates such as glucose, butyrate, starch, or dextran [164]. Acetate is a small organic molecule which has only two carbons, thus it can easily be degraded. This leads to high coulombic efficiency, 65 – 90 % [164]. In most cases, oxidation of acetate produces 8 electrons (**Eq. 84**).

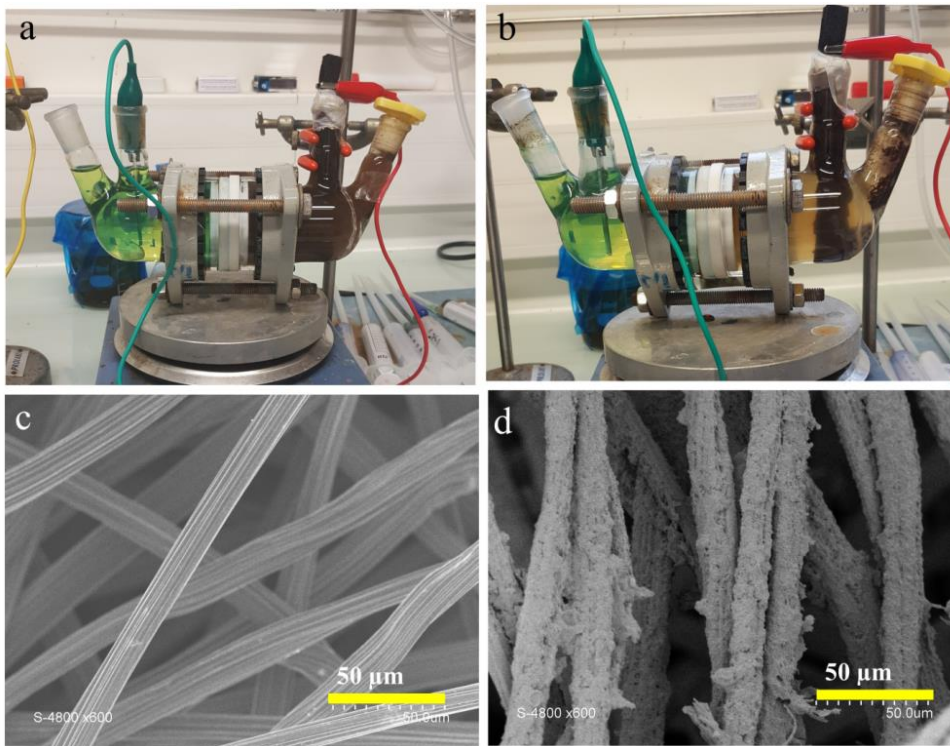
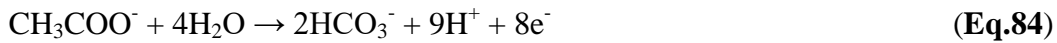


Figure 52 DCMFC operation (a) during the beginning period, before and (b) after biofilm growth on the anode after around 15 days. Close up of (c) bare anode and (d) anode covered by biofilm under SEM examination

3.1.2 Growing the bioanode

A bioanode or microbial anode is an anode that is covered by electroactive biofilm. Electroactive bacteria in an inoculum source may grow on the anode to form biofilm in two ways: 1) natural colonization of the microbe on the anode surface and 2) applied constant potential stimulation. In this research, we compared both bioanode-growing methods carried out using garden compost leachate.

3.1.2.1 Self-growth bioanode

In the first method, the bioanode was grown as the DCMFC started. At the beginning period (the first two weeks), so-called initiation step, most bacteria are still present in planktonic state in the solution (**Figure 52a**). Over time, the bacteria start to colonize on the anode surface and form a biofilm. As the colony grows larger, the biofilm becomes visible (**Figure 52b**). Owing to no external potential was applied during the DCMFC operation to growth the biofilm, then we referred this method as self-growth bioanode. The self-developed current may contribute to biofilm development.

Figure 52c shows a clean and smooth surface of the carbon felt fibers, the initial condition before the colonization started. Whereas, **Figure 52d** gives a closer look that reveals how the biofilm covers the entire of carbon-felt-fiber's surface. Thus, the communication from cell-to-anode can be built intensively through this intact attachment. The biofilm, as developed from garden compost, most probably contains multi-species as reported by Cercado, et al. [74].

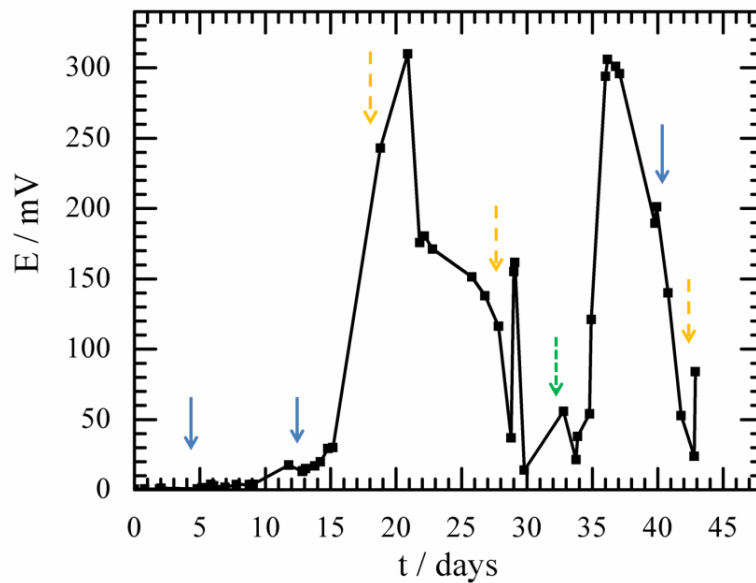


Figure 53 Voltage evolution of the garden compost DCMFC showing the self growth of biofilm (<20 days) and the performance of the DCMFC after growing biofilm (>20 days). The blue solid arrows show the addition of acetate, the yellow dash arrows show refreshing ferricyanide solution, and the green short dash show refreshing the anodic solution.

Figure 53 shows a plot of the voltage generation of the MFC vs. time. The generated voltage expresses the potential difference between the CF anode in the anodic chamber containing the compost garden leachate solution and the stainless steel plate cathode in the cathodic chamber with 20 mM ferricyanide solution. In the beginning, the observed voltages are very low because the potential difference between the bare CF anode and the cathode is narrow. Along with the biofilm growth, we observe an increase in voltage generation. The potential difference between the anode and the cathode becomes wider, mainly due to the formation of electroactive biofilm on the anode surface. Biofilm attachment involves extracellular polymeric substances (EPS) that can facilitate electron transfer from cell-to-anode [157][165]. EPS surrounds the microbial cell which acts as a transient media in the extracellular electron transfer (EET) process. Xiao, et al. suggested the molecular mechanism of this electron transfer through EPS is electron hopping as illustrated in **Figure 54** [165].

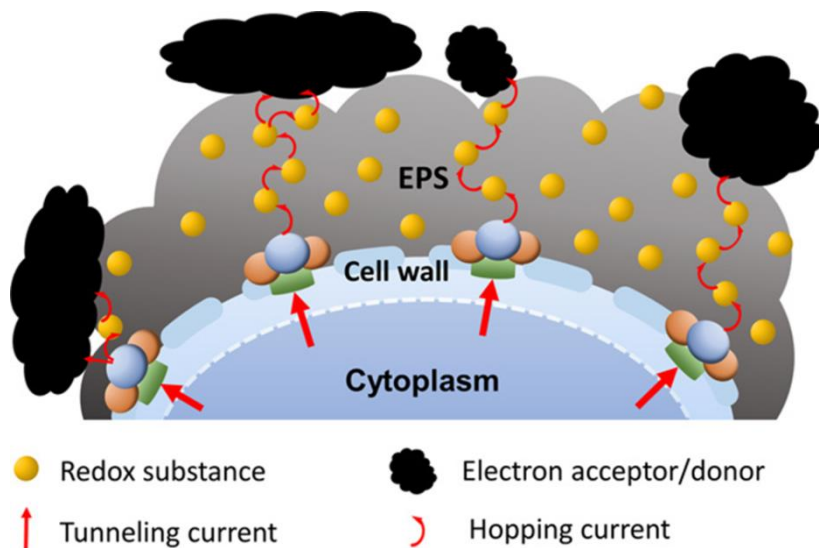


Figure 54 Electron hopping, the molecular mechanism of extracellular electron transfer through EPS, as a natural pathway of microbial extracellular electron transfer [165]

At the 28th day, the MFC's voltages declined, which can be caused by the depletion of ferricyanide in the cathodic solution and/or the depletion of substrate, nutrient, and mineral in the anodic solution those lead to lower activity of the bacterial or even death. Herein, we firstly refreshed the ferricyanide solution as

we found its color was getting clear/yellowish fade. After refreshing this cathodic solution, the voltage immediately increased but then decreased sharply and further remained lower for around four days. Thus, we can consider that the decreasing MFC's performance also due to the anodic solution. Therefore at 34th day, we changed the anodic solution with a fresh garden compost leachate that contains fresh acetate as substrate. Afterall, we observed the MFC's voltages, which rose and reached 300 mV and stayed almost stable for around four days. The next declining of MFC's voltage was due to the depletion of ferricyanide which was indicated by the decolorization of cathodic solution.

The potential changes of the anode, before and after biofilm formation, were measured by LSV. **Figure 55a** shows the LSV curve of the clean anode (CF) and bioanode (CF@Biofilm). It is clear that the presence of biofilm on the anode has shifted the open circuit potential (OCP) values from positive toward negative potential. The OCP value for the clean anode was +0.1 V vs. Ag/AgCl, whereas for the bioanode was -0.4 V vs. Ag/AgCl. This negative OCP value of the bioanode means that the anodic potential oxidation has increased (where organic substrate oxidation occurred) and also indicates that the electroactivity of the biofilm originated from the garden compost. The presence of biofilm was also proved by the emergence of an oxidation peak at potential +0.3 V vs. Ag/AgCl as measured electrochemically by CV (**Figure 55b**). This peak corresponds to the electrochemical reaction of acetate oxidation catalyzed by the cellular metabolism of the bacteria. The CV also revealed a reduction peak at potential -0.5 V vs. Ag/AgCl, which corresponds to the oxygen reduction reaction due to the presence of oxygen in the anodic part at the beginning. Over time, the oxygen content decreases due to its direct utilization for microbial respiration which explains that it has disappeared in the CF@biofilm (**Figure 55b**). The dissolved oxygen in the anodic part accepts electrons released by the microbes, which leads to a decrease of the total current generated. This unwanted reaction due to the respiratory metabolism should be avoided by keeping strict anaerobic conditions in the anodic chamber during MFC operation. For certain bacterial species, such as *Pseudomonas aeruginosa*, anaerobic conditions also support robust biofilm formation [166].

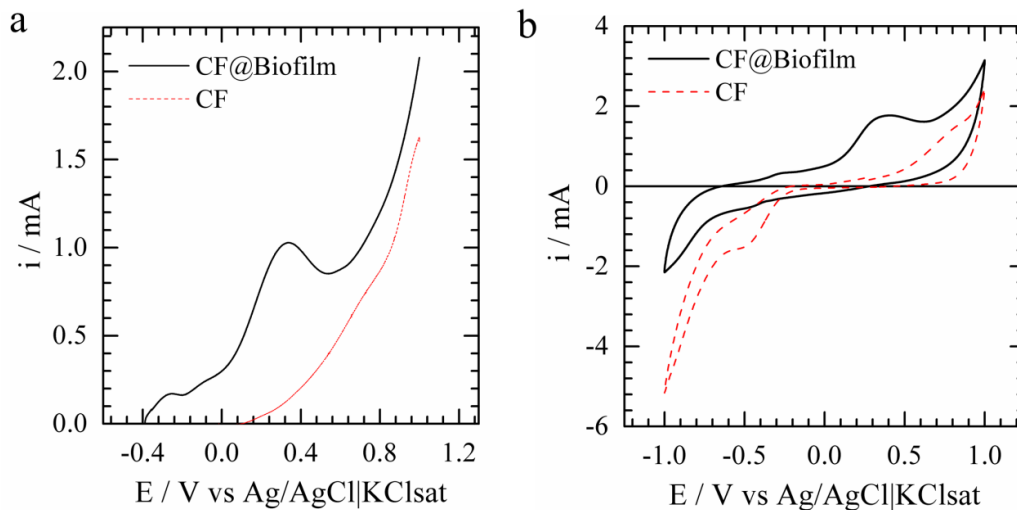


Figure 55 Electrochemical behavior of the anode before and after biofilm formation: (a) by LSV, as recorded at scan rate of 5 mV s^{-1} , and (b) by CV as measured in the anodic solution (garden compost leachate containing acetate) at scan rate of 10 mV s^{-1} .

3.1.2.2 Electrochemical bioanode growth

Bioanodes can also be developed by applying a constant potential to an electrode in an electrochemical cell over a period of time [18,161]. For this purpose, we were applying a fixed potential, $-0.16 \text{ V vs. Ag/AgCl}$, for 21 days consecutively, adapted to these previous works.

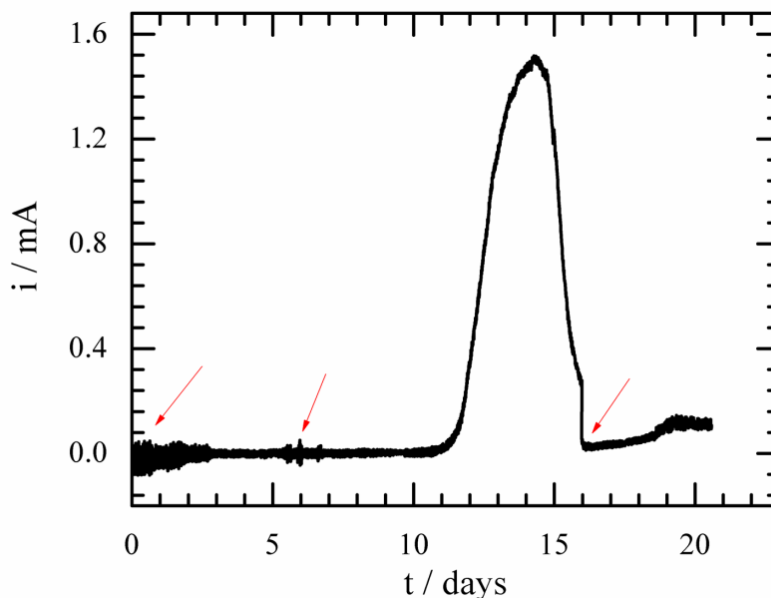


Figure 56 CA at $-0.16 \text{ V vs. Ag/AgCl}$ in the DCMFC reactor grows the biofilm on the CF anode for 21 days. The anodic compartment contained garden compost leachate and acetate, while the cathodic part contained 0.1 M KCl solution. The red arrows indicate the addition of acetate.

Figure 56 shows a plot of current evolution vs. time by applying a constant potential for growing a bioanode. The initial condition of the anodic solution was fresh garden compost leachate with 20 mM of acetate as substrate. A very low current was generated during the first consecutive 10 days. We consider that during this period, the oxidation of the acetate as substrate on the clean CF anode, at potential of -0.16 vs Ag/AgCl, is too low. On the 12th day, the biofilm was visible and the current started to increase. The presence of the biofilm on the anode also is detected by CV (**Figure 57**).

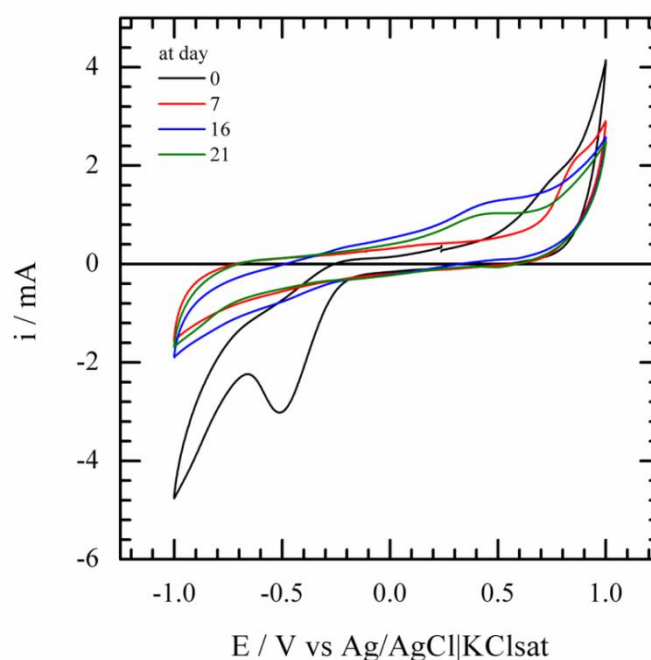


Figure 57 CV measurement at scan rate 10 mV s^{-1} to observe electrochemical biofilm formation. CV measurements were conducted on day 0, 7, 16, and 21.

The positive current evolution implies that the oxidation of the acetate was enhanced significantly by the presence of the electroactive biofilm. After 15 days, the current started to decrease, most probably due to the depletion of the acetate. The same evolution was noted for oxygen reduction, as previously explained. The addition of acetate on the 16th day readily caused a small rise of the current. The application of potential was terminated on the 21st day. Then, the resulted bioanode was directly used to run the DCMFC. The performance of the DCMFC with this bioanode is shown either as daily voltage evolution or power density curve in **Figures 58** and **59** respectively.

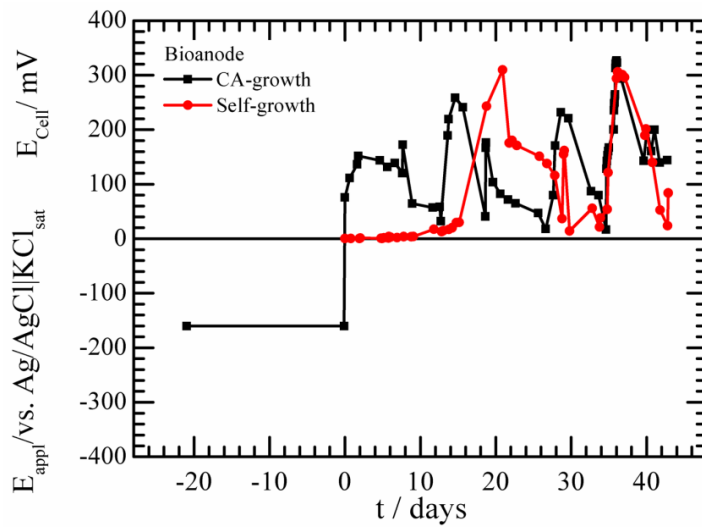


Figure 58 The comparison of voltage evolution of the DCMFC with CA- (black line) and self-growth (red line) bioanode. The negative x- and y-axis mean the period during the potential is applied for growing biofilm (-0.16 V vs. Ag/AgCl) prior to its application in DCMFC.

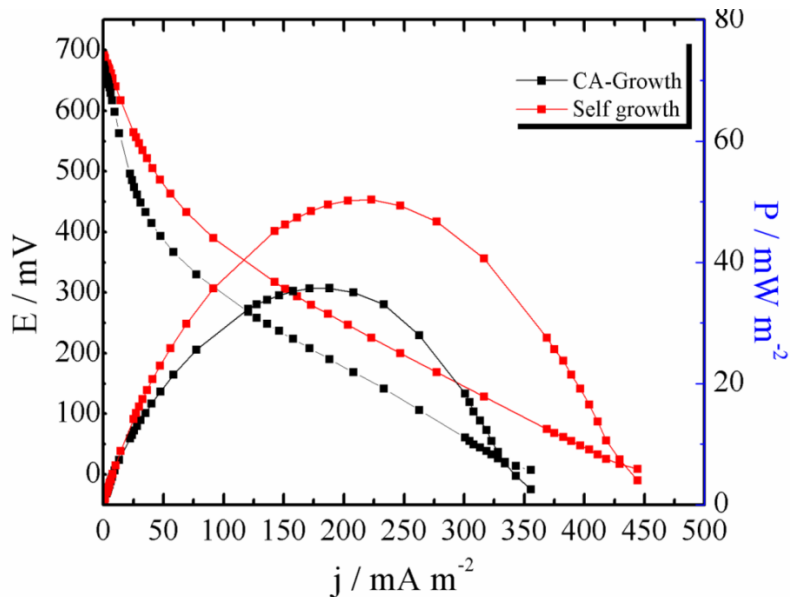


Figure 59 The polarization and power density curve of the DCMFC with self- and CA-growth bioanode.

The black line curve in **Figure 58** represents the voltages during the two time periods. The first period is between the -21st and the 0th day in which the voltage was applied to the anode for biofilm formation. The second period, between the 0th and the 40th day, demonstrates the voltages generated of the DCMFC after the application of the CA-grown bioanode. The result shows an immediate voltage evolution to reach 80 mV as the DCMFC ran. For comparison, the red line

represents the voltages generated by the DCMFC, starting with a clean anode, which took more than 15 days to reach a high voltage. This indicates the contribution of the readily available biofilm on the anode surface.

Surprisingly, the DCMFC with CA-growth bioanode, as presented in **Figures 58** and **59**, had lower generated voltages, power density, and OCV than that with a self-grown bioanode. This unexpected lower result emerges due to many factors:

1. The applied potential was not being an optimum condition
2. The different configuration of the electrochemical cell: we used a DCMFC configuration instead of a half-cell one.
3. Perturbation due to LSV and CV interruption in monitoring biofilm growth during the application of potential
4. The presence of trace oxygen in the anodic chamber.

This experiment raised the possibility of developing a bioanode directly in DCMFC configuration by using the CA method from garden compost leachate. However, the both methods result in almost the same performance. Also, the CA method also leads to higher cost and consumes more time. Thus, for our further experiments, we decided to develop the bioanode using the self-growth method.

3.1.3 Effect of structure of anode material

In this research, we used carbon felt (CF) and a graphite bar (GB) for the anode in MFC. Both materials showed their biocompatibility for microbial growth, indicated by the evolution of a significant current. The CF anode clearly produced higher current density than the graphite bar, as shown in **Figure 60a**. Indeed, CF's fibrous structure gives contribution to the high real surface area that enables to maximize bacterial attachment over the whole anode surface. The power density curve (**Figure 60b**) expresses the generated power at various external resistances, which enables us to observe the power density maximum and the open circuit voltage (OCV) of the cell. The MFC with CF anode produced higher power density and a higher OCV. Owing to its more flexible and manageable textural properties, we preferred to use CF further as anode material in this research.

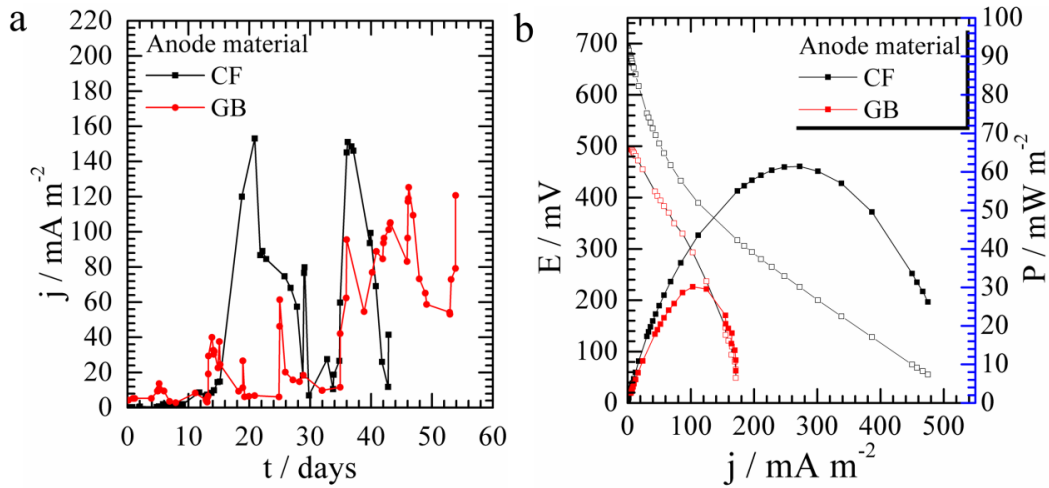


Figure 60 (a) Current density generation of the DCMFC with carbon felt (CF) and graphite bar (GB) anode (note: acetate addition was done for every four days) (b) power density and polarization curve of the MFC with CF and GB anode. Normalization of the current is toward the geometric surface area of the anode.

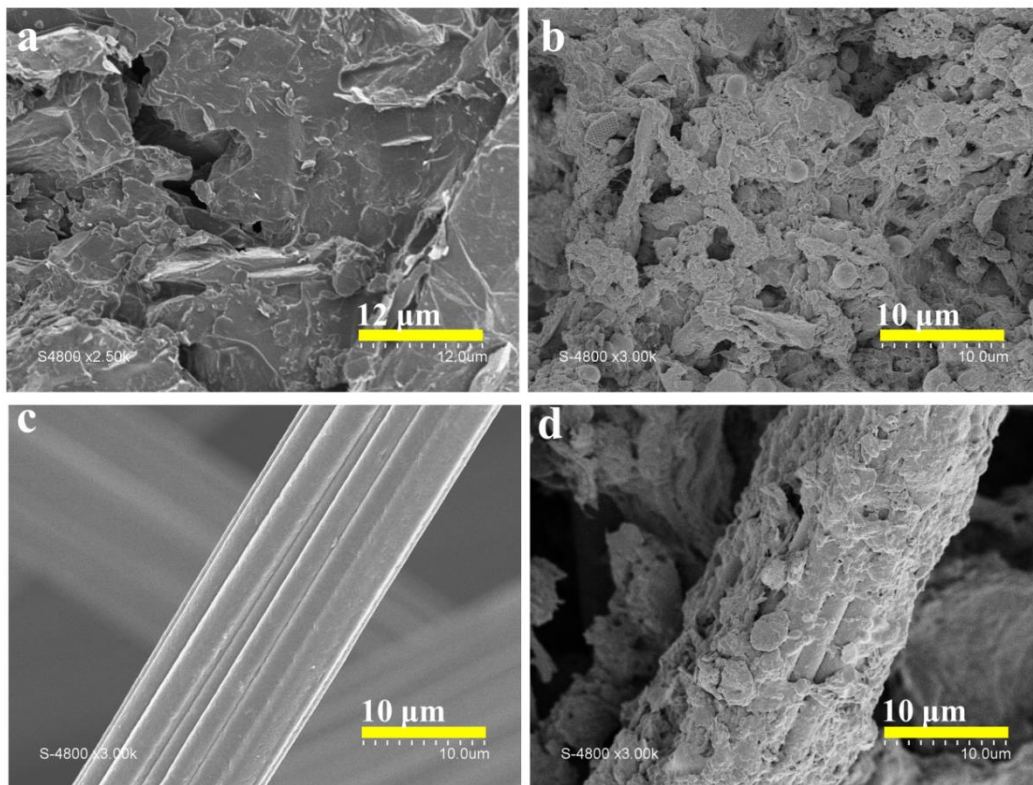


Figure 61 Morphology of the clean unmodified GB (a) and CF (c) and biofilm covering GB (b) and CF (d) observed under SEM.

The SEM images in **Figure 61** show the physical morphology of the clean anode and the anode covered with the biofilm. The clean GB had a rougher surface (**Figure 61a**) comparing to the CF's fibers (**Figure 61c**). This rough surface may contribute to better attachment of the biofilm as shown in **Figure 61b**, where it can be seen that the biofilm covers the GB's surface very well. On the CF-based anode, the biofilm covers every fiber entirely, as shown in **Figure 61d**. CF's fibrous structure may contribute to the roughness of the surface to facilitate bacterial attachment. Furthermore, it also provides a higher surface area for biofilm coverage.

The behavior of the biofilm attached to the anode can be studied by CV, as shown in **Figure 62**. The presence of the biofilm led to higher CV area on both the carbon felt anode and graphite bar one. The CV of the clean CF initially showed an oxidation peak at 0.75 V vs. Ag/AgCl which may correspond to acetate oxidation on the bare anode surface. As the biofilm formed, the oxidation peak was shifted to 0.25 V vs. Ag/AgCl and the current increased as well (**Figure 62a**). This shows that the improvement of the electrode's electroactivity corresponds to the biofilm formation. The observed reduction peak at -0.5 V vs. Ag/AgCl corresponds to oxygen reduction due to the presence of trapped oxygen in the anodic solution at the beginning time. **Figure 62b** shows the CV behavior of the bare GB anode with and without biofilm. In this case, the oxidation peak of both electrodes emerged at the same potential, i.e. at 0.3 V vs. Ag/AgCl. Indeed, the higher oxidation current corresponds to the biofilm electroactivity.

The anodic polarization shown in **Figure 63** indicates that the presence of biofilm increased the anodic electroactivity since its open circuit potential, OCP, shifted to a more negative potential. Basically, the anode's OCP was between -0.4 to -0.5 V vs. Ag/AgCl [74]. We found that the OCP value of the bioanode based on CF was very close to that found in the literature. Therefore, the lower anodic overpotential contributed to higher voltage generation. The LSV curves of the two bioanodes show sigmoidal shapes, which imply a typical electrocatalytic activity correspond to substrate oxidation [167,168] as the formation of electroactive biofilm. The sigmoidal curve of CF@Biofilm has a higher anodic current

compared to the GB@Biofilm. The high surface of CF enables to provide higher surface area for bacterial attachment, which leads to wider biofilm coverage on the anode surface hence results in a higher current improvement.

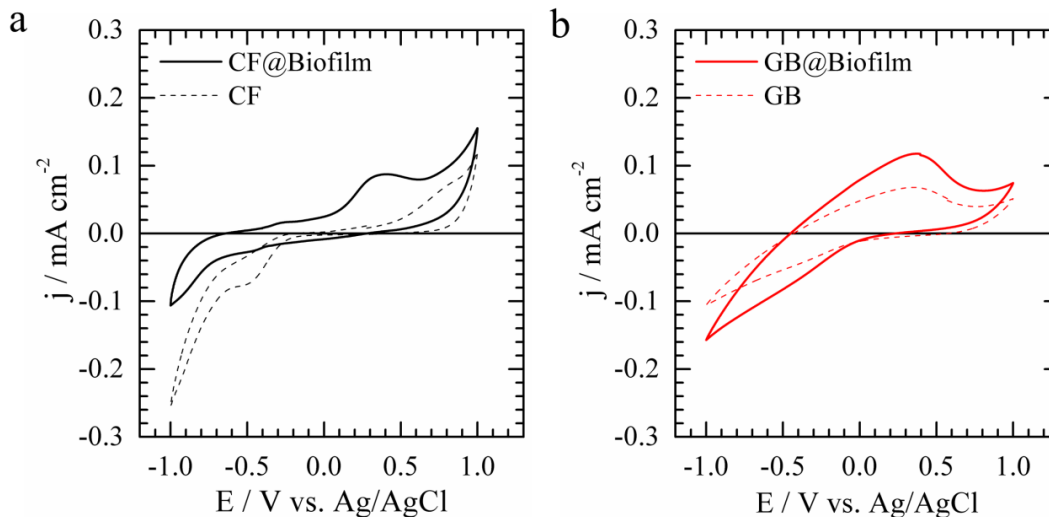


Figure 62 CV behavior of the clean anode and the bioanode based on CF (a) and GB (b) respectively, recorded at scan rate of 10 mV s^{-1} .

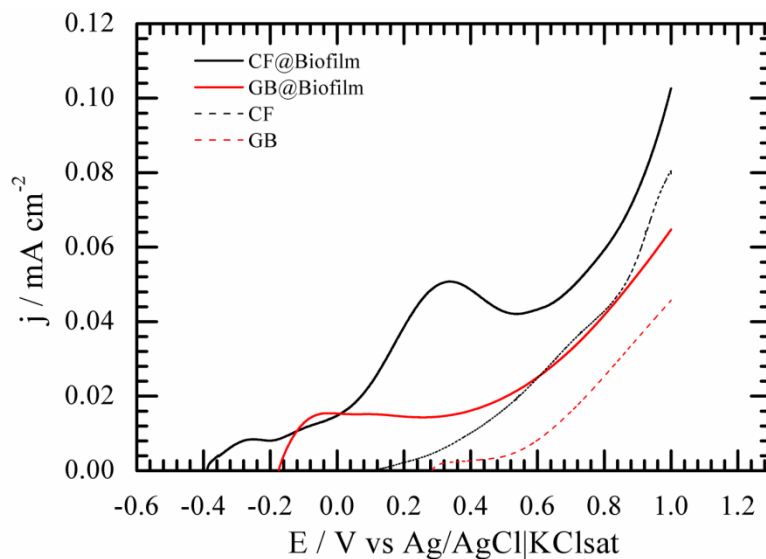


Figure 63 LSV curves, recorded at scan rate of 5 mV s^{-1} , for the polarization of the anodes based on CF and GB, respectively, before and after biofilm formation.

3.1.4 Modification of the anode

Incorporating a nanoscale material such as metallic nanoparticles (NPs) seems promising to provide better interaction with the biological system due to its

comparable dimension and special electronic properties [169]. For example, gold nanoparticles have been reported to promote an efficient electron transfer at biological interfaces [169]. Anchoring metal nanocatalyst is also commonly used as strategy to enhance the electrochemical surface active area and spread catalytic active sites as well [170]. Pt nanocatalyst is well known as efficient catalyst for most electrochemical reactions [170]. Thus, we tried to elaborate Pt nanoparticle-modified CF (CF@Pt) as anode in our DCMFC system.

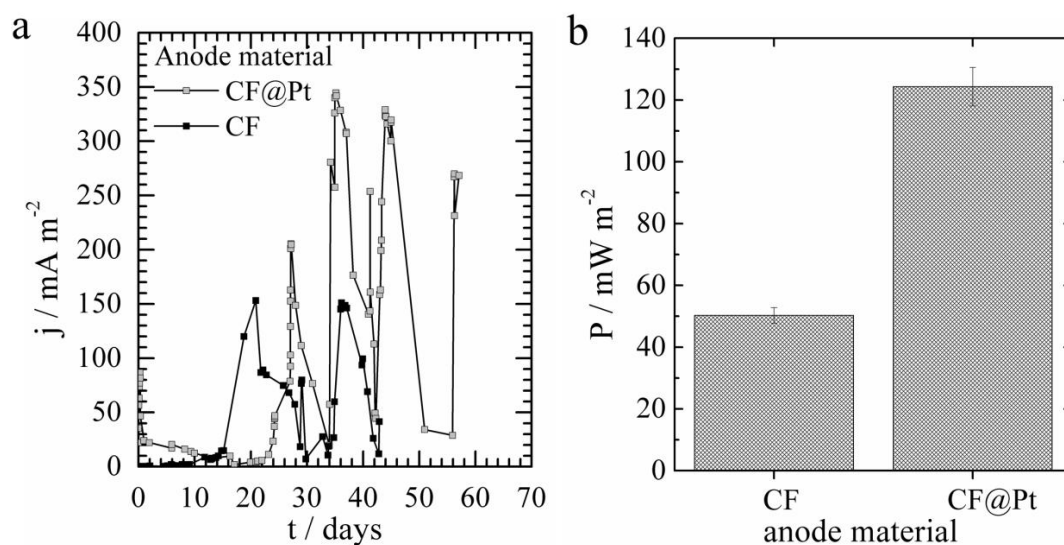


Figure 64 (a) Current density and (b) power density resulted from the DCMFC with different anodes: carbon felt (CF) and platinum NPs-modified carbon felt (CF@Pt) respectively.

Figure 64 shows the current evolution curve of the MFC with Pt modified anode. Herein, we observe a longer initiation period (black curve) during the application of CF@Pt, i.e. 20 days, which longer than for the bare CF. It seems that the presence of the Pt lowered the kinetics of the biofilm formation on the anode. During the initiation period (0-25 days), the current generated by the MFC with the Pt anode was low. The effect of the platinum seems to decrease the kinetic of biofilm formation. After the biofilm formation (>25 days), the current was boosted compared to the conventional anode. This could indicate a contribution of the Pt nanoparticles on the anode surface. The Pt slows down the biofilm formation but does not permanently modify the electrical connection. Indeed, the current observed after this step showed a large increase. The role of the Pt can be considered to enhance the extracellular electron transfer (EET) but it may also

stimulate the generation of mediator by its interaction with the biofilm membrane and many species in the solution. The generated power density is also three times higher (**Figure 64b**).

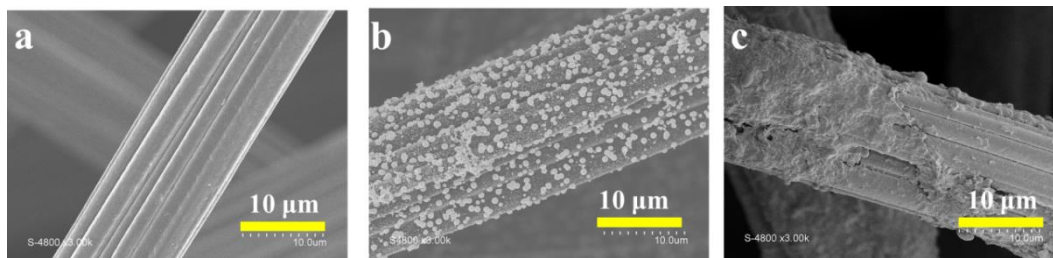


Figure 65 SEM overview of (a,b) clean anode of unmodified CF and Pt nanoparticles modified carbon felt (CF@Pt), and (c) biofilm covered CF@Pt, CF@Pt@Biofilm, (bioanode).

The SEM image, shown in **Figure 65b**, displays a very good distribution of Pt NPs through out the CF's fibers as expected for the enhancement of electron transfer process. The **Figure 65c** shows the biofilm covering the CF@Pt anode, which implies the biocompatibility of this modified anode. Indeed, the presence of Pt NP provides a new environment for the existing microorganisms. Thus, they need time for adapting to such this surface.

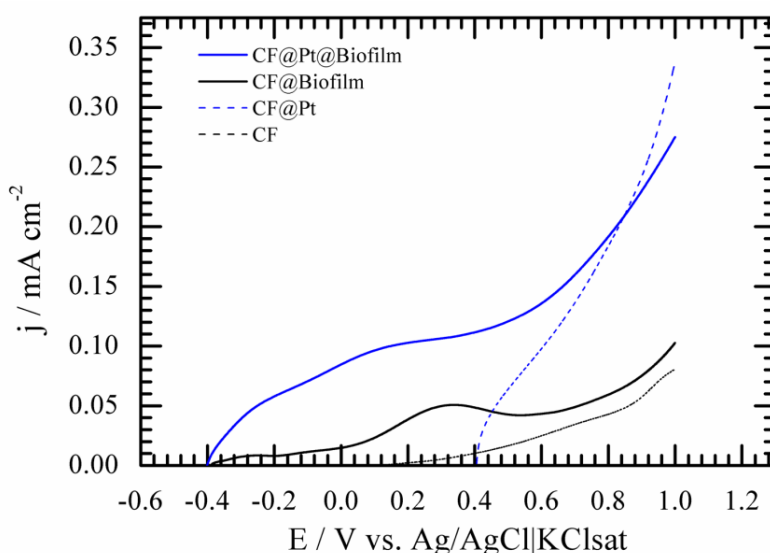


Figure 66 LSV curves indicating the polarization of the clean anode and the bioanodes based on CF and CF@Pt substrate respectively

Pt, as universal catalyst, exhibits electrocatalytic activity toward various species contained in the anodic compartment. This leads to higher oxidation and higher reduction current. As the biofilm grows on this anode, the Pt NPs was

automatically covered, as shown in the SEM image (**Figure 65c**). A negative shift of OCP and an increase of oxidation current can be observed in the **Figure 66**.

3.1.5 Stability of the bioanode

Analog to the common procedure of enzyme electrode stability testing, the bioanode recovered from the terminated DCMFC was kept at 4 °C for long-term storage. Herein, the bioanode was stored for one month and subsequently re-applied in a fresh DCMFC in order to evaluate its activity. For this purpose, the anode solution was electrolyte and substrate only (60 mM KCl and 20 mM acetate) without garden compost leachate. By this way, we can suppose that the generated performance is due to the activity of the attached biofilm on the anode rather than any other bacteria. The activity of the two old bioanode representatives, CF and CF@Pt, in the DCMFC is presented as a generated voltage curve in **Figure 67**.

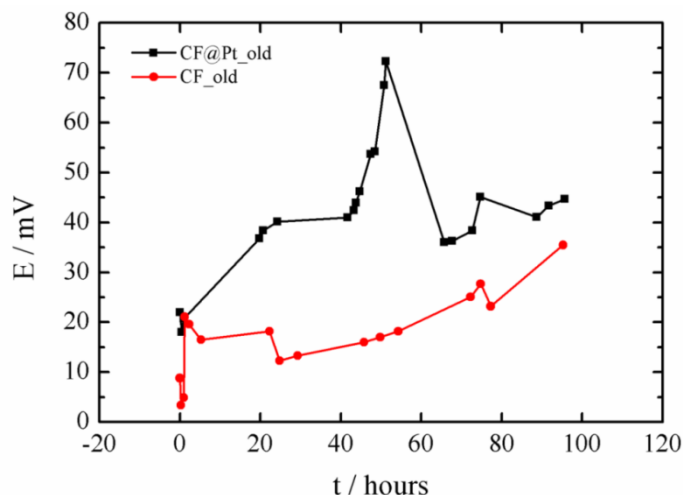


Figure 67 Voltage generation indicating the performance of old bioanodes i.e. the CF@Pt@biofilm and the CF@Biofilm respectively in the DCMFC. The anodic solution contained only 60 mM KCl contain 20 mM acetate whereas cathodic solution was a ferricyanide solution.

In general, both old bioanodes showed an initial generated voltage of 20 mV that increased progressively over time. This implies that the old bioanodes remained active after one-month storage. Indeed, the bioanode containing Pt NPs, CF@Pt@Biofilm, revealed faster as well as higher voltage generation. This most probably related to the contribution of Pt NPs, which improve the extracellular electron transfer between microbial membrane cell and anode. The bioanode

without the Pt NPs not only resulted in significantly lower but also slower voltage generation due to its poor electronic transfer. The voltage seems to start increasing after 60 hours, which indicates a slower beginning of bioelectroactivity for this electrode.

3.1.6 Biocompatibility of the garden compost leachate toward phosphate buffer in MFC

It is obvious to elaborate the buffer system, such as phosphate buffer, in MFC experiment [161]. The purposes of buffer addition are to maintain a constant pH that supports bacterial life, to improve the proton transport inside the biofilm [161], and to increase the conductivity of the medium [161]. In this research, we conducted three independent experiments that used buffered anodic solution. The experiments were carried out by switching the non-buffered garden compost leachate in an on-going DCMFC to a fresh buffered one. At the same time, the cathodic solution was also replaced with the fresh ferricyanide solution. Thus, we obtained the new fresh conditions for both compartments of the MFC. We referred to this as the new initial condition for the MFC with buffer system medium. Furthermore, we compared the power generation with the related non-buffered MFC over an equal period of time. The three experiments with the buffered medium systems are presented in **Figure 68**.

The voltage generation listed in **Figure 68** shows that phosphate buffer is compatible with garden compost leachate and its electroactive bacteria inside the anodic compartment of the MFC. The voltages increased and reached its maximum value around twice faster in the buffered system than in the non-buffered one. In the first experiment, **Figure 68a**, shows significant enhancement of the voltage. While, the second experiment (**Figure 68b**) shows the voltage that increased readily after changing the anodic medium with the buffered system. In the non-buffered system, the voltage took longer to reach its maximum value. **Figure 68c** shows the buffered system not only generated voltage faster but also resulted in better stabilization. **Table 15** indicates that the buffered systems are able to maintain the anodic pH during the operation. In general, the presence of a buffer gives a positive contribution to the performance of the MFC.

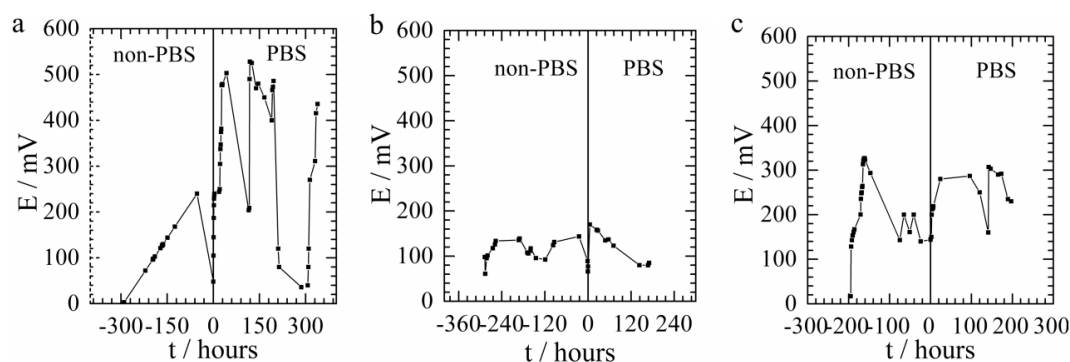


Figure 68 Voltage generation profile of the three independent DCMFC experiments before and after switching to buffer system of the anodic solution. Each experiment was starting from a different old running DCMFC i.e. (a) 42 days old (b) a 56 days old and (c) 64 days old.

Table 15 Anodic solution pH as recorded at the beginning and the end of DCMFC operation

DCMFC Experimental condition	Entry	pH	
		Initial	Final
Anode: CF@Bioanode Cathode: SSP Anodic solution: non-PBS Cathodic solution: ferricyanide	1	6.58	6.07
	2	6.43	6.88
Anode: CF@Bioanode Cathode: SSP Anodic solution: PBS Cathodic solution: ferricyanide	1	6.85	6.61
	2	6.7	6.8
	3	6.7	6.78
Anode: CF@Pt@Bioanode Cathode: SSP Anodic solution: non-PBS Cathodic solution: ferricyanide	1	6.43	6.66

3.1.7 Cathodic compartment of the DCMFC

In our DCMFC experiment, we used ferricyanide solution as terminal electron acceptor in the cathodic part. Ferricyanide is well known as a common powerful terminal electron acceptor in MFC. Ferricyanide has low overpotential which results in a faster reaction and higher power output [8]. The ferricyanide species are reduced on the cathode to ferrocyanide according to **Eq. 85**.



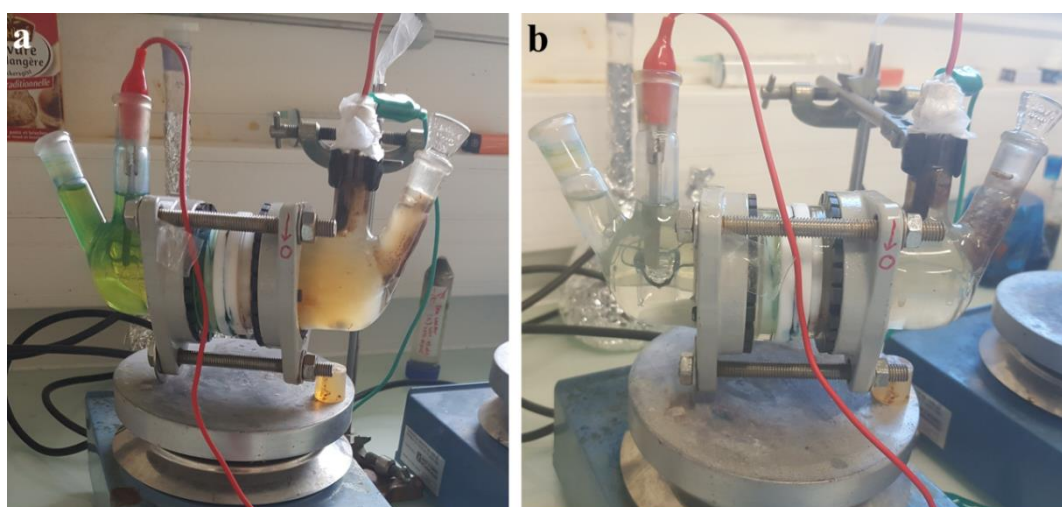


Figure 69 The ferricyanide solution in the cathodic part: its initial color (a) and turned colorless (b) indicating the consumption of ferricyanide upon the DCMFC operation.

The electrons arriving at the cathode readily reduce the available $[\text{Fe}(\text{CN})_6]^{3-}$ species around the cathode surface. Stirring the cathodic solution can help to bring out these species from the bulk solution toward the cathode, hence the reduction reaction can proceed thoroughly. The reduction of $[\text{Fe}(\text{CN})_6]^{3-}$ into $[\text{Fe}(\text{CN})_6]^{4-}$ leads to a color change of the cathodic solution. The original color of ferricyanide solution is yellow, while its reduced form is a pale yellow. Upon the DCMFC operation, we observed the yellow cathodic solution progressively turning colorless (**Figure 69**), accompanied by a decrease of the voltage. This indicates the consumption of electron acceptor during the power generation. However, a transition yellow-greenish solution was also occasionally found. This is probably due to the partial formation of prussian blue which may occur because of the possible combination of either $\text{Fe}^{3+} + [\text{Fe}(\text{CN})_6]^{4-}$ or $\text{Fe}^{2+} + [\text{Fe}(\text{CN})_6]^{3-}$ [171] in the cathodic solution. The Fe^{3+} and/or Fe^{2+} species present in the solution probably due to the modification of the $[\text{Fe}(\text{CN})_6]^{3-}$ and/or $[\text{Fe}(\text{CN})_6]^{4-}$ complexes (such as substitution of CN by H_2O). During the experiment, we also observed colloidal matter (jelly-like) fouled on the cathode or on the membrane surface which faced the cathodic solution (**Annex 3**). We consider this is a flocculation of the iron species due to alkalization of the solution. Alkalization might occur due to the presence of the oxygen in the cathodic solution (open air cathodic compartment) which can consume protons (H^+), thus the pH solution increases. In

order to avoid this fouling, the pH of cathodic solution should be maintained by the addition of buffer and/or by closing the cathodic chamber to avoid the O₂ entrance.

3.1.8 Consumption of the catholyte

Ferricyanide solution is an effective terminal electron acceptor in the classical MFC systems. However, once it is consumed, it is hard to regenerate it chemically. Therefore, the ferricyanide needs to be refreshed periodically to maintain power production. We observed that consumption of ferricyanide solution depends on the performance of the MFC. The higher the voltage produced, the faster the ferricyanide is consumed as shown in **Figure 70**.

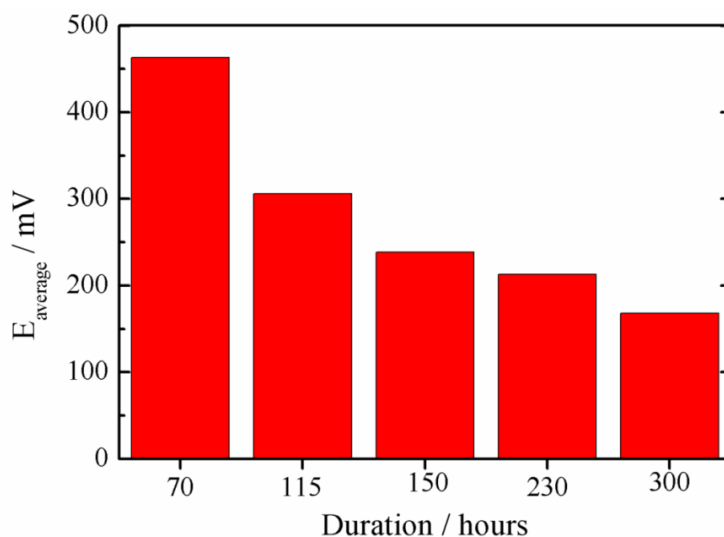


Figure 70 Histogram giving the life-time of ferricyanide solution in hours as a function of the average potential of the cell.

Herein, an MFC that produces 300 mV on average depletes ferricyanide in around five days (115 hours). This means that to maintain this performance, we need to reload the ferricyanide weekly. Roughly calculated, one unit of our DCMFC system needs almost 500 mL ferricyanide solution per month. This indicates the poor sustainability of the ferricyanide solution as terminal electron acceptor in a DCMFC system.

3.1.9 Effect of the cathode

In the DCMFC experiments, we have involved several cathode materials such as unmodified commercial stainless steel plate (SSP), electroactivated carbon felt

(ACF) and Pt-modified carbon felt (ACF@Pt). **Figures 71** and **72** show the performance of the DCMFC with the application of these cathodes. The results show that ACF@Pt gave the best performance. Indeed, the presence of platinum increased the electron transfer process and lowered the overpotential. The ACF gave better performance than the SSP due to its fibrous structure, which provides a larger real surface area. The different results of these experiments may also imply that the performance of the MFC is limited by the cathodic part.

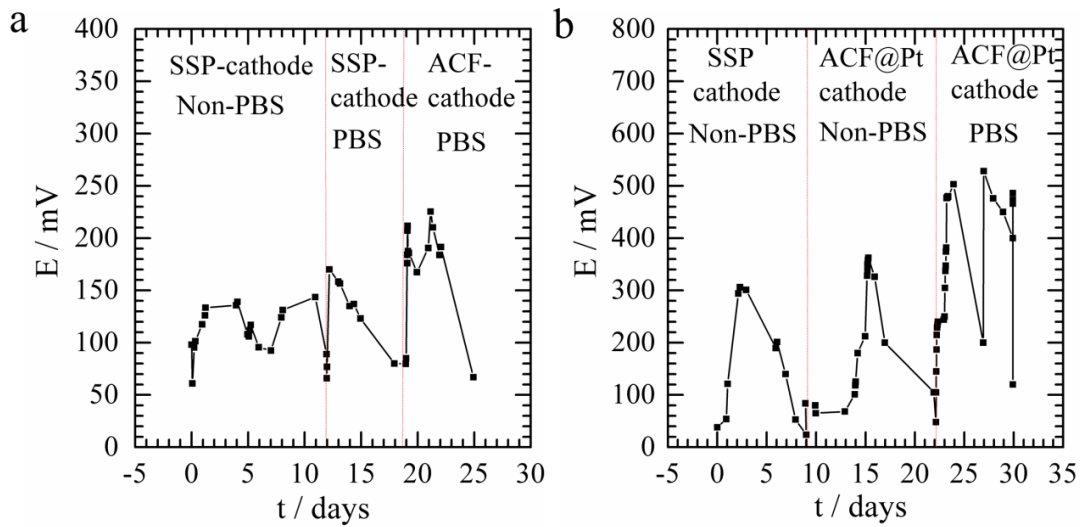


Figure 71 Voltage evolution of the two independent DCMFC experiments corresponding to the cathode material change. (a) from SSP to ACF cathode, (b) from SSP to ACF@Pt cathode.

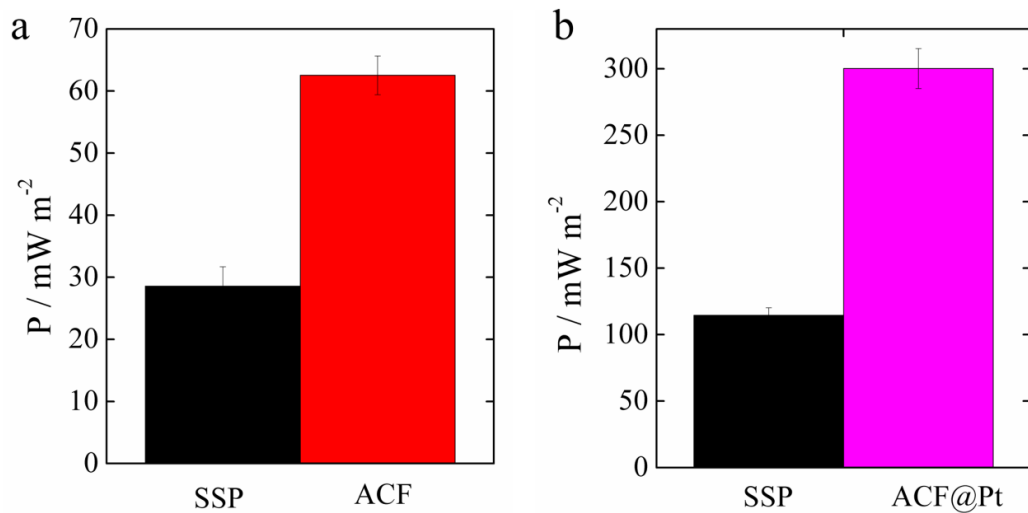


Figure 72 Histogram of the power density of the DCMFC as a function of the cathodic material.

3.1.10 Microbial fuel cell-vanadium redox flow battery (MFC-VRFB) system

The poor sustainability of ferricyanide solution led us to look for another terminal electron acceptor. We considered that the vanadium system might be a proper candidate as an alternative terminal electron acceptor [70–72]. Elaboration of vanadium solution in the cathodic part of an MFC mimics the vanadium redox flow battery (VRFB), leading to a new system, so-called bio-VRFB.

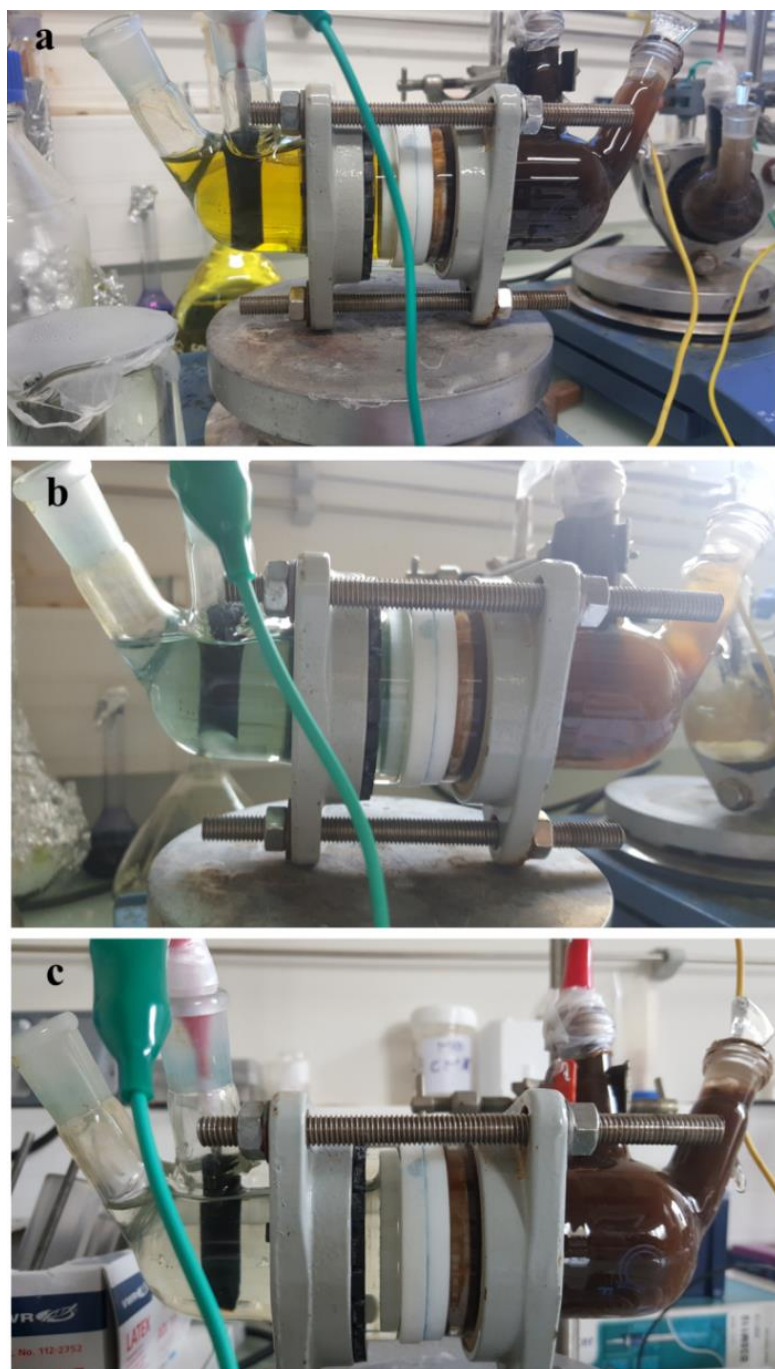
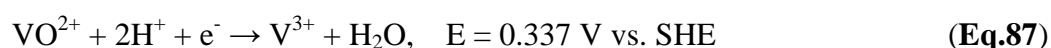


Figure 73 Progressive vanadium solution color change at (a) 1st day (b) 3rd day and (c) 7th day of DCMFC operation.

Vanadium (V), VO_2^+ , can be generated by dissolution of sodium metavanadate (NaVO_3) in an acid solution (pH 2) which presents as yellow solution. Upon the DCMFC operation, the solution rapidly (in around three days) turns green, which indicates the mixture between the yellow vanadium (V), VO_2^+ and the blue vanadium (IV), VO^{2+} . The reduction of VO_2^+ to VO^{2+} is shown in **Eq. 86**. The green colour may also originate from the vanadium (III), V^{3+} , as the further reduction of VO^{2+} (**Eq. 87**). Longer DCMFC operation without refreshing the vanadium solution leads to a completely clear solution, which indicates the depletion of vanadium (V) and decreasing voltage as well. A progressive colour change of vanadium solution during DCMFC operation is shown in **Figure 73**. The DCMFC with the vanadium electron acceptor has generated almost the same voltage (**Figure 74**) as that with the ferricyanide system (at the same concentration). However, the vanadium is depleted around three times faster than the ferricyanide which indicated by its rapid color change. The higher kinetic of reduction vanadium can be considered due to its higher potential reduction (+0.991 V vs. SHE) than ferricyanide (+0.361 V vs. SHE). Thus, more frequent cathodic solution replacement is needed to maintain the performance.



Herein we involved the low pH (2 at the beginning) in the cathodic solution. There is a possibility of proton to cross the membrane toward the anodic solution which can create an acidic condition. However, we observed the pH in the anodic part relatively stable due to the use of PBS in garden compost leachate. The PBS can maintain the pH in the anodic solution. The pH fresh garden compost leachate with PBS was 6.8 at the beginning. While, at the end of MFC operation, the pH of garden compost leachate became 6.4. The other possibility is the protons in the cathodic solution were consumed to reduce the vanadium species, as shown in the **Eqs. 86** and **87**. Thus, no proton across the membrane toward the anodic solution. The measured pH of the cathodic solution at the beginning and at the end of MFC operation respectively was 2.18 and 8.32.

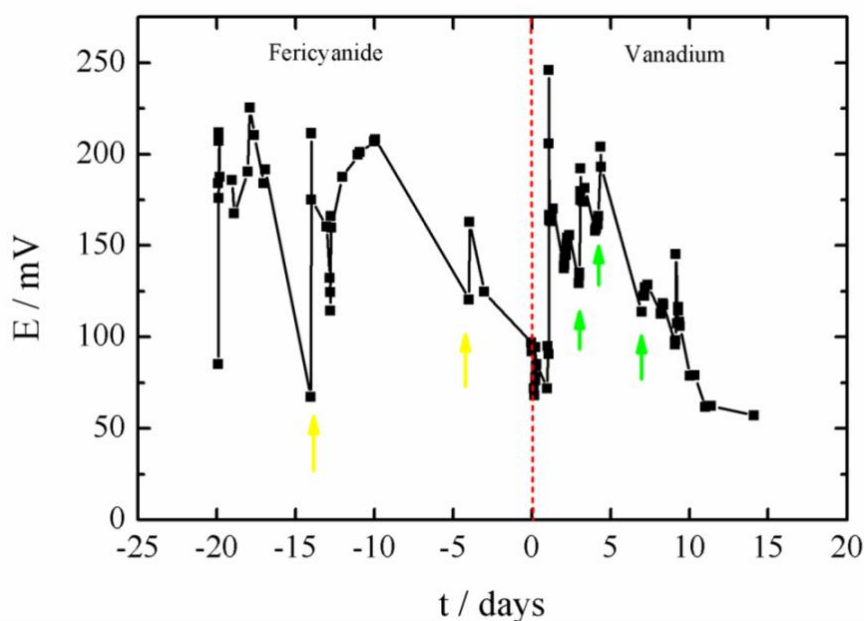


Figure 74 Comparison of ferricyanide and vanadium solution, at the same concentration, as electron acceptor in the DCMFC, toward its voltage evolution. Anode was carbon felt based bioanode (CF@Biofilm) and cathode was electroactivated carbon felt (ACF). Yellow arrows shows the refreshing ferricyanide solution and green arrows imply refreshing of vanadium solution.

3.1.11 Effect of acidic catholyte solution

The elaboration of an acidic solution in the cathodic part of the DCMFC with the ACF@Pt electrode results in a highly fluctuating voltage generation, as shown in **Figure 75**. An acidic solution, or a high proton (H^+) concentration, stimulates high voltage generation. This implies the presence of proton reduction, which contributes to increase of voltage. Where, the presence of Pt NPs on the electrode contributes largely to catalysis of the proton reduction. The protons were consumed rapidly as indicated by the immediately increasing or decreasing voltage. Owing to the cathodic batch system, it was difficult to maintain the constant pH. It was observed that at low voltage, pH increased up to 9-10 due to the protons depletion. This phenomenon would raise other promising applications of the DCMFC system, for example as a hydrogen generator, which usually helped by applying an external potential so-called microbial electrolysis cell (MEC) [172].

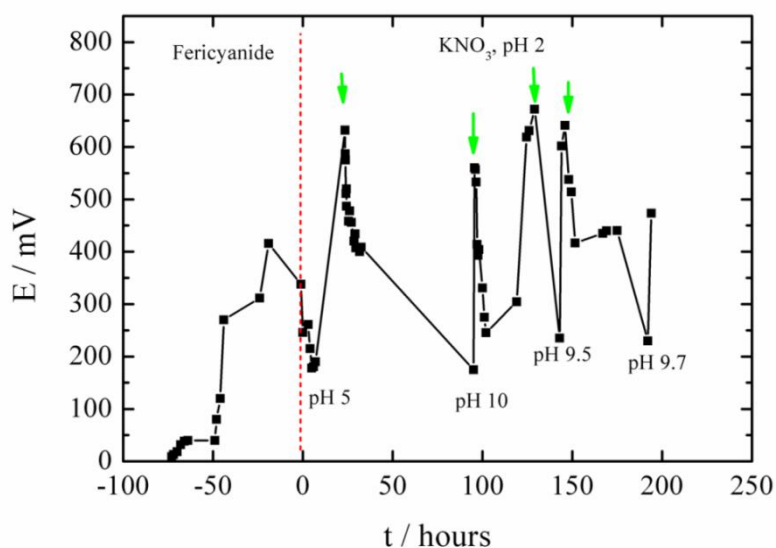


Figure 75 The voltage evolution of the DCMFC with ferricyanide solution in cathodic part with ACF@Pt cathode (< 0 hour). Fluctuating voltage evolution is corresponding to pH instability in the cathodic part (of batch system) with the ACF@Pt cathode in 0.1 M KNO₃ solution at pH 2 (from 0 – 200 hours). The green arrows indicate to the refreshed cathodic solution with fresh pH 2 electrolyte.

When buffer solution (pH 7) was used in the cathodic solution with ACF@Pt as the cathode, a constant voltage was obtained (**Figure 76**). Its lower voltage also indicates that the proton reduction was limited. Another test was done with the ACF cathode in acidic cathodic solution. It clearly showed that, without Pt, the generated voltage was constant and significantly lower.

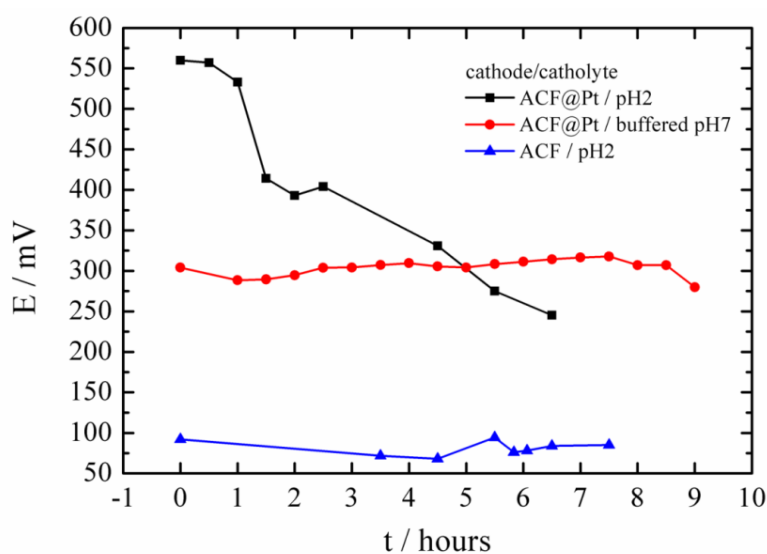


Figure 76 Stability of the voltage evolution corresponding to the pH of the cathodic solution

Summarizing **Section 3.1**, garden compost as an abundant source of electroactive bacteria can ensure the sustainability of DCMFC operation. The DCMFC using garden compost is able to result in considerably high power if coupled with an effective electron acceptor such as ferricyanide. However, the generated higher power automatically leads to the faster consumption of ferricyanide. Thus, it reveals the common limitation of DCMFC systems i.e. the necessity to either reload aqueous phase catholyte or to continuously supply the electron acceptor. Therefore, the development of single chamber MFC (SCMFC) by replacement of the aqueous phase of the cathodic part with an air-breathing cathode could overcome this drawback and lead to more sustainable power generation.

3.2 Air-breathing cathode for SCMFC: preliminary experiment

As the classical DCMFC system suffers many drawbacks, so the development of a single chamber MFC (SCMFC) is the research of interest. An SCMFC involves an air-breathing cathode system that replaces the aqueous phase of the cathodic system of the DCMFC. The air-breathing cathode is designed to be exposed directly to free air and to use oxygen as terminal electron acceptor. This system automatically eliminates the need of additional energy and cost to provide any other electron acceptor species toward the cathodic part.

In this research, we selected carbon felt (CF) material for the air-breathing cathode. CF is a kind of carbonaceous material that consists of tubular shaped of graphite with a small diameter [173,174]. Graphite is composed of sheets of hexagonal rings of covalently bonded carbon atoms (**Figure 77**). This typical chemical structure leads to high hydrophobicity [175]. The fibrous structure is able to provide a high surface area and porosity, which facilitate electrosorption reactions [174], and abundant sites to spread the catalyst as well. CF also has a good electrical conductivity, so it is commonly used as an electrode or electrode support material.

CV measurements of CF in 10 mM ferricyanide in 0.1 M KNO₃ solution show the electrochemical properties of the material. The reduction and oxidation of the [Fe(CN)₆]³⁻ and the [Fe(CN)₆]⁴⁻ redox couple on the CF show a ratio of I anodic

peak / I cathodic peak equal to 1 (**Figure 78a**). The poor reversibility may be due to kinetic limitations. Furthermore, the plot of the cathodic and anodic current peak toward the square root of the scan rate shows a good linearity (**Figure 78b**).

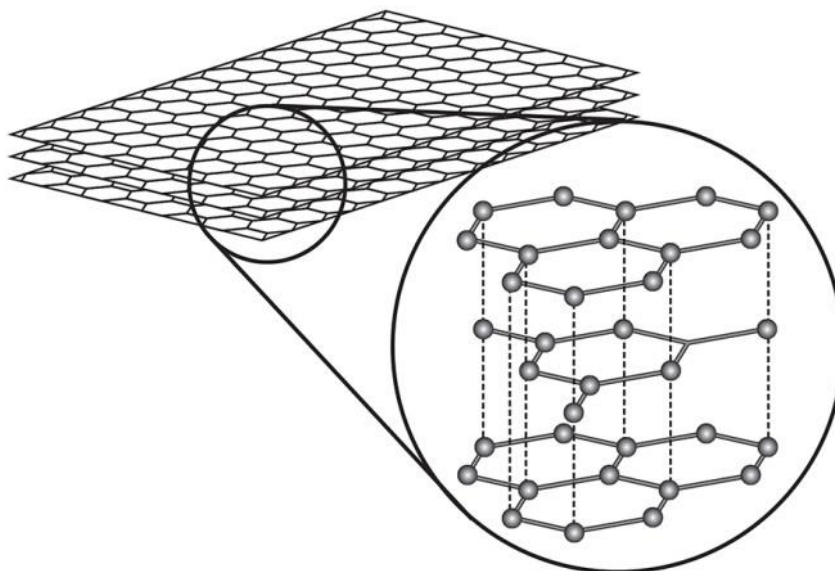


Figure 77 Chemical structure of graphite [176]

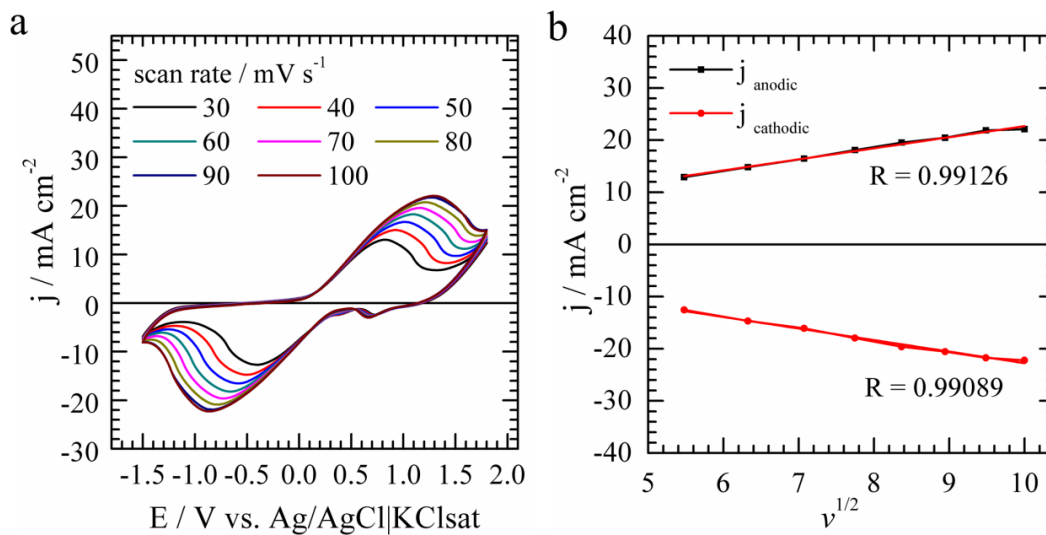


Figure 78 (a) CV of CF in 10 mM of ferricyanide solution that containing 0.1 M KNO₃ at various scan-rates and (b) plot of anodic and cathodic peak current vs. the square root of scan rate.

Because its fibrous structure and hydrophobicity, mimics the gas diffusion layer, its conductivity and high surface area for loading catalyst, CF is suitable for air-breathing cathode in MFC application [116].

We started our experiments by the electrochemical characterization of CF in an air-breathing electrode configuration (i.e. under oxygen). The CV profile of the CF air-breathing cathode in PBS solution (pH 7) (**Figure 79a**) gives a well-defined voltammogram, which shows the reduction of oxygen at the negative region (-0.6 V vs. Ag/AgCl). The plot of oxygen reduction current toward the square root of various scan rates from 10 mV s^{-1} to 100 mV s^{-1} gives a straight line (**Figure 79b**) as predicted by Randles-Sevcik equation [177] which is characteristic of a reaction limited by the diffusion. This results show the capability of CF to facilitate ORR process in neutral pH solution in an electrochemical system.

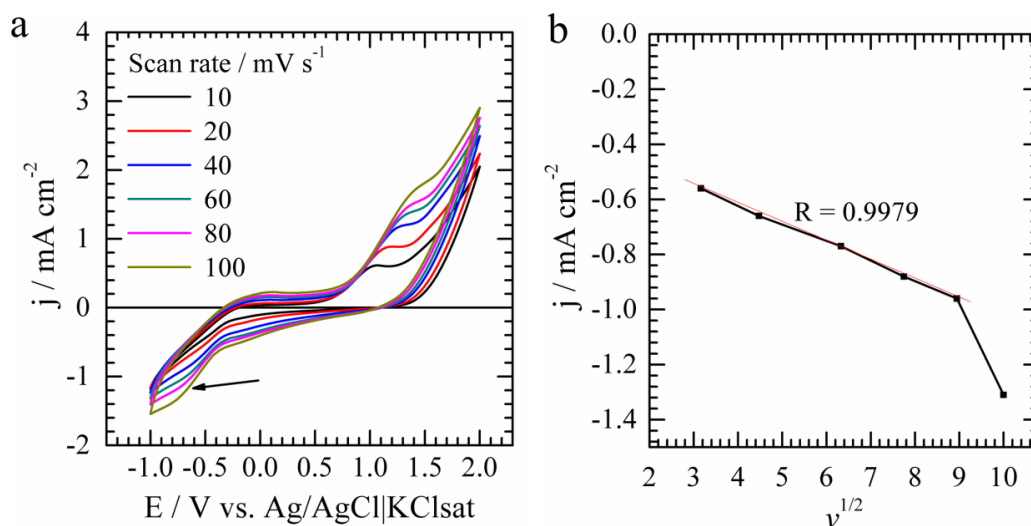


Figure 79 The CV voltammogram show oxygen reduction peak at region -0.6 V vs. Ag/AgCl (black arrow) (a) and plot of cathodic wave current versus square root of scan rate (b) for CF in air-breathing configuration in 50 mM PBS solution. As described in the experimental part, one side of the electrode is in contact with oxygen whereas the other side is in contact with PBS solution.

Further investigation of CF as air-breathing electrode was the study of its electrochemical response in an air-breathing configuration under different exterior gas atmospheres i.e. nitrogen, free air, and oxygen. In this experiment, the studied gas was flowed into the second chamber during electrochemical measurement to allow interfacial contact with the CF air-breathing electrode. **Figure 80** shows the chronoamperometric (CA) response of the air-breathing cathode toward the external atmosphere (N_2 , free-air, and O_2 respectively). The CF's air-breathing electrode responded differently toward each surrounding atmosphere. These

results express the appropriateness of CF as air-breathing electrode. Moreover, the highest resulted current, as recorded under oxygen atmosphere reveals the potential of CF to facilitate electroreduction of oxygen as an important reaction in the air-breathing cathode system.

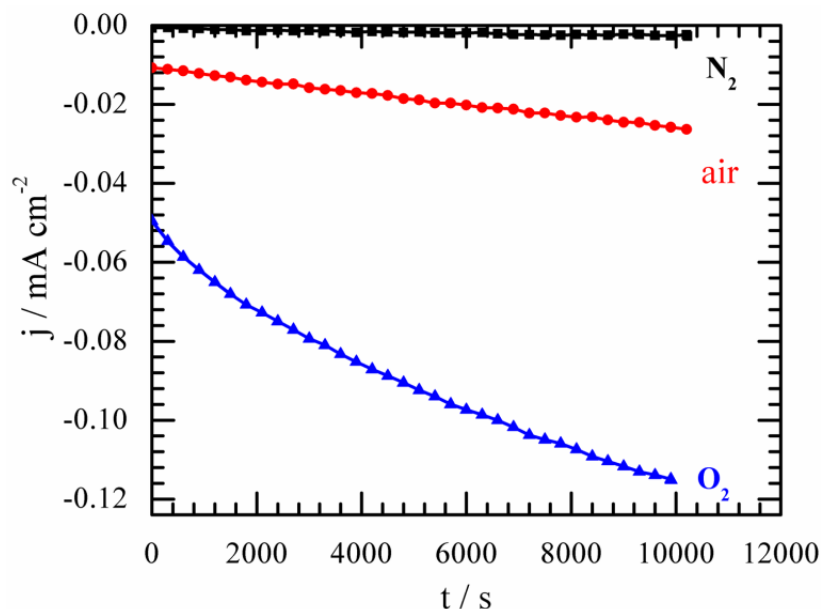


Figure 80 Chronoamperometric characterization of CF air-breathing electrode as recorded in PBS solution under respectively nitrogen, free-air, and oxygen exterior atmospheres respectively.

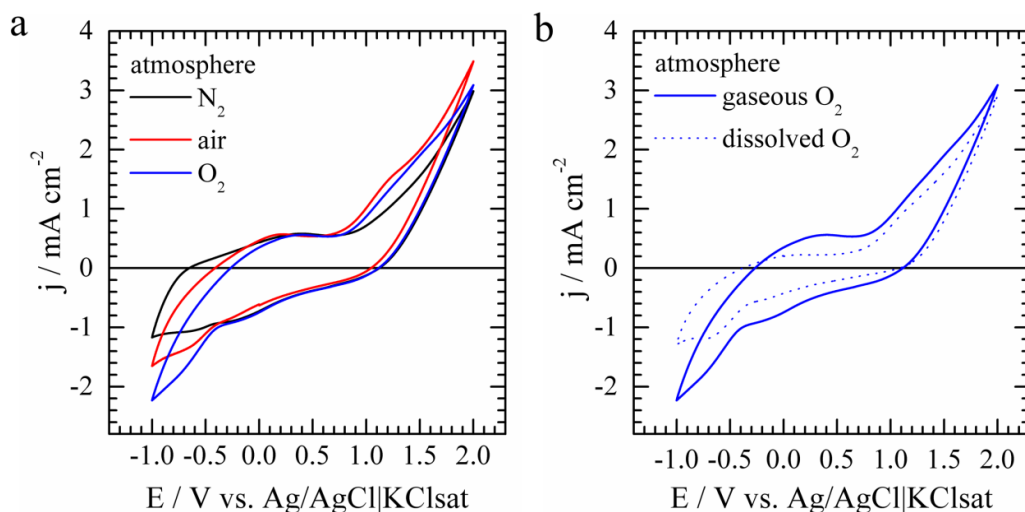


Figure 81 CV in PBS solution (anodic) at scan rate 20 mV s^{-1} in air-breathing cathode configuration (a) under exterior atmosphere influence (nitrogen, air, and oxygen atmosphere) (b) as comparison between under exterior free-air containing gaseous oxygen and dissolved oxygen (by filling the free air space with oxygen-saturated water).

We also studied the ORR performance of the CF air-breathing electrode under external dissolved-oxygen atmosphere. In this experiment, the second chamber was filled with oxygen-saturated water during electrochemical measurement. The results (**Figure 81b**) clearly show a decrease of ORR current signal of CF air-breathing electrode under this dissolved-oxygen environment due to more limited oxygen content.

In short, this section revealed that CF is a proper material to be used for air-breathing cathode substrate. However, its direct application as air-breathing cathode is not attractive due to its low ORR performance. Therefore, modification of the CF is necessary to yield a high performance air-breathing cathode.

3.3 Polypyrrole-platinum modified carbon felt (CF@PPy@Pt) air-breathing cathode: preparation, characterization, and application

3.3.1 Preparation of air-breathing cathode

In this work, modification of CF was carried out by integrating conductive polymer i.e. polypyrrole with platinum nanoparticles as common catalyst for ORR. The modification of CF by polypyrrole-Pt involved two main steps: 1) coating polypyrrole through electropolymerization; 2) electrodeposition of Pt. Both electropolymerization and electrodeposition (**Figure 82a,b**) were conducted in our customized cell (**Figure 42**).

The polypyrrole was directly electropolymerized onto a localized area of the CF surface through CV method in an electrochemical cell with air-breathing configuration. The addition of a PPy layer on the CF surface aimed to introduce N functional groups, which may generate hydrogen bonds than improve aqueous solution-contacted ability properties of the material. Moreover, the presence of N functional groups may also hold ionic Pt before electroreduction. This will help to distribute the Pt throughout the projected area.

3.3.2 Electrochemical characterization

The CV of CF, CF@PPy, and CF@PPy@Pt respectively was also conducted directly on air-breathing electrode configuration in PBS solution at pH 7 and room

temperature under nitrogen atmosphere. The addition of PPy gives an increasing peak at potential of -0.5 V vs. Ag/AgCl, which revealed its ORR potential improvement, emerging from the nitrogen content (**Figure 83a**). However, the voltammogram (**Figure 83b**) skyrockets after Pt loading. **Figure 83b** shows a typical CV for Pt or Pt-containing material. This is indicated by the presence of characteristic oxidation/reduction peaks in the potential range between -0.75 and -0.25 V vs. Ag/AgCl, which corresponds to hydrogen desorption/adsorption on the Pt surface. A sharp peak below -0.75 V vs. Ag/AgCl is related to the reduction of protons to hydrogen, also called hydrogen evolution reaction.

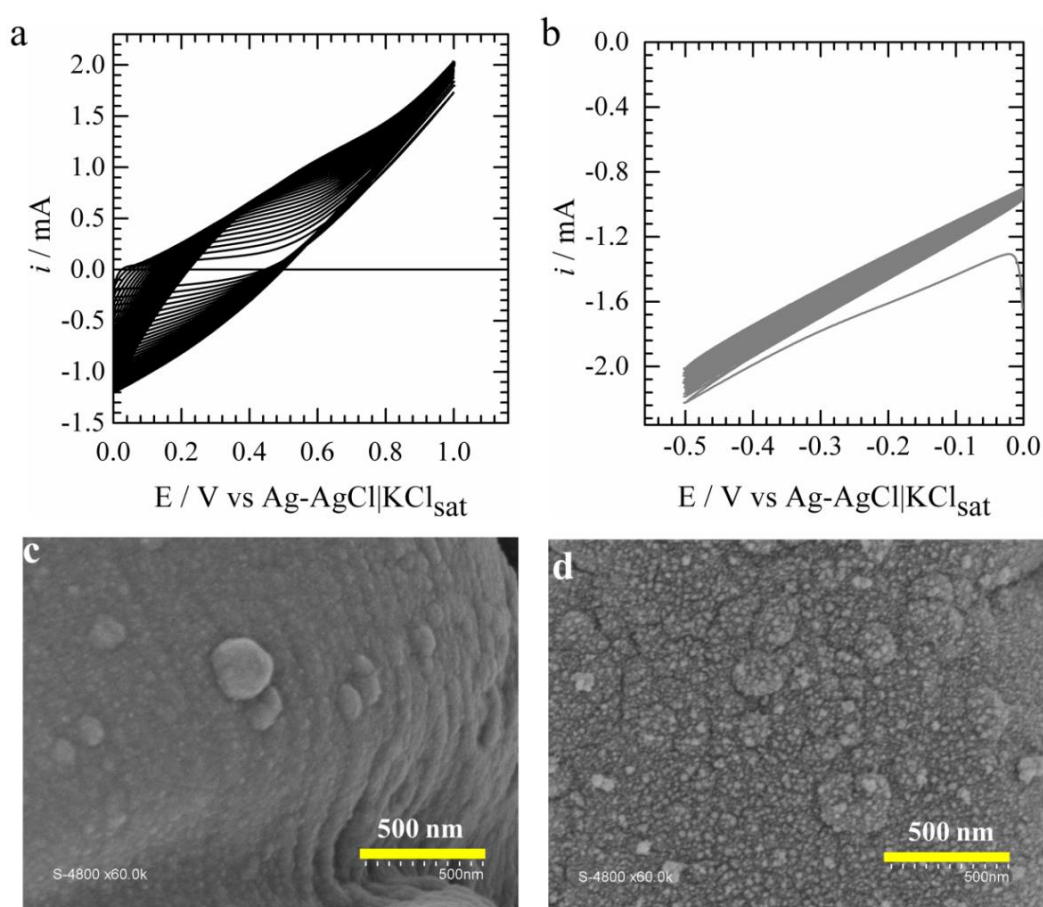


Figure 82 CV voltammogram of pyrrole electropolymerization on the CF surface (in aqueous phase side) at 20 mV s^{-1} for 30 cycles, and (a) CV voltammogram of electroreduction of Pt on previous resulted CF@PPy surface from $2 \text{ mM H}_2\text{PtCl}_6$ solution at 20 mV s^{-1} for 20 cycles. SEM image of resulted (c) CF@PPy and CF@PPy@Pt(d).

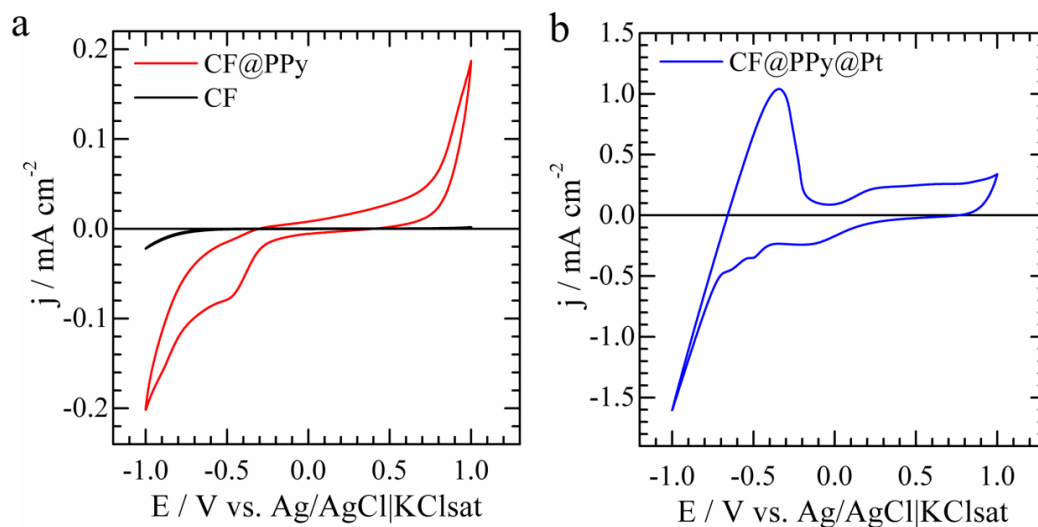


Figure 83 In situ CV of CF and CF@PPy (a) and CF@PPy@Pt (b) air-breathing electrode at scan rate of 20 mV s^{-1} in PBS solution under nitrogen atmosphere.

The LSV measurements of the three air-breathing electrodes were also carried out in PBS solution under external oxygen atmosphere to evaluate the ORR performance of each electrode. From the LSV curve presented in **Figure 84a**, the presence of Pt NPs boosted the ORR performance of the air-breathing electrode. The CA curves of the three air-breathing electrodes (**Figure 84b**) show their stability toward ORR. It is clear that the platinum-modified type generated the highest current compared to the two others. It is also important to compare the LSV curve of CF@PPy@Pt in nitrogen, air, and oxygen atmosphere respectively, as shown in **Figure 84c** to give a proof that the high peak current is really correlated to ORR rather than to proton reduction due to Pt. The LSV curve (**Figure 84c**) under nitrogen atmosphere shows that the proton reduction seems to have occurred at potential below $-0.8 \text{ V vs. Ag/AgCl}$. Therefore the contributions of Pt toward ORR and proton reduction can be differentiated from each other. **Figure 84d** shows a comparison of the CA curve in PBS solution at $-0.6 \text{ V vs. Ag/AgCl}$ under the three atmospheres (nitrogen, oxygen, air). Each gaseous atmosphere leads to a different reduction current value. With the potential at $-0.6 \text{ V vs. Ag/AgCl}$, the reduction current under oxygen atmosphere achieved around four-times higher than under nitrogen atmosphere. This gives an additional proof that ORR is more prominent at this potential than proton reduction.

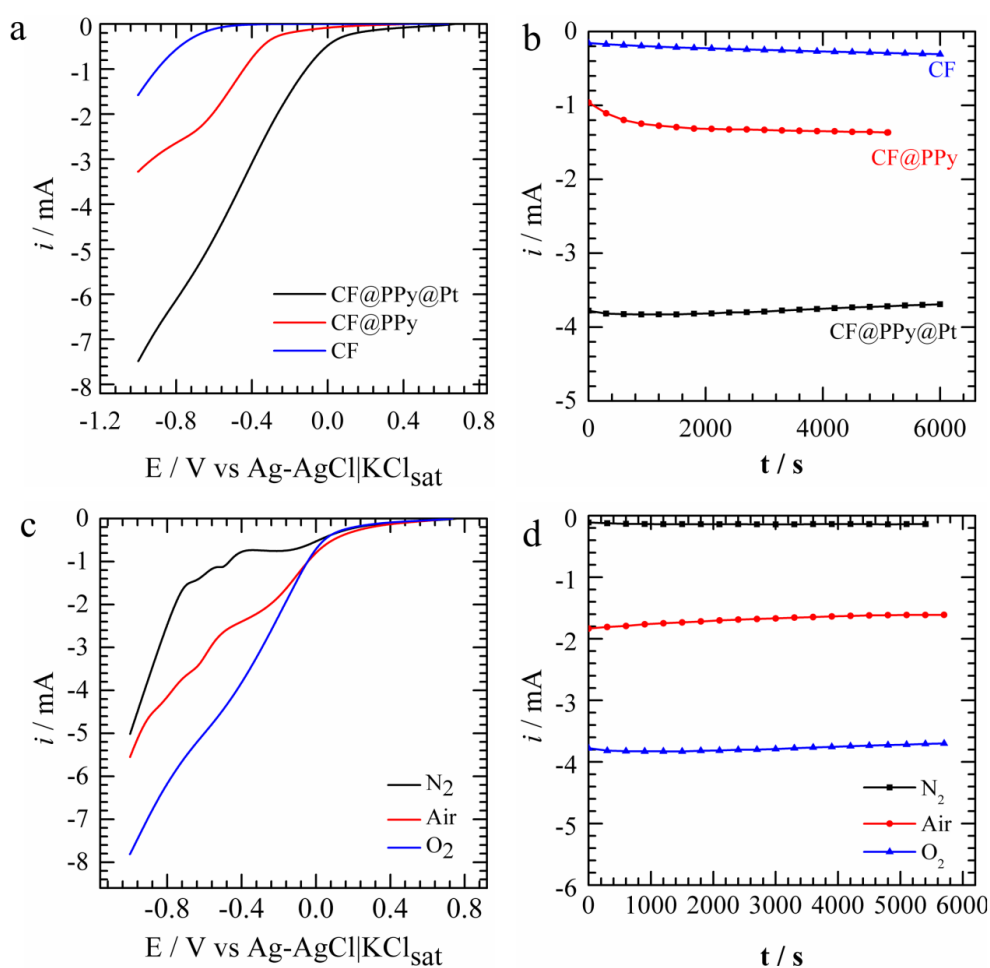


Figure 84 LSV at scan rate 20 mV s^{-1} (a) and CA at -0.6 V vs. Ag/AgCl of (b) the CF, CF@PPy, and CF@PPy@Pt air-breathing electrodes respectively, under oxygen atmosphere. The LSV curve (c) and CA at -0.6 V vs. Ag/AgCl (d) of CF@PPy@Pt air-breathing electrode under nitrogen, free air, and oxygen atmosphere.

3.3.3 Air-breathing cathode for SCMFC: application of CF@PPy@Pt

Having found the potential performance of CF@PPy@Pt as air-breathing electrode, we then tried to elaborate it as air-breathing cathode in an MFC system powered by garden compost. Initially, we performed the MFC operation in a square acrylic reactor as previously described for electrochemical characterization. **Figure 85** shows CF@PPy@Pt as a promising air-breathing cathode.

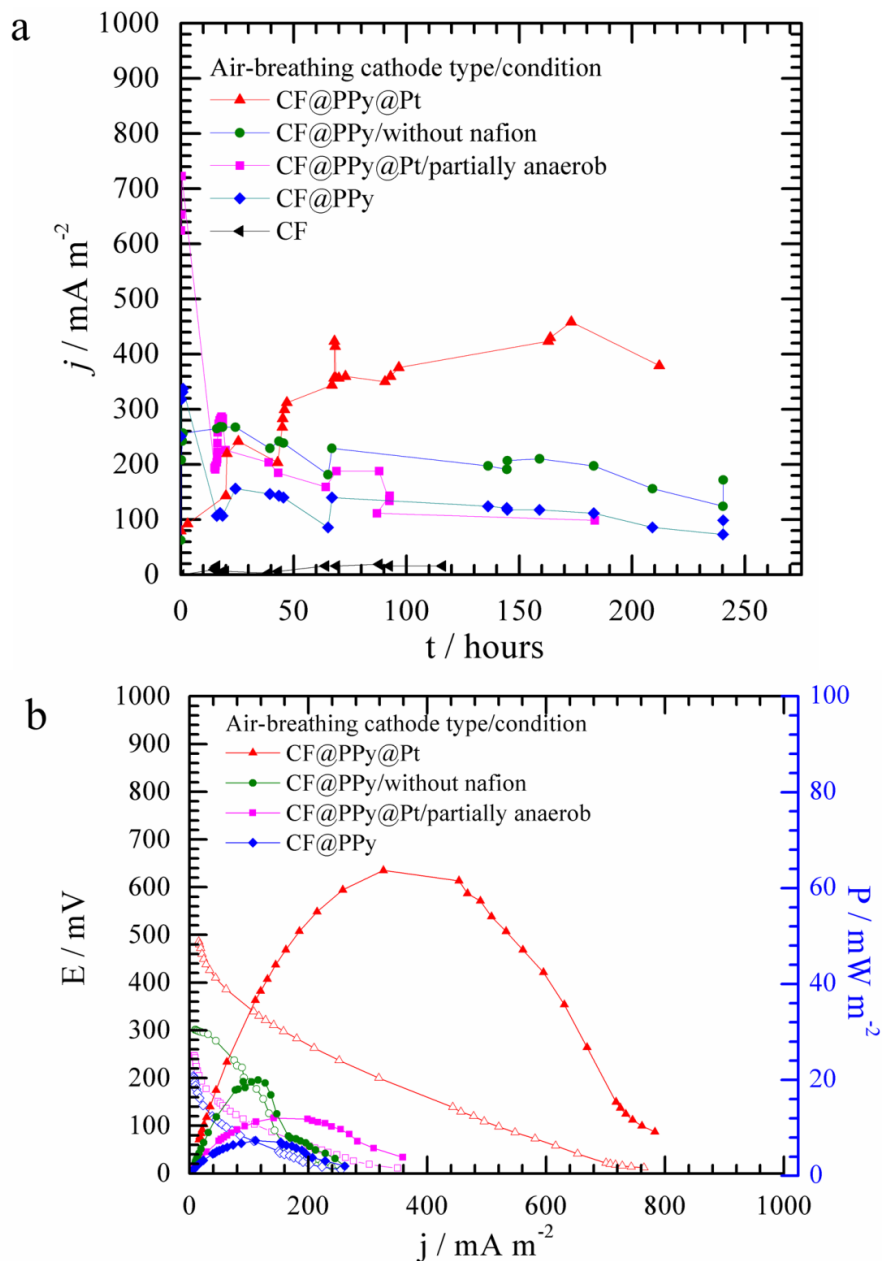


Figure 85 Various MFC performances depicted as daily generated current density (a) and power density (b) curves. Either current density or power density were normalized toward the exposed surface area of air-breathing cathode.

Herein, the role of Pt is very important since we observed very low performance by the MFC with unmodified CF air-breathing cathode. It is generally known that Pt is an excellent catalyst, especially for ORR. Therefore, Pt is the most frequently used catalyst in air-breathing cathode systems for fuel cells. However, the generated current from our MFC was not yet satisfactory. This was suspected to

be due to the design of the MFC reactor, which had a large top opening, which then disturbed the anaerobic environment in the anodic chamber (**Figure 86a**). This suspicion was then confirmed after we turn the MFC operation into a glass tube-shaped reactor with a narrower top opening (**Figure 86b**), which allows a completely anaerobic environment in the anodic chamber. The current generated was boosted significantly in anaerobic conditions. The presence of oxygen in a partially anaerobic chamber may capture the generated electrons, which decreases the total generated current. Therefore, the anaerobic conditions in the anodic chamber should be maintained strictly during MFC operation to prevent these losses.

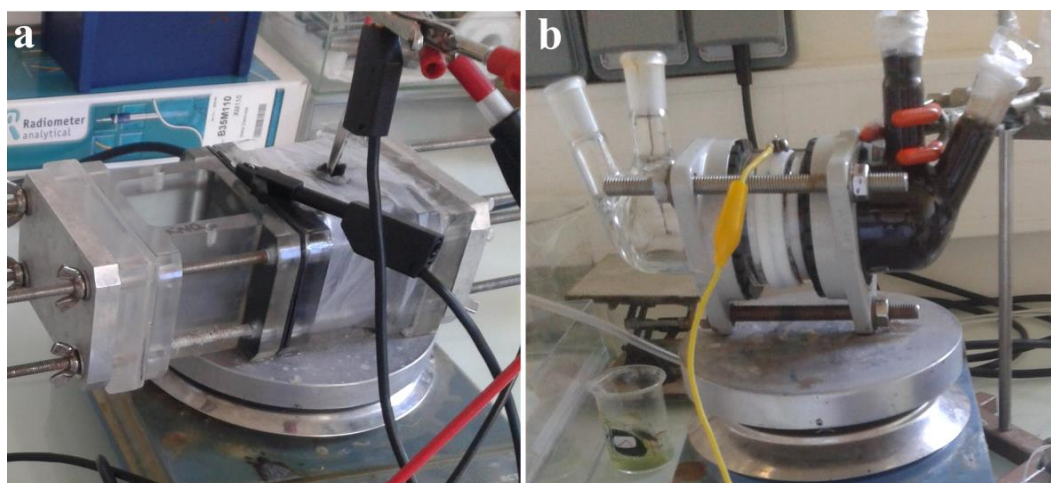


Figure 86 SCMFC experiment with CF@PPy@Pt air-breathing cathode in different reactor: (a) square-shaped acrylic with its wide top opening, which allow partially anaerob condition in anodic chamber, and (b) tube-shaped glass reactor with narrower top opening, which keeps better anaerobic condition in anodic chamber

Table 16 OCV determined from the polarization curve

Air-breathing cathode	OCV (mV)
CF@PPy@Pt-partially anaerob	247
CF@PPy@Pt	486
CF@PPy	204
CF@PPy-membrane-less	301
CF	~0

Table 16 summarizes the OCV value extracted from polarization curve. Incomplete anaerobic conditions in the anodic part also drastically dropped the OCV value of the MFC. The presence of oxygen may increase the anodic overpotential [178], and hence decrease the OCV. Indeed, the Pt-modified air-breathing cathode (CF@PPy@Pt) has lower cathodic overpotential than its non Pt-modified (CF@PPy), therefore it generates a higher OCV value.

We also applied CF@PPy as air-breathing cathode in MFC operation to find out the role of each part in the cathode. **Figure 85** clearly shows the MFC performance greatly correlates with the presence of Pt in the air-breathing cathode system. However, PPy itself has a role in increasing the MFC's performance when compared to using a CF air-breathing cathode. Incorporating a conductive polymer such as PPy means addition of active sites for electrocatalytic reaction on the air-breathing cathode [179].

The remaining part of our study involved comparing a membrane and a membraneless MFC performance with the CF@PPy air-breathing cathode. The membrane is used as proton exchange membrane, connected directly to the air-breathing cathode, which is aimed not only at facilitating selective transport of protons [99] but also at preventing transfer of oxygen into the anode chamber [180,181]. However, removing Nafion in this MFC operation was increased the current generated and its power density instead of decreasing them. This result also aligns with has been reported by Liu, et al [99]. The addition of PEM increases the internal resistance, which lowers the MFC power output [180,181]. The improved performance of membraneless MFC with the CF@PPy air-breathing cathode is definitely due to PPy contribution. The PPy layer is considered to facilitate proton transfer and gas distribution, prevent leakage, and catalyze ORR as well [182]. Due to its multifunctional properties, PPy layer incorporation has been routed to develop a membraneless SCMFC [182]. The elimination of PEM in the MFC system reduces operation costs significantly [99,181].

Finally, we compared the SCMFC performance with its equivalent DCMFC. In DCMFC operation, we involved ferricyanide solution as powerful terminal acceptor electron instead of oxygen [183]. Unsurprisingly, the performance of DCMFC in this experiment was slightly higher than that of the SCMFC (**Figure 87**). However, elaborating ferricyanide and generally any other liquid-phase terminal electron acceptor provokes other problem issues, especially unsustainability and potential wastes [183]. The power density and OCV of the SCMFC turned out to be comparable. Optimistically, the SCMFC system can be improved to exceed the DCMFC's performance.

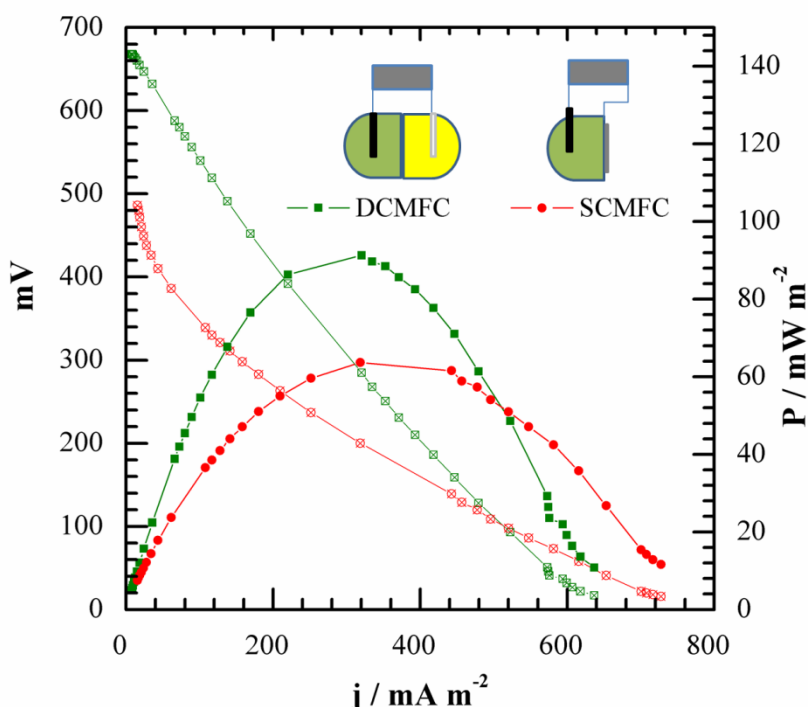


Figure 87 Comparison of MFC performance between classical double chamber and single chamber MFC with air-breathing cathode system, as expressed in power density and polarization curve.

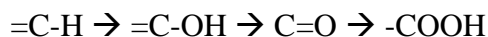
To conclude **Section 3.3**, the elaboration of either conductive polymer or Pt NP catalyst in materials for air-breathing cathode proposes a different approach of material development. Herein, air-breathing cathode was fabricated by electropolymerization of pyrrole directly onto carbon felt following by electrodeposition of Pt. The SCMFC with this air-breathing cathode system also showed a promising performance, which underpin a successful transformation of double chamber MFC into single chamber one.

3.4 Platinum-modified carbon felt (ACF@Pt): material development and characterization

3.4.1 Pre-synthesis of material

In this work, we have grown Pt directly on CF without using any other binders or additives in an attempt to obtain a simple and easy route for synthesis process. However, the preliminary experiment showed that direct electrodeposition of Pt on raw CF gave unsatisfactory results. The high hydrophobicity of the CF resulted in strong repulsion force that led to inadequate contact between the aqueous electrolyte and the surface. Indeed, this poor wettability limits its electrochemical activity. Therefore, pretreatment of raw CF is necessary prior to further processing.

Pretreatment of raw CF was carried out by electrochemistry in sulfuric acid to form electroactivated CF (ACF). Electrochemical oxidation of carbon fiber-based material in strong oxidizing acids such as nitric acid, sulfuric acid, phosphoric acid, or their mixture have been reported [184,185]. Introducing an oxygenated surface compound by electrochemical oxidation may follow the consecutive formation of hydroxyl, carbonyl, and carboxyl groups according to the following reaction sequence:



Electroactivation was carried out by CV at potential range 0 to 1.5 V vs. Ag/AgCl for 30 cycles. Applying this potential to the surface of the CF in acidic solution enables to oxidize carbonaceous structure, generating oxygenated functional groups on the CF surface. The oxidation of carbon in acidic condition induces the reactions given in **Eqs. 88** and **89**.



Structural investigation of the generated oxygenated functional groups was conducted by XPS. This surface analysis technique ables to reveal the chemical composition of CF, before and after electroactivation. **Figure 88** shows the survey scan spectra of both materials with characteristic peaks of C1s and O1s at binding

energy 284.5 eV and 532 eV respectively. Herein, the characteristic O1s spectrum of the ACF is almost five times higher than that of the CF. Moreover, the increase of O1s intensity was automatically accompanied by a decrease of C1s. These are confirming the successful generation of oxygenated functional groups after electroactivation.

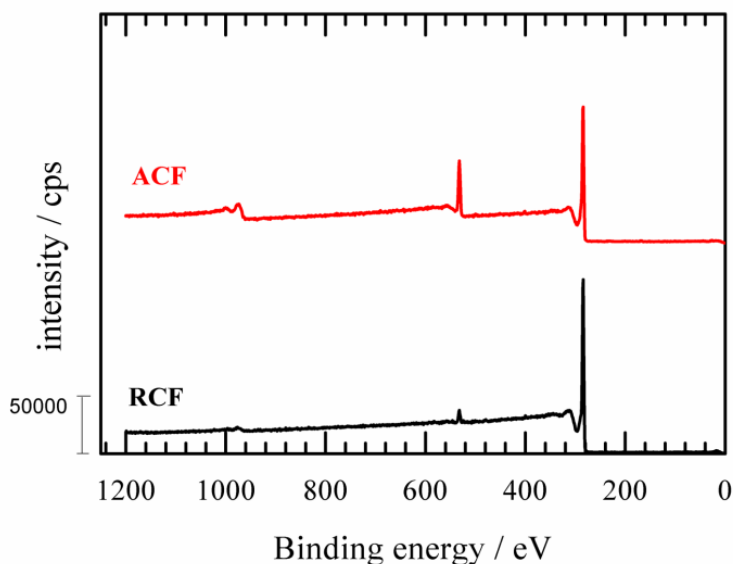


Figure 88 Survey scan of XPS spectrum of raw carbon felt (RCF) and activated carbon felt (ACF)

Further deconvolution of C1s spectrum makes it possible to examine the generated functional groups more precisely. **Figure 89a** reveals the presence of three types of C functionalities on the RCF corresponding to C=C (284 eV), C-C-O (285 eV), and C-O (286 eV). Meanwhile, for the ACF (**Figure 89b**), the deconvolution of C1s spectrum results in five peaks corresponding to C=C (284 eV), C-C-O (285 eV), C-O (286 eV), C=O (287 eV), and O-C=O (289 eV).

The generated oxygenated functional groups are able to form hydrogen bonds that will increase the hydrophilic character of the material as shown by the water droplet test presented in **Figure 90**. **Figure 90a** shows the slow penetration of a droplet onto the RCF. This result indicates the low hydrophilicity of RCF compared to ACF. The water droplet disappears readily once it is dropped on the surface (**Figure 90b**).

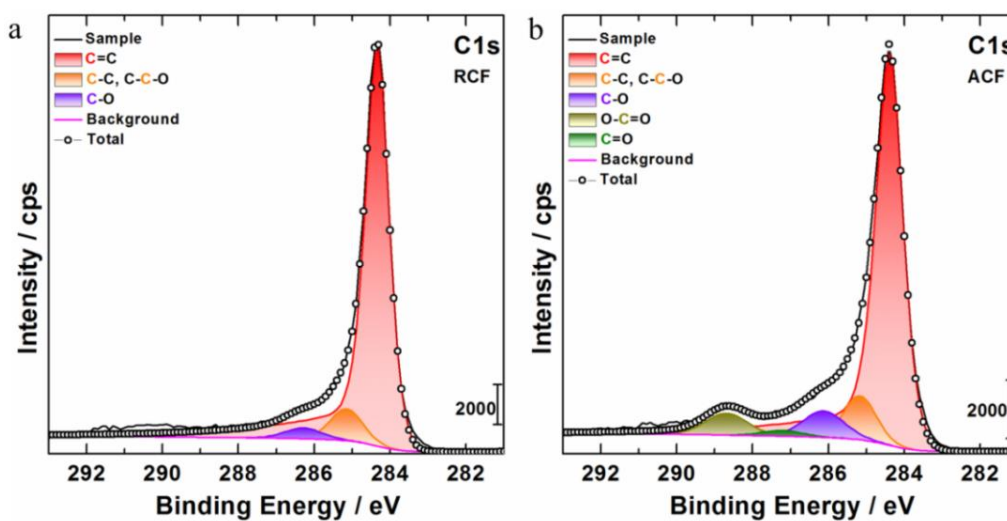


Figure 89 Deconvolution of C1s peak at 284 eV of (a) RCF and (b) ACF.

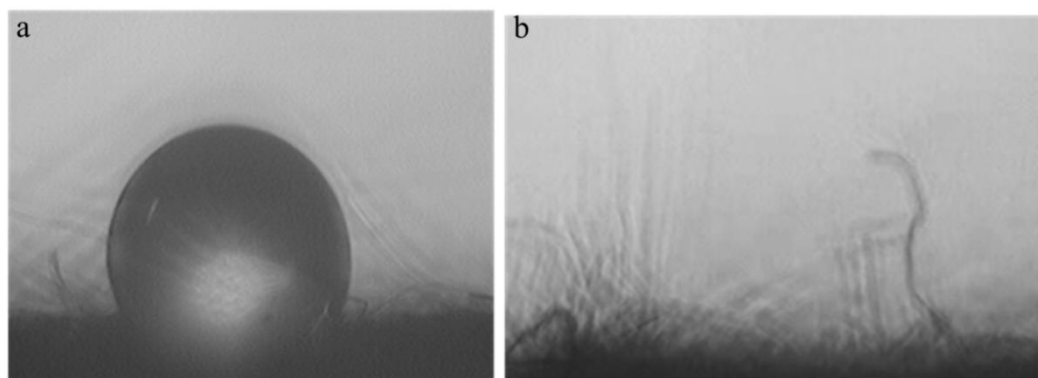


Figure 90 Water droplet test on (a) RCF and (b) ACF surface. Both photos were taken immediately after water was dropped.

Since the ACF is hydrophilic, it becomes more accessible toward electroactive species. Therefore, the redox process occurs over the entire surface, which results in higher both oxidation and reduction currents, as shown in **Figure 91**. The electroactive surface area can be calculated based on the Randles-Sevcick equation (**Eq. 90**). The calculated electroactive surface area is then 7 cm² for RCF and 46.9 cm² for ACF. This increase is mainly related to the increase of the hydrophilicity of the surface after oxidation step.

$$I_p = 2.687 \times 10^5 \cdot A \cdot C \cdot n^{3/2} \cdot D^{1/2} \cdot \nu^{1/2} \quad (\text{Eq.90})$$

Where, I_p is peak current (A), A is the electroactive area (cm²), C is concentration of electroactive molecule (mol cm⁻³), n is the number of exchanged electrons, D is the diffusion coefficient (cm² s⁻¹), and ν is the scan rate (V s⁻¹).

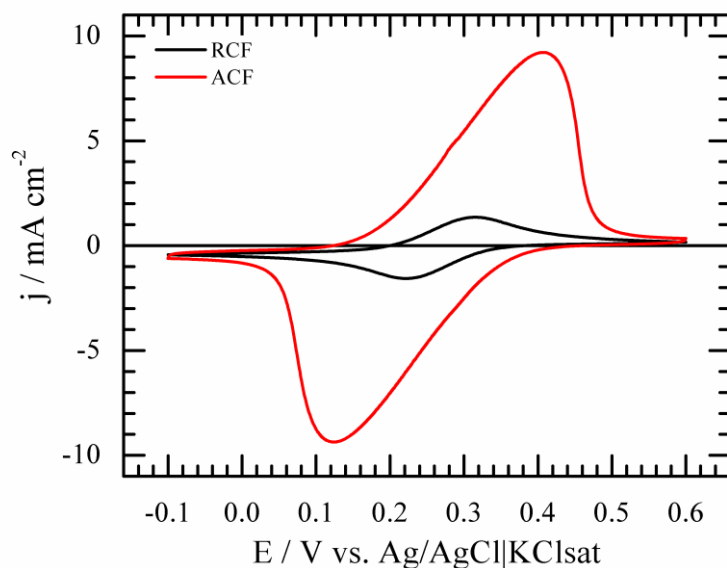


Figure 91 Voltammograms obtained on RCF and ACF under nitrogen atmosphere and 10 mM $K_3Fe(CN)_6$ (in 1 M KNO_3) at 10 mV s^{-1} .

3.4.2 Electrodeposition of Pt on ACF

In this section, we have grown Pt nanoparticles directly on the ACF surface by electrodeposition method with the advantages of being able to work under mild operation conditions (ambient room condition)[187] and at low concentrations [187].

Herein, we used chloroplatinic acid (H_2PtCl_6) aqueous solution as Pt precursor at concentration from 1 to 7 mM). The resulting pH was 2. The species present at this acidic pH are $PtCl_6^{2-}$ and its hydrolysis products according to **Eqs. 91** and **92** [188].



Before electrodeposition, we then adjusted the solution to pH 9. This alkaline condition is able to minimize hydrogen evolution reaction, which is well known to cause low efficiency during Pt electrodeposition [187]. In alkaline solution, $H_2Pt(OH)_6$ is predominant since a high concentration of hydroxyl shift the equilibrium reaction (**Eq. 93**) rightward [187].



Than the electrodeposition reaction can be generalized, as expressed in **Eq. 94** [187].



Electrodeposition was conducted by chronoamperometry (CA), at -0.6 V vs. Ag/AgCl that significantly lower than the standard redox potential (0.5 V vs Ag/AgCl). This large overpotential was aimed at ensuring the driving force was thermodynamically sufficient for deposition and growth of Pt(IV) to Pt(0) [93]. The large overpotential is also important to drive nucleation [189].

3.4.3 Electrochemical performance

We used the LSV method to evaluate the ORR performance and the CV method to calculate electrochemical surface active area (ECSA).

3.4.3.1 Oxygen reduction reaction (ORR)

Oxygen reduction can proceed through two mechanisms: 1) oxygen combines with 4 electrons and protons directly (4-e transfer mechanism), 2) oxygen is reduced in two consecutive steps involving a 2-electron transfer, which produces hydrogen peroxide as the intermediate (2-e transfer mechanism) [124]. As the material will be routed to the air-breathing cathode in the MFC, therefore the ORR is expected to follow the 4-electron transfer mechanism (**Eq. 95**). [190].



The ORR performance evaluation of RCF, ACF, and ACF@Pt respectively was conducted by LSV under saturated oxygen atmosphere (**Figure 92a**). The ORR performance is rationally increased in the progressive order, RCF<ACF<ACF@Pt.

Figure 92b shows the polarization curve recorded in KOH solution on the ACF@Pt electrode under nitrogen (dashed line) and oxygen (solid line) atmosphere. The LSV curve under oxygen atmosphere exhibits a significantly higher current over the entire potential region. The ORR polarization curve obtained was a typical LSV curve which can be divided into two regions, as adapted to Ref [191]: 1) a steep reduction wave at $-0.2 < E < 0.1$ V vs. Ag/AgCl

indicating a mixed kinetic-diffusion control, and 2) a wave (plateau for RDE curve) at $-0.9 < E < -0.2$ V vs. Ag/AgCl showing diffusion-limited current density.

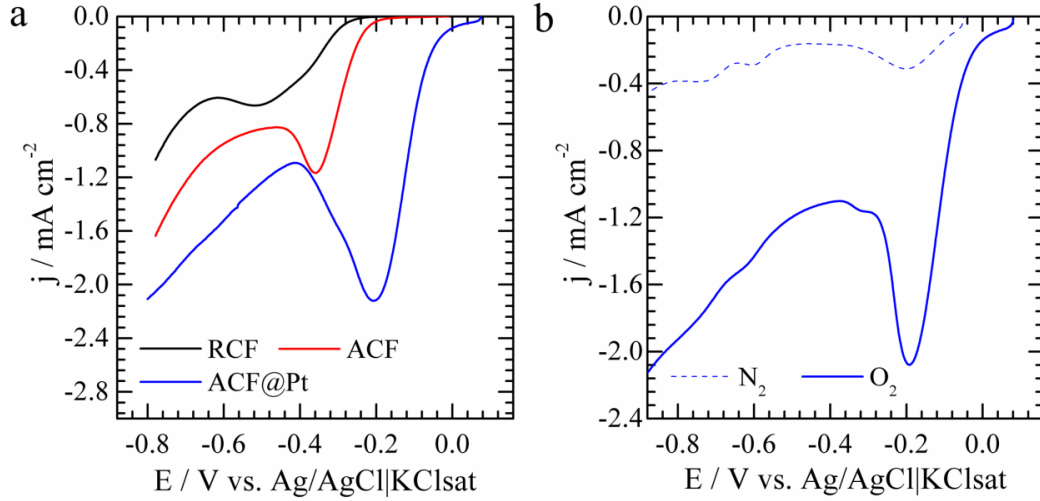


Figure 92 LSV curve in 0.1 M KOH solution at scan rate 5 mV s^{-1} of (a) RCF, ACF and ACF@Pt under saturated oxygen atmosphere and (b) ACF@Pt electrode under saturated nitrogen and oxygen atmosphere.

3.4.3.2 Electrochemical active surface area (ECSA)

The CV of the material was recorded in KOH solution under nitrogen atmosphere (**Figure 93**). We can divide the CV into three regions: 1) at potential $-0.9 < E < -0.5$ V vs. Ag/AgCl as typical hydrogen adsorption/desorption wave on the Pt electrode surface 2) the region at $-0.5 < E < -0.3$ V vs. Ag/AgCl as double layer charging and 3) region at $-0.3 < E < 0$ V vs. Ag/AgCl as Pt surface oxidation and Pt oxide reduction in the positive-going scan and at its reverse, respectively.

The ECSA can be determined from the hydrogen desorption charge ($Q_{\text{exchange-charge}}$) wave in the first region in the positive-going scan. $Q_{\text{exchange-charge}}$ was calculated with **Eq. 96** using Origin 9 software application and corrected by double layer charge (green raster in **Figure 93**). Then, the electrochemical active surface area was calculated using **Eq. 97**. Whereas, $Q_{\text{monolayer}}$ is associated with the adsorption/desorption of the formed Pt_{Hads} monolayer.

$$Q_{\text{exchanged-charge}} = \frac{1}{\nu} \left(\int_{E_{\text{initial}}}^{E_{\text{final}}} i(E) dE \right) \quad (\text{Eq. 96})$$

$$ECSA(cm^2) = \frac{Q_{exchanged-charge}(\mu C)}{Q_{monolayer}(\mu C.cm^{-2})} \quad (\text{Eq. 97})$$

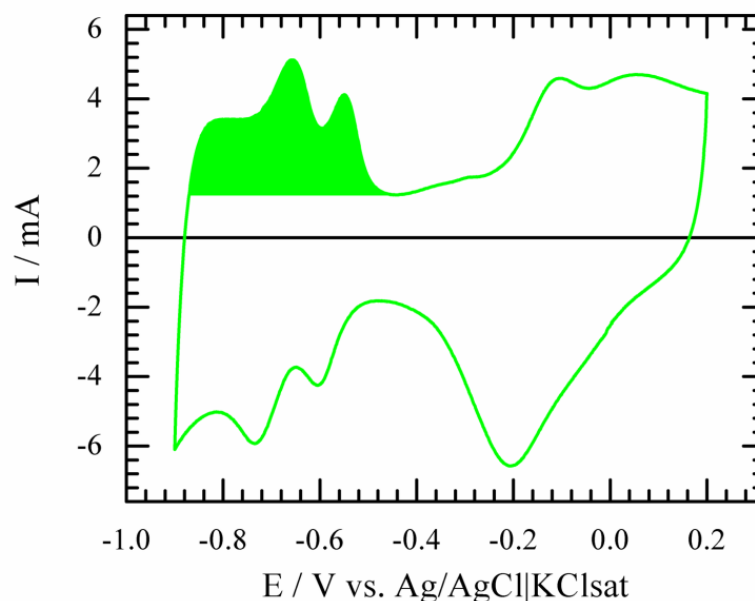


Figure 93 CV voltammogram of ACF@Pt electrode in 0.1 M KOH solution at 5 mV s^{-1} under nitrogen atmosphere showing the PtH desorption region (green raster) used to determine the electrochemical surface active area (ECSA).

It is also obvious to calculate the specific electrochemical active surface area (SECSA) by normalization toward the geometric surface area (A_g) of the electrode and the Pt loading (L_{Pt}). SECSA is commonly reported as $\text{m}^2 \text{ g}_{Pt}^{-1}$ [191]. ECSA and SECSA values according to our results are presented in **Tables 17** and **18**.

3.4.4 Effect of electrodeposition method

The electrodeposition of Pt on the ACF has been conducted both by CV and CA method. The CA electrodeposition method leads to higher ECSA and better ORR performance (**Figure 94**). This gap corresponds to the amount of deposited Pt. The CV electrodeposition method applies cyclic scanning at different potentials which might reoxidize the already deposited Pt.

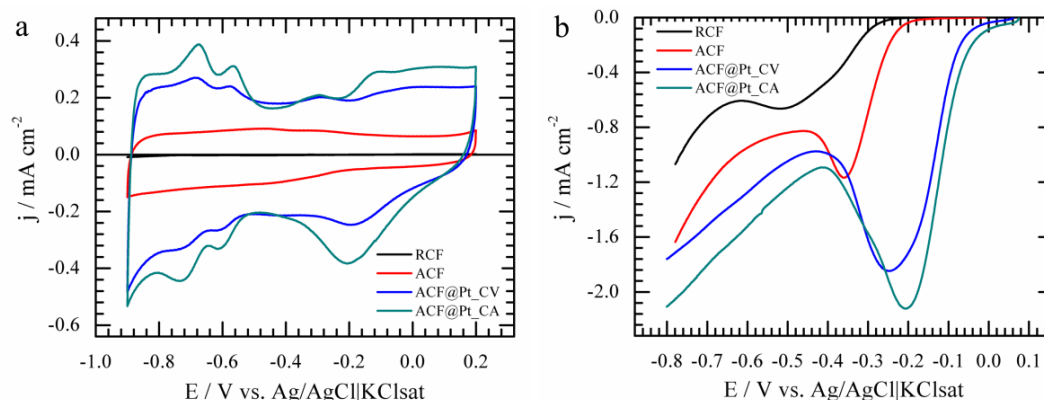


Figure 94 (a) CV under nitrogen atmosphere and (b) LSV under oxygen atmosphere at 5 mV s^{-1} in 0.1 M KOH solution of the as-synthesized ACF@Pt_CV and ACF@Pt_CA.

3.4.5. Effect of nitrogen atmosphere saturation

The presence of oxygen in the cell during electrodeposition of Pt will create a competitive reduction reaction when applied a very large overpotential is applied, i.e. $-0.6 \text{ V vs. Ag/AgCl}$ for Pt electrodeposition. Therefore, it is important to expel all of the oxygen content in the electrochemical solution by flowing nitrogen during electrodeposition. **Figure 95** shows a clear enhancement both in ORR performance and ECSA of the material prepared under nitrogen saturation.

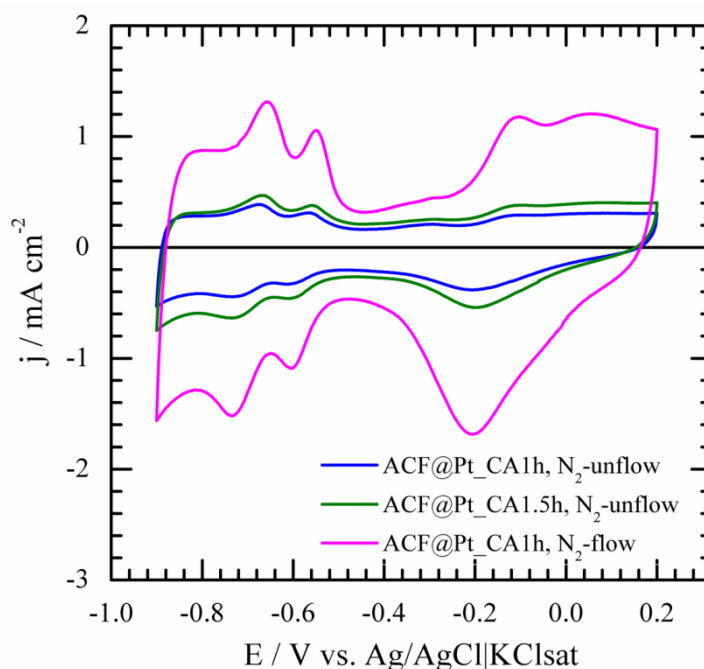


Figure 95 Cyclic voltammograms of the ACF@Pt in 0.1 M KOH solution at scan rate of 5 mV s^{-1} under unflow and flow of nitrogen

3.4.6 Effect of time

In order to optimize the synthesis conditions, we studied the time dependence of electrodeposition by CA method. **Figures 96a,c** show the CV for ORR and LSV in KOH solution (pH 13). All curves show the typical CV pattern of an electrode containing Pt at slightly different currents. The highest current of the ORR curve and the ECSA/SECSA were achieved from the material with 1 hour electrodeposition, ACF@Pt_CA-T1. This was taken as the best Pt electrodeposition time for use further in this research.

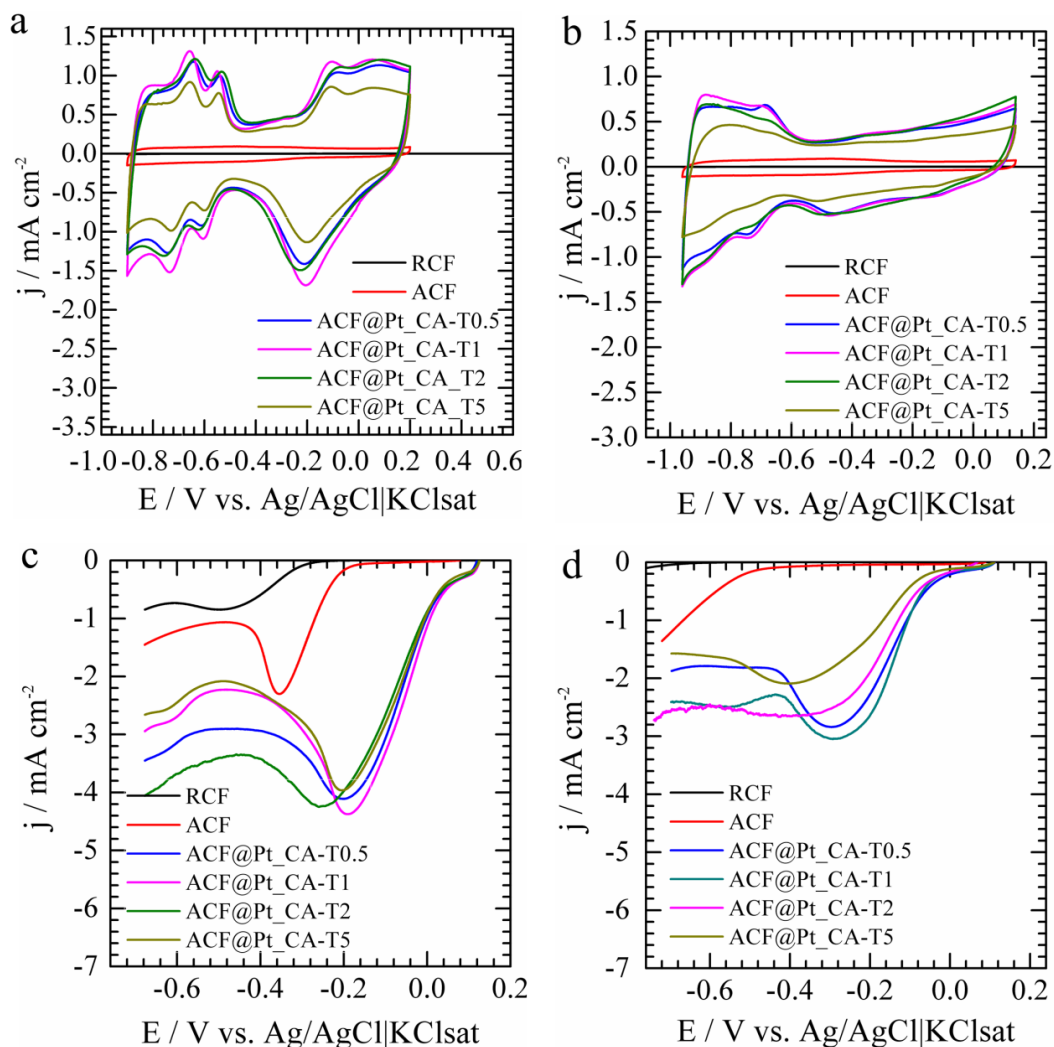


Figure 96 Electrochemical characterization of the ACF@Pt electrode by (a,b) CV at scan rate $5\ mV\ s^{-1}$ under nitrogen atmosphere at pH 13 (0.1 M KOH) and (b) pH 7 (50 mM PBS (50 mM KCl)), (c,d) LSV) at scan rate $5\ mV\ s^{-1}$ under oxygen atmosphere at pH 13 (c) and 7 (d).

To mimic its real application in an MFC, it is also necessary to record the LSV and ECSA of the electrode in neutral pH to mimics its real application in MFC. The LSV curve and CV in PBS solution (pH 7) exhibit the same behavior as in KOH solution (**Figures 96b, d**). However, the resulted lower current density in the PBS solution is considered due to the lower pH.

Both the ECSAs and SECSAs were calculated, as summarized in **Table 17**. The highest SECSA was achieved after 1 hour electrodeposition either in KOH or PBS solution. Electrodeposition during 0.5 hour resulted in both lower SECSA and ORR performance because of a lower amount of deposited Pt. Meanwhile, a longer electrodeposition time ($t > 1$) leads to bigger particles which lowering utilization efficiency.

Table 17 Electrochemical active surface area (ECSA) and specific electrochemical active surface area (SECSA) derived from voltammogram in alkaline and neutral solution

Time (h)	Sample code: ACF@Pt_CA-Tx	ECSA (cm ²)		SECSA-th(m ² /g)		SECSA-exp (m ² /g)	
		In KOH	In PBS	In KOH	In PBS	In KOH	In PBS
0.5	T0.5	680.1±6.9	422.4±6.1	3.5	2.2	9	5.6
1	T1	825.1±8.7	454.8 ±11.3	4.2	2.3	9	5
2	T2	716.9±7.6	356.9±2.6	3.7	1.8	5	2.5
5	T5	537.0±3.1	181.8±8.4	2.8	0.9	nd.	nd.

3.4.7 Effect of concentration

To maximize the Pt particle loading, its dependence toward hexachloroplatinic acid concentration as the precursor was also studied, with a reaction time of 1 hour as the best compromise. **Figure 97** shows the electrochemical characterization (LSV and CV) of the electrodes, recorded both in KOH and PBS solution. The CV voltammograms (**Figures 97a,b**) of the electrodes, in both solutions, show gradual enhancement as the concentration increases. The LSV curve, shown in **Figure 97c**, shows the ORR performance in the KOH solution of the resulted electrodes as the concentration dependent. The three electrodes,

prepared from 1 to 3 mM, revealed a progressive ORR peak current enhancement. While, those were resulted from 3 to 7 mM seemed to reach a plateau ORR performance. The electrode, as resulted from 7 mM concentration, revealed lower ORR performance in the PBS solution (**Figure 97d**). Thus, we considered 5 mM to be the best precursor concentration to develop the ACF@Pt electrode. A higher concentration will result in the formation of bigger particles, which decreases the utilization efficiency of the catalyst. Hence, the accessibility of O₂ molecules to all Pt atoms in each particle is limited [93].

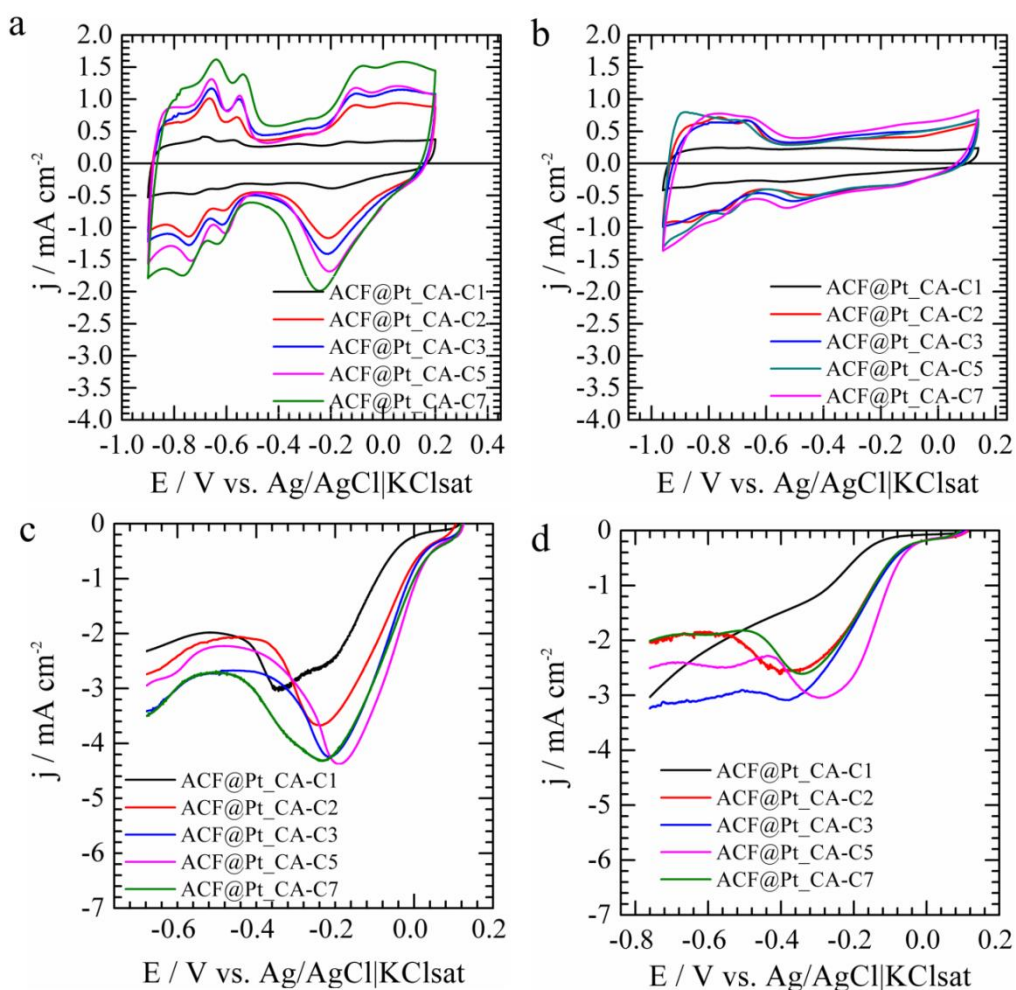


Figure 97 CV voltammogram under nitrogen atmosphere at scan rate 5 mV s^{-1} (a,b) and LSV curve under oxygen atmosphere at scan rate 5 mV s^{-1} (c,d) in 0.1 M KOH pH 13 for (a,c) and in 50 PBS (50 mM KCl) pH 7 for (b,d).

Table 18 Electrochemical active surface area (ECSA) and specific electrochemical active surface area (SECSA) of electrodes as concentration dependent derived from voltammogram in alkaline and neutral solution

[C]/ mM	Sample code: ACF@ Pt_CA-Cx	ECSA (cm ²)		SECSA- th(m ² /g)		SECSA-exp (m ² /g)	
		In KOH	In PBS	In KOH	In PBS	In KOH	In PBS
1	C1	100.0±3.2	18.0±0.9	2.3	0.4	6	1.1
2	C2	451.4±16.1	369.5±9.1	6.3	5.1	nd.	nd.
3	C3	537.2±4.8	293.5±10.6	6.6	3.6	10	5.5
5	C5	825.1±8.7	454.8±11.3	4.2	2.3	9	5.0
7	C7	876.8±13.6	331.7±10.4	3.2	1.2	nd.	nd.

3.4.8 Effect of thermal treatment

Thermal treatment plays an important role in the transformation of the Pt layer into very well defined Pt particles and in the elimination of contaminants [192]. Therefore we carried out heat treatment at temperatures of 400, 600, and 1000 °C respectively under nitrogen atmosphere for 1 hour. The results are presented in **Figure 98**. A strong decrease of the electrochemical signal was observed of the thermal treatment both in KOH and buffer solution (**Figure 98a, b**), which is definitively due to severe structural modifications. Moreover, the ORR performance of all electrodes had decreased after thermal treatment (**Figure 98c**). The voltammogram recorded in the ferricyanide solution (**Figure 98d**) also exhibited the decreasing trend of real surface area due to the thermal process effect. Further investigation under SEM (**Figure 103**), revealed that the Pt particles were melted at this high temperature and subsequently decreased the its performance [193].

3.4.9 Platinum mass loading quantification

Platinum mass loading is one of the key parameters in developing cost-effective catalysis materials. High Pt loading leads to increase the construction costs.

Moreover, a large Pt loading decreases the SECSA. Nevertheless, Pt loading that is too low also lead to more H₂O₂ produced [194]. Herein, we determined the Pt mass loading through both theoretical calculation and experiments. Experimentally, we carried out thermogravimetric analysis (TGA) and inductively couple plasma (ICP) to several representative samples to determine the exact amount of Pt loading. The Pt mass loading of all representative samples are listed in **Table 19**.

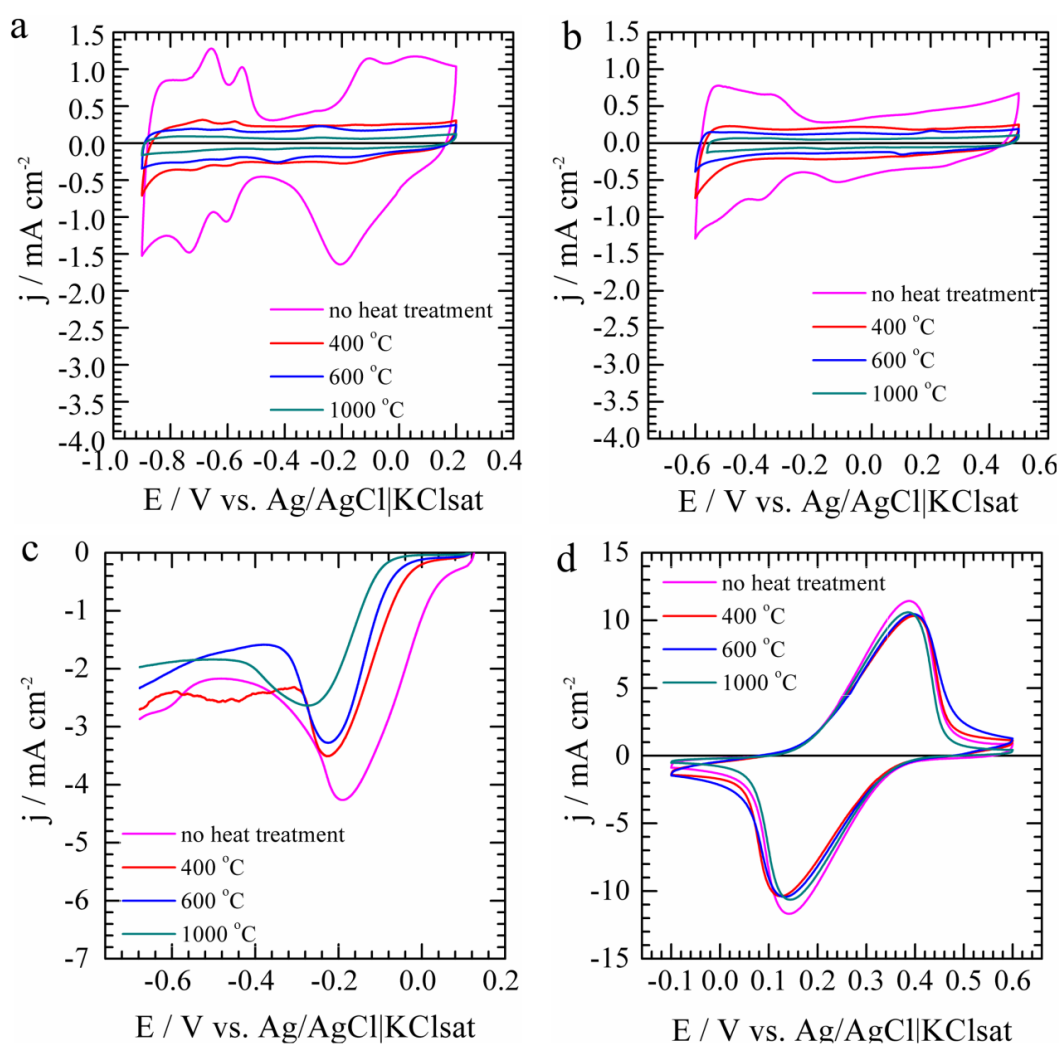


Figure 98 Electrochemical characterization after thermal treatment for ACF@Pt electrodes recorded (a,b) at 5 mV s^{-1} in 0.1 M KOH and 50 mM PBS (in 50 mM KCl) solution respectively (d) at 10 mV s^{-1} in 10 mM $\text{K}_3\text{Fe}(\text{CN})_6$ (in 1 M KNO_3) under nitrogen atmosphere and (c) LSV curve at 5 mV s^{-1} under oxygen atmosphere

Table 19 Summarized Pt mass loading from theoretical calculation, Faradic mass, TGA, and ICP

Time, [PtCl ₆] ²⁻	Sample code	Theoretical mass		Faradic mass		TGA / wt. %	ICP / wt. %
		mg	wt. %	mg	wt. %		
0.5 h, 5 mM	ACF@Pt_CA-T0.5	19.5	24.5	10.4	14.8	11	nd
1 h, 5 mM	ACF@Pt_CA-T1	19.5	24.5	12.8	17.6	13	13.4
2 h, 5 mM	ACF@Pt_CA-T2	19.5	24.5	37.2	38.3	20	nd
5 h, 5 mM	ACF@Pt_CA-T5	19.5	24.5	117.4	66.2	nd	nd
1 h, 1 mM	ACF@Pt_CA-C1	4.3	6.7	1.6	2.6	2.9	2.0
1 h, 2 mM	ACF@Pt_CA-C2	7.2	10.7	2.8	4.5	nd	nd
1 h, 3 mM	ACF@Pt_CA-C3	8.2	12.0	10.4	14.8	8.6	8.9
1 h, 5 mM	ACF@Pt_CA-C5	19.5	24.5	12.8	17.6	13	13.4
1 h, 7 mM	ACF@Pt_CA-C7	27.3	31.27	45.7	43.24	nd	nd

The theoretical calculation of Pt mass loading is possible according to **Eq. 98**. This correlates to the maximum amount of Pt that can be loaded.

$$m_{Pt-th} = V \cdot C \cdot M_{Pt} \quad (\text{Eq. 98})$$

Where, V and C are respectively volume and concentration of chloroplatinic acid as platinum source, M is atomic molar mass of platinum.

The electrodeposited Pt mass was also evaluated by Faraday's Law applied to our electrolysis conditions (**Eq.99**).

$$m = \frac{Q}{F} \times \frac{M}{z} \quad (\text{Eq. 99})$$

Where,

m : mass of deposited Pt (gram)

Q : total electric charge (Coulomb)

M : atomic weight of Pt (g mol⁻¹)

F : Faraday's constant (96,485 C mol⁻¹)

z: the number of transferred electrons per ion (4)

Herein, we found that the Pt content, as calculated by Faraday's law is higher than theoretical and experimental result. This due to the evolved current (I) during electrodeposition was larger than expected, hence give a larger total electric charge (Q) that involve in Faradic mass calculation.

Figure 99 shows TGA curves for the ACF@Pt samples and the blanks (RCF, ACF). Carbon combustion started at around 450 °C for all samples. Indeed, the samples containing Pt were burned faster because Pt NPs are obviously good catalysts for the reaction [195]. However, the weight loss between 600 and 700 °C indicates partial oxidation of carbon that is probably due to the characteristic interaction of Pt-carbon. Complete combustion processes are obtained above 750 °C. Thus, the real Pt content was determined at 800 °C. The obtained values for the reaction times of 0.5 and 1 hour confirmed the calculated data (**Table 19**). For 2 hours, 20 wt. % is in agreement with the theoretical maximum value (i.e. ~ 25 wt. %) based on a Faradic rate of 100%. The Pt content of some selected samples, analyzed by TGA, conforms with those analyzed by ICP.

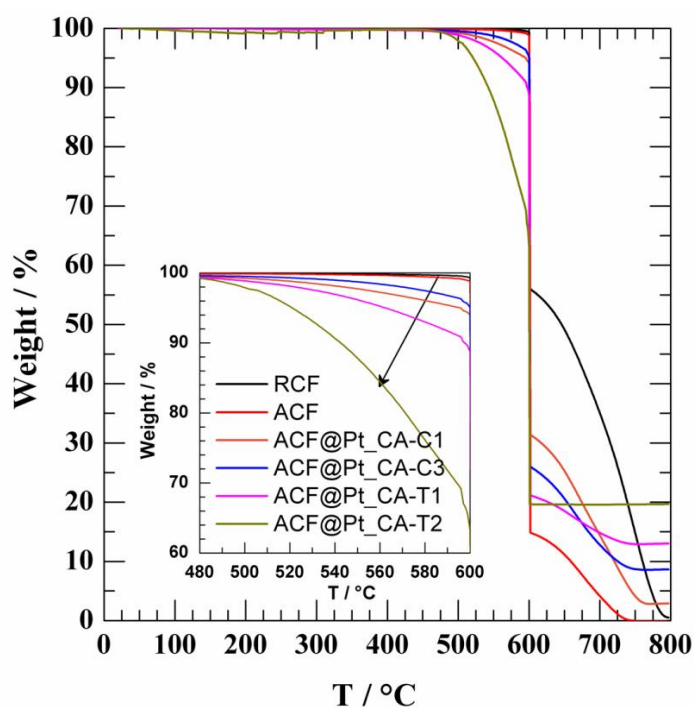


Figure 99 Thermogravimetric analysis curves of RCF, ACF and ACF@Pt representatives (inset shows the weight loss between 480 and 600 °C)

3.4.10 Morphological structure of the material

SEM images of some ACF@Pt samples at various magnifications are presented in **Figure 100**. The Pt particles cover the entire fiber surface, as can be seen in **Figure 100a**. The SEM image at higher magnification in **Figure 100b** reveals an array of Pt nodules. The closer overview in **Figure 100c** gives the detailed shape of the nodules as a well-defined 3D sponge-like structure with a diameter of 500 nm. Under this high resolution view, we also observe the 50-100 nm intermediates size of Pt particles spread out among the larger Pt particles. This is the expected physical morphology that enhances the catalytic performance of the as prepared material.

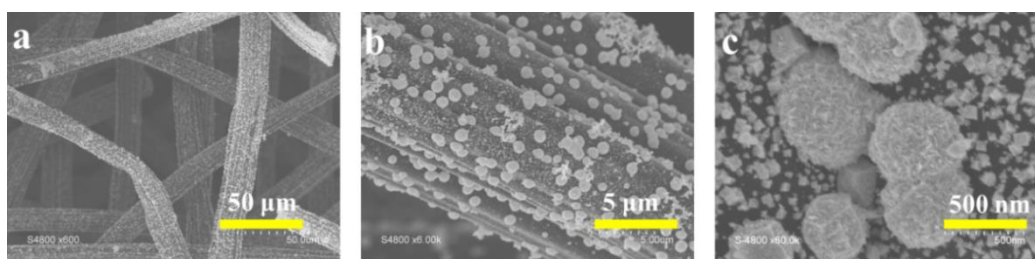


Figure 100 SEM image of the Pt particles grown on ACF from 5 mM of precursor with reaction times 1 hour: (a) overview at 50 µm (b) 5 µm, and (c) zoomed single particle at 500 nm magnification.

The surface morphology of the ACF@Pt also depends on the synthesis conditions. The duration of electrodeposition mainly affects the density of the particle array. Electrodeposition for more than one hour results in a denser Pt array (**Figure 101c,f**) because the longer exposure toward PtCl_6^{2-} induces the formation of bigger nodules. Moreover, the interconnected nodules lead to aggregation, which decreases the utilization efficiency of the metal. Electrodeposition below one hour seems to result in incomplete Pt nodule particles. The small and intermediate size Pt spread out on the CF fiber surface forms unexpected structures, as can be seen in **Figure 101a,d**.

The concentration dependence of the Pt particle morphology is shown in **Figure 102**. Generally, the representative samples for concentration at 1, 3, and 5 mM show a typical Pt nodule array as previously described. However, the development of Pt nodules at a concentration below 5 mM seems insufficient to

form a clear array. This is probably related to the kinetic rate of the electrodeposition.

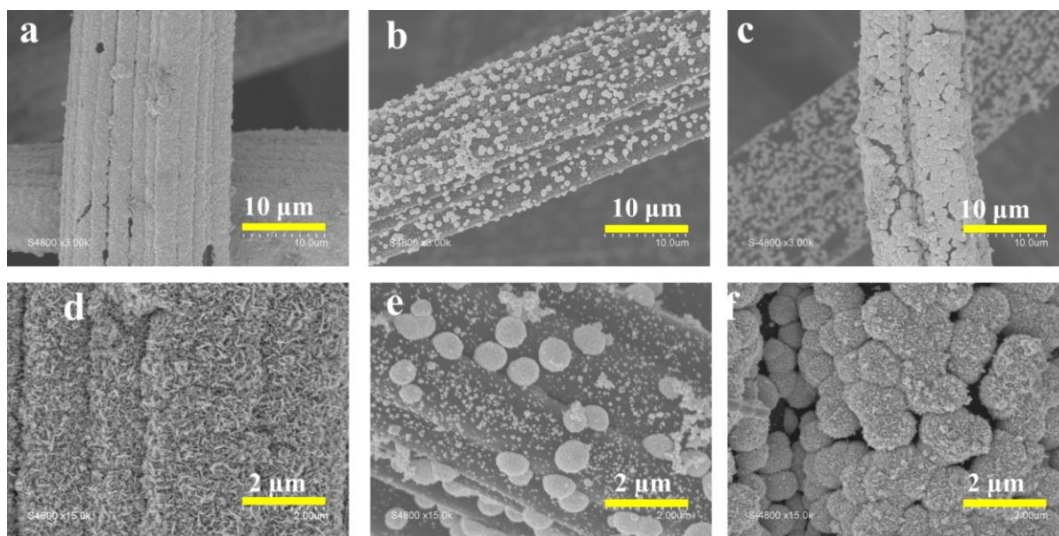


Figure 101 SEM images of the Pt particles growth on ACF for reaction time (a,d) 0.5 hour, (b,e) 1 hour and (c,f) 2 hours.

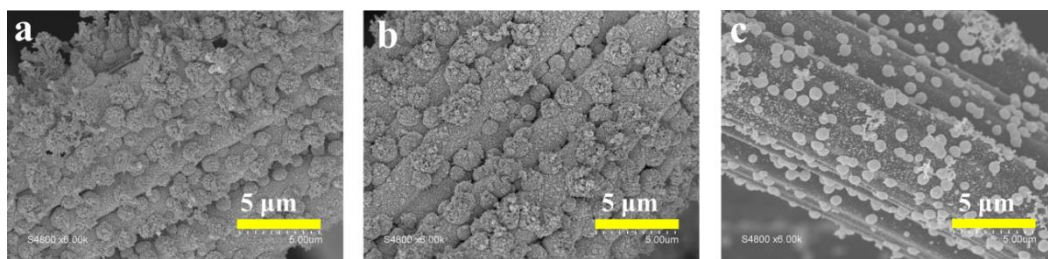


Figure 102 SEM image of the Pt particles grown on ACF for a reaction time of 1 hour from concentration of precursor (a) 1 mM, (b) 3 mM and (c) 5 mM.

The effect of heating treatment toward the Pt morphology is shown in **Figure 103**. The melting point of Pt particles depends on both the size and shape [193]. The Pt particle with diameter below than 10 nm can melt at temperature as low as 800 K (527 °C) [193]. The crystallite size of Pt NPs in our developed material range between 4.5 – 11.6 nm according to XRD spectra-based calculation (**Table 20**). Although the large Pt particles has diameter 500 nm, they are constituted of nanoscale domain on their surface. Therefore, the developed Pt NPs are easily to melt as they are exposed to heat. **Figure 103b** show heating treatment at 400 °C has led the Pt particles to start melting and then each other tend to attached each

other, which destroy the Pt's morphology. Heating treatment at 1000 °C has completely turned the Pt particles into agglomerates (**Figure 103c**) and automatically lost their nanoparticles and particles character. The both resulted structures, as shown in **Figure 103b,c**, lead to poor electrochemical performance of the ACF@Pt electrode as shown in **Figure 98**, which significantly decrease both its CV profile and electrocatalytic ORR performance.

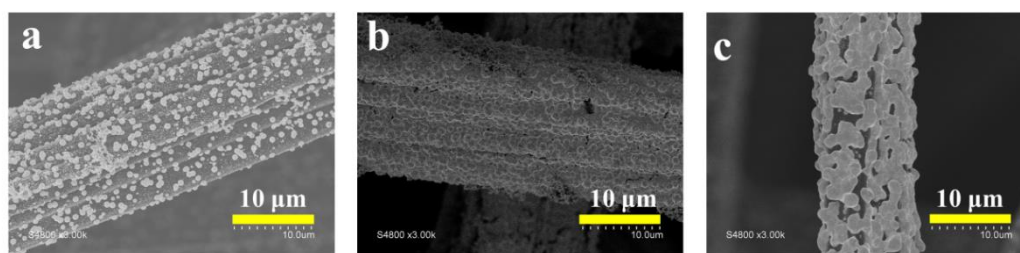


Figure 103 SEM image of ACF@Pt without (a) and with heat treatment at (b) 400 °C and (b) 1000 °C

3.4.11 Structure of the materials

XRD analysis was conducted to evaluate the crystallinity properties of the resulted materials. Bulk analysis by XRD indicated the presence of metallic platinum. The XRD spectra of some representative samples are shown in **Figure 104**. The broad diffraction peak at Bragg's angle 25° corresponds to the graphite (002) plane, while the one at 43° belongs to diamond (111) [6,195]. The Pt related peaks are situated at 39.43° , 45.85° , and 67.01° , originating respectively from the Pt crystallographic planes (111), (200), and (220) of the face-centered cubic (fcc) lattice in the ACF@Pt material. These results also reveal the polycrystallinity of the deposited Pt particles. The slight decrease of these positions compared to those of either bulk Pt (XRD reference code 90-007-641439: 39.76° , 46.23° , and 67.45°) or Pt Vulcan (39.84° , 46.30° , and 67.73°) [195] is probably due to Pt-carbon electronic interaction [196].

We were using Bragg's law and the Debye-Scherrer equation to determine the lattice parameter (a_{Pt}) and crystallite size (L_v) [195] (**Eq.100**). Herein, the determined parameter of $a_{Pt} \sim 3.95 \text{ \AA}$ is in agreement with that of the bulk Pt. The

calculated crystallite sizes of $L_v \sim 9\text{-}11$ nm indicate the formation of the nanoscale domains (a high-resolution SEM analysis confirmed this hypothesis).

$$L_v = \frac{K\lambda}{\beta \cos \theta} \quad (\text{Eq. 100})$$

Where, L_v is crystallite size, K is a constant, based on the assumption of uniform size small cubic crystals, $K=0.93944$, λ is the X-ray wavelength 1.540598 \AA , β is the half-peak width for Pt in radian, and θ is the Bragg's angle. The calculated crystallite size ranges from 4.5 to 11.6 nm (summarized in **Table 20**).

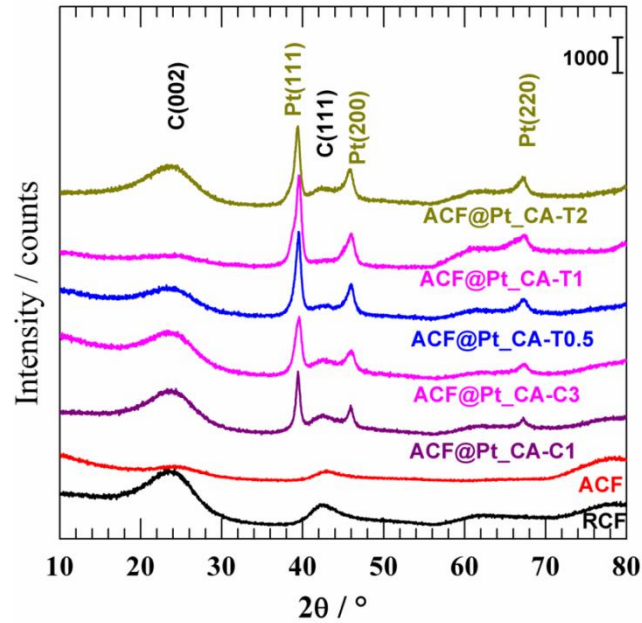


Figure 104 XRD patterns of CF, ACF, and selected ACF@Pt samples

Table 20 Calculated crystallite size derived from the Debye-Scherrer equation

hkl plane	Time electrodeposition (hour)	Sample code: ACF@Pt_CA-Tx	L_v (nm)
111	0.5	T0.5	11.04
	1	T1	9.06
	2	T2	11.61
200	0.5	T0.5	8.27
	1	T1	6.17
	2	T2	6.71
220	0.5	T0.5	7.31
	1	T1	4.53
	2	T2	7.64

3.4.12 Surface analysis

XPS is a useful surface analysis technique that enables us to gain deeper insight into oxidation state and the surface's chemical composition. **Figure 105** shows the XPS survey spectra of ACF@Pt samples along with pristine material as control material for an overview and a brief qualitative analysis. The intense peak at around binding energy, BE, 70 eV indicates the presence of Pt since it only appears in the ACF@Pt sample.

Deconvolution of this peak resulted in **Figure 106c**, which enable to deep analysis into its core level. The deconvoluted of Pt 4f reveals the doublets related to the spin-orbit splitting ($x \pm 1/2$, $x = 3$ for the f band) located at BEs of 71.0 eV (Pt 4f_{7/2}) and 74.4 eV (Pt 4f_{5/2}) for metallic platinum. Meanwhile, those situated at 72.1 and 75.2 eV belong to 4f_{7/2} and 4f_{5/2} levels of PtO_x ($x > 2$), respectively. The unexpected platinum oxide occurrence is considered due to the natural oxidation of the noble metal when exposed to ambient air (a thin layer protects the surface from deep oxidation) [197]. The peak of C 1s, situated at around BE 280 eV, emerges in every sample corresponding to its carbon-based material. The intensity decreases progressively in the following order: RCF > ACF > ACF@Pt, which is relevant to the acquired chemical treatment. Electroactivation of RCF enables the introduction of oxygenated species on the surface that consequently reduce its carbon content. Furthermore, the addition of Pt species leads to further lowering of the carbon signal. The signal of oxygen was found at BE 532 eV which significantly increases from RCF to ACF that notify the addition of oxygen. The electrodeposition of Pt on ACF may replace the existing oxygen. Therefore, the oxygen signal automatically decreases from ACF to ACF@Pt. Finally, the surface atomic composition of the sample presented in **Figure 106d**, which demonstrates RCF (97 atom % C, and 3 atom % O), ACF (87 atom % C, and 13 atom % O), and ACF@Pt (57 atom % C, 13 atom % O and 30 atom % Pt (i.e. 23 atom % from metallic platinum and 7 atom % of the total contribution from oxidized platinum) substantiates surface enrichment in O-containing functional groups.

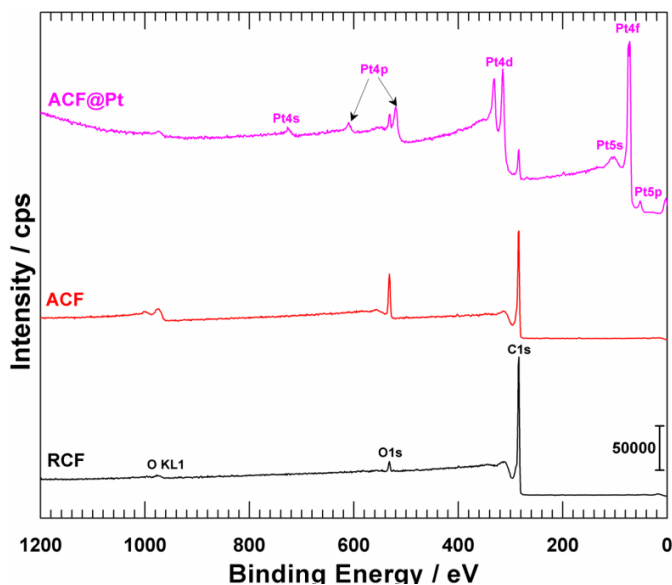


Figure 105 XPS survey spectrum of RCF, ACF and ACF@Pt

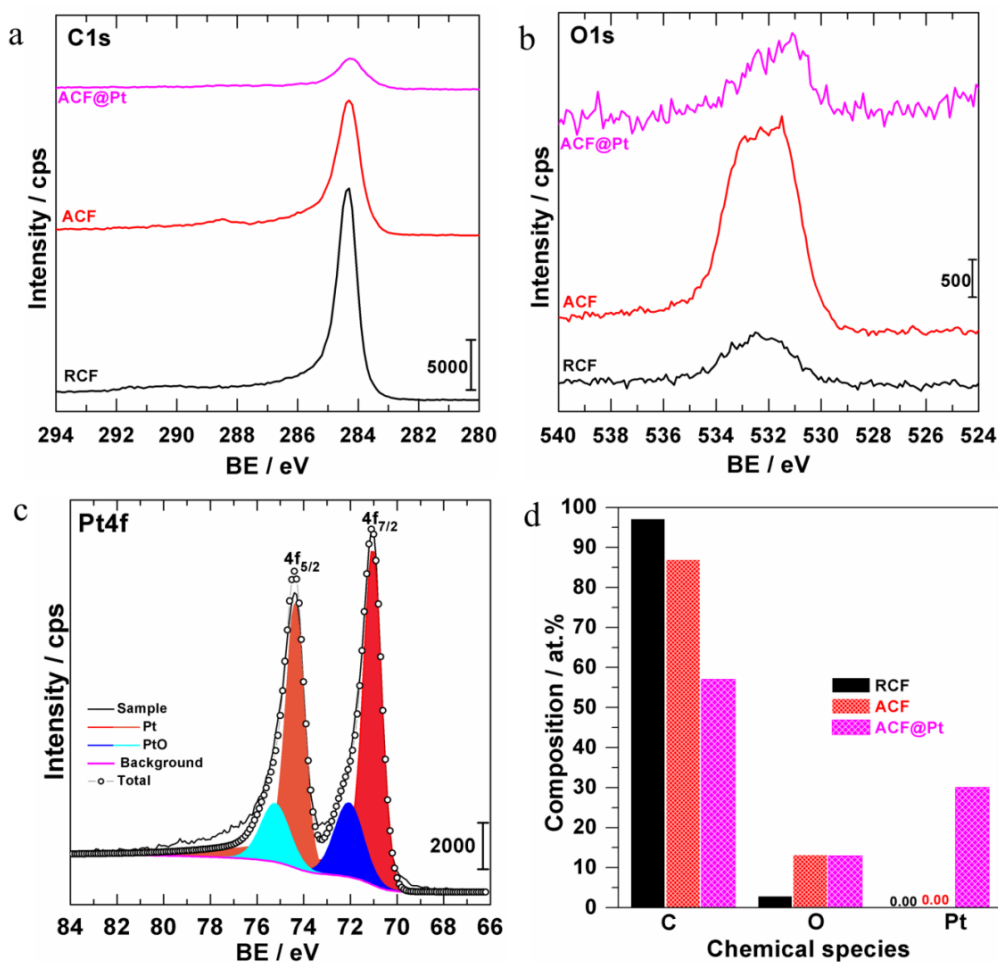


Figure 106 High resolution XPS spectra of (a) C1s and (b) O1s of the RCF, ACF and ACF@Pt (c) Pt4f core level of ACF@Pt sample (d) surface atomic composition.

3.4.13 Electrochemical impedance spectroscopy (EIS)

EIS experiments were implemented to evaluate both the ionic conductivity of the system and the electron-transfer ability of the electrodes. Complex-plane Nyquist impedance plots for the RCF, ACF and ACF@Pt electrodes were recorded at the open circuit potential of the RCF, ACF, and ACF@Pt respectively. **Figure 107** shows a typical Nyquist plot, where the slightly depressed semicircles for ACF and ACF@Pt imply a charge-transfer process (with contribution of diffusion within the 3D network of RCF). The ohmic resistance (R_{Ω}) is determined from the intersection between the Nyquist curve and x axis at high frequencies. R_{Ω} was about $3.2 \Omega \text{ cm}^2$ for RCF, $2.3 \Omega \text{ cm}^2$ for ACF and $1.2 \Omega \text{ cm}^2$ for ACF@Pt. R_{Ω} , also refers to cell resistance, comprising the resistance between the reference electrode and the surface of the working electrode in a conventional three-electrode measurement, connections, electrolyte, and electrode material. The charge-transfer resistances (RCT), determined from the diameter of semicircular Nyquist plot, were 1.2, 3.9, and $> 100 \Omega \text{ cm}^2$ respectively for the ACF@Pt, ACF, and RCF. The larger R_{ct} is, the lower the kinetic rate and the smaller the driving force. Therefore, the ACF@Pt is effective in performing faster electron-transfer.

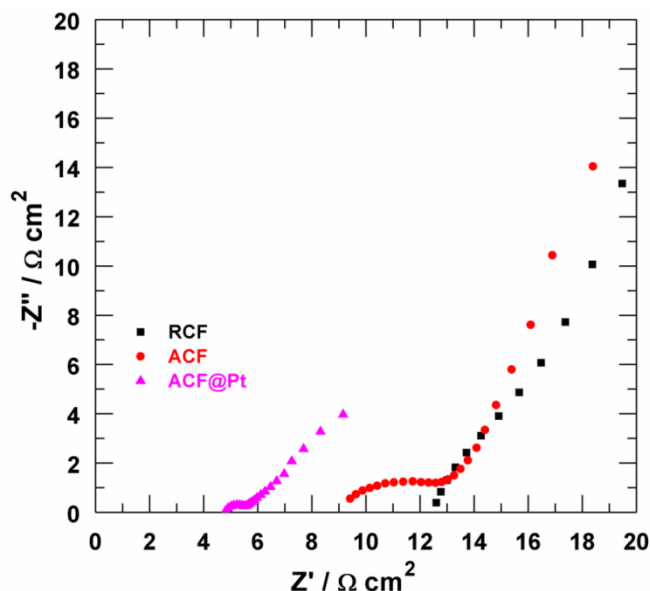


Figure 107 Complex-plane Nyquist impedance plots for RCF, ACF and ACF@Pt electrodes recorded at the open circuit potential (i.e. 0.35, 0.42 and 0.41 V vs. RHE for RCF, ACF and ACF@Pt, respectively) in 10 mM $\text{K}_3[\text{Fe}(\text{CN})_6]$ + 1 M KNO_3 aqueous solution. The normalization is based on an estimated geometric surface area of 3.9 cm^2 for the working electrode.

3.4.14 Fourier Transform Infra Red (FTIR) Spectroscopy

Figure 108 presents the FTIRS spectra, which confirm a signal increase in the region between 900 and 1240 cm^{-1} corresponding to C-OH (hydroxyl groups). So far, the obtained results support the enhancement of the electroactive surface area, reduced charge transfer resistance, and improved ORR kinetics [93].

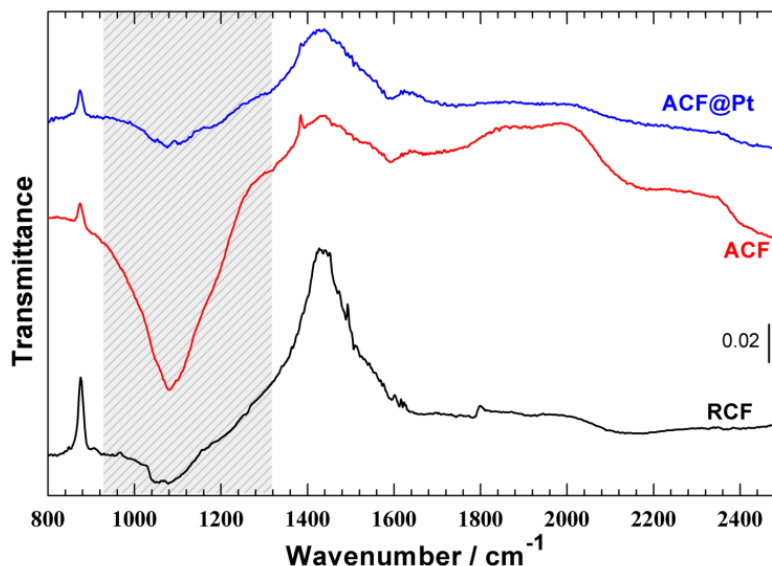


Figure 108 FTIR spectra of the ACF@Pt, ACF, and RCF

3.4.15 Electrochemical performance toward ORR following 4-electron transfer mechanism

Owing to the presence of Pt particles, we hypothesize that the ORR at the ACF@Pt electrode follow a 4-e transfer mechanism. Thus, it is predicted to produce only OH^- at pH 13 according to **Eq. 101**. In order to confirm this hypothesis, we tracked any produced H_2O_2 from an incomplete ORR in a two-electron process in the form of HO_2^- as expressed in **Eq. 102**. The produced HO_2^- in alkaline aqueous solution is stable enough to be determined, since the pK_a $\text{H}_2\text{O}_2/\text{HO}_2^-$ at 25 $^\circ\text{C}$ is 11.75.



For this test, reductions at different potentials were carried out during 1 hour in alkaline solution under saturated oxygen atmosphere to record the current (I). Herein, the RCF and ACF were also tested as control. The applied potentials were

determined from the LSV ORR curve. The current plot versus time (s) was used to determine the charge (Q). After 1 hour CA, the treated solution was collected and acidified to pH 3.5, which bring HO_2^- into H_2O_2 and ready to be further quantified using UV-Vis spectrophotometer. The resulting H_2O_2 was initially reacted with titanium oxalate solution to form coloured complex of $\text{H}_2\text{O}_2\text{-Ti(IV)}$ solution that absorb at 390 nm. Then, a calibration curve was set up to determine the H_2O_2 in the collected sample. **Figure 109a** shows a comparison of the involved current at each electrode for different applied potentials (E_{appl}). The current is quite constant that notify a good stability. The total electric charge (Q), as integrated from current curve, is shown in **Figure 109b**. The data is listed in **Table 21**.

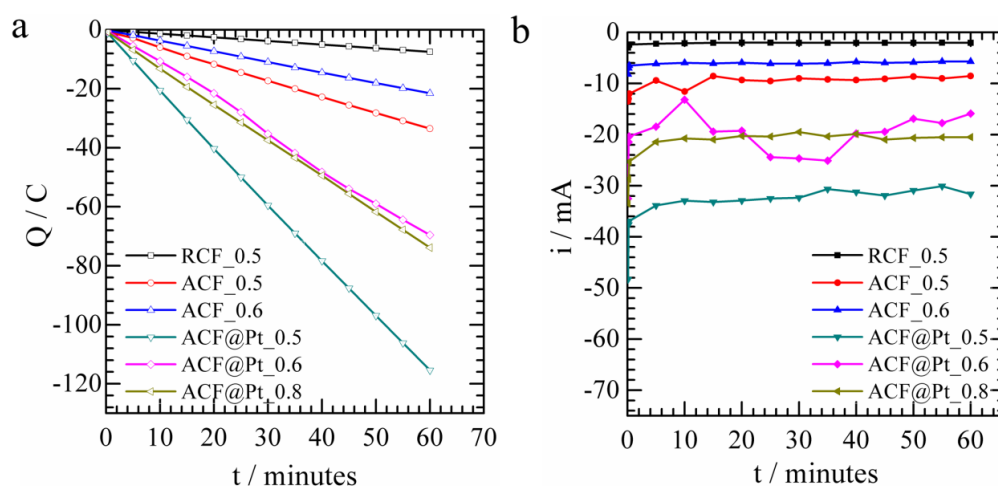


Figure 109 (a) Behavior of I and (b) Q during one hour CA in 0.1 M KOH aqueous solution under oxygen atmosphere on the RCF, ACF and ACF@Pt electrodes at various electrode potentials

Table 21 Data obtained from electroanalytical study of O_2 reduction.

Sample	E_{appl} vs. Ag/AgCl for 1 h CA	Q / C	$[\text{H}_2\text{O}_2] / \mu\text{M}$	Mol, n / μmol		
				n_{total}^1	n_{exp}^2	n_{real}^3
RCF	-0.5 V	7.46	227.07 ± 7.21	77.36	4.54	9.08
ACF	-0.5 V	33.51	1.03 ± 0.04	0.35	0.02	0.04
	-0.4 V	21.52	552.67 ± 27.53	223.035	11.05	22.11
ACF@Pt	-0.5 V	115.44	35.44 ± 1.04	1196.43	0.71	1.42
	-0.4 V	69.57	6.61 ± 2.08	721.03	0.13	0.26
	-0.2 V	73.86	19.22 ± 1.04	765.513	0.38	0.77

¹ n_{total} determined from Q , i.e. $n_{total} = -\frac{Q}{F}$, $Q = -|Q|$ and $F = 96\,485\text{ C mol}^{-1}$, Faraday's

constant

² n_{exp} determined from $[H_2O_2]$, as measured spectrophotometrically by UV-Vis, i.e. $n_{exp} = [H_2O_2] \times V_{solution}$

³ n_{real} is the real quantity of electron that used for production H_2O_2 through the net reaction $O_2 + H_2O + 2e^- \rightarrow HO_2^- + OH^-$, thus $n_{real} = n(e^-) = 2 \times n(HO_2^-) = 2 \times n_{exp}$

Therefore the Faradic efficiency toward ORR with 2-e transfer mechanism can be calculated according to **Eq. 103**.

$$\sigma_F = \frac{n_{real}}{n_{total}} \times 100\% \quad (\text{Eq. 103})$$

Whereas the Faradic efficiency toward ORR with 4-e transfer mechanism is determined by subtracting 1 by the mol ratio and convert to percentage according to **Eq. 104**.

$$\sigma_{F'} = \left(1 - \frac{n_{real}}{n_{total}}\right) \times 100\% \quad (\text{Eq. 104})$$

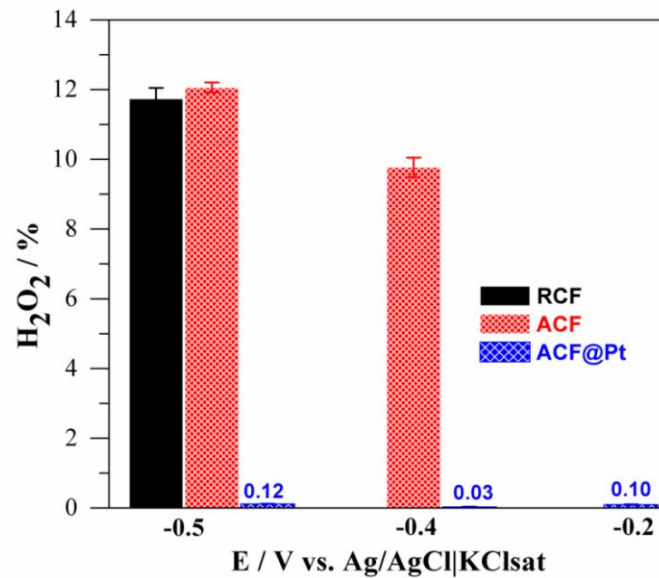


Figure 110 Potential-dependent production of H_2O_2 from ORR as quantified from UV-Vis assay

Finally, as calculated Faradic efficiency of ORR for the production of hydrogen peroxide is presented in **Figure 110**, which shows the as-quantified H_2O_2 from the UV-vis assays, wherein a negligible intermediate amount is detectable on the ACF@Pt material, thus underpinning the conclusion that the ORR is performed in a four-electron process. The durability of the electrodes in strong corrosive conditions is one of the major issues encountered during the design of an efficient electrocatalyst.

In conclusion of **Section 3.4**, the research showed the strategy to develop an advanced material that can be readily scaled up by directly growing Pt particles on a high surface area to fabricate a scalable electrode using a conventional electro-deposition method under mild conditions. Herein, the carbon felt with platinum nanoparticles grown on its surface shows excellent ORR catalytic properties that meet the requirements of an air-breathing cathode in bio- and/or fuel cell application.

3.5 Air-breathing cathode for SCMFC: application of platinum modified carbon felt (ACF@Pt)

3.5.1 Application of ACF@Pt as air-breathing cathode in SCMFC and its comparison to DCMFC

In this study, we applied the ACF@Pt as air-cathode in an MFC powered by garden compost leachate. For comparison, we also run the classical DCMFC with ferricyanide as the cathodic solution by continuous reloading of ferricyanide solution in cathodic part to maintain power generation. The application of an SCMFC system eliminates this limitation. The performance of both systems for current generation is shown in **Figure 111**. The current starts to increase after a period of time that corresponds to the formation of electroactive biofilm on the anode surface [164]. It took almost one month for the DCMFC to generate a high current. Whereas, the current generation for the SCMFC happened three-times faster. Besides, the SCMFC produced a higher current density than the DCMFC. The current density values of both systems were normalized to the cathodic exposure surface area.

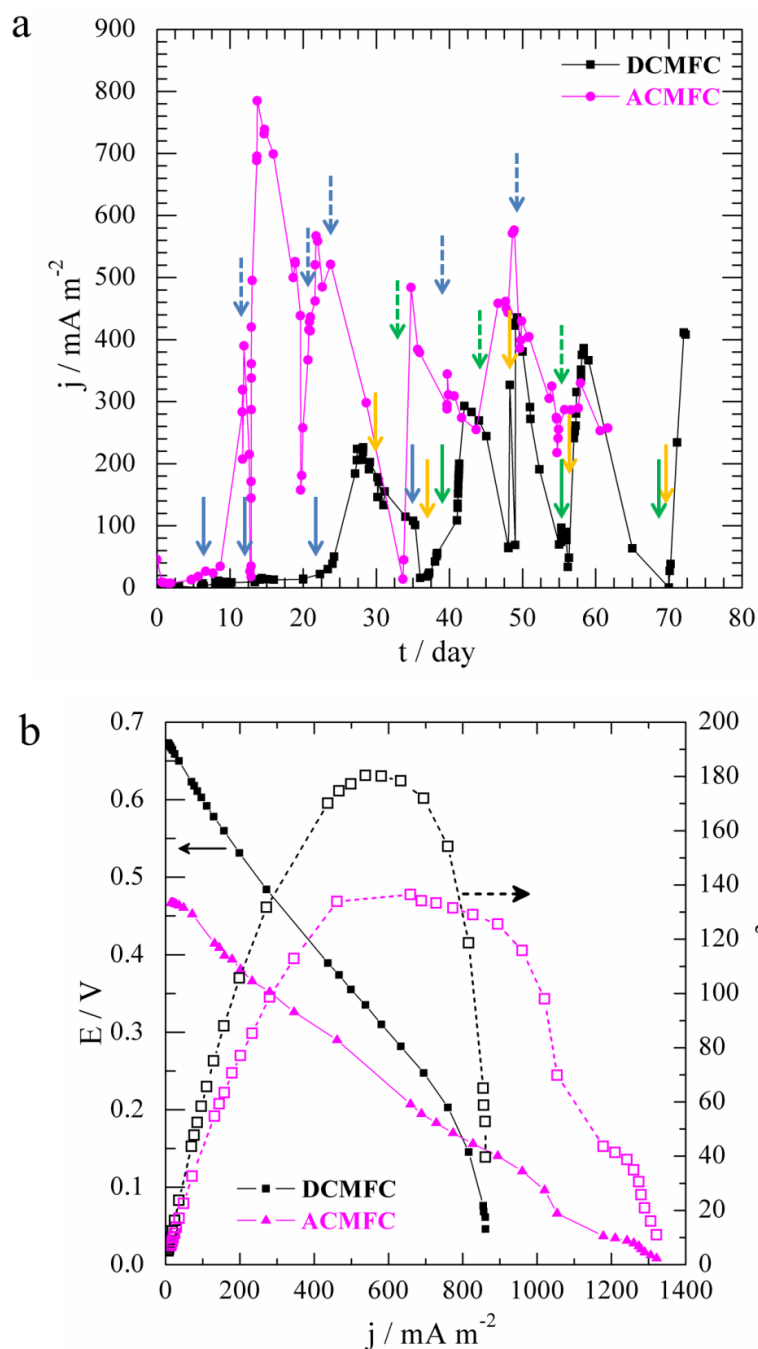


Figure 111 (a) Performance of SCMFC and DCMFC exhibited by current generation at a load resistance of 1 k Ω connected to the MFC (b) MFC polarization curve (iR -uncorrected). Nafion 115 PEM separated both side: anodic chamber contains garden compost leachate while the cathodic chamber (in DCMFC) contain ferricyanide solution. The addition of acetate is indicated by solid blue arrows for DCMFC and blue dash arrows for SCMFC. The refreshing anodic solution is noted by green solid (DCMFC) and dash (SCMFC) arrows. The yellow arrows show the refreshing of ferricyanide solution in DCMFC.

The current of both systems was maintained by feeding with acetate weekly. When current depression failed to be prevented, we changed the old anolyte with fresh leachate containing 20 mM of acetate. Then, the current was immediately recovered. The addition of fresh leachate, of course, also means to introduce not only fresh culture but also native nutrients that are important to support microbial life. Hence, we consider that the current drop may be caused by microbial death and/or depletion of nutrients. The decreasing of power generation also may be related to thicker biofilm formation on the anode surface which may increase proton transfer resistance and inhibit substrate diffusion [178].

Note that in previous compost garden MFCs [18,160,162], biofilm was grown under polarization. Herein we avoid the application of potential to develop electroactive biofilm on anodic surface, which would be an advantage for application in a real system.

Polarization curves for both systems, DCMFC and SCMFC, were recorded by varying resistance from 100.000 to 0 Ω . The data were picked when the current density reached maximum value i.e. at 49th day for the DCMFC and at 13th day for the SCMFC, as shown in **Figure 111a**. Both systems produce typical bell-shaped power density curves, shown in **Figure 111b**, which mean that rate-limiting did not come from bioanode [162]. Therefore, we can consider the rate-limiting originates from cathodic part which are clearly different one each other. The maximum power density obtained for DCMFC and SCMFC were 180 mW m^{-2} and 140 mW m^{-2} respectively.

Polarization curves exhibit typical characteristics for MFCs which can be divided into three regions [198]. Here we marked them as region I, II, and III. Region I, with high potential and low current, corresponds to activation losses. The voltage drop in this region is due to energy lost in initiating redox reaction and transferring electron from the microbe to the anode. The OCV was 672 mV and 467 mV for DCMFC and SCMFC respectively. The higher OCV value for DCMFC is due to a different age of the system as previously mentioned. An older system may have larger biofilm on the anodic surface. Region II expresses ohmic losses that may

emerged from electrolyte and cation exchange membrane resistance. Ohmic losses for DCMFC are higher since it involves electrolytes in both chambers. Region III corresponds to concentration or mass transfer losses. We also observed a higher voltage drop in this region for the DCMFC which means high electricity resistance. Therefore, the SCMFC system has better performance with lower resistance. The voltage decrease of the SCMFC was mainly due to ohmic losses, since its curve seems nearly linear [198,199].

In order to support the explanation, that our ACF@Pt developed material has an excellent performance as a homemade air-breathing cathode in a garden compost MFC, we recorded the LSV profile the ACF@Pt as air-breathing cathode in the SCMFC configuration to evaluate its performance in a real biofuel cell system. The LSV curve (**Figure 112**) shows the significant ORR performance of the air-breathing cathode due to the contribution of Pt. A very low overpotential was achieved with an OCP value of around +0.6 V vs. Ag/AgCl. Moreover, the reduction current generated at potential -0.1 V vs. Ag/AgCl was almost seven times higher than that of the non-Pt air-breathing cathode.

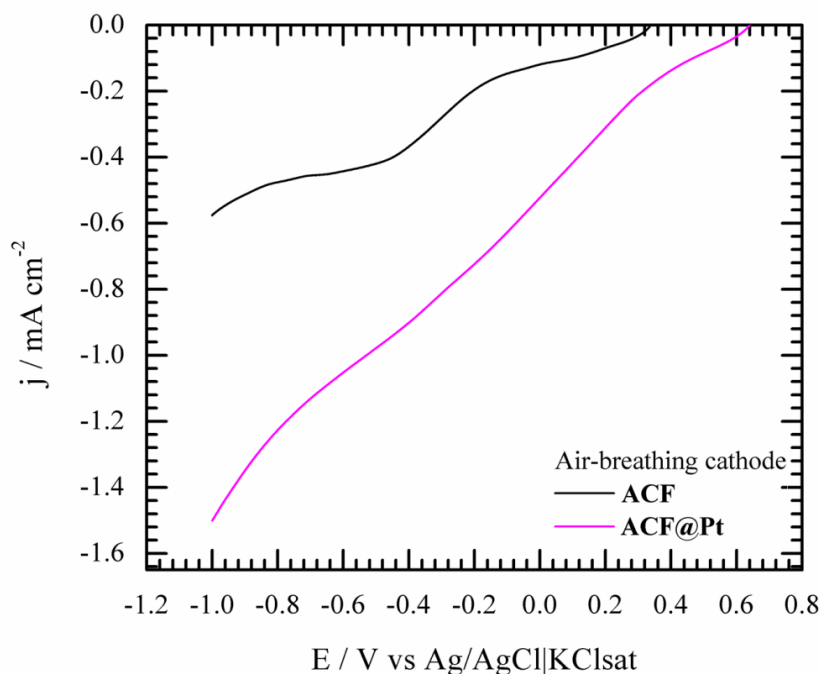


Figure 112 LSV measurement of air-breathing cathode (ACF@Pt) and ACF as blank control (scan rate of 5 mV s^{-1}) in SCMFC containing garden compost leachate.

3.5.2 Elaboration of Pt modified carbon felt (ACF@Pt) as anode in SCMFC

Having found that Pt modified CF (ACF@Pt) boosts the MFC performance in a double chamber system (Section 3.1). Then, we studied the elaboration of this anode in an SCMFC system with our developed home made air-breathing cathode. Whereby, both materials, for anode and air-breathing cathode, were principally identical. **Figure 113a** shows the performance of the SCMFC expressed in daily generated current density.

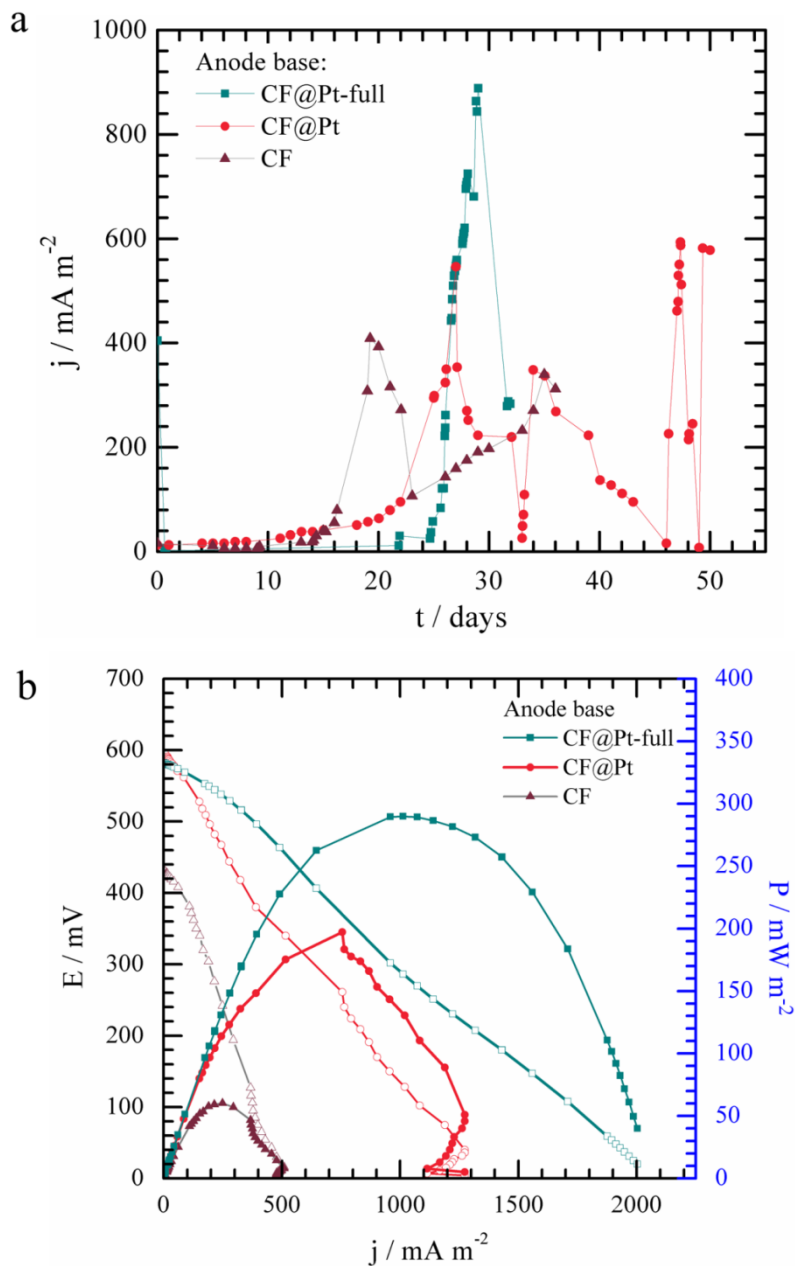


Figure 113 SCMFC performance with various anode expressed by daily current generated (a) and polarization and power density (b) curves.

The presence of Pt particles on the CF anode clearly enhanced the performance of the SCMFC. However, Pt NPs are slowing down the biofilm growth kinetics on the anode surface, as can be seen clearly from **Figure 113a**: without Pt on the anode surface, the current increases rapidly. When the anode containing Pt particles was applied, the increase of the produced current are getting slower. It can be inferred that the enhanced MFC performance clearly appeared after biofilm formation on the anode surface. Therefore, it implies that this improvement is due to the synergic effect between the biofilm and Pt. We observe at the beginning time, the produced current are very low either with or without Pt on the CF anode.

Finally, we compared the performances of the SCMFC and the DCMFC as shown in **Figure 114**, which implies that Pt-based anode in SCMFC generally results in a higher current density than DCMFC. On the other hand, OCV and maximal power density are not so far. The comparison of the performance, (OCV and power density) between the SCMFC and the DCMFC are listed in **Table 22**.

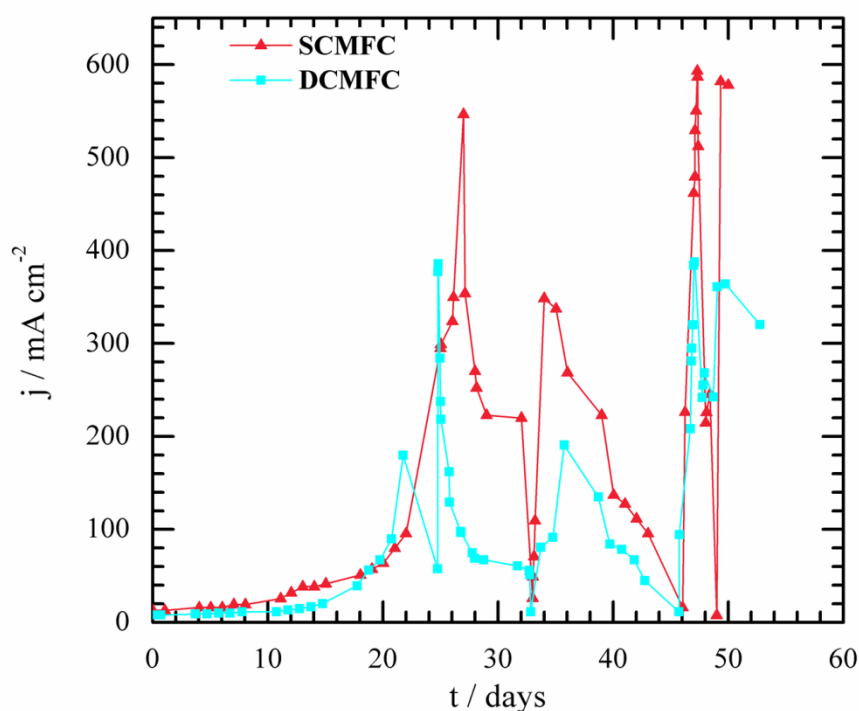


Figure 114 Current generation of DCMFC and SCMFC system with platinum based bioanode.

Table 22 Performances comparison of the MFC system

MFC system	OCV	Pmax (mW m ⁻²)
SCMFC	596.9	197.2
DCMFC	686	191.6

3.5.3 SCMFC for the study of the electron transfer mechanism

According to our result, an air-breathing cathode can be considered more fixed than aqueous phase cathode system, since no need of reloading and/or refreshing the catholyte solution during its operation. Thereafter, we used our SCMFC with the air-breathing cathode system to evaluate the mechanism of electron transfer from cell to anode. For this purposes we took a running SCMFC (**Figure 115a**) with ACF@Pt air-breathing cathode, CF@Biofilm anode, in garden compost leachate as anodic solution. Herein, we firstly assumed that the generated voltage correspond to the electrons, which were resulted in from both attached biofilm on the anode and planktonic bacteria in the anodic solution. The electron transfer from bacterial-to-anode can be directly as physical contact of biofilm to anode and/or in a mediated way for the planktonic bacteria. Our hypothesis, we can define the origin of electrons, i.e. from biofilm, planktonic bacteria, and/or mixture, by comparing the SCMFC voltage before and after separating the planktonic bacteria to remove or reduce its quantity in the anodic solution as shown in **Figure 115b**.

The plot of the SCMFC's voltages before and after planktonic bacteria separation is shown in **Figure 116**. Herein, the plot below and after 0th day represent the SCMFC's voltages before and after separation respectively. We noted the voltages before separation are averagely around 25 mV. After separation, the volume of solution was clearly decreased and only 1/3 of anode was contact with the solution. Surprisingly, we found the SCMFC's voltages are equal to those before separation and achieved in only 7 hours after the SCMFC started. Logically, if the planktonic bacteria give a major contribution toward the electron transfer process, so the voltage will decrease as they drawn from the anodic

solution. From this result, we can consider that the attached biofilm on anode is responsible in electron generation through a dominantly direct transfer. Although only 1/3 of anode surface in contact with the solution, the biofilm was covering the total anode surface and capillary effect could draw the solution containing the acetate substrate upward the anode, hence keep the voltage value.



Figure 115 SCMFC operation with anodic compartment contain garden compost leachate (a) before and (b) after separation

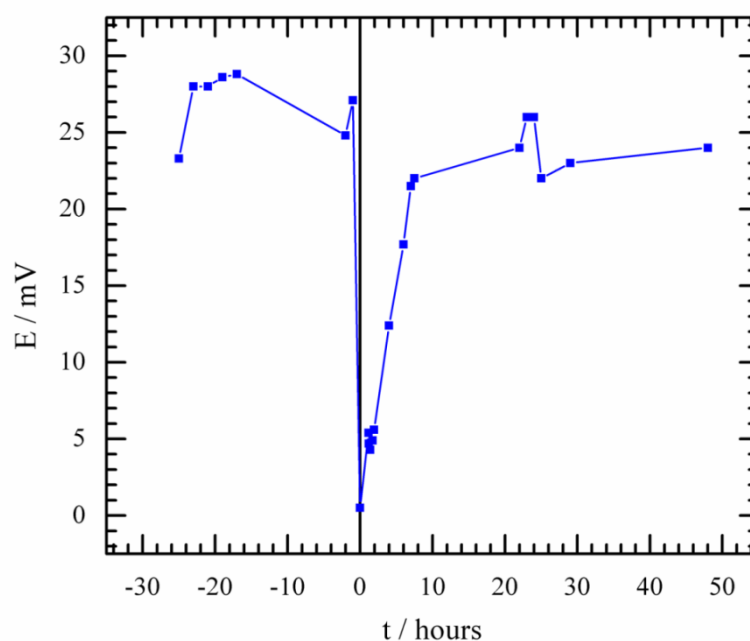


Figure 116 The evolution of voltage before (minus x axis) and after separation

The separation of planktonic bacteria from the anodic solution was conducted by centrifugation as a common method for bacterial separation. First, we drawn all anodic solution in the SCMFC but kept the bioanode inside. Carefull handling is important to avoid the detachment of biofilm on the anode into the solution. The anodic solution contains bacteria and remaining compost fragments, which give the optical density at 600 nm (OD_{600nm}) 1.4, as shown in **Figure 117**, 1st bar. Centrifugation at 4400 rpm for 10 minutes removed 36 % of the solid part of compost fragments in the leachate (**Figure 117**, 2nd bar). We took this condition as 0 hour of new SCMFC operation.

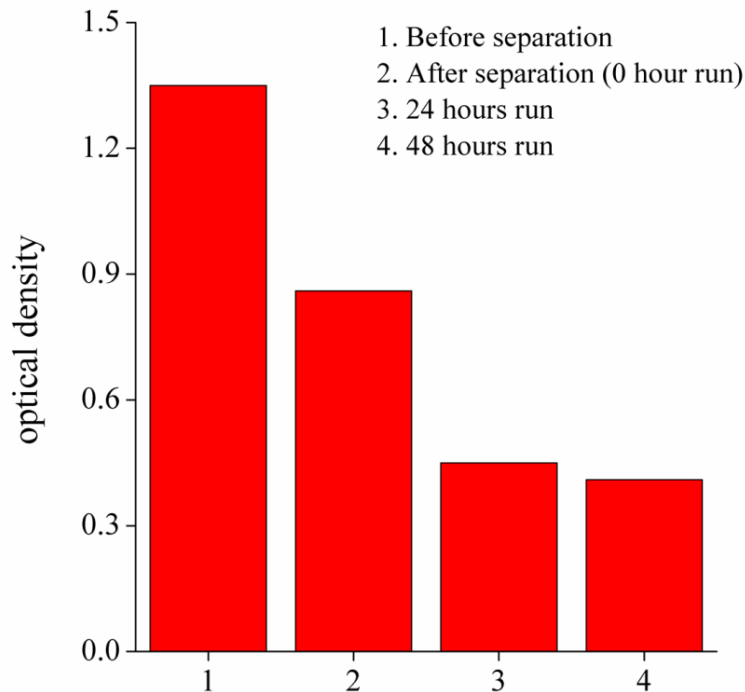


Figure 117 The optical density of compost garden leachate at 600 nm determined for different cases.

Although we intended to separate all planktonic bacteria, some were still present in the solution. This indicated by the decreasing of its OD_{600nm} by almost 50 % (**Figure 117**, 3rd bar) after 24 hours SCMFC operation. We consider this half of the initial bacterial was grown as new biofilm on the anode, as observed visibly at the bottom of the anode (**Figure 118b**), over 24 hours SCMFC operation. This fresh grown biofilm may also contribute to the electron generation and hence voltage improvement. After 48 hours (**Figure 118c**), the solution absorbance

remained constant and no more biofilm growth was noticeable. We may suppose that steady state conditions were reached.

In addition, we also monitored the consumption of acetate during this SCMFC operation (**Table 23**). At the beginning period, the consumption of acetate was only 3.5 %, which probably due to the adaptation. At the 2nd day, the acetate consumption rises up to 21.65 %. The efficiency of electron production was only 7.98 %, as roughly calculated using Faraday's Law. (The calculation is presented in **Annex 1**)

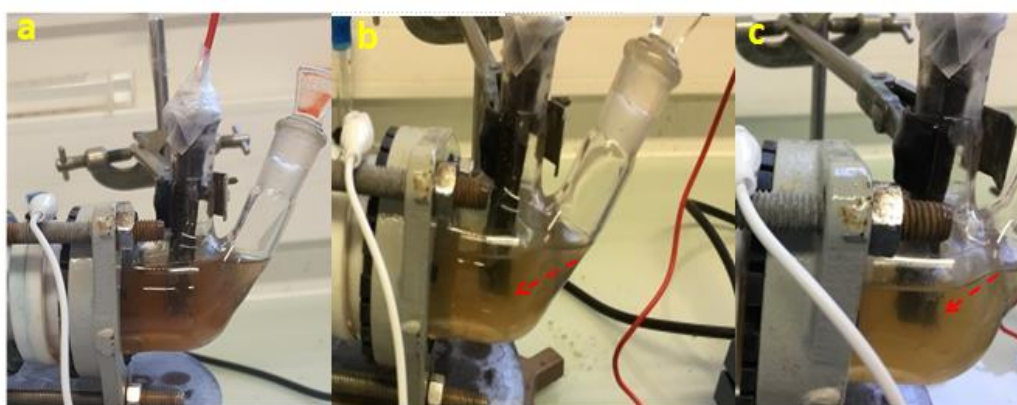


Figure 118 Anodic compartment at 0 h (a), 24 h (b) and 48 h (c)

Table 23 The consumption of acetate

Time (days)	Acetate / mg L ⁻¹	Acetate / mM
0	2079	25.4
1	2010.5	24.5
2	1562.0	19.0

As conclusion to **Section 3.5**, the integration of the developed ACF@Pt material, as a homemade air-breathing cathode in an SCMFC system has the ability to generate a comparable power as its equal DCMFC system. The SCMFC was also can be improved as the application of the ACF@Pt material in the anodic part. Herein, the SCMFC with air-breathing cathode has been shown to be useful in studying the electron transfer mechanism.

3.6 Manganese oxide modified carbon felt (ACF@MnOx): material development and characterization

In the previous part, we have successfully constructed an air-breathing cathode based on Pt modified carbon felt, ACF@Pt, and applied it to the garden compost SCMFC system. Indeed, Pt is an obvious and undoubtedly effective catalyst for ORR in the air-breathing cathode of fuel cell system which considered still realistic at laboratory scale. However, the utilization of Pt catalyst in large scale MFC application contributes to high operation costs. Therefore, the development of a low cost non-Pt catalyst for air-cathode systems is an essential step in the MFC scale up route.

Manganese oxides are considered as a cost-effective ORR catalyst in an air-breathing electrode as a substitute for Pt [124]. Many studies on the catalytic properties of manganese oxide in the air-breathing cathodes have been reported [200].

3.6.1 Electrodeposition of manganese oxide (MnOx)

Preparation of MnOx using a conventional precipitation method often results in an uncontrolled morphological structure and size [124]. Therefore, we preferred the electrodeposition method to prepare the MnOx and to deposit it directly onto the ACF support.

MnOx was prepared from manganese chloride solution in the presence of sodium nitrate solution as electrolyte. Manganese can exist in various oxidation states (II, III, and IV). Therefore, various oxides such as MnO, MnO₂, Mn₂O₃ and Mn₃O₄ may be formed [201]. The overall deposition of MnO₂ is given by **Eq. 105** [202].



In order to obtain its precise potential oxidation, it is important to conduct preliminary cyclic voltammetry toward the ACF electrode in the precursor solution. **Figure 119** shows the CV profile after applying cycled-potential scan at range -1.0 and +1.0 V vs. Ag/AgCl at scan rate 5 mV s⁻¹ both under nitrogen and oxygen atmosphere. It also shows the voltammogram in electrolyte solution only as control. We observed a strong peak at potential +1.25 V vs. Ag/AgCl under

both atmospheres, corresponding to oxidation of Mn^{2+} to Mn^{4+} . In the reverse scan direction, strong reduction peak was also observed which may correspond to the reduction of the Mn^{4+} . These two peaks indicate that the Mn redox reaction in the region of 0-1.5 V vs. Ag/AgCl is reversible. The lower reduction peak at potential 0 V vs. Ag/AgCl corresponds to further reduction of Mn(II) to Mn(0). Meanwhile, the strong peak at potential -0.4 V vs. Ag/AgCl only appears on the CV under oxygenated atmosphere, which means that it corresponds to reduction oxygen.

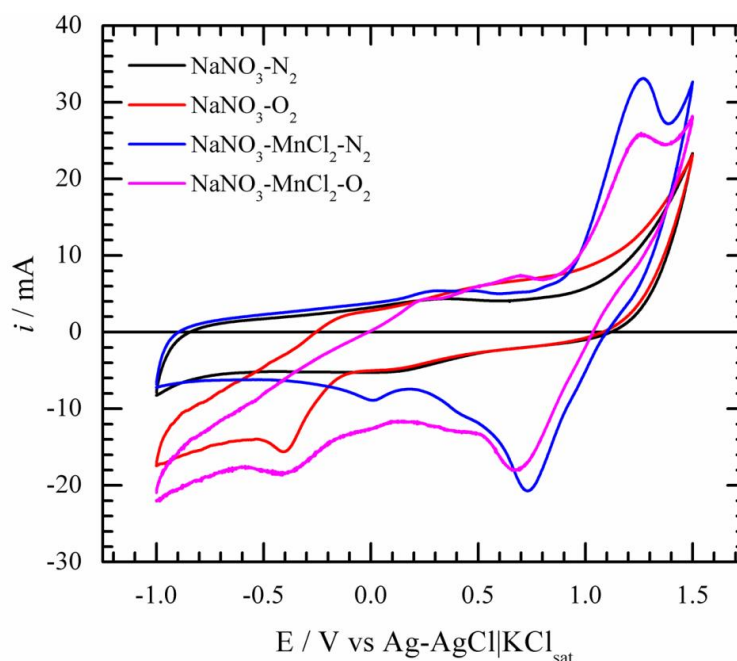


Figure 119 Voltammograms of ACF electrode at scan rate 5 mV s^{-1} in manganese precursor (2.5 mM MnCl_2 in 200 mM NaNO_3) and only electrolyte (200 mM NaNO_3) solution under nitrogen and oxygen atmosphere.

3.6.1.1 Electrodeposition using CV method

Knowing the potential oxidation from the above preliminary CV, then we limited the potential region to 0-1.6 V vs Ag/AgCl as the working potential for electrodeposition using the CV method. Electrodeposition was conducted in 25 mM MnCl_2 solution in 200 mM NaNO_3 at 50 mV s^{-1} for 50 cycles as the starting point. In order to obtain the precise optimal synthesis conditions for the CV method, we designed four experimental sets. The first two sets involved CV electrodeposition at various potential ranges. The potential range in the first set was 0 – 1.0 V vs. Ag/AgCl, 0 – 1.1 V vs. Ag/AgCl, 0 – 1.2 V vs. Ag/AgCl, 0 – 1.3 V vs. Ag/AgCl, 0 – 1.4 V vs. Ag/AgCl, 0 - 1.5 V vs. Ag/AgCl, and 0 – 1.6 V

vs. Ag/AgCl. Since the potential range 0 – 1.4 V vs. Ag/AgCl resulted in ORR curve with the highest current density, we used another potential range for the second experimental set by put 1.4 V vs Ag/AgCl as the upper limit (0.2 – 1.4 V vs. Ag/AgCl, 0.4 – 1.4 V vs. Ag/AgCl, 0.6 – 1.4 V vs. Ag/AgCl, 0.8 – 1.4 V vs. Ag/AgCl, 1.0 – 1.4 V vs. Ag/AgCl, and 1.2 – 1.4 V vs. Ag/AgCl). All resulted electrodes from these various potential ranges were characterized by LSV in PBS solution pH 7 under oxygen atmosphere to evaluate their performance toward ORR. **Figure 120** shows a comparison the ORR curve of the electrode sets as dependence toward potential range cyclization.

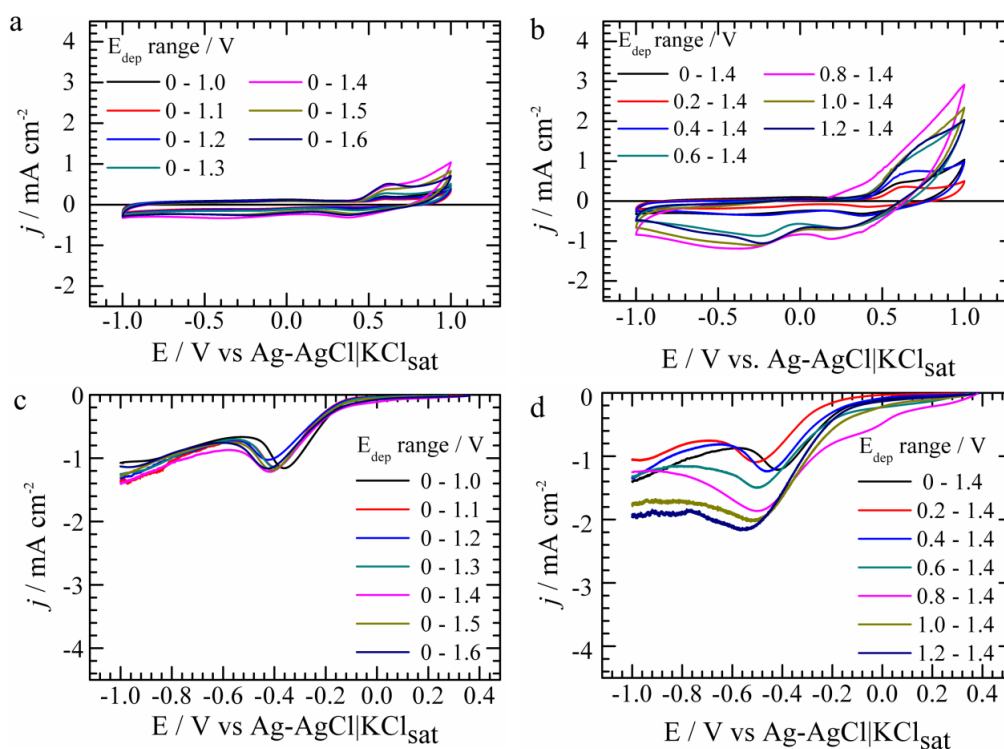


Figure 120 (a,c) Voltammogram at scan rate 10 mV s^{-1} under nitrogen atmosphere and (b,d) LSV curve at scan rate 5 mV s^{-1} under oxygen atmosphere of the ACF@MnOx electrodes resulted by CV electrodeposition at various potential ranges (two experimental sets).

CV electrodeposition with the first experimental set resulted in electrodes with very low ORR current (**Figure 120a,b**). Indeed, as shown in **Figure 119**, the CV in this region could drive the reversible reaction, which leads to poor deposition. Narrowing the potential region by fixing the upper limit at 1.4 V vs. Ag/AgCl and shifting the lower limit progressively from 0 to 1.2 V vs. Ag/AgCl improved electrodeposition (**Figure 120c,d**). The electrodeposition at potential range 0.8 –

1.4 V vs. Ag/AgCl showed the best performance over the entire potential range optimization experiment. Applying CV over this potential range enables us to route oxidation as the predominant reaction. However, a small part of reduction might be needed to reform the structure and give better ORR performance.

The next experiment involved the CV electrodeposition at various numbers of cycles i.e. 30, 50, 70 and 100 cycles. The number of cycles may correlate to the mass loading and the features of electrodeposited MnOx distribution over the substrate. Lower cycles may result in a less coverage of electrodeposited MnOx, while higher cycles may cause structures overlapping each other, leading to decrease in catalytic performance. In this experiment, CV over 50 cycles gave the best ORR performance (**Figure 121a,b**).

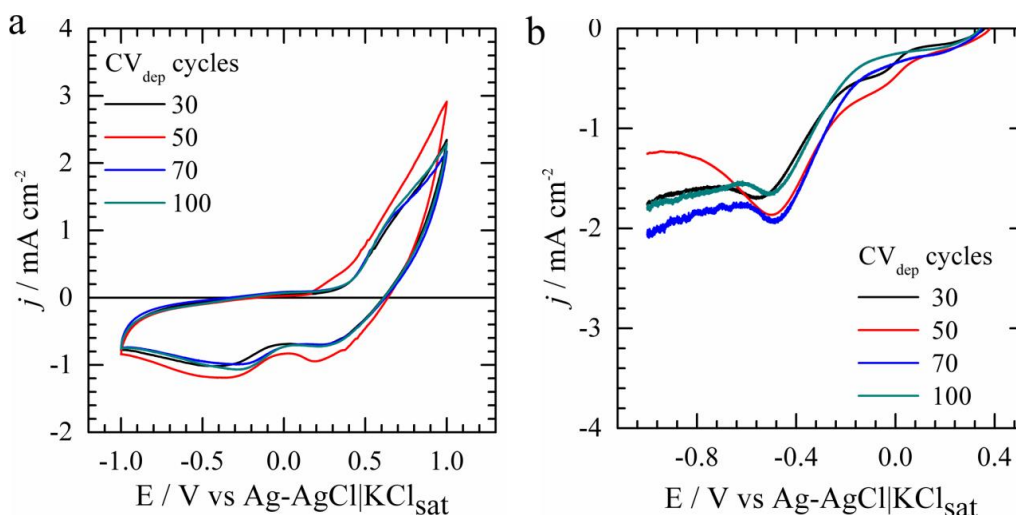


Figure 121 (a) Voltammogram under nitrogen atmosphere at scan rate 10 mV s^{-1} and (b) LSV curve under oxygen atmosphere at scan rate 5 mV s^{-1} , in 50 mM PBS solution of the developed ACF@MnOx electrodes resulted through CV electrodeposition at potential range 0.8 – 1.4 V vs. Ag/AgCl at various numbers of cycles.

We also studied the scan rate dependence in CV electrodeposition toward the ORR catalytic performance. The scan rate correlates to the time of material interaction toward potential exposure. A lower scan rate leads to a careful interaction, which enables a thorough reaction on the electrode surface. Owing to this interaction, the different morphological structures can be developed. Herein, we found 20 mV s^{-1} as the best scan rate for electrodepositing MnOx onto the ACF surface (**Figure 122a,b**).

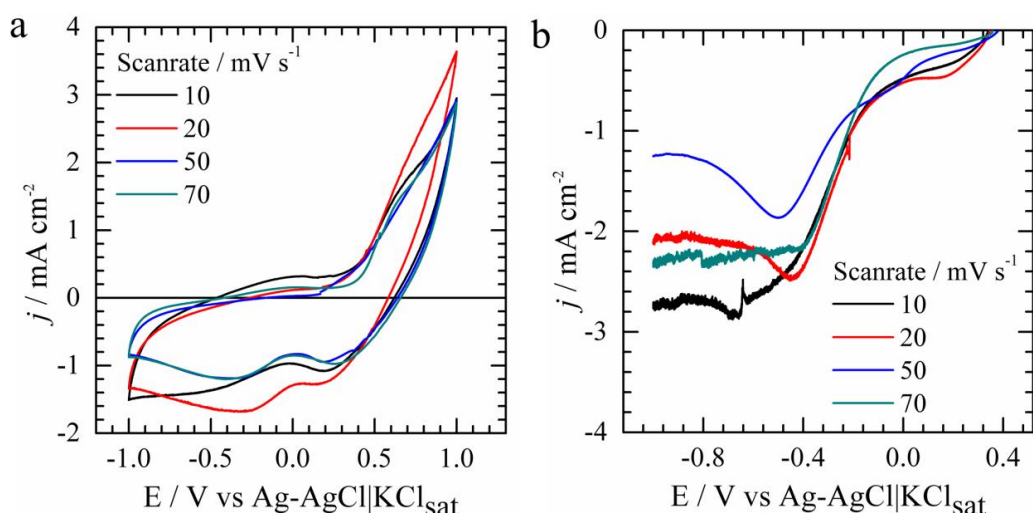


Figure 122 (a) Voltammogram under nitrogen atmosphere at scan rate 10 mV s^{-1} and (b) LSV curve under oxygen atmosphere at scan rate 5 mV s^{-1} , in 50 mM PBS solution of the developed ACF@MnOx electrodes resulted through CV electrodeposition at potential range $0.8 - 1.4 \text{ V}$ vs. Ag/AgCl at various scan rates.

3.6.1.2 Electrodeposition using the CA method

We also conducted electrodeposition using the CA method. For this, we designed three experimental sets to obtain the precise optimal synthesis conditions: electrodeposition potential, time, and concentration dependence.

a. Effect of electrodeposition potential

In order to study potential dependence, we set the experiment of CA electrodeposition (in 25 mM MnCl_2 solution in 200 mM NaNO_3 as electrolyte) for one hour at various fixed potentials i.e. 1.1 , 1.2 , 1.25 , 1.3 , and 1.4 V vs. Ag/AgCl. The applied potential is a given energy to make the reaction thermodynamically favorable. The ORR LSV curves corresponding to electrodeposition at different potentials are shown in **Figure 123**. Electrodeposition at low potential ($< 1.25 \text{ V}$ vs. Ag/AgCl) resulted in an electrode with low ORR performance. While the electrodeposition at potentials 1.25 , 1.3 , and 1.4 V vs. Ag/AgCl resulted in better ORR performances.

b. Effect of electrodeposition time

We also sought the time dependence by conduct the CA electrodeposition at various time periods (0.5 , 1 , 2 , 4 and 6 hours). The optimum time reaction

generates the electrode with the best ORR performance. **Figure 124** shows the ORR LSV curve of the experimental set corresponding to various time periods. Herein, better ORR performance was obtained for 4 hours of electrodeposition.

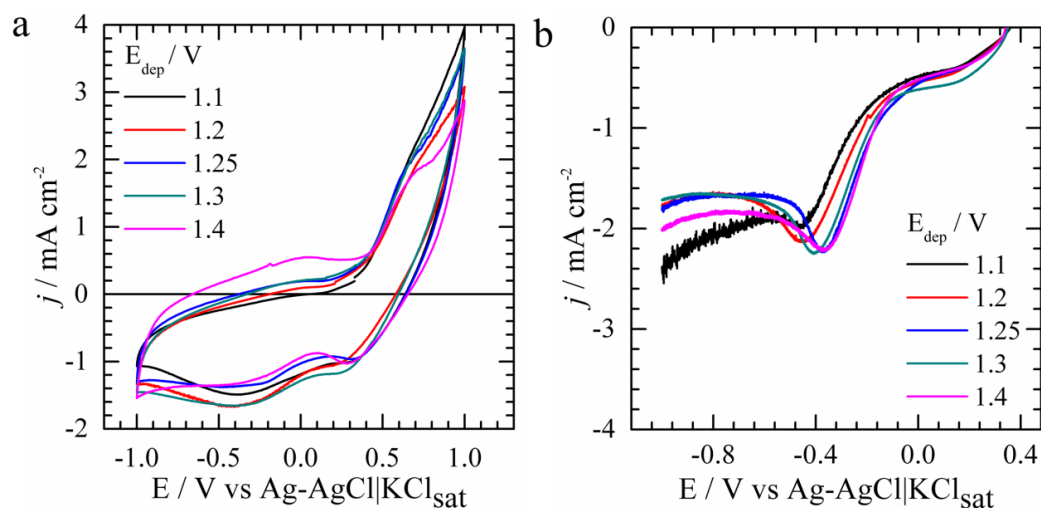


Figure 123 (a) Voltammogram under nitrogen atmosphere at scan rate 10 mV s^{-1} and (b) LSV curve under oxygen atmosphere at scan rate 5 mV s^{-1} , in 50 mM PBS solution of the developed ACF@MnOx electrodes resulted through one hour CA electrodeposition at various electrodeposition potentials.

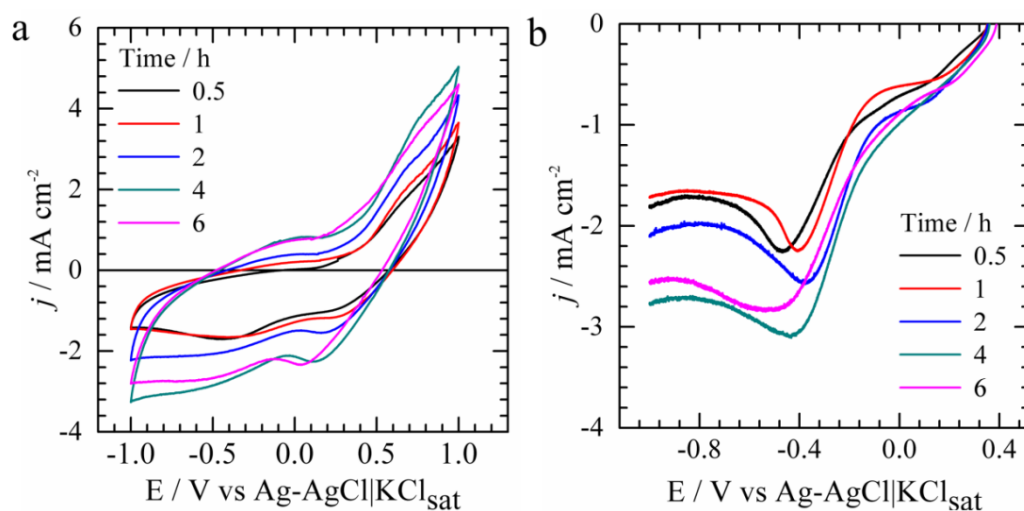


Figure 124 (a) Voltammogram under nitrogen atmosphere at scan rate 10 mV s^{-1} and (b) LSV curve under oxygen atmosphere at scan rate 5 mV s^{-1} , in 50 mM PBS solution of the developed ACF@MnOx electrodes resulted through CA electrodeposition at 1.3 V vs. Ag/AgCl at various time periods of electrodeposition.

c. Effect of precursor concentration

We observed the linear correlation between the precursor concentration and the mass loading of the electrodeposited MnOx (**Figure 127f**). Moreover, the maximum current density at higher overpotential was also linear with the loading mass at range 10 – 180 mM. As the concentration increased, we observed an increase of the current density of the ORR LSV curve, as shown in **Figure 125**. Herein, we took three types of ORR LSV curves of the resulted material from 25 mM, 90 mM and 180 mM for further experimentation.

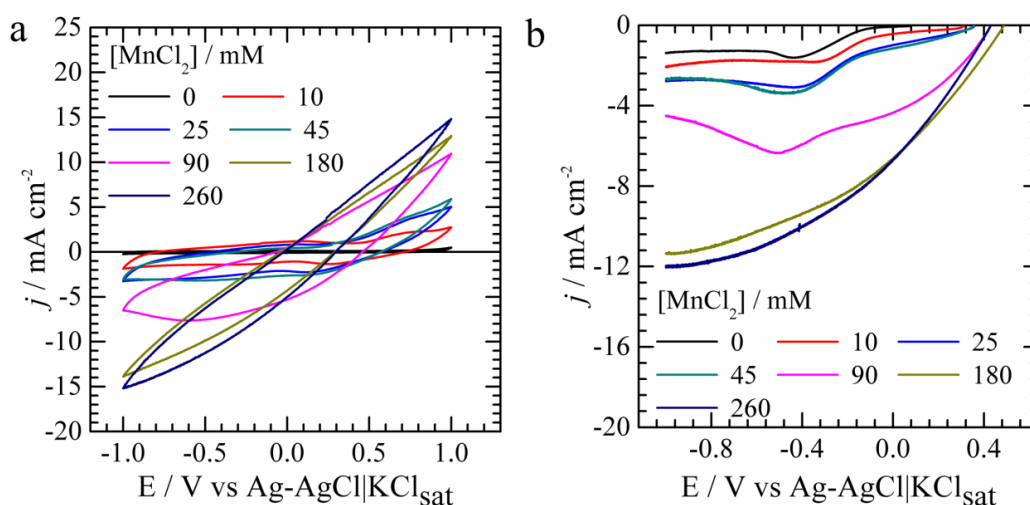


Figure 125 (a) Voltammogram under nitrogen atmosphere at scan rate 10 mV s⁻¹ and (b) LSV curve under oxygen atmosphere at scan rate 5 mV s⁻¹, in 50 mM PBS solution of the developed ACF@MnOx electrodes resulted through CA electrodeposition at 1.3 V vs. Ag/AgCl for 4 hours at various precursor concentrations.

3.6.2 MnOx mass loading

3.6.2.1 MnOx mass loading as resulted by CV electrodeposition

High MnOx mass loading leads to high generated energy density [203]. **Figure 126a** shows the correlation between applied energy of electrodeposition and MnOx mass loading. The black and red bar corresponds to the ACF@MnOx as resulted by electrodeposition at a broad (experimental set I) and a narrow (experimental set II) potential range respectively. The electrodeposition at broad range potential results in very low MnOx mass loading. As previously explained, the electrodeposition at this broad range of potential was poor because it suffers the reversible reaction. The MnOx mass loading increased progressively as the

potential shifted to higher values and its range become narrower (red bar). This implies that proper selection of potential range is essential in CV electrodeposition. Herein, we also observed that the higher MnOx mass loading resulted in a higher ORR current. The higher number of CV cycles and the slower scan rate during electrodeposition also slightly increased the mass loading as shown in **Figure 126b**. Indeed, a higher number of cycles led to more reaction. Generally, we assume that the generated energy density correlates with the MnOx mass loading.

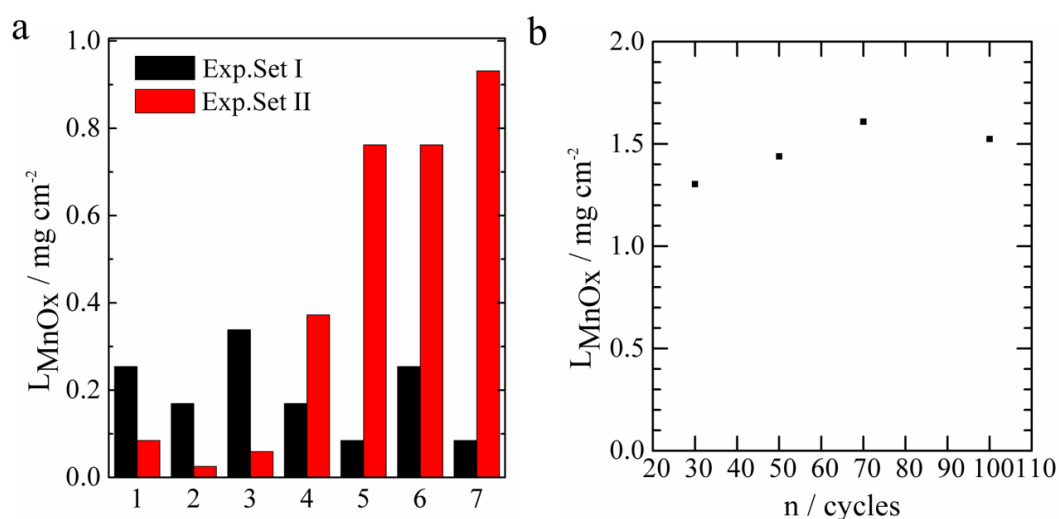


Figure 126 Correlation of MnOx mass loading with (a) potential range, and (b) number of cycles.

3.6.2.2 MnOx mass loading as resulted from CA electrodeposition

Electrodeposition using the CA method enables us to calculate the Faradic mass apart from its theoretical and manually weighed. The theoretical and the Faradic mass respectively were calculated through **Eqs. 106** and **107**, referring to the molecular weight of MnO_2 .

$$m_{\text{MnOx}} = C \cdot V \cdot M_{\text{MnO}_2} \quad (\text{Eq. 106})$$

Where,

m_{MnOx} : MnOx mass loading (g)

C : concentration of precursor (M)

V : volume of solution (L)

M_{MnO_2} : molecular weight of MnO_2 (g mol^{-1})

$$m_{\text{MnOx}} = \frac{Q}{F} \times \frac{M_{\text{MnO}_2}}{z} \quad (\text{Eq. 107})$$

Where,

m_{MnOx} : MnOx mass loading

Q : total electric charge (C)

F : Faraday's constant (96,485 C mol⁻¹)

M_{MnO_2} : molecular weight of MnO₂

z : number of electrons transferred per ion (2)

Figure 127a shows the CA curve at various electrodeposition potentials for one hour of electrodeposition. The higher the deposition potential is, the higher the Faradic mass. **Figure 127b** shows the correlation between MnOx mass loading and deposition potential. The Faradic mass (blue line) increased slightly as the potential went up.

Herein, the calculated Faradaic mass was found to be about four times lower than the calculated theoretical mass (black line). This implies poor MnOx deposition because more manganese species still remained in the solution. The manually weighed mass of MnOx (red line) was found higher than the Faradic mass. This may indicate the formation of different oxides such as MnO, MnO₃, Mn₂O₃, Mn₃O₄ or any other manganese oxide. Increasing the electrodeposition time clearly improved the MnOx mass loading on the ACF, as shown in **Figure 127d**. Indeed, prolonging the reaction time enables us to bring the remaining manganese species in the solution onto the electrode surface as manganese oxide. Therefore, both Faradic and manually weighed get closer to the theoretical value. We assume the optimum electrodeposition time to be four hours. Electrodeposition for a longer time led to a decrease in ORR performance (**Figure 124b**).

The dependence MnOx mass loading toward electrodeposition time was also confirmed with the developed morphological structure revealed under SEM, which will be discussed latter. **Figure 127e** shows the CA electrodeposition curve at various precursor concentrations for 4 hours. Variation of the concentration precursor from 10 to 90 mM reveals a typical CA curve with Q increasing

progressively. However, electrodeposition in more concentrated precursor solutions (180 and 260 mM) resulted in different CA curve shapes, building a very large Q. This may imply a large oxidation and also evolution of chlorine gas that originating from the precursor solution, manganese chloride. **Figure 127f** shows a linear correlation between precursor concentration and MnOx mass loading.

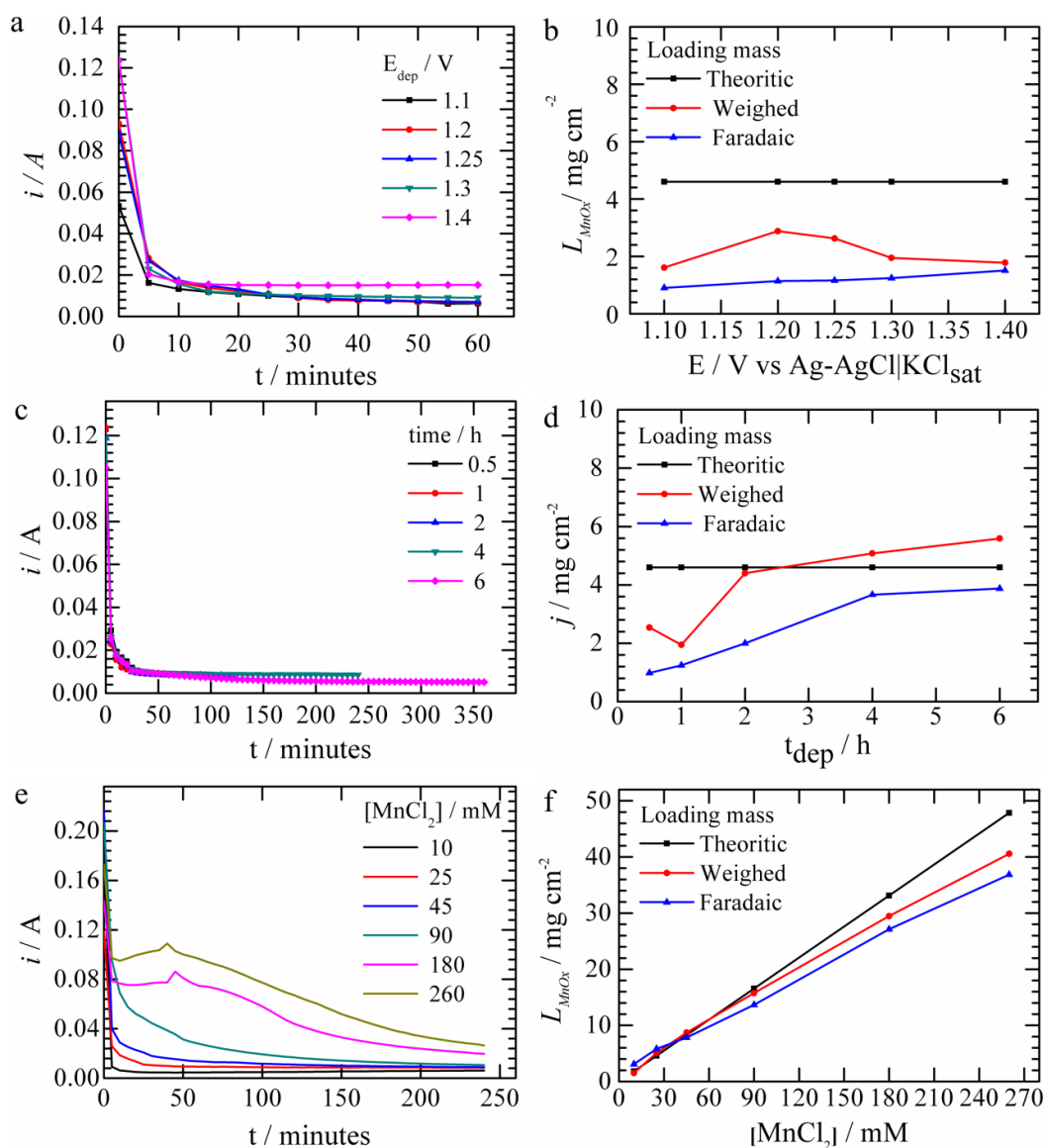


Figure 127 Behavior of developed CA curve and the correlation of MnOx mass loading (theoretical, experimentally weighed, and Faradic) of the ACF@MnOx material as resulted at various (a,b) potentials (c,d) reaction time and (e,f) precursor concentration dependence.

3.6.3 Physico-chemical characterization

3.6.3.1 Scanning electron microscopy/energy dispersive X-ray spectroscopy (SEM/EDX)

The EDX spectra of pure ACF and modified ACF are shown in **Figure 128a,b**. The spectrum of ACF, as unmodified material, only shows C and O. The modification of ACF through electrodeposition in manganese solution resulted in the addition of Mn and O (**Figure 128c,d**). This qualitatively indicates a brief successful of electrodeposition process. Many traces of Na, N, and Cl were also found, which originated from the electrolyte solution.

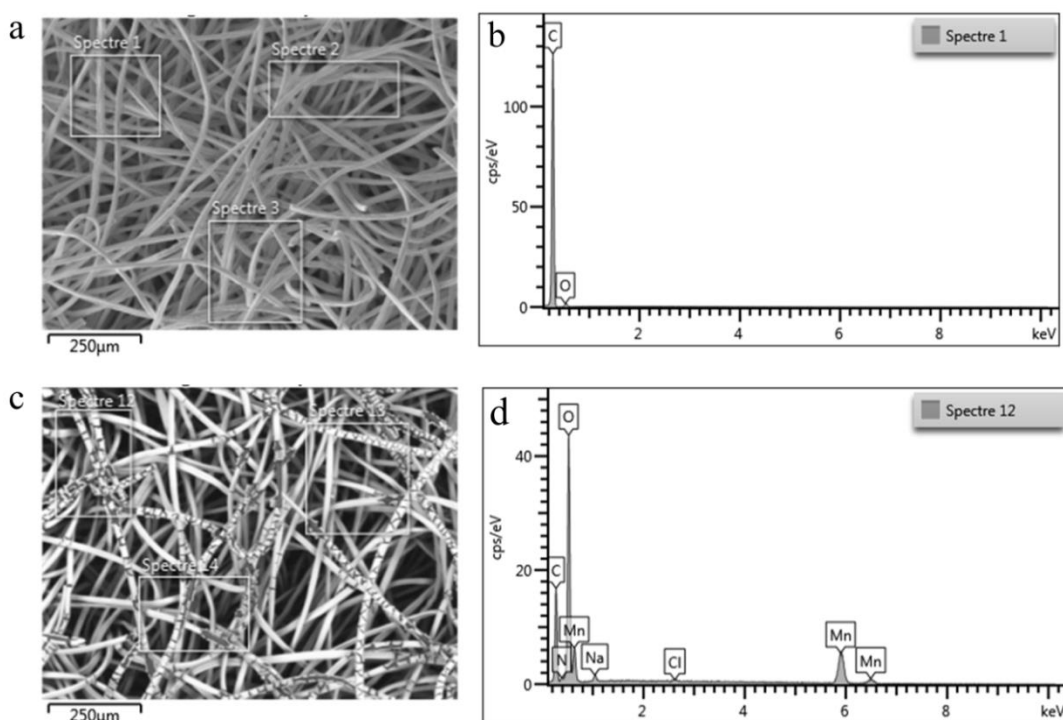


Figure 128 EDX spectrum of (a) ACF and (b) ACF@MnO_x resulted after one hour of CA electrodeposition at 1.3 V vs. Ag/AgCl from 25 mM of precursor

Herein, we recorded EDX for three representative samples prepared at different electrodeposition potentials i.e. 1.25, 1.3 and 1.4 V vs. Ag/AgCl. The detailed compositions of these three samples are summarized in **Figure 129** and **Table 24**.

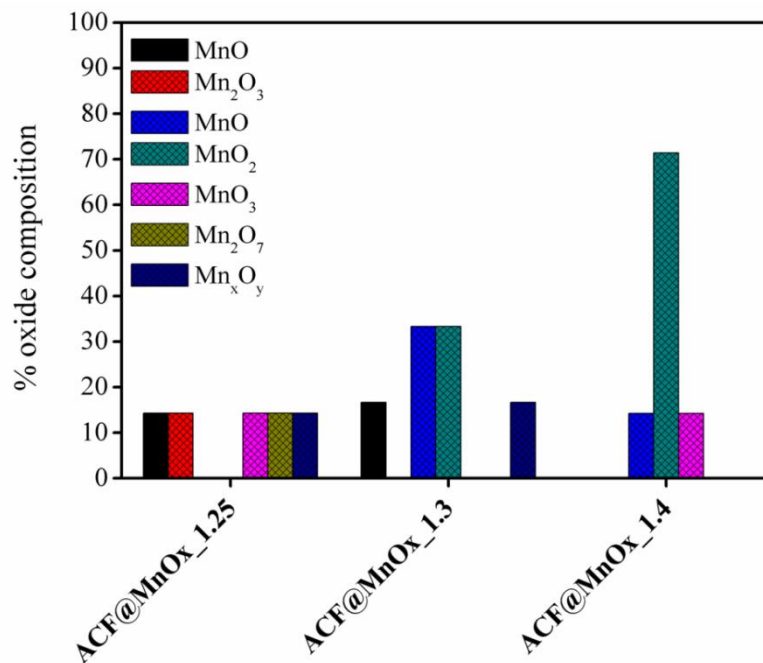


Figure 129 Predicted manganese oxide composition of the resulted ACF@MnOx at various electrodeposition potentials as calculated based on EDX spectra.

Table 24 Prediction of developed manganese oxide (MnOx) based on chemical composition as roughly calculated from EDX spectra.

Oxide, oxidation number	Ref.		ACF@MnOx_1.25		ACF@MnOx_1.3		ACF@MnOx_1.4	
	% Mn	% O	% Mn	% O	% Mn	% O	% Mn	% O
MnO, Mn(II)	77.45	22.55	76.20	23.80	76.64	23.36	n.a	n.a
Mn ₂ O ₃ , Mn(III)	69.60	30.40	69.95	30.05	n.a	n.a	n.a	n.a
Mn ₂ O ₇ , Mn(VII)	49.52	50.48	51.50	48.50	n.a	n.a	n.a	n.a
Mn ₃ O ₄ , Mn(III)	72.03	27.97	n.a	n.a	71.14	28.86	71.90	28.10
MnO ₂ , Mn(IV)	63.19	36.81	n.a	n.a	65.74	34.26	63.82	36.18
MnO ₃ , Mn(VI)	53.37	46.63	54.89	45.11	n.a	n.a	56.45	43.55

We screened 5 to 6 EDX spectra of each samples to analyze their chemical composition. Four of the seven EDX spectra of 1.25 V vs. Ag/AgCl electrodeposition revealed varied chemical compositions, each closes to that of standard manganese oxide, respectively comprising MnO, Mn₂O₃, Mn₂O₇, and MnO₃. Meanwhile, the electrodeposition at 1.3 V vs. Ag/AgCl resulted in manganese oxide, whose chemical composition can be associated with MnO, Mn₃O₄, and MnO₂. Herein, we took six spectra, where two spectra represented Mn₃O₄, two others were close to MnO₂, one correlated to MnO, and the remaining showed no fit to any manganese oxide. Hence, we can hypothesize a rough composition of the resulted manganese oxide as 33 % Mn₃O₄, 33 % MnO₂, and 16.67 % MnO and 16.67 % an unknown manganese oxide. Meanwhile, the electrodeposition at 1.4 V vs. Ag/AgCl resulted in Mn₃O₄, MnO₂, and MnO₃. The five screened spectra of this sample were correlated to the composition of MnO₂, while the two others were fitted to Mn₃O₄ and MnO₃. Thus, electrodeposition at this potential resulted in higher MnO₂ content, roughly predicted at 71 %.

Let us now consider the Mn oxidation states of MnO and MnO₂, which are 2 and 4 respectively. The MnO was resulted at lower electrodeposition potential and decreased progressively as the potential increased (**Table 24**). In contrast, the MnO₂ was mostly produced at the higher electrodeposition potential. This implies that a high potential provides enough energy to oxidize Mn(II) into Mn(IV).

3.6.3.2 Crystallinity properties of the ACF@MnOx

Figure 130a shows the XRD spectra of three representative ACF@MnOx samples corresponding to various electrodeposition potentials (1.25, 1.3, and 1.4 V vs. Ag/AgCl). These indicate that the developed material was semi-crystalline tending to amorphous. The broad peak at 25° corresponds to a graphite (002) plane of carbon and the sharp peak at 43° corresponds to diamond (111) [93]. The peaks that emerged after ACF modification generally show its low intensity, which indicates a low crystallinity. The only strong peak, at 30°, reveals α -MnO₂ (310) [204,205], which appears from the ACF@MnOx_E1.4. The weaker peak at this position also found progressively on both the ACF@MnOx_E1.3 and the ACF@MnOx_E1.25, which means less resulted α -

MnO₂. These results seem to conform to the previous EDX's manganese oxide composition, which predicted that MnO₂ mostly resulted from electrodeposition at 1.3 and 1.4 V vs. Ag/AgCl. The other small-identified peaks of the ACF@MnOx_E1.4 located at 32° and 40° correspond to MnO (111) and MnO (200). The additional peak of the ACF@MnOx_E1.3 located at 37° may correspond to Mn₃O₄ (211). More small peaks are emerged in the ACF@MnOx_E1.25, positioned at 33° and 42° are belonging to MnO, whereas the peaks at 57.5°, 58.5°, and 65.5° may correspond to a mixture of Mn₂O₃ and Mn₃O₄[205]. **Figure 130b** shows the XRD spectra of ACF@MnOx_E1.3 at different electrodeposition times. Prolonging electrodeposition didn't change the crystallinity properties of the resulted manganese oxide.

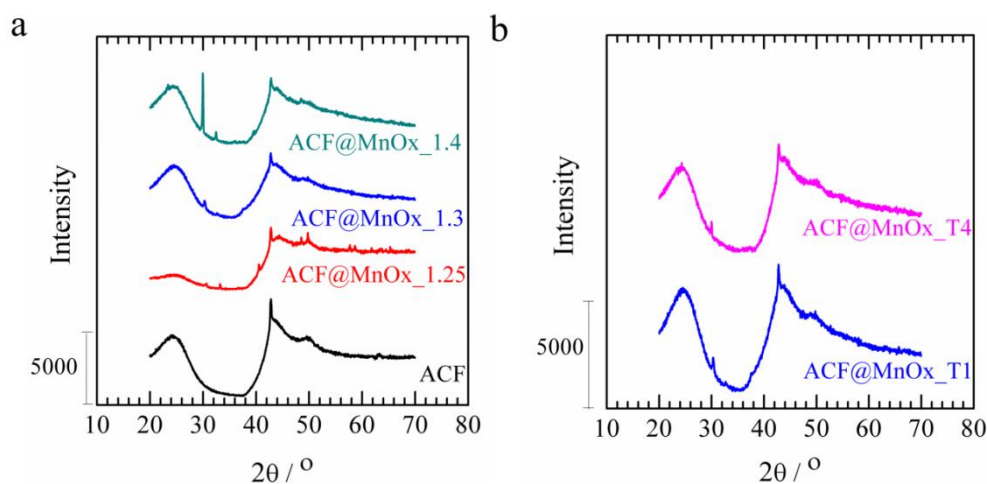


Figure 130 (a) Survey scan XRD spectra of the developed ACF@MnOx electrode at various electrodeposition potentials and (b) XRD spectra of ACF@MnOx resulted from electrodeposition for 1 and 4 hours respectively.

3.6.3.3 Morphological structure of ACF@MnOx

The SEM images in **Figure 131** show the MnOx electrodeposited onto the ACF fibers. The outer coating shows many fragments due to cracking during drying process. The image at higher magnification gives insight in the nanostructure view, which was quite similar for the three samples. Increasing time electrodeposition brings the better coverage of MnOx on the ACF fiber's surface (**Figure 132b**). Indeed, this led to increase of MnOx loading. It was also shown that a longer time electrodeposition may create a rougher MnOx surface (**Figure 133b,d**). This morphology supports an increase of the ORR performance.

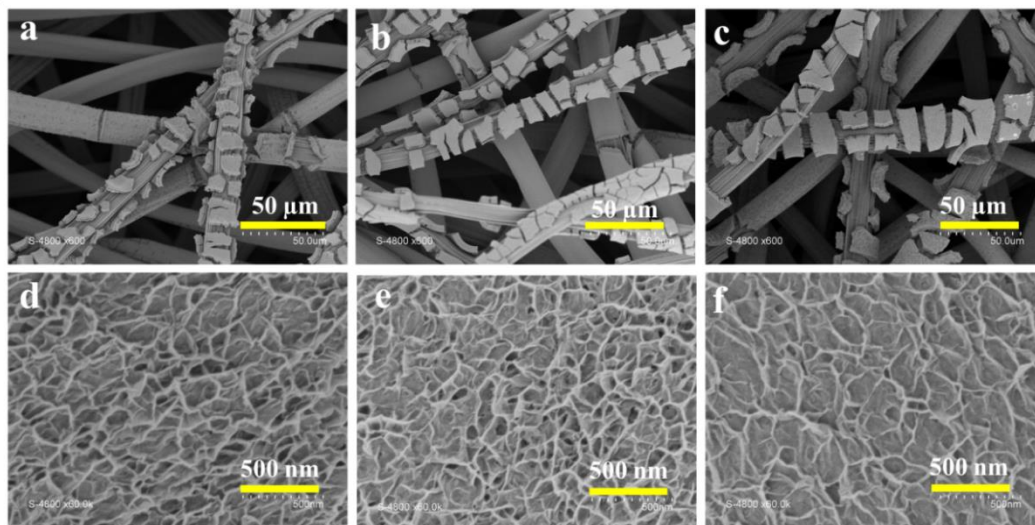


Figure 131 Overview (a,b,c) and closed-up view (d,e,f) of the morphological structure of ACF@MnO_x material resulted from electrodeposition potentials respectively of 1.25, 1.3 and 1.4 V vs. Ag/AgCl

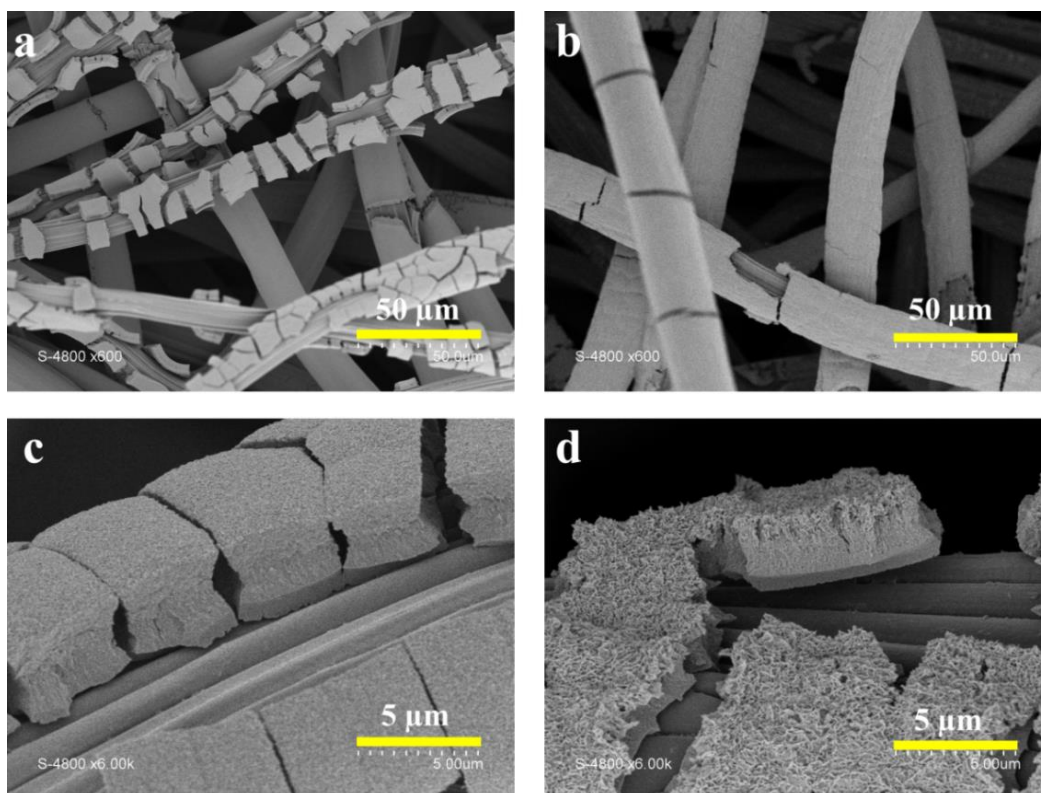


Figure 132 SEM images of as resulted ACF@MnO_x from electrodeposition at 1.3 V vs. Ag/AgCl (a,c) for one hour and (b,c) four hours

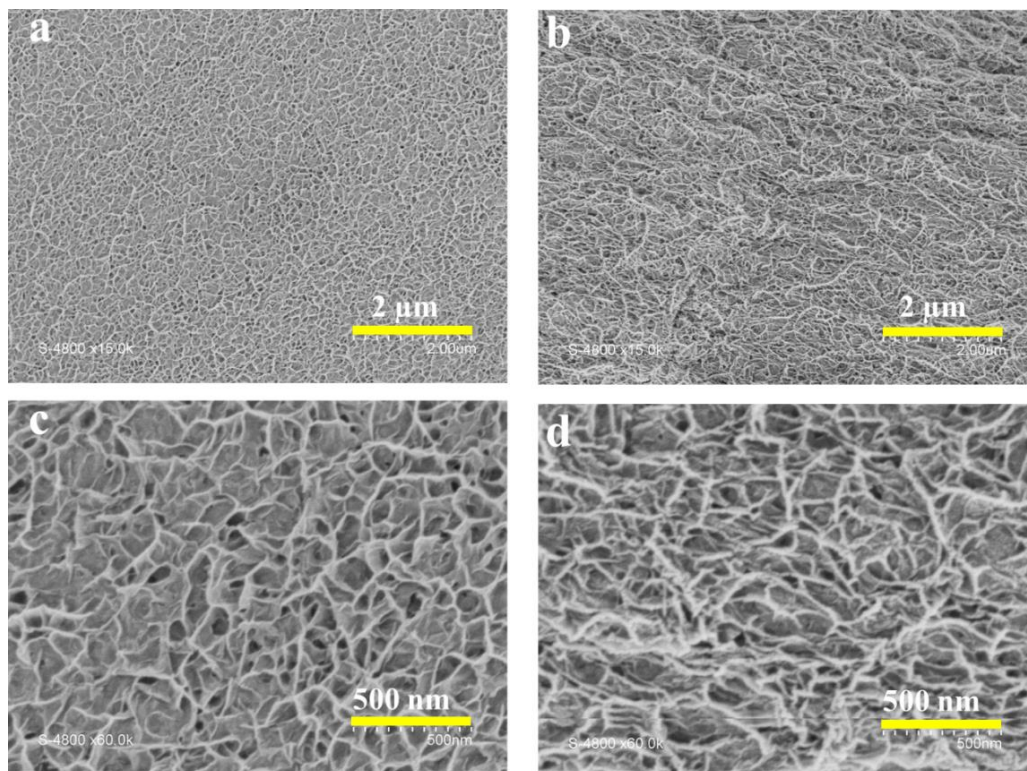


Figure 133 SEM images of ACF@MnO_x at higher magnification resulted from electrodeposition at 1.3 V vs. Ag/AgCl (a,c) for one hour and (b,c) four hours.

3.6.4 Determination of H₂O₂ production

The oxygen reduction reaction over MnO_x electrocatalysis may follow 4-e transfer or 2-e transfer mechanism. In order to specify this, we conducted a test to determine the produced H₂O₂ production in the same way as in the previous ACF@Pt cases. Herein, we selected three ACF@MnO_x electrodes resulted from electrodeposition at the different precursor concentrations, i.e. 25, 90, and 180 mM respectively. In this test, each electrode was subjected to reduce oxygen in a one-hour CA experiment that was conducted in oxygen saturated solution (0.1 M Na₂SO₄) at fixed potential both +0.1 V vs. Ag/AgCl and -0.4 V vs. Ag/AgCl respectively.

Figure 134 shows the CA curves of oxygen reduction at various potential for all selected electrodes. As shown by the LSV ORR curve, the ORR at potential around -0.4 V vs. Ag/AgCl reached optimum Faradic efficiency. Therefore, the CA at more negative potential resulted in more effective ORR indicated by the higher developed Q. Herein, the production of H₂O₂ in relative neutral solution

might follow **Eq. 108**. The sulfuric acid was immediately added to the resulted solution in order to keep the H_2O_2 species in the solution. The reaction of H_2O_2 with titanium solution in acidic pH readily forms clear yellowish solution of $\text{H}_2\text{O}_2\text{-Ti}$ complex according to **Eq. 109**. Then, the quantity of produced H_2O_2 can be determined by spectrophotometry.

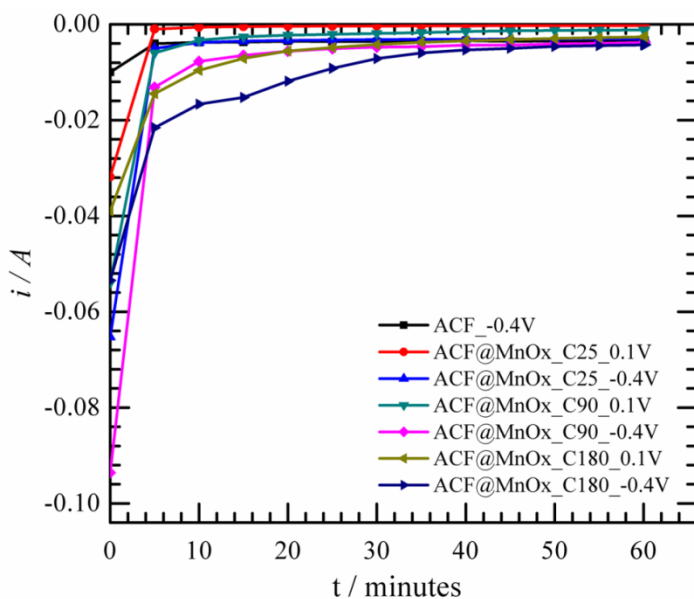


Figure 134 CA curves of oxygen reduction for various ACF@MnOx electrodes at various applied potentials.

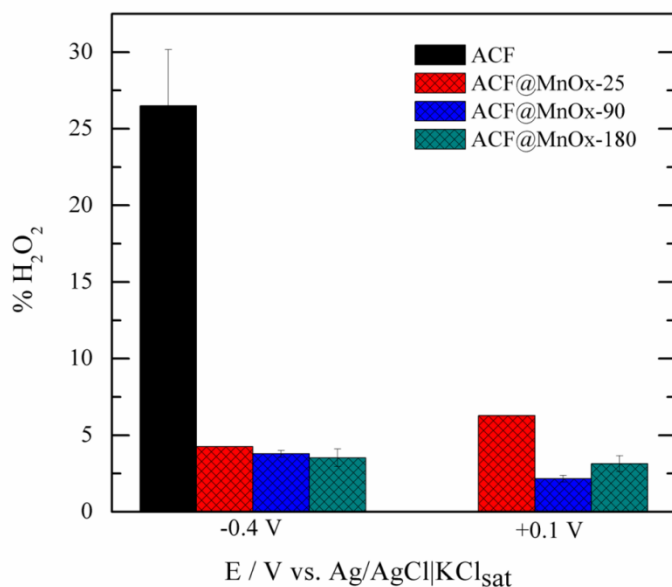


Figure 135 As quantified H_2O_2 after one hour of CA for various electrodes at various applied potentials.

The ORR at ACF electrode resulted in around 25 % of H₂O₂, as shown in **Figure 135**. Meanwhile, the ORR at the ACF@MnO_x electrode produced about five times less H₂O₂. Herein, we propose two possibilities: 1) the ORR over ACF@MnO_x catalyst follows 4-e transfer mechanism which directly produces water; 2) owing to MnO₂ being a well-known catalyst that degrade the H₂O₂ to form water and oxygen, then we suggest that the as-produced H₂O₂ during ORR readily degraded into water. Thus, we hypothesize that the quantified H₂O₂ above was the remaining H₂O₂ or undegraded H₂O₂.

3.6.5 Degradation of H₂O₂

Considering our previous hypothesis, we carried out the degradation of H₂O₂ at the ACF@MnO_x electrode. Herein, the electrode was dipped in the stirred H₂O₂ solution. The degradation of H₂O₂ at the ACF@MnO_x electrode proceeded according to **Eq. 110**.

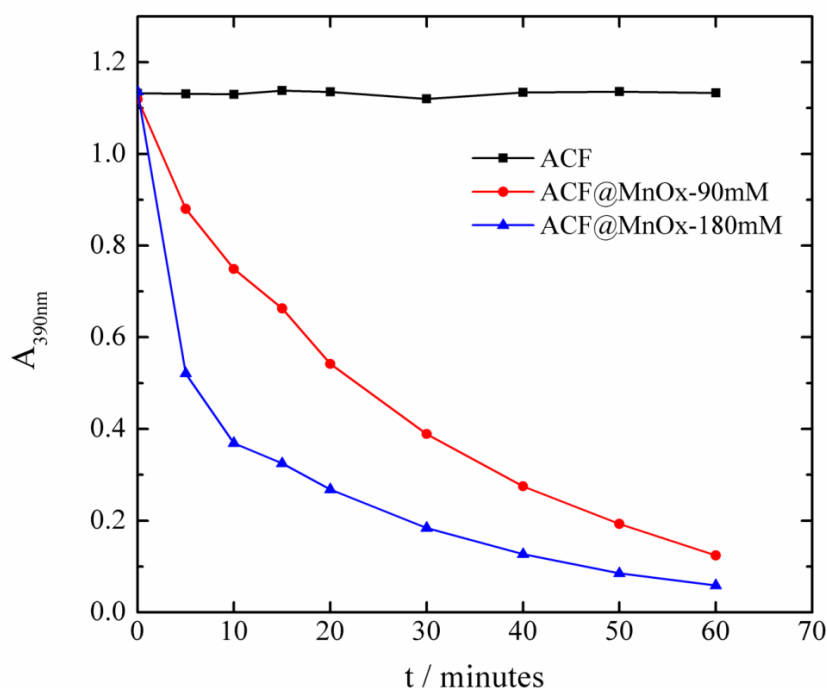


Figure 136 Degradation of H₂O₂ at the ACF and the ACF@MnO_x electrodes

In order to observe the H₂O₂ degradation process, each sample was taken periodically (every 5 minutes) during one hour. Reacting with titanium solution allows it to turn into a yellowish solution, which can be measured

spectrophotometrically. **Figure 136** shows the absorbance curve versus time, which indicates the degradation of H_2O_2 over the ACF@MnO_x . The higher MnO_x mass loading can perform faster degradation.

This subsection briefly showed the feasibility of developing a material based on manganese oxide modified carbon felt. The simultaneous synthesis and deposition of manganese oxide onto a carbon felt surface through a conventional electro-deposition method, i.e. cyclic voltammetry and/or chronoamperometry, results in a material that is a good ORR catalyst. In general, the physicochemical and electrochemical characterizations of the developed material indicate its suitability to be applied as air-breathing cathode in an MFC.

3.7 Air-breathing cathode for SCMFC: application of manganese oxide modified carbon felt (ACF@MnO_x)

Considering the three different generated ORR LSV curves, generated by electrodeposition from 180, 90, and 25 mM of precursor solutions, have attracted our interest to test manganese oxide modified carbon felt as air-breathing cathode material in a garden-compost MFC. Moreover, the three electrodes also showed very low produced H_2O_2 which meets the requirements of an air-breathing cathode in a fuel cell. The performances of these three air-breathing cathodes in the MFC are shown in **Figure 137**.

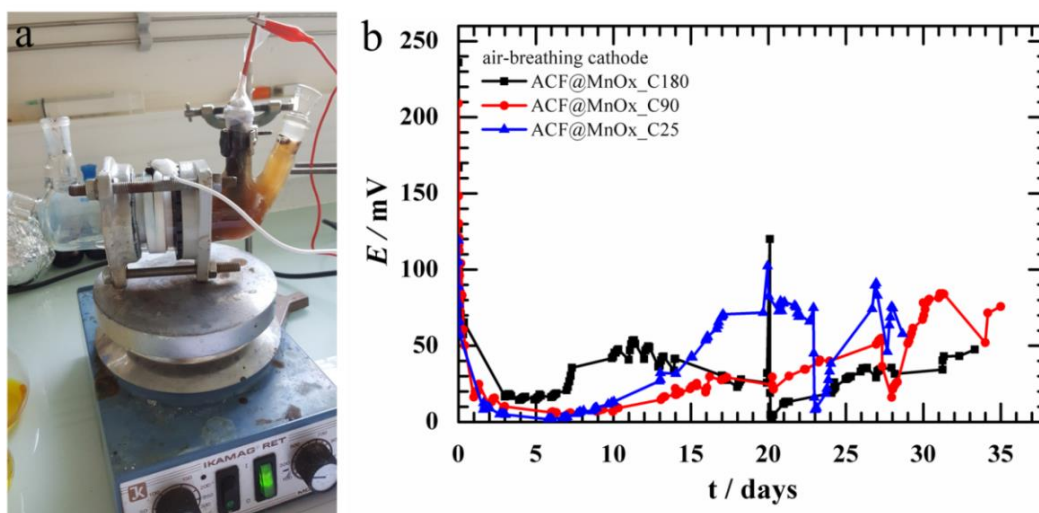


Figure 137 (a) SCMFC operation and (b) its daily-monitored voltage evolution using the $\text{ACF@MnO}_x\text{C180}$, $\text{ACF@MnO}_x\text{C90}$, and $\text{ACF@MnO}_x\text{C25}$ air-breathing cathode respectively.

Among the three air-breathing cathodes, the ACF@MnO_x_C180 showed either higher or faster voltage generation during the beginning period (0-15 days) (**Figure 137b**). The generated voltage indicates the potential difference between the reduction reaction in the cathodic part and the oxidation reaction in the anodic part. In this period, the oxidation in the anodic part was very low due to the lack of biofilm. Therefore, the voltage generated mainly corresponds to the cathodic part. This high initial voltage may enable to drive electron flow from the anode that stimulates the formation of bioelectroactive film faster, as indicated by the increased voltage (black line) at day 7. However, the generated voltage seemed to stay lower and constant up to day 20. Even after refreshing the anodic solution, at 20th day, the voltage values remained unchanged (**Figure 137b**).

The ORR mechanism on the air-breathing cathode contain MnO_x catalyst in an SCMFC has been illustrated by Liu, et al., as shown in **Figure 138** [124].

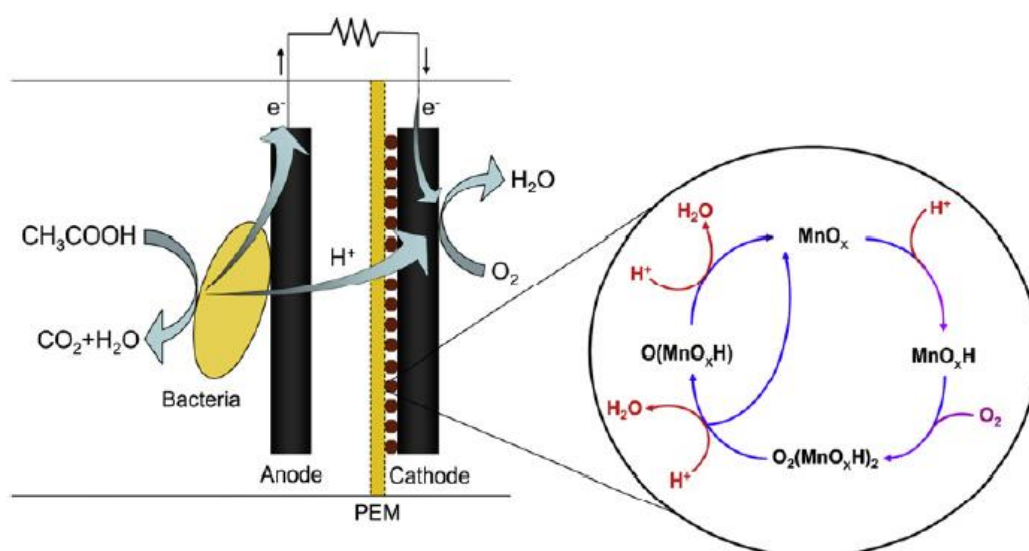


Figure 138 The illustration of ORR catalysis on the air-breathing cathode which contain manganese oxide catalyst [124]

At the end of the process, we found severe biofouling attached on the membrane (**Annex 4**). This fouling generates very high internal resistance as measured by EIS (**Figure 139**). Indeed, this inhibits the proton transfer process toward the cathodic part, which significantly lowers the generated voltage. Moreover, the ACF@MnO_x_C180 contained 30 mg cm⁻² of the MnO_x deposition. This MnO_x overloaded may block the gas diffusion layer and limit the oxygen supply, which

leads to ineffective air-breathing cathode performance. The best MFC performance within this experimental set was obtained by air-breathing cathode ACF@MnOx_C25. This seems contrary to the previous LSV curve, which showed a lower ORR current. Air-breathing cathode ACF@MnOx_C25 contained only 5 mg cm⁻² of MnOx which is not only able to perform catalysis but also maintains the air circulation to ensure the oxygen supply. In fact, it needed longer initiation time due to a lower initial potential drive. The voltage started to increase after more than 10 days. We also observed significantly lower internal resistance of the SCMFC with ACF@MnOx_C25 air-breathing cathode due to only minor biofouling found that attached on the membrane. The air-breathing ACF@MnOx_C90 also showed poor performance, which may be due to its MnOx overload and its high internal resistance due to its severe biofouling.

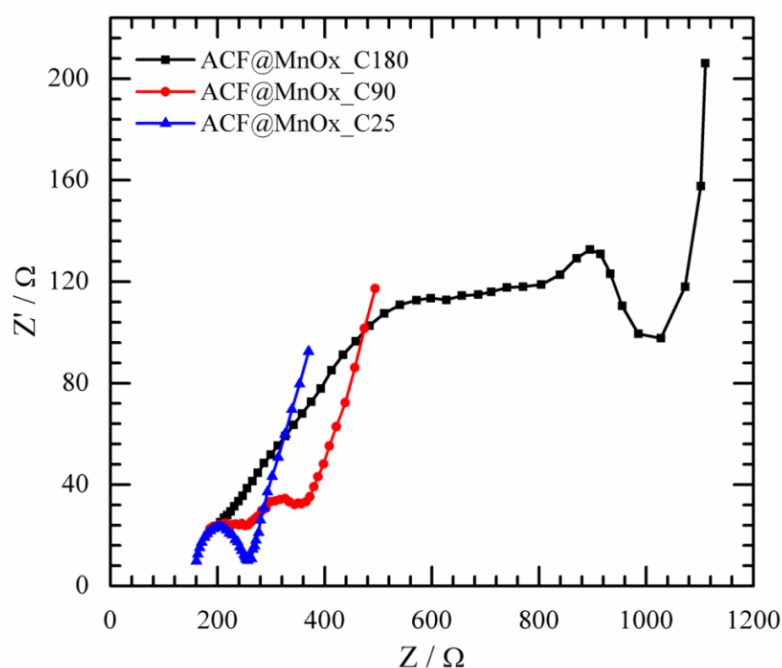


Figure 139 EIS of various ACF@MnOx air-breathing cathodes in single chamber microbial fuel cell

The recorded power density of the MFC with ACF@MnOx_C25 also showed a better stability over three weeks, as shown in **Figure 140**. The SCMFC with ACF@MnOx based air-breathing cathodes showed lower performance than those with platinum modified air-breathing cathode system. However, this opens up many challenges to improve manganese oxide based material in order to reach optimum SCMFC performance.

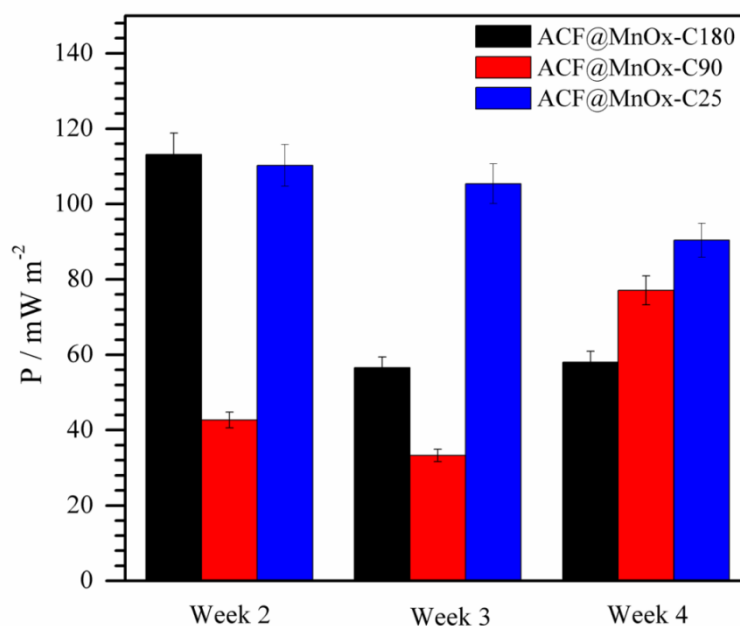


Figure 140 Power density of single chamber MFC with various ACF@MnOx air-breathing cathodes

3.8 Other applications of the developed material

3.8.1 ACF@Pt electrode for hydrogen evolution reaction (HER) electrocatalysis

HER is a very important reaction for splitting water, which resulted in hydrogen (H_2) to be supplied to the proton-exchange membrane fuel cells (PEMFCs) or chemical feedstock in the modern industry [23]. Experimentally, HER was performed by LSV started at -0.98 vs. Ag/AgCl reference electrodes. In this section, we prefer to present the reference toward reversible hydrogen electrode, RHE, using $E(\text{V vs. RHE}) = E(\text{V vs. Ag/AgCl}) + 0.06\text{pH} + E^0\text{Ag/AgCl} (\text{V vs. SHE})$ in order to ease the comparison with other works. **Figure 141a** shows the LSV curves of HER for the ACF@Pt electrode in 0.1 M KOH that starts at 0 V vs. RHE. As comparison, the HER over control electrode (ACF) showed a large overpotential of 400 mV. A current density of $|j| = 10 \text{ mA cm}^{-2}$ is an obvious value for HER catalysts evaluation in acidic media and $|j| = 5 \text{ mA cm}^{-2}$ is commonly used in alkaline solutions [206–209]. Therefore, we used these metrics as benchmark to evaluate the performance of our ACF@Pt electrode toward HER electrocatalysis. Herein, the current density of -5 and -10 mA cm^{-2} were reached at quite low overpotential i.e. 55 and 75 mV respectively, revealing that the

ACF@Pt electrode is an effective electrode for hydrogen generation. Moreover, the ACF@Pt electrode also shows satisfactory durability toward a long-term CA (**Figure 141b**), mimicking its real operation in electrocatalysis.

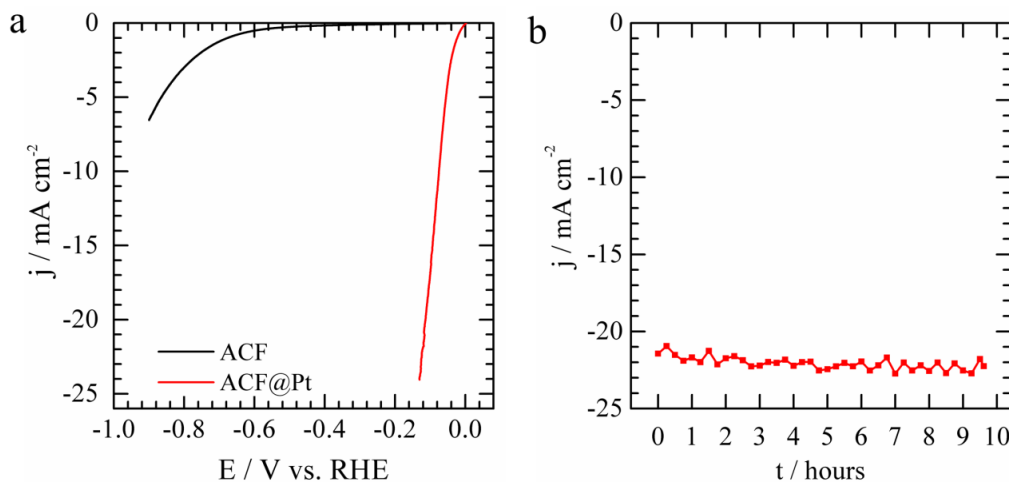


Figure 141 (a) HER polarization curves as recorded at 5 mV s⁻¹ on ACF and ACF@Pt in N₂-saturated 0.1 M KOH solution (b) durability of ACF@Pt at at -0.98 vs. Ag/AgCl (-0.12 V vs. RHE)

3.8.2 ACF@MnOx electrode for electro-Fenton-like (EF-like) process

The application of manganese oxide (MnOx) as Fenton-like catalyst has been shown to be effective for the degradation of methylene blue at neutral pH [210]. MnOx has a multivalent nature (+3 and +4), which can induce the decomposition of H₂O₂ to produce radical species, as expressed in **Eqs. 111** and **112** [210].

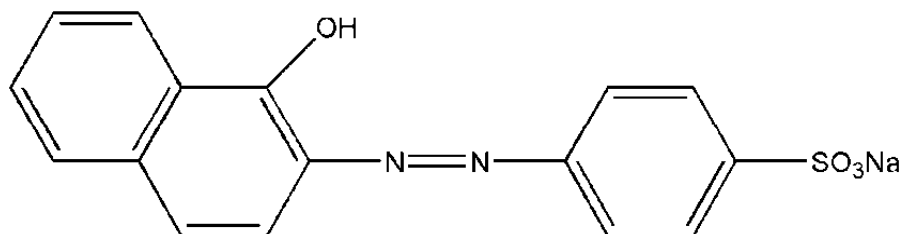


Figure 142 The molecular structure of acid orange 7, AO7

This brings us to the application of our developed material, ACF@MnOx, as an electrode in an electro-Fenton-like (EF-like) reaction to degrade azo dye, acid orange II, commonly called as AO7 (**Figure 142**). This is a synthetic dye that is

hard to degrade both chemically and biologically [211]. AO7 is considered as a model substrate for aromatic azo dye. A study of its degradation has been reported elsewhere [211].

The performance of the developed ACF@MnOx toward oxygen reduction reaction has been studied in **Section 3.5.7** that implies its possibility to generate H₂O₂. However, the amount of H₂O₂ resulted from all ACF@MnOx electrodes was very low. It is well known that MnOx catalyzes the degradation of H₂O₂ into water according to **Eq. 113**. This was also confirmed by our experiment on the degradation of H₂O₂ over the ACF@MnOx material (**Section 3.5.8**). Thus, we hypothesized that the small of resulted H₂O₂ was the remaining quantity that non-degraded by the MnOx.



Therefore, we infer that the ACF@MnOx exhibits dual catalyst activity. It can electrocatalyze the ORR to produce H₂O₂ and subsequently perform a Fenton-like reaction by catalyzing the resulted H₂O₂ to form hydroxyl radical ([•]OH). The combination of these dual activities may result in a new electro-Fenton-like system.

Figure 143a shows the degradation of AO7 by applying a fixed current at 18 mA at the Pt, ACF, and ACF@MnOx cathodes respectively versus a Pt mesh anode. The degradation of AO7 was observed faster at the ACF@MnOx electrode than at the ACF and Pt electrodes. Applying a current toward both ACF and ACF@MnOx enables to generate H₂O₂ by the reduction of oxygen through the 2-electron mechanism according to **Eq. 114**. Meanwhile, the electroreduction of oxygen at the Pt electrode follows the 4-electron transfer mechanism, which directly converts oxygen into water (**Eq. 115**).



The presence of MnOx on the ACF@MnOx electrode catalyzes the formation of hydroxyl radical ([•]OH) from the generated H₂O₂. Owing to the generation of these radicals, the oxidation of AO7 is then stimulated. A schematic degradation

pathway of the AO7 by the electrogenerated hydroxyl radicals have been described [211,212]. The degradation of AO7 is commonly initiated by breaking of the azo bond as the most active functional group in the structure. This cleavage results in many simpler aromatic compounds that are further broken down into the final simplest products, i.e. CO₂ and water, by the hydroxyl radicals through a number of steps. In order to achieve a complete degradation, it is essential to ensure the availability of the hydroxyl radicals.

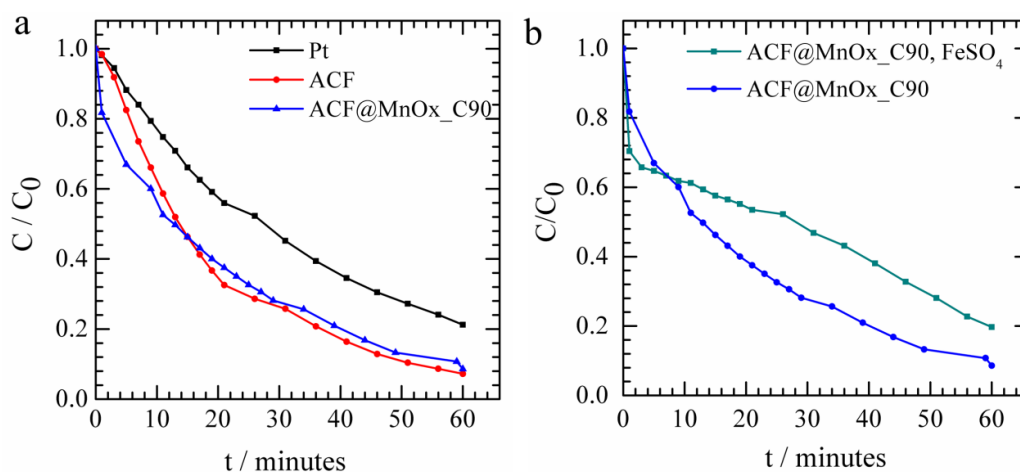


Figure 143 Kinetic degradation of AO7 at Pt, ACF, and ACF@MnOx cathode by applying a 18 mA current (a) at normal pH (b) for comparison with the presence of common Fenton catalyst FeSO₄.

The degradation leads to a decrease of the total organic carbon (TOC). Thus, TOC removal becomes the main parameter of the quality of degradation. **Table 25** shows TOC for 1 hour of the EF process at the Pt, ACF, and ACF@MnOx electrodes. We observed that effective TOC removal (20 %) only found at the ACF@MnOx electrode through the EF-like process. Whereas, the EF process both at the Pt and the ACF electrode failed to perform demineralization since the TOC increased rather than decreased. This indicates the limited of generated hydroxyl radicals during the EF process over these two electrodes.

The addition of iron as a classical Fenton catalyst into this EF process at the ACF@MnOx electrode showed poor demineralization of the AO7 (**Figure 143b**). The EF process with iron catalyst is commonly done at acidic pH 2-3 in order to prevent iron catalyst precipitation. However, in this EF process, we worked at natural pH (5 – 6) of AO7, which seems unsuitable for the dissolution iron

catalyst or generate precipitation. Another reason might be a competitive reaction between the MnO_x and iron. Thus, the need for additional catalyst in this EF process is negligible, which leads to the additional advantages.

Table 25 Demineralization through EF and EF-like treatment of AO7 at various electrodes

Entry	Electrode	TOC initial (ppm)	TOC 1h (ppm)
1	Pt	16.43 ± 0.18	17.19 ± 0.16
2	ACF		17.33 ± 0.26
3	ACF@MnO _x		12.53 ± 0.49
4	ACF@MnO _x , 0.1 mM FeSO ₄		14.62 ± 0.005

In EF process, the applied current is an important parameter related to operational costs and process efficiency. **Figure 144a** shows the degradation of AO7 during 1 hour of EF process at the ACF@MnO_x electrode at various applied currents. A significant improvement was observed by increasing the applied current from 18 mA to 72 mA, reaching optimum at 54 mA. This optimum current also increased the TOC removal up to 35% after 1 hour EF treatment.

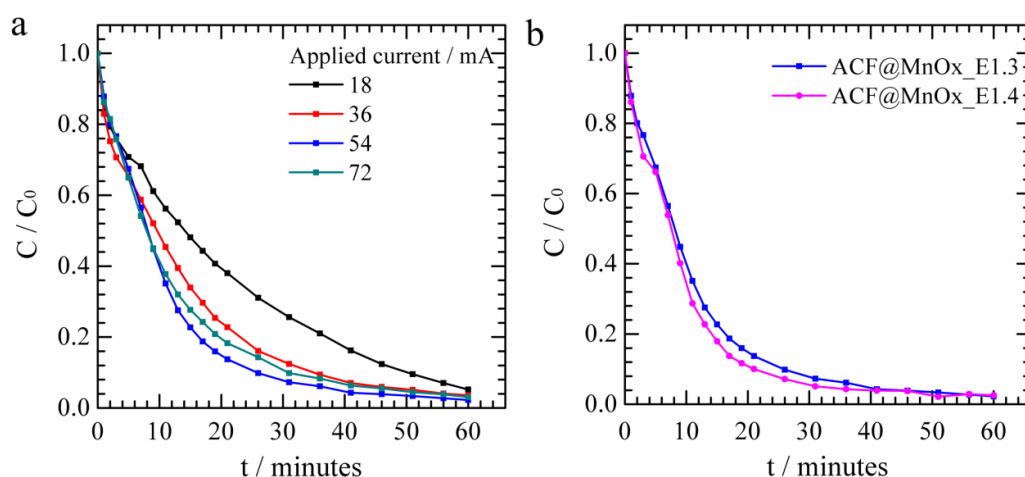


Figure 144 Kinetic degradation of AO7 at normal pH: (a) at various applied currents, and (b) at different electrodes

Based on the XRD spectra in **Section 3.5.6** that the as-prepared ACF@MnOx by electrodeposition at 1.4 V vs Ag/AgCl had a better crystallinity. Therefore, we evaluated its performance as electrode in the EF process to degrade AO7. **Figure 144b** shows the comparison of the two electrodes with different crystallinity properties. Indeed, the ACF@MnOx with better crystallinity showed better degradation performance.

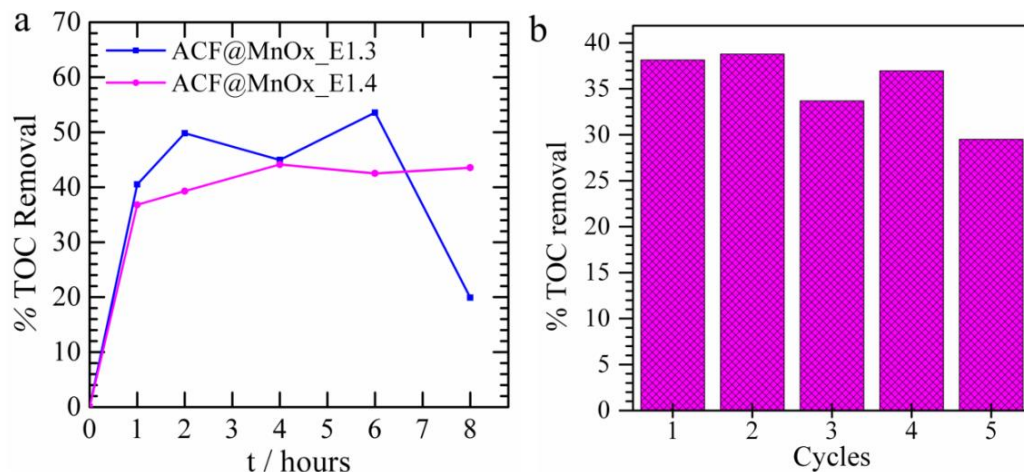


Figure 145 Demineralization over the two electrodes (a) at total 4 hours of EF treatment and (b) at 5 consecutives cycles

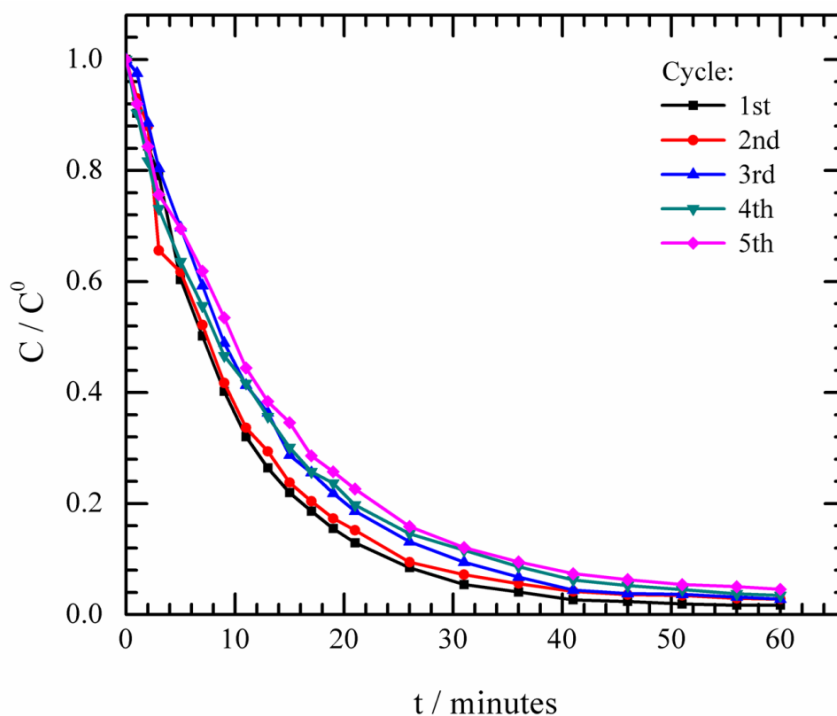


Figure 146 Kinetic degradation of AO7 over five consecutives cycles, revealing the stabilization of the developed electrode

Figure 145a shows the TOC removal of AO7 after 8 hours of EF process over the two electrodes within 8 hours. Herein, although the ACF@MnO_x_1.4 is considered had a better crystallinity, it doesn't show better TOC removal capability. In both cases, the TOC removal reaches ~40 % within two hours of EF-like treatment and starts to stabilize at > 2 hours.

Stabilization is also a key parameter for environmental application. Herein, we conducted a stabilization test by reusing the electrode over 5 consecutive cycles. **Figure 145b** shows the demineralization performance stability, which starts to decrease after 5 cycles. Moreover, the electrode also showed a stable kinetic of colour degradation as shown in **Figure 146**.

To conclude this last section, the present research underpins the versatility of either the method or the developed material for important processes such as hydrogen evolution reaction and electro-Fenton-like process. The developed ACF@Pt electrode reveals excellent catalysis toward HER. Meanwhile, the as-synthesized ACF@MnO_x showed a promising performance toward degradation of bio-refractory pollutants.

General Conclusion and Perspective

General Conclusion and Perspective

Garden compost, an abundant source of electroactive bacteria, reveals its potential to empower microbial fuel cell. The applications of garden compost in DCMFC result in higher power as it coupled with effective electron acceptor. In order to maintain the generated power, it automatically needs continuous reload of electron acceptor in the cathodic part. This treatment is an obvious limitation of the DCMFC system. Thus, the replacement an aqueous phase cathodic system by an air-breathing cathode system and turn the DCMFC into SCMFC system are a priority to improve the system.

Carbon felt was selected as substrate for air-breathing cathode due to its supporting properties such as conductivity, porosity, high surface area, and mechanically strength. Owing to the need of effective catalyst for ORR, catalysts have been loaded on the carbon felt through a conventional electrodeposition method.

In this research, we firstly developed air-breathing cathode by electropolymerizing a polypyrrole following by electrodepositing Pt on the conductive polymer's surface. In this approach, both electropolymerization and electrodeposition were conducted directly on air-breathing cathode that fixed in an electrochemical cell. PPy and/or PPy/Pt was coated only on carbon felt area that in contact with solution. So, this method proposes the idea to perform partial modification. The resulting material, CF@PPy@Pt and CF@PPy, reveal a significant improvement in ORR catalysis i.e. the LSV current at -0.6 V vs. Ag/AgCl by five times (5 mA) and twice (2.5 mA) respectively, comparing to the CF pristine. These two materials also show a promising application as air-breathing cathode in single chamber MFC powered by garden compost. The contribution of Pt nanoparticles in the air-breathing cathode is clear by showing the highest MFC performance (power density of 60 mW m^{-2}) among those with CF@PPy.

We also modified CF for air-breathing cathode material by directly growing Pt nanoparticles on CF's surface. This method was selected in order to obtain the simplest way and avoid the use of binder and or surfactant such as conductive polymer, as firstly demonstrated. For this purpose, the electrochemical pretreatment i.e. electroactivation of CF, which resulted in ACF, was needed to reduce the hydrophobicity of the CF. Various parameters have been studied in order to obtain optimum condition of the material synthesis. Electrodeposition from 5 mM chloroplatinic acid solution for one hour resulted in better morphology of grown Pt particles and nanoparticles entire the fiber surface. The resulted material, denoted as ACF@Pt, shows ORR improvement catalysis by almost five times higher than pristine CF and twice higher than its base, ACF. The performance of SCMFC with ACF@Pt as a homemade air-breathing cathode was twice higher (power density of 140 mW m^{-2}) than the CF@PPy@Pt (**Annex 2**). Moreover, the elaboration of Pt modified CF as anode, CF@Pt, in the SCMFC with ACF@Pt air-breathing cathode has also doubled the power density, which achieved up to 300 mW m^{-2} .

Owing to the platinum is an obvious expensive catalyst therefore we turned the attention to modify the CF by manganese oxide catalyst in order to realize the cost-effective air-breathing cathode fabrication. Manganese oxide was grown on the carbon felt by electrodeposition method. Then, the fabrication of air-breathing cathode was conducted based on the optimum synthesis condition. The SCMFC performance with ACF@MnOx air-breathing cathode shows a better power density (110 mW m^{-2}) than the CF@PPy@Pt one which only slightly lower than ACF@Pt based material (**Annex 2**). The feasibility of the developed ACF@MnOx air-breathing cathode opens the opportunity to bring the SCMFC become economically reasonable for large scale application.

Furthermore the developed material also reveal another important application i.e. the ACF@Pt for hydrogen evolution reaction and ACF@MnOx for electro-Fenton-like process to degrade bio-refractory material. These applications underpin the versatilities of the developed material in electrocatalysis.

Many ideas emerge from this research either in garden compost microbial fuel cell experiment or material development based on carbon felt. The DCMFC with garden compost reveals its compatibility with electron acceptor such as vanadium. Thus it opens the challenge to build a novel MFC-VRFB system that combines microbial activities in anodic part to generate power and vanadium (V) in cathodic part as electron acceptor. Garden compost as unlimited microbial source and the vanadium can be regenerated easily. Therefore, the MFC-VRFB system could result in more sustainable power generation both in anodic and cathodic parts. We also hypothesize that garden compost in anodic part of the DCMFC system can be coupled with many other electron acceptors such as Cr(VI) and permanganate those can be present in waste water as pollutant. Thus, the garden compost DCMFC can be applied for reduction of metal containing waste water. Moreover, the garden compost DCMFC also can be developed into carbon dioxide reduction system by elaborating CO₂ in cathodic part as an electron acceptor. Our developed material, ACF@MnOx, has shown a promising performance in electro-Fenton-like process for degradation azo compound (**Annex 5**). Thus, it opens the challenge to combine the garden compost MFC with electro-Fenton system as zero energy depollution system. The application of DCMFC for only power generation seems impractical since it needs continuous reload of electron acceptor. Therefore, the SCMFC with air-breathing cathode is more promising for this purpose. The garden compost SCMFC also can be developed into a stack system to multiply its generated power.

Publication

Journal

Widya Ernayati Kosimaningrum, Thi Xuan Huong Le, Yaovi Holade, Michael Bechelany, Sophie Tingry, Buchari Buchari, Indra Noviandri, Christophe Innocent, and Marc Cretin, Surfactant- and Binder-Free Hierarchical Platinum Nanoarrays Directly Grown onto a Carbon Felt Electrode for Efficient Electrocatalysis, ACS Appl. Mater. Interfaces, 2017, 9, 22476-22489

Widya Ernayati Kosimaningrum, Mekhaissia Ouis, Yaovi Holade, Buchari Buchari, Indra Noviandri, Marc Cretin, and Christophe Innocent, Platinum Nanoarrays Directly Grown onto a 3D-Carbon Felt as a Bifunctional Material for Garden Compost Microbial Fuel Cell, (submission)

Widya Ernayati Kosimaningrum, Buchari Buchari, Indra Noviandri, Marc Cretin, and Christophe Innocent, Polypyrrole-Platinum on Carbon felt for Air-Breathing Cathode in Single Chamber Microbial Fuel Cell (in preparation)

Widya Ernayati Kosimaningrum, Buchari Buchari, Indra Noviandri, Marc Cretin, and Christophe Innocent, Platinum-Modified Carbon Felt Anode for Garden Compost Microbial Fuel Cell, (in preparation)

Widya Ernayati Kosimaningrum, Buchari Buchari, Indra Noviandri, Marc Cretin, and Christophe Innocent, Manganese-Oxide-Modified Carbon Felt for Efficient Electrode of Electro-Fenton-Like Process in The Degradation of Azo Dye Compound (in preparation)

Poster

Widya Ernayati Kosimaningrum, Yaovi Holade, Buchari Buchari, Indra Noviandri, Marc Cretin, and Christophe Innocent, Single Compartement Microbial Fuel Cells with Air-Breathing Cathode and Platinum-Modified Anode, XXIV International Symposium on Bioelectrochemistry and Bioenergetics, 3-7 July, 2017, Lyon, France

Oral Presentation

Widya Ernayati Kosimaningrum, Yaovi Holade, Buchari Buchari, Indra Noviandri, Marc Cretin and Christophe Innocent, Platinum Modified Electrode Applied for Garden Compost Single Chamber Microbial Fuel Cell with Air-Breathing Cathode, The Symposium European Conference of Physical Chemistry, September 24-27, 2017, Borgo, Corsica-France

Widya Ernayati Kosimaningrum, Yaovi Holade, Buchari Buchari, Indra Noviandri, Marc Cretin and Christophe Innocent, Piles microbiennes à compartiment unique : cathode à air et bioanode modifiée avec du platine, Journée d'Electrochemistry, 26 – 29 June 2017

Widya Ernayati Kosimaningrum, Yaovi Holade, Buchari Buchari, Indra Noviandri, Marc Cretin and Christophe Innocent, Platinum Nanoarrays Directly Grown onto a Carbon Felt for Compost garden Based Air-Cathode Microbial Fuel cell, III^{ème} Journée des Doctorants de l'IEM, 3 Mai 2017, Institut Européen des Membranes, Université de Montpellier, France

Widya Ernayati Kosimaningrum, Yaovi Holade, Buchari Buchari, Indra Noviandri, Marc Cretin and Christophe Innocent, Surfactant and Binder-Free Hierarchical Platinum Nanoarrays for Efficient Electrocatalysis, Journée Scientific IP2, 11 Mai 2017, Institut Européen des Membranes, Université de Montpellier, France

Widya Ernayati Kosimaningrum, Christophe Innocent, Buchari Buchari, Indra Noviandri, Marc Cretin and Yaovi Holade, Construction of Air-Breathing Cathode for Microbial Fuel Cell Application, 12 Mai 2017, Comité de Suivi Individuel de Doctorant, ED Sciences Chimiques Balard, Université de Montpellier

Widya Ernayati Kosimaningrum, Christophe Innocent, Buchari Buchari, Indra Noviandri, Marc Cretin, Construction of Air-Breathing Cathode for Microbial Fuel Cell Application, April 2016, Comité de Suivi Individuel de Doctorant, ED Sciences Chimiques Balard, Université de Montpellier

REFERENCES

- [1] M.D. Khan, N. Khan, S. Sultana, R. Joshi, S. Ahmed, E. Yu, K. Scott, A. Ahmad, M.Z. Khan, Bioelectrochemical conversion of waste to energy using microbial fuel cell technology, *Process Biochem.* 57 (2017) 141–158. doi:10.1016/j.procbio.2017.04.001.
- [2] O.Z. Sharaf, M.F. Orhan, An overview of fuel cell technology: Fundamentals and applications, *Renew. Sustain. Energy Rev.* 32 (2014) 810–853. doi:10.1016/j.rser.2014.01.012.
- [3] Glenn Research Center, Fuel Cells: A Better Energy Source for Earth and Space, (2018). https://www.nasa.gov/centers/glenn/technology/fuel_cells.html (accessed November 17, 2018).
- [4] Birth of Electrochemistry, (n.d.). <https://www.electrochem.org/birth-of-electrochemistry> (accessed January 22, 2018).
- [5] K. Scott, E.H. Yu, M.M. Ghangrekar, B. Erable, N.M. Duteanu, Biological and microbial fuel cells, *Compr. Renew. Energy.* 4 (2012) 277–300. doi:10.1016/B978-0-08-087872-0.00412-1.
- [6] T.X. Huong Le, R. Esmilaire, M. Drobek, M. Bechelany, C. Vallicari, D.L. Nguyen, A. Julbe, S. Tingry, M. Cretin, Design of a novel fuel cell-Fenton system: a smart approach to zero energy depollution, *J. Mater. Chem. A.* 4 (2016) 17686–17693. doi:10.1039/C6TA05443A.
- [7] G.S. Jadhav, M.M. Ghangrekar, Performance of microbial fuel cell subjected to variation in pH, temperature, external load and substrate concentration, *Bioresour. Technol.* 100 (2009) 717–723. doi:10.1016/j.biortech.2008.07.041.
- [8] D. Ucar, Y. Zhang, I. Angelidaki, An overview of electron acceptors in microbial fuel cells, *Front. Microbiol.* 8 (2017) 1–14. doi:10.3389/fmicb.2017.00643.
- [9] K. Watanabe, Recent Developments in Microbial Fuel Cell Technologies for Sustainable Bioenergy, 106 (2008) 528–536. doi:10.1263/jbb.106.528.
- [10] S. Venkata Mohan, G. Velvizhi, J. Annie Modestra, S. Srikanth, Microbial fuel cell: Critical factors regulating bio-catalyzed electrochemical process and recent advancements, *Renew. Sustain. Energy Rev.* 40 (2014) 779–797. doi:10.1016/j.rser.2014.07.109.
- [11] Z. Du, H. Li, T. Gu, A state of the art review on microbial fuel cells: A promising technology for wastewater treatment and bioenergy, 25 (2007) 464–482. doi:10.1016/j.biotechadv.2007.05.004.
- [12] L. Wei, H. Han, J. Shen, Effects of cathodic electron acceptors and potassium ferricyanide concentrations on the performance of microbial fuel

- cell, *Int. J. Hydrogen Energy*. 37 (2012) 12980–12986. doi:10.1016/j.ijhydene.2012.05.068.
- [13] S. Oh, B. Min, Cathode Performance as a Factor in Electricity Generation in Microbial Fuel Cells, 38 (2004) 4900–4904.
- [14] I. Herrmann, Challenges and Constraints of Using Oxygen Cathodes in Microbial Fuel, 40 (2006) 5193–5199.
- [15] H. Liu, B. Logan, Electricity Generation Using an Air-Cathode Single Chamber Microbial Fuel Cell in the Presence and Absence of a Proton Exchange Membrane, *Environ. Sci. Technol.* 38 (2004) 4040–4046.
- [16] M.K. Debe, Electrocatalyst approaches and challenges for automotive fuel cells, (2012). doi:10.1038/nature11115.
- [17] Z. Chen, D. Higgins, H. Tao, R.S. Hsu, Z. Chen, Highly Active Nitrogen-Doped Carbon Nanotubes for Oxygen Reduction Reaction in Fuel Cell Applications, (2009) 21008–21013.
- [18] J. Champavert, S. Ben Rejeb, C. Innocent, M. Pontié, Microbial fuel cell based on Ni-tetra sulfonated phthalocyanine cathode and graphene modified bioanode, *J. Electroanal. Chem.* 757 (2015) 270–276. doi:10.1016/j.jelechem.2015.09.012.
- [19] M. Ouis, M. Kameche, C. Innocent, M. Charef, H. Kebaili, Electropolymerization of pyrrole on graphite electrode: enhancement of electron transfer in bioanode of microbial fuel cell, *Polym. Bull.* 75 (2018) 669–684. doi:10.1007/s00289-017-2048-5.
- [20] C. Santoro, C. Arbizzani, B. Erable, I. Ieropoulos, Microbial fuel cells: From fundamentals to applications. A review, *J. Power Sources*. 356 (2017) 225–244. doi:10.1016/j.jpowsour.2017.03.109.
- [21] Q. Deng, X. Li, J. Zuo, A. Ling, B.E. Logan, Power generation using an activated carbon fiber felt cathode in an upflow microbial fuel cell, *J. Power Sources*. 195 (2010) 1130–1135. doi:10.1016/j.jpowsour.2009.08.092.
- [22] D. Hidalgo, T. Tommasi, S. Bocchini, A. Chiolerio, A. Chiodoni, I. Mazzarino, B. Ruggeri, Surface modification of commercial carbon felt used as anode for Microbial Fuel Cells, *Energy*. 99 (2016) 193–201. doi:10.1016/j.energy.2016.01.039.
- [23] Y. Shi, B. Zhang, Recent advances in transition metal phosphide nanomaterials: synthesis and applications in hydrogen evolution reaction, *Chem. Soc. Rev.* 45 (2016) 1529–1541. doi:10.1039/C5CS00434A.
- [24] U.S. Department of Energy, Fossil, (n.d.). <http://www.energy.gov/science-innovation/energy-sources/fossil> (accessed March 3, 2018).
- [25] The World Energy Council, World Energy Resources, (n.d.).

<https://www.worldenergy.org/work-programme/strategic-insight/survey-of-energy-resources-and-technologies/> (accessed March 11, 2018).

- [26] Institut of Health Metrics and Evaluation, Global Burden of Air Pollution, (2013). <http://www.healthdata.org/infographic/global-burden-air-pollution> (accessed March 11, 2018).
- [27] Internal Energy Agency, World Energy Outlook 2017, (2017). <https://www.iea.org/weo2017/> (accessed March 11, 2018).
- [28] Agency for the Assessment and Application of Technology, Indonesia Energy Outlook 2017: Clean Energy Technology Development Initiatives, Center for Technology of Energy Resources and Chemical Industry, Agency for the Assessment and Application of Technology, Jakarta, 2017.
- [29] Agency for the Assessment and Application of Technology, Indonesia Energy Outlook 2018: Sustainable Energy for Land Transportation, Agency for The Assessment and Application of Technology, Jakarta, 2018. <https://www.bppt.go.id/unduh/outlook-energi>.
- [30] Science Daily, Renewable Energy, (n.d.). https://www.sciencedaily.com/terms/renewable_energy.htm (accessed March 11, 2018).
- [31] J. Wee, Contribution of fuel cell systems to CO₂ emission reduction in their application fields, 14 (2010) 735–744. doi:10.1016/j.rser.2009.10.013.
- [32] P. Lianos, Production of electricity and hydrogen by photocatalytic degradation of organic wastes in a photoelectrochemical cell. The concept of the Photofuelcell: A review of a re-emerging research field, J. Hazard. Mater. 185 (2011) 575–590. doi:10.1016/j.jhazmat.2010.10.083.
- [33] K. Ren, Y. X., Advances in Photoelectrochemical Fuel Cell Research, Small-Scale Energy Harvest. (2012) 3–26. doi:10.5772/50799.
- [34] C.Y. Chang, C.H. Wang, C.J. Tseng, K.W. Cheng, L.W. Hourng, B.T. Tsai, Self-oriented iron oxide nanorod array thin film for photoelectrochemical hydrogen production, Int. J. Hydrogen Energy. 37 (2012) 13616–13622. doi:10.1016/j.ijhydene.2012.01.136.
- [35] H. Zhang, J. Xuan, H. Xu, M.K.H. Leung, H. Wang, D.Y.C. Leung, L. Zhang, X. Lu, A theoretical study on photocatalytic fuel cell, Energy Procedia. 61 (2014) 246–249. doi:10.1016/j.egypro.2014.11.1099.
- [36] M. Grätzel, Photoelectrochemical cells, Nature. 414 (2001) 338. <https://doi.org/10.1038/35104607>.
- [37] K. Park, S. Han, J. Lee, Photo (UV) -enhanced performance of Pt – TiO₂ nanostructure electrode for methanol oxidation, 9 (2007) 1578–1581. doi:10.1016/j.elecom.2007.02.020.
- [38] M. Antoniadou, P. Lianos, Photoelectrochemical oxidation of organic substances over nanocrystalline titania: Optimization of the

- photoelectrochemical cell, 144 (2009) 166–171. doi:10.1016/j.cattod.2009.02.024.
- [39] M.H. Osman, A.A. Shah, F.C. Walsh, Recent progress and continuing challenges in bio-fuel cells. Part II: Microbial, Biosens. Bioelectron. 26 (2010) 953–963. doi:10.1016/j.bios.2010.08.057.
- [40] G.T.R. Palmore, G.M. Whitesides, Microbial and Enzymatic Biofuel Cells, in: *Enzym. Convers. Biomass Fuels Prod.*, 1994: pp. 271–290. doi:10.1021/bk-1994-0566.ch014.
- [41] D. Pant, G. Van Bogaert, L. Diels, K. Vanbroekhoven, Bioresource Technology A review of the substrates used in microbial fuel cells (MFCs) for sustainable energy production, *Bioresour. Technol.* 101 (2010) 1533–1543. doi:10.1016/j.biortech.2009.10.017.
- [42] V. Sharma, P.P. Kundu, Biocatalysts in microbial fuel cells, *Enzyme Microb. Technol.* 47 (2010) 179–188. doi:10.1016/j.enzmictec.2010.07.001.
- [43] A. Habrioux, G. Merle, K. Servat, K.B. Kokoh, C. Innocent, M. Cretin, S. Tingry, Concentric glucose/O₂biofuel cell, *J. Electroanal. Chem.* 622 (2008) 97–102. doi:10.1016/j.jelechem.2008.05.011.
- [44] U. Schröder, Anodic electron transfer mechanisms in microbial fuel cells and their energy efficiency, *Phys. Chem. Chem. Phys.* 9 (2007) 2619–2629. doi:10.1039/B703627M.
- [45] Y. Chen, P. Gai, J. Zhang, J. Zhu, Design of an enzymatic biofuel cell with large power output, *J. Mater. Chem. A Mater. Energy Sustain.* 3 (2015) 11511–11516. doi:10.1039/C5TA01432H.
- [46] H. Wang, J.-D. Park, Z.J. Ren, Practical Energy Harvesting for Microbial Fuel Cells: A Review, *Environ. Sci. Technol.* 49 (2015) 3267–3277. doi:10.1021/es5047765.
- [47] B.E. Logan, B. Hamelers, R. Rozendal, U. Schröder, J. Keller, S. Freguia, P. Aelterman, W. Verstraete, K. Rabaey, Microbial fuel cells: Methodology and technology, *Environ. Sci. Technol.* 40 (2006) 5181–5192. doi:10.1021/es0605016.
- [48] O. Schaetzle, F. Barrière, K. Baronian, Bacteria and yeasts as catalysts in microbial fuel cells: electron transfer from micro-organisms to electrodes for green electricity, *Energy Environ. Sci.* 1 (2008) 607. doi:10.1039/b810642h.
- [49] P. Jursthuik, Bacterial Metabolism, in: S. Baron (Ed.), *Med. Microbiol.*, 4th editio, University of Texas Medical Branch at Galveston, Galveston, Texas, 1996. <https://www.ncbi.nlm.nih.gov/books/NBK7919/>.
- [50] J. Berg, J. Tymoczko, S. L., Glycolysis Is an Energy-Conversion Pathway in Many Organisms, in: *Biochemistry*, 5th ed., W.H. Freeman and

- Company, New York, 2002. <https://www.ncbi.nlm.nih.gov/books/NBK22593/>.
- [51] J.M. Berg, J.L. Tymoczko, L. Stryer, The Citric Acid Cycle, in: *Biochemistry*, 5th ed., W.H. Freeman and Company, New York, 2002. <https://www.ncbi.nlm.nih.gov/books/NBK21163/>.
- [52] A. Soult, The Citric Acid Cycle, (n.d.). [https://chem.libretexts.org/LibreTexts/University_of_Kentucky/UK%3A_CHE_103__Chemistry_for_Allied_Health_\(Soult\)/Chapters/Chapter_15%3A_Metabolic_Cycles/15.2%3A_The_Citric_Acid_Cycle](https://chem.libretexts.org/LibreTexts/University_of_Kentucky/UK%3A_CHE_103__Chemistry_for_Allied_Health_(Soult)/Chapters/Chapter_15%3A_Metabolic_Cycles/15.2%3A_The_Citric_Acid_Cycle) (accessed June 2, 2018).
- [53] B.E. Logan, Exoelectrogenic Bacteria That Power Microbial Fuel Cells, *Nat. Rev. Microbiol.* 7 (2009).
- [54] L. Fan, S. Xue, Overview on Electricigens for Microbial Fuel Cell, (2016) 398–406. doi:10.2174/1874070701610010398.
- [55] S.A. Patil, F. Harnisch, B. Kapadnis, U. Schröder, Electroactive mixed culture biofilms in microbial bioelectrochemical systems: The role of temperature for biofilm formation and performance, *Biosens. Bioelectron.* 26 (2010) 803–808. doi:10.1016/j.bios.2010.06.019.
- [56] T. Ewing, P.T. Ha, J.T. Babauta, N.T. Tang, D. Heo, H. Beyenal, Scale-up of sediment microbial fuel cells, *J. Power Sources.* 272 (2014) 311–319.
- [57] B. Yu, J. Tian, L. Feng, Remediation of PAH polluted soils using a soil microbial fuel cell: Influence of electrode interval and role of microbial community, *J. Hazard. Mater.* 336 (2017) 110–118. doi:10.1016/j.jhazmat.2017.04.066.
- [58] M. Toyofuku, T. Inaba, T. Kiyokawa, N. Obana, Y. Yawata, N. Nomura, Environmental factors that shape biofilm formation, *Biosci. Biotechnol. Biochem.* 80 (2016) 7–12. doi:10.1080/09168451.2015.1058701.
- [59] K.K. Jefferson, What drives bacteria to produce a biofilm?, *FEMS Microbiol. Lett.* 236 (2004) 163–173. doi:10.1016/j.femsle.2004.06.005.
- [60] D.R. Korber, J.R. Lawrence, D.E. Caldwell, Effect of Motility on Surface Colonization and Reproductive Success of *Pseudomonas-Fluorescens* in Dual-Dilution Continuous-Culture and Batch Culture Systems 1, *Appl. Environ. Microbiol.* 60 (1994) 1421–1429. isi:A1994NJ57700004.
- [61] S.A. Patil, C. Hägerhäll, L. Gorton, Electron transfer mechanisms between microorganisms and electrodes in bioelectrochemical systems, *Bioanal. Rev.* 1 (2014) 71–129. doi:10.1007/11663_2013_2.
- [62] G. Reguera, K.D. McCarthy, T. Mehta, J.S. Nicoll, M.T. Tuominen, D.R. Lovley, Extracellular electron transfer via microbial nanowires, *Nature.* 435 (2005) 1098–1101. doi:10.1038/nature03661.
- [63] Y.A. Gorby, S. Yanina, J.S. McLean, K.M. Rosso, D. Moyles, A.

- Dohnalkova, T.J. Beveridge, I.S. Chang, B.H. Kim, K.S. Kim, D.E. Culley, S.B. Reed, M.F. Romine, D.A. Saffarini, E.A. Hill, L. Shi, D.A. Elias, D.W. Kennedy, G. Pinchuk, K. Watanabe, S. Ishii, B. Logan, K.H. Nealson, J.K. Fredrickson, Electrically conductive bacterial nanowires produced by *Shewanella oneidensis* strain MR-1 and other microorganisms, *Proc. Natl. Acad. Sci.* 103 (2006) 11358–11363. doi:10.1073/pnas.0604517103.
- [64] Y. Qiao, S. Bao, C.M. Li, Electrocatalysis in microbial fuel cells—from electrode material to direct electrochemistry, *Energy Environ. Sci.* 3 (2010) 544. doi:10.1039/b923503e.
- [65] U. Mardiana, C. Innocent, H. Jarrar, M. Cretin, Buchari, S. Gandasmita, Electropolymerized neutral red as redox mediator for yeast fuel cell, *Int. J. Electrochem. Sci.* 10 (2015) 8886–8898.
- [66] M.A. Rodrigo, P. Cañizares, J. Lobato, Effect of the electron-acceptors on the performance of a MFC, *Bioresour. Technol.* 101 (2010) 7014–7018. doi:10.1016/j.biortech.2010.04.013.
- [67] K. Kinoshita, *Electrochemical Oxygen Technology*, John Wiley and Sons, Inc., New York, 1992.
- [68] B.E. Logan, *Microbial Fuel Cells*, John Wiley and Sons, Inc., 2007.
- [69] A. Rhoads, H. Beyenal, Z. Lewandowski, Microbial Fuel Cell using Anaerobic Respiration as an Anodic Reaction and Biomineralized Manganese as a Cathodic Reactant, *Env. Sci Technol.* 39 (2005) 4666–4671.
- [70] B. Zhang, H. Zhao, C. Shi, S. Zhou, J. Ni, Simultaneous removal of sulfide and organics with vanadium (V) reduction in microbial fuel cells, *J Chem Technol Biotechnol.* 84 (2009) 1780–1786.
- [71] B. Zhang, C. Feng, J. Ni, J. Zhang, W. Huang, Simultaneous reduction of vanadium (V) and chromium (VI) with enhanced energy recovery based on microbial fuel cell technology, *J. Power Sources.* 204 (2012) 34–39. doi:10.1016/j.jpowsour.2012.01.013.
- [72] B. Zhang, C. Tian, Y. Liu, L. Hao, Y. Liu, C. Feng, Y. Liu, Z. Wang, Simultaneous microbial and electrochemical reductions of vanadium (V) with bioelectricity generation in microbial fuel cells, *Bioresour. Technol.* 179 (2015) 91–97. doi:10.1016/j.biortech.2014.12.010.
- [73] K.J. Kim, M.-S. Park, Y.-J. Kim, J.H. Kim, S.X. Dou, M. Skyllas-Kazacos, A technology review of electrodes and reaction mechanisms in vanadium redox flow batteries, *J. Mater. Chem. A.* 3 (2015) 16913–16933. doi:10.1039/C5TA02613J.
- [74] B. Cercado, N. Byrne, M. Bertrand, D. Pocaznoi, M. Rimboud, W. Achouak, A. Bergel, Garden compost inoculum leads to microbial

- bioanodes with potential-independent characteristics., *Bioresour. Technol.* 134 (2013) 276–84. doi:10.1016/j.biortech.2013.01.123.
- [75] M.S. Whittingham, R.F. Savinell, T. Zawodzinski, Introduction: Batteries and Fuel Cells, *Chem. Rev.* 104 (2004) 4243–4244. doi:10.1021/cr020705e.
- [76] X.-Z. Yuan, H. Wang, PEM Fuel Cell Fundamentals, in: J. Zhang (Ed.), *PEM Fuel Cell Electrocatal. Catal. Layer Fundam. Appl.*, Springer, London, 2008: pp. 1–79.
- [77] F. Zhao, R.C.T. Slade, J.R. Varcoe, Techniques for the study and development of microbial fuel cells: an electrochemical perspective, *Chem. Soc. Rev.* 38 (2009) 1926–1939. doi:10.1039/B819866G.
- [78] Y. Holade, A. Both Engel, S. Tingry, A. Cherifi, D. Cornu, K. Servat, T.W. Napporn, K.B. Kokoh, Insights on Hybrid Glucose Biofuel Cells Based on Bilirubin Oxidase Cathode and Gold-Based Anode Nanomaterials, *ChemElectroChem.* 1 (n.d.) 1976–1987. doi:10.1002/celec.201402142.
- [79] Y. Holade, M. Yuan, R.D. Milton, D.P. Hickey, A. Sugawara, C.K. Peterbauer, D. Haltrich, S.D. Minteer, Rational Combination of Promiscuous Enzymes Yields a Versatile Enzymatic Fuel Cell with Improved Coulombic Efficiency, *J. Electrochem. Soc.* 164 (2017) H3073–H3082. doi:10.1149/2.0111703jes.
- [80] B.R. Ringeisen, E. Henderson, P.K. Wu, J. Pietron, R. Ray, B. Little, J.C. Biffinger, J.M. Jones-Meehan, High Power Density from a Miniature Microbial Fuel Cell Using *Shewanella oneidensis* DSP10, *Environ. Sci. Technol.* 40 (2006) 2629–2634. doi:10.1021/es052254w.
- [81] C. Forrestal, Z. Huang, Z.J. Ren, Percarbonate as a naturally buffering catholyte for microbial fuel cells, *Bioresour. Technol.* 172 (2014) 429–432. doi:10.1016/j.biortech.2014.09.014.
- [82] X. Quan, B. Sun, H. Xu, Anode decoration with biogenic Pd nanoparticles improved power generation in microbial fuel cells, *Electrochim. Acta.* 182 (2015) 815–820. doi:10.1016/j.electacta.2015.09.157.
- [83] H.F. Cui, L. Du, P.B. Guo, B. Zhu, J.H.T. Luong, Controlled modification of carbon nanotubes and polyaniline on macroporous graphite felt for high-performance microbial fuel cell anode, *J. Power Sources.* 283 (2015) 46–53. doi:10.1016/j.jpowsour.2015.02.088.
- [84] S. Gupta, A. Yadav, N. Verma, Simultaneous Cr (VI) reduction and bioelectricity generation using microbial fuel cell based on alumina-nickel nanoparticles-dispersed carbon nanofiber electrode, *Chem. Eng. J.* 307 (2017) 729–738.
- [85] S. Cheng, H. Liu, B.E. Logan, Increased performance of single-chamber microbial fuel cells using an improved cathode structure, *Electrochem.*

- Commun. 8 (2006) 489–494. doi:10.1016/j.elecom.2006.01.010.
- [86] E. HaoYu, S. Cheng, K. Scott, B. Logan, Microbial fuel cell performance with non-Pt cathode catalysts, *J. Power Sources*. 171 (2007) 275–281. doi:10.1016/j.jpowsour.2007.07.010.
- [87] T. Catal, S. Xu, K. Li, H. Bermek, H. Liu, Electricity generation from polyalcohols in single-chamber microbial fuel cells, *Biosens. Bioelectron.* 24 (2008) 849–854. doi:10.1016/j.bios.2008.07.015.
- [88] Q. Wen, S. Wang, J. Yan, L. Cong, Z. Pan, Y. Ren, Z. Fan, MnO₂-graphene hybrid as an alternative cathodic catalyst to platinum in microbial fuel cells, *J. Power Sources*. 216 (2012) 187–191. doi:10.1016/j.jpowsour.2012.05.023.
- [89] Y. Yuan, S. Zhou, L. Zhuang, Polypyrrole/carbon black composite as a novel oxygen reduction catalyst for microbial fuel cells, *J. Power Sources*. 195 (2010) 3490–3493. doi:10.1016/j.jpowsour.2009.12.026.
- [90] Y. Feng, Q. Yang, X. Wang, B.E. Logan, Treatment of carbon fiber brush anodes for improving power generation in air-cathode microbial fuel cells, *J. Power Sources*. 195 (2010) 1841–1844. doi:10.1016/j.jpowsour.2009.10.030.
- [91] Y. Ahn, I. Ivanov, T.C. Nagaiah, A. Bordoloi, B.E. Logan, Mesoporous nitrogen-rich carbon materials as cathode catalysts in microbial fuel cells, *J. Power Sources*. 269 (2014) 212–215. doi:10.1016/j.jpowsour.2014.06.115.
- [92] T.-S. Song, D.-B. Wang, H. Wang, X. Li, Y. Liang, J. Xie, Cobalt oxide/nanocarbon hybrid materials as alternative cathode catalyst for oxygen reduction in microbial fuel cell, *Int. J. Hydrogen Energy*. 40 (2015) 3868–3874. doi:10.1016/j.ijhydene.2015.01.119.
- [93] W.E. Kosimaningrum, T.X.H. Le, Y. Holade, M. Bechelany, S. Tingry, B. Buchari, I. Noviadri, C. Innocent, M. Cretin, Surfactant- and Binder-Free Hierarchical Platinum Nanoarrays Directly Grown onto a Carbon Felt Electrode for Efficient Electrocatalysis, *ACS Appl. Mater. Interfaces*. 9 (2017) 22476–22489. doi:10.1021/acsami.7b04651.
- [94] H. Liu, *Microbial Fuel Cell: Novel Anaerobic Biotechnology for Energy Generation from Wastewater*, in: S.K. Khanal (Ed.), *Anaerob. Biotechnol. Bioenergy Prod. Princ. Appl.*, Blackwell Publishing, 2008.
- [95] K. Rabaey, N. Boon, S.D. Siciliano, W. Verstraete, M. Verhaege, Biofuel Cells Select for Microbial Consortia That Self-Mediate Electron Transfer, *Appl. Environ. Microbiol.* 70 (2004) 5373–5382. doi:10.1128/AEM.70.9.5373.

- [96] Z. He, S.D. Minteer, L.T. Angenent, Electricity Generation from Artificial Wastewater Using an Upflow Microbial Fuel Cell, *Environ. Sci. Technol.* 39 (2005) 5262–5267. doi:10.1021/es0502876.
- [97] K. Rabaey, P. Clauwaert, P. Aelterman, W. Verstraete, Tubular Microbial Fuel Cells for Efficient Electricity Generation, *Environ. Sci. Technol.* 39 (2005) 8077–8082. doi:10.1021/es050986i.
- [98] Z. He, N. Wagner, S.D. Minteer, L.T. Angenent, An Upflow Microbial Fuel Cell with an Interior Cathode: Assessment of the Internal Resistance by Impedance Spectroscopy, *Environ. Sci. Technol.* 40 (2006) 5212–5217. doi:10.1021/es060394f.
- [99] H. Liu, B.E. Logan, Electricity Generation Using an Air-Cathode Single Chamber Microbial Fuel Cell in the Presence and Absence of a Proton Exchange Membrane, *Environ. Sci. Technol.* 38 (2004) 4040–4046. doi:10.1021/es0499344.
- [100] B. Logan, S. Cheng, V. Watson, G. Estadt, Graphite Fiber Brush Anodes for Increased Power Production in Air-Cathode Microbial Fuel Cells, *Environ. Sci. Technol.* 41 (2007) 3341–3346. doi:10.1021/es062644y.
- [101] H. Liu, R. Ramnarayanan, B.E. Logan, Production of Electricity during Wastewater Treatment Using a Single Chamber Microbial Fuel Cell, *Environ. Sci. Technol.* 38 (2004) 2281–2285. doi:10.1021/es034923g.
- [102] B. Min, B.E. Logan, Continuous electricity generation from domestic wastewater and organic substrates in a flat plate microbial fuel cell, *Environ. Sci. Technol.* 38 (2004) 5809–5814. doi:10.1021/es0491026.
- [103] J. Wei, P. Liang, X. Huang, Recent progress in electrodes for microbial fuel cells, *Bioresour. Technol.* 102 (2011) 9335–9344. doi:10.1016/j.biortech.2011.07.019.
- [104] M. Zhou, M. Chi, J. Luo, H. He, T. Jin, An overview of electrode materials in microbial fuel cells, *J. Power Sources.* 196 (2011) 4427–4435. doi:10.1016/j.jpowsour.2011.01.012.
- [105] H. Liu, S. Cheng, B.E. Logan, Power Generation in Fed-Batch Microbial Fuel Cells as a Function of Ionic Strength, Temperature, and Reactor Configuration, *Environ. Sci. Technol.* 39 (2005) 5488–5493. doi:10.1021/es050316c.
- [106] X.I.N. Wang, S. Cheng, Use of Carbon Mesh Anodes and the Effect of Different Pretreatment Methods on Power Production in Microbial Fuel Cells, 43 (2009) 6870–6874.
- [107] H. Liu, S. Cheng, B.E. Logan, Production of Electricity from Acetate or Butyrate Using a Single-Chamber Microbial Fuel Cell, *Environ. Sci. Technol.* 39 (2005) 658–662. doi:10.1021/es048927c.
- [108] H.O. Mohamed, E.T. Sayed, H. Cho, M. Park, M. Obaid, H. Kim, N.A.M.

- Barakat, Effective strategies for anode surface modification for power harvesting and industrial wastewater treatment using microbial fuel cells, *J. Environ. Manage.* 206 (2018) 228–235. doi:10.1016/j.jenvman.2017.10.022.
- [109] Q. Zhang, J. Hu, D. Lee, *Bioresource Technology* Microbial fuel cells as pollutant treatment units: Research updates, *Bioresour. Technol.* 217 (2016) 121–128. doi:10.1016/j.biortech.2016.02.006.
- [110] D. Paul, M.T. Noori, P.P. Rajesh, M.M. Ghangrekar, A. Mitra, Modification of carbon felt anode with graphene oxide-zeolite composite for enhancing the performance of microbial fuel cell, *Sustain. Energy Technol. Assessments.* 26 (2018) 77–82. doi:10.1016/j.seta.2017.10.001.
- [111] N. Zhu, X. Chen, T. Zhang, P. Wu, P. Li, J. Wu, Improved performance of membrane free single-chamber air-cathode microbial fuel cells with nitric acid and ethylenediamine surface modified activated carbon fiber felt anodes, *Bioresour. Technol.* 102 (2011) 422–426. doi:10.1016/j.biortech.2010.06.046.
- [112] Z. Lv, D. Xie, X. Yue, C. Feng, C. Wei, Ruthenium oxide-coated carbon felt electrode: A highly active anode for microbial fuel cell applications, *J. Power Sources.* 210 (2012) 26–31. doi:10.1016/j.jpowsour.2012.02.109.
- [113] Z. Wang, G.D. Mahadevan, Y. Wu, F. Zhao, Progress of air-breathing cathode in microbial fuel cells, *J. Power Sources.* 356 (2017) 245–255. doi:10.1016/j.jpowsour.2017.02.004.
- [114] P.K. Shen, PEM Fuel Cell Catalyst Layers and MEAs, in: J. Zhang (Ed.), *PEM Fuel Cell Electrocatal. Catal. Layer Fundam. Appl.*, Springer, London, 2008: pp. 355–374.
- [115] C.R.K. Rao, D.C. Trivedi, Chemical and electrochemical depositions of platinum group metals and their applications, *Coord. Chem. Rev.* 249 (2005) 613–631. doi:10.1016/j.ccr.2004.08.015.
- [116] I. Merino-Jimenez, C. Santoro, S. Rojas-Carbonell, J. Greenman, I. Ieropoulos, P. Atanassov, Carbon-Based Air-Breathing Cathodes for Microbial Fuel Cells, *Catalysts.* 6 (2016).
- [117] X. Li, G. Liu, F. Ma, S. Sun, S. Zhou, R.E.A. Ardhi, J.K. Lee, H. Yao, Enhanced power generation in a single-chamber dynamic membrane microbial fuel cell using a nonstructural air-breathing activated carbon fiber felt cathode, *Energy Convers. Manag.* 172 (2018) 98–104. doi:10.1016/j.enconman.2018.07.011.
- [118] A.N. Ghadge, M.M. Ghangrekar, Performance of low cost scalable air-cathode microbial fuel cell made from clayware separator using multiple electrodes, *Bioresour. Technol.* 182 (2015) 373–377. doi:10.1016/j.biortech.2015.01.115.

- [119] Z. Wang, C. Cao, Y. Zheng, S. Chen, F. Zhao, Abiotic Oxygen Reduction Reaction Catalysts Used in Microbial Fuel Cells, *ChemElectroChem*. 1 (2014) 1813–1821. doi:10.1002/celec.201402093.
- [120] R.D. Milton, F. Giroud, A.E. Thumser, S.D. Minteer, R.C.T. Slade, Bilirubin oxidase bioelectrocatalytic cathodes: the impact of hydrogen peroxide, *Chem. Commun.* 50 (2014) 94–96. doi:10.1039/C3CC47689H.
- [121] R. Burkitt, T.R. Whiffen, E.H. Yu, Iron phthalocyanine and MnOx composite catalysts for microbial fuel cell applications, *Appl. Catal. B Environ.* 181 (2016) 279–288. doi:10.1016/j.apcatb.2015.07.010.
- [122] C. Song, J. Zhang, *Electrocatalytic Oxygen Reduction Reaction BT - PEM Fuel Cell Electrocatalysts and Catalyst Layers: Fundamentals and Applications*, in: J. Zhang (Ed.), Springer London, London, 2008: pp. 89–134. doi:10.1007/978-1-84800-936-3_2.
- [123] N. Markovic, Surface science studies of model fuel cell electrocatalysts, *Surf. Sci. Rep.* 45 (2002) 117–229. doi:10.1016/S0167-5729(01)00022-X.
- [124] X. Liu, X. Sun, Y. Huang, G. Sheng, K. Zhou, H. Yu, Nano-structured manganese oxide as a cathodic catalyst for enhanced oxygen reduction in a microbial fuel cell fed with a synthetic wastewater, 4 (2010) 3–10. doi:10.1016/j.watres.2010.06.065.
- [125] Yeager Ernest, The 1985 Berzelius Lecture, *J. Mol. Catal.* 38 (1986) 5–25.
- [126] G. Gnana kumar, Z. Awan, K. Suk Nahm, J. Stanley Xavier, Nanotubular MnO₂/graphene oxide composites for the application of open air-breathing cathode microbial fuel cells, *Biosens. Bioelectron.* 53 (2014) 528–534. doi:10.1016/j.bios.2013.10.012.
- [127] M. Lu, S. Kharkwal, H.Y. Ng, S.F.Y. Li, Carbon nanotube supported MnO₂ catalysts for oxygen reduction reaction and their applications in microbial fuel cells, *Biosens. Bioelectron.* 26 (2011) 4728–4732. doi:10.1016/j.bios.2011.05.036.
- [128] F. Shahbazi Farahani, B. Mecheri, M. Reza Majidi, M.A. Costa de Oliveira, A. D’Epifanio, F. Zurlo, E. Placidi, F. Arciprete, S. Licoccia, MnOx-based electrocatalysts for enhanced oxygen reduction in microbial fuel cell air cathodes, *J. Power Sources.* 390 (2018) 45–53. doi:10.1016/j.jpowsour.2018.04.030.
- [129] M.R. Majidi, F. Shahbazi Farahani, M. Hosseini, I. Ahadzadeh, Low-cost nanowired α -MnO₂/C as an ORR catalyst in air-cathode microbial fuel cell, *Bioelectrochemistry.* 125 (2019) 38–45. doi:10.1016/j.bioelechem.2018.09.004.
- [130] S. Zhang, W. Su, Y. Wei, J. Liu, K. Li, Mesoporous MnO₂ structured by ultrathin nanosheet as electrocatalyst for oxygen reduction reaction in air-cathode microbial fuel cell, 401 (2018) 158–164.

- [131] Y. Chen, Z. Lv, J. Xu, D. Peng, Y. Liu, J. Chen, X. Sun, C. Feng, C. Wei, Stainless steel mesh coated with MnO₂/carbon nanotube and polymethylphenyl siloxane as low-cost and high-performance microbial fuel cell cathode materials, *J. Power Sources*. 201 (2012) 136–141. doi:10.1016/j.jpowsour.2011.10.134.
- [132] P. Zhang, K. Li, X. Liu, Carnation-like MnO₂ modified activated carbon air cathode improve power generation in microbial fuel cells, 264 (2014) 248–253.
- [133] V.G. Khomenko, V.Z. Barsukov, A.S. Katashinskii, The catalytic activity of conducting polymers toward oxygen reduction, *Electrochim. Acta*. 50 (2005) 1675–1683. doi:10.1016/j.electacta.2004.10.024.
- [134] N. Shaigan, Electrodeposition for Electrochemical Energy Conversion and Storage Devices, in: S.S. Djokic (Ed.), *Electrodepos. Theory Pract.*, Springer New York, New York, NY, 2010: pp. 117–162. doi:10.1007/978-1-4419-5589-0_3.
- [135] A.J. Bard, L.R. Faulkner, *Electrochemical Methods: Fundamentals and Applications*, 2nd ed., John Wiley and Sons, Inc., New York, 2001.
- [136] C.R.K. Rao, D.C. Trivedi, Chemical and electrochemical depositions of platinum group metals and their applications, *Coord. Chem. Rev.* 249 (2005) 613–631. doi:10.1016/j.ccr.2004.08.015.
- [137] A.G. Tekerlekopoulou, S. Pavlou, D. V. Vayenas, Removal of ammonium, iron and manganese from potable water in biofiltration units: A review, *J. Chem. Technol. Biotechnol.* 88 (2013) 751–773. doi:10.1002/jctb.4031.
- [138] W. Wei, X. Cui, W. Chen, D.G. Ivey, Improved electrochemical impedance response induced by morphological and structural evolution in nanocrystalline MnO₂ electrodes, *Electrochim. Acta*. 54 (2009) 2271–2275. doi:https://doi.org/10.1016/j.electacta.2008.10.031.
- [139] M. and Singh, R N, Madhu, R. Awasthi, *Polypyrrole Composites : Electrochemical Synthesis , Characterizations and Applications*, (2011).
- [140] R.N. Singh, *Polypyrrole Composites: Electrochemical Synthesis, Characterizations and Applications*, in: M. Chemicals, E. Schab-Balcerzak (Eds.), InTech, Rijeka, 2011: p. Ch. 7. doi:10.5772/29083.
- [141] F.A. Harraz, Porous Silicon and Conductive Polymer Nanostructures via Templating, in: L. Canham (Ed.), *Handb. Porous Silicon*, Springer International Publishing, Cham, 2021: pp. 1–10. doi:10.1007/978-3-319-04508-5_63-1.
- [142] S.J. Hendel, E.R. Young, Introduction to Electrochemistry and the Use of Electrochemistry to Synthesize and Evaluate Catalysts for Water Oxidation and Reduction, (2016). doi:10.1021/acs.jchemed.6b00230.
- [143] I. Streeter, G.G. Wildgoose, L. Shao, R.G. Compton, Cyclic voltammetry

- on electrode surfaces covered with porous layers: An analysis of electron transfer kinetics at single-walled carbon nanotube modified electrodes, *Sensors Actuators, B Chem.* 133 (2008) 462–466. doi:10.1016/j.snb.2008.03.015.
- [144] J.L. Elgrishi, N., Rountree, K.J., McCarthy, B.D., Rountree, E.S., Eisenhart, T.T., Dempsey, A Practical Beginner's Guide to Cyclic Voltammetry, *J. Chem. Educ.* (2017). doi:10.1021/acs.jchemed.7b00361.
- [145] D. Kashyap, P. Dewedi, J. Pandey, Y.H. Kim, G.M. Kim, A. Sharma IITK, S. Goel, Application of electrochemical impedance spectroscopy in bio-fuel cell characterization: A review, *Int. J. Hydrogen Energy.* 39 (2014) 20159–20170.
- [146] N.S. Ramaraja P Ramasamy, Electrochemical Impedance Spectroscopy for Microbial Fuel Cell Characterization, *J. Microb. Biochem. Technol.* (2013). doi:10.4172/1948-5948.S6-004.
- [147] N. Wagner, Electrochemical Impedance Spectroscopy, in: H. Wang, X.-Z. Yuan, H. Li (Eds.), *PEM Fuel Cell Diagnostic Tools*, CRC Press, Boca Raton, 2012.
- [148] Gamry Instruments, Basics of Electrochemical Impedance Spectroscopy, (n.d.). <https://www.gamry.com/application-notes/EIS/basics-of-electrochemical-impedance-spectroscopy/> (accessed June 2, 2018).
- [149] A.I. Zia, S.C. Mukhopadhyay, *Impedance Spectroscopy and Experimental Setup*, 2016. doi:10.1007/978-3-319-32655-9_2.
- [150] T. Le, C. Charmette, M. Bechelany, M. Cretin, Facile Preparation of Porous Carbon Cathode to Eliminate Paracetamol in Aqueous Medium Using Electro-Fenton System, 2015. doi:10.1016/j.electacta.2015.12.005.
- [151] K.J. Kim, S.-W. Lee, T. Yim, J.-G. Kim, J.W. Choi, J.H. Kim, M.-S. Park, Y.-J. Kim, A new strategy for integrating abundant oxygen functional groups into carbon felt electrode for vanadium redox flow batteries, *Sci. Rep.* 4 (2014) 6906. <http://dx.doi.org/10.1038/srep06906>.
- [152] X-Ray Powder Diffraction, (n.d.). https://serc.carleton.edu/research_education/geochemsheets/techniques/XRD.html (accessed June 10, 2018).
- [153] J. Roller, X-Ray Diffraction, in: H. Wang, X.-Z. Yuan, H. Li (Eds.), *PEM Fuel Cell Diagnostic Tools*, CRC Press, Boca Raton, 2012.
- [154] D.A. Skoog, E.J. Holler, S.R. Crouch, *Principles of Instrumental Analysis*, 6th ed., Thomson Brooks/Cole, Canada, 2007.
- [155] N.H. Turner, B.I. Dunlap, R.J. Colton, Surface analysis: x-ray photoelectron spectroscopy, Auger electron spectroscopy and secondary ion mass spectrometry, *Anal. Chem.* 56 (1984) 373–416. doi:10.1021/ac00269a026.

- [156] Introduction to ICP-MS, (n.d.). <https://crustal.usgs.gov/laboratories/icpms/intro.html> (accessed June 10, 2018).
- [157] C.W. Lin, C.H. Wu, W.T. Huang, S.L. Tsai, Evaluation of different cell-immobilization strategies for simultaneous distillery wastewater treatment and electricity generation in microbial fuel cells, *Fuel*. 144 (2015) 1–8. doi:10.1016/j.fuel.2014.12.009.
- [158] K. Inoue, T. Ito, Y. Kawano, A. Iguchi, M. Miyahara, Y. Suzuki, K. Watanabe, Electricity generation from cattle manure slurry by cassette-electrode microbial fuel cells, *J. Biosci. Bioeng.* 116 (2013) 610–615. doi:10.1016/j.jbiosc.2013.05.011.
- [159] C.T. Wang, C.M.J. Yang, Z.S. Chen, Rumen microbial volatile fatty acids in relation to oxidation reduction potential and electricity generation from straw in microbial fuel cells, *Biomass and Bioenergy*. 37 (2012) 318–329. doi:10.1016/j.biombioe.2011.09.016.
- [160] B. Cercado-quezada, M. Delia, A. Bergel, Bioresource Technology Testing various food-industry wastes for electricity production in microbial fuel cell, *Bioresour. Technol.* 101 (2010) 2748–2754. doi:10.1016/j.biortech.2009.11.076.
- [161] D. Pocaznoi, B. Erable, L. Etcheverry, M.L. Delia, A. Bergel, Towards an engineering-oriented strategy for building microbial anodes for microbial fuel cells, *Phys. Chem. Chem. Phys.* 14 (2012) 13332–13343. doi:10.1039/c2cp42571h.
- [162] M. Oliot, L. Etcheverry, A. Bergel, Removable air-cathode to overcome cathode biofouling in microbial fuel cells, *Bioresour. Technol.* 221 (2016) 691–696. doi:10.1016/j.biortech.2016.09.095.
- [163] J. Champavert, Développement d'électrodes modifiées et d'un bioréacteur électrochimique à flux continu pour une application aux biopiles microbiennes, UNIVERSITE DE MONTPELLIER, 2016.
- [164] S. Parot, M.L. Délia, A. Bergel, Acetate to enhance electrochemical activity of biofilms from garden compost, *Electrochim. Acta*. 53 (2008) 2737–2742. doi:10.1016/j.electacta.2007.10.059.
- [165] Y. Xiao, E. Zhang, J. Zhang, Y. Dai, Z. Yang, H.E.M. Christensen, J. Ulstrup, F. Zhao, Extracellular polymeric substances are transient media for microbial extracellular electron transfer, *Sci. Adv.* (2017) 1–9. <http://advances.sciencemag.org/>.
- [166] A. Furiga, B. Lajoie, S. El Hage, G. Baziard, C. Roques, Impairment of *Pseudomonas aeruginosa* Biofilm Resistance to Antibiotics by Combining the Drugs with a New Quorum-Sensing Inhibitor, *Antimicrob. Agents Chemother.* . 60 (2016) 1676–1686. doi:10.1128/AAC.02533-15.

- [167] B. Virdis, P.G. Dennis, The nanostructure of microbially-reduced graphene oxide fosters thick and highly-performing electrochemically-active biofilms, *J. Power Sources*. 356 (2017) 556–565. doi:10.1016/j.jpowsour.2017.02.086.
- [168] K. Fricke, F. Harnisch, U. Schröder, On the use of cyclic voltammetry for the study of anodic electron transfer in microbial fuel cells, *Energy Environ. Sci.* 1 (2008) 144–147. doi:10.1039/B802363H.
- [169] X. Jiang, J. Hu, A.M. Lieber, C.S. Jackan, J.C. Biffinger, L.A. Fitzgerald, B.R. Ringeisen, C.M. Lieber, Nanoparticle Facilitated Extracellular Electron Transfer in Microbial Fuel Cells, *Nano Lett.* 14 (2014) 6737–6742. doi:10.1021/nl503668q.
- [170] G. Gnana kumar, C.J. Kirubaharan, S. Udhayakumar, C. Karthikeyan, K.S. Nahm, Conductive Polymer/Graphene Supported Platinum Nanoparticles as Anode Catalysts for the Extended Power Generation of Microbial Fuel Cells, *Ind. Eng. Chem. Res.* 53 (2014) 16883–16893. doi:10.1021/ie502399y.
- [171] A.A. Karyakin, Prussian Blue and Its Analogues: Electrochemistry and Analytical Applications, *Electroanal.* 13 (2001) 813–819. doi:10.1002/1521-4109(200106)
- [172] B.E. Logan, D. Call, S. Cheng, H.V.M. Hamelers, T.H.J.A. Sleutels, A.W. Jeremiase, R.A. Rozendal, Microbial Electrolysis Cells for High Yield Hydrogen Gas Production from Organic Matter, *Environ. Sci. Technol.* 42 (2008) 8630–8640. doi:10.1021/es801553z.
- [173] T.X. Huong Le, M. Bechelany, M. Cretin, Carbon felt based-electrodes for energy and environmental applications: A review, *Carbon N. Y.* 122 (2017) 564–591. doi:10.1016/j.carbon.2017.06.078.
- [174] J.-H. Lee, H.-J. Ahn, D. Cho, J.-I. Youn, Y.-J. Kim, H.-J. Oh, Effect of surface modification of carbon felts on capacitive deionization for desalination, *Carbon Lett.* 16 (2015) 93–100. doi:10.5714/CL.2015.16.2.093.
- [175] R.E.G. Smith, T.J. Davies, N.D.B. Baynes, R.J. Nichols, The electrochemical characterisation of graphite felts, *J. Electroanal. Chem.* 747 (2015) 29–38. doi:10.1016/j.jelechem.2015.03.029.
- [176] S.M. Dambrot, Helps Athlete Keep Moving, *ChemMatters*. (2016). www.acs.org/chemmatters.
- [177] V. Gau, S.-C. Ma, H. Wang, J. Tsukuda, J. Kibler, D.A. Haake, Electrochemical molecular analysis without nucleic acid amplification, *Methods*. 37 (2005) 73–83. doi:10.1016/j.ymeth.2005.05.008.
- [178] C. Santoro, Y. Lei, B. Li, P. Cristiani, Power generation from wastewater using single chamber microbial fuel cells (MFCs) with platinum-free

- cathodes and pre-colonized anodes, *Biochem. Eng. J.* 62 (2012) 8–16. doi:10.1016/j.bej.2011.12.006.
- [179] C. Feng, F. Li, H. Liu, X. Lang, S. Fan, A dual-chamber microbial fuel cell with conductive film-modified anode and cathode and its application for the neutral electro-Fenton process, *Electrochim. Acta.* 55 (2010) 2048–2054. doi:10.1016/j.electacta.2009.11.033.
- [180] M. Rahimnejad, G. Bakeri, M. Ghasemi, A. Zirepour, A review on the role of proton exchange membrane on the performance of microbial fuel cell, *Polym. Adv. Technol.* 25 (2014) 1426–1432. doi:10.1002/pat.3383.
- [181] Y.-Y. Lee, T.G. Kim, K. Cho, Effects of proton exchange membrane on the performance and microbial community composition of air-cathode microbial fuel cells, *J. Biotechnol.* 211 (2015) 130–137. doi:10.1016/j.jbiotec.2015.07.018.
- [182] C. Feng, Q. Wan, Z. Lv, X. Yue, Y. Chen, C. Wei, One-step fabrication of membraneless microbial fuel cell cathode by electropolymerization of polypyrrole onto stainless steel mesh, *Biosens. Bioelectron.* 26 (2011) 3953–3957. doi:10.1016/j.bios.2011.02.046.
- [183] A. Rinaldi, B. Mecheri, V. Garavaglia, S. Licoccia, P. Di Nardo, E. Traversa, Engineering materials and biology to boost performance of microbial fuel cells: a critical review, *Energy Environ. Sci.* 1 (2008) 417–429. doi:10.1039/B806498A.
- [184] W. Zhang, J. Xi, Z. Li, H. Zhou, L. Liu, Z. Wu, X. Qiu, Electrochemical activation of graphite felt electrode for $\text{VO}_2^+/\text{VO}^{2+}$ redox couple application, *Electrochim. Acta.* 89 (2013) 429–435. doi:10.1016/j.electacta.2012.11.072.
- [185] G. Caballero-Manrique, E. Brillas, F. Centellas, J. Garrido, R. Rodríguez, P.-L. Cabot, Electrochemical Oxidation of the Carbon Support to Synthesize Pt(Cu) and Pt-Ru(Cu) Core-Shell Electrocatalysts for Low-Temperature Fuel Cells, *Catalysts.* 5 (2015) 815–837. doi:10.3390/catal5020815.
- [186] Y. Shao, G. Yin, J. Zhang, Y. Gao, Comparative investigation of the resistance to electrochemical oxidation of carbon black and carbon nanotubes in aqueous sulfuric acid solution, 51 (2006) 5853–5857. doi:10.1016/j.electacta.2006.03.021.
- [187] L.F. Arenas, C.P. de León, R.P. Boardman, F.C. Walsh, Electrodeposition of Platinum on Titanium Felt in a Rectangular Channel Flow Cell, *J. Electrochem. Soc.* 164 (2017) D57–D66. doi:10.1149/2.0651702jes.
- [188] H.M. Yasin, G. Denuault, D. Pletcher, Studies of the electrodeposition of platinum metal from a hexachloroplatinic acid bath, *J. Electroanal. Chem.* 633 (2009) 327–332. doi:10.1016/j.jelechem.2009.06.020.

- [189] M.M.E. Duarte, A.S. Pilla, J.M. Sieben, C.E. Mayer, Platinum particles electrodeposition on carbon substrates, *Electrochem. Commun.* 8 (2006) 159–164. doi:10.1016/j.elecom.2005.11.003.
- [190] S. Khilari, S. Pandit, D. Das, D. Pradhan, Biosensors and Bioelectronics Manganese cobaltite / polypyrrole nanocomposite-based air-cathode for sustainable power generation in the single-chambered microbial, *Biosens. Bioelectron.* 54 (2014) 534–540. doi:10.1016/j.bios.2013.11.044.
- [191] Y. Garsany, O.A. Baturina, K.E. Swider-Lyons, S.S. Kocha, Experimental methods for quantifying the activity of platinum electrocatalysts for the oxygen reduction reaction, *Anal. Chem.* 82 (2010) 6321–6328. doi:10.1021/ac100306c.
- [192] T.X.H. Le, M. Bechelany, A.B. Engel, M. Cretin, S. Tingry, Gold particles growth on carbon felt for efficient micropower generation in a hybrid biofuel cell, *Electrochim. Acta.* 219 (2016) 121–129. doi:10.1016/j.electacta.2016.09.135.
- [193] G. Guisbiers, G. Abudukelimu, D. Hourlier, Size-dependent catalytic and melting properties of platinum-palladium nanoparticles, *Nanoscale Res. Lett.* 6 (2011) 1–5. doi:10.1186/1556-276X-6-396.
- [194] S. Taylor, E. Fabbri, P. Levecque, T.J. Schmidt, O. Conrad, The Effect of Platinum Loading and Surface Morphology on Oxygen Reduction Activity, *Electrocatalysis.* (2016) 287–296. doi:10.1007/s12678-016-0304-3.
- [195] Y. Holade, C. Morais, K. Servat, T.W. Napporn, K.B. Kokoh, Enhancing the available specific surface area of carbon supports to boost the electroactivity of nanostructured Pt catalysts, *Phys. Chem. Chem. Phys.* 16 (2014) 25609–25620. doi:10.1039/C4CP03851G.
- [196] J. Ma, A. Habrioux, M. Pisarek, A. Lewera, N. Alonso-Vante, Induced electronic modification of Pt nanoparticles deposited onto graphitic domains of carbon materials by UV irradiation, *Electrochem. Commun.* 29 (2013) 12–16. doi:10.1016/j.elecom.2012.12.028.
- [197] Y. Holade, S. Tingry, K. Servat, T. Napporn, D. Cornu, K. Kokoh, Nanostructured Inorganic Materials at Work in Electrochemical Sensing and Biofuel Cells, *Catalysts.* 7 (2017) 31. doi:10.3390/catal7010031.
- [198] D. Hidalgo, T. Tommasi, S. Bocchini, A. Chiolerio, A. Chiodoni, I. Mazzarino, B. Ruggeri, Surface modification of commercial carbon felt used as anode for Microbial Fuel Cells, *Energy.* 99 (2016) 193–201. doi:10.1016/j.energy.2016.01.039.
- [199] M. Kodali, R. Gokhale, C. Santoro, A. Serov, K. Artyushkova, P. Atanassov, High Performance Platinum Group Metal-Free Cathode Catalysts for Microbial Fuel Cell (MFC), *J. Electrochem. Soc.* 164 (2017) H3041–H3046. doi:10.1149/2.0061703jes.

- [200] P. Zhang, K. Li, X. Liu, Carnation-like MnO₂ modified activated carbon air cathode improve power generation in microbial fuel cells, *J. Power Sources*. 264 (2014) 248–253. doi:10.1016/j.jpowsour.2014.04.098.
- [201] M.B. Zakaria, C. Li, M. Pramanik, Y. Tsujimoto, M. Hu, V. Malgras, S. Tominaka, Y. Yamauchi, Nanoporous Mn-based electrocatalysts through thermal conversion of cyano-bridged coordination polymers toward ultra-high efficiency hydrogen peroxide production, *J. Mater. Chem. A*. 4 (2016) 9266–9274. doi:10.1039/C6TA01470D.
- [202] S. Nijjer, J. Thonstad, G.M. Haarberg, Oxidation of manganese(II) and reduction of manganese dioxide in sulphuric acid, *Electrochim. Acta*. 46 (2000) 395–399. doi:10.1016/S0013-4686(00)00597-1.
- [203] S. Xi, Y. Zhu, Y. Yang, Y. Liu, Direct Synthesis of MnO₂ Nanorods on Carbon Cloth as Flexible Supercapacitor Electrode, 2017 (2017) 8. doi:10.1155/2017/7340961.
- [204] Y. Zhang, H. Liu, Z. Zhu, K. Wong, R. Mi, *Electrochimica Acta* A green hydrothermal approach for the preparation of graphene / γ -MnO₂ 3D network as anode for lithium ion battery, *Electrochim. Acta*. 108 (2013) 465–471. doi:10.1016/j.electacta.2013.07.002.
- [205] Q. Zhu, H. Hu, G. Li, C. Zhu, Y. Yu, *Electrochimica Acta* TiO₂ Nanotube Arrays Grafted with MnO₂ Nanosheets as High-Performance Anode for Lithium Ion Battery, *Electrochim. Acta*. 156 (2015) 252–260. doi:10.1016/j.electacta.2015.01.023.
- [206] R. Subbaraman, D. Tripkovic, K.-C. Chang, D. Strmcnik, A. P Paulikas, P. Hirunsit, M. Chan, J. Greeley, V. Stamenkovic, N. Marković, Trends in activity for the water electrolyser reactions on 3d M(Ni,Co,Fe,Mn) hydr(oxy)oxide catalysts, *Nat. Mater.* 11 (2012) 550–557.
- [207] J. Luo, J.-H. Im, M.T. Mayer, M. Schreier, M.K. Nazeeruddin, N.-G. Park, S.D. Tilley, H.J. Fan, M. Grätzel, Water photolysis at 12.3% efficiency via perovskite photovoltaics and Earth-abundant catalysts, *Science* (80-.). 345 (2014) 1593–1596. doi:10.1126/science.1258307.
- [208] X. Zou, Y. Zhang, Noble metal-free hydrogen evolution catalysts for water splitting, *Chem. Soc. Rev.* 44 (2015) 5148–5180. doi:10.1039/C4CS00448E.
- [209] J.D. Benck, T.R. Hellstern, J. Kibsgaard, P. Chakthranont, T.F. Jaramillo, Catalyzing the Hydrogen Evolution Reaction (HER) with Molybdenum Sulfide Nanomaterials, *ACS Catal.* 4 (2014) 3957–3971. doi:10.1021/cs500923c.
- [210] E.J. Kim, D. Oh, C.S. Lee, J. Gong, J. Kim, Y.S. Chang, Manganese oxide nanorods as a robust Fenton-like catalyst at neutral pH: Crystal phase-dependent behavior, *Catal. Today*. 282 (2017) 71–76. doi:10.1016/j.cattod.2016.03.034.

- [211] A. Özcan, M.A. Oturan, N. Oturan, Y. Şahin, Removal of Acid Orange 7 from water by electrochemically generated Fenton's reagent, *J. Hazard. Mater.* 163 (2009) 1213–1220. doi:10.1016/j.jhazmat.2008.07.088.
- [212] H. Zhao, Y. Sun, L. Xu, J. Ni, Chemosphere Removal of Acid Orange 7 in simulated wastewater using a three-dimensional electrode reactor: Removal mechanisms and dye degradation pathway, *Chemosphere.* 78 (2010) 46–51. doi:10.1016/j.chemosphere.2009.10.034.

ANNEXES

Annex 1: The calculation of electron production efficiency

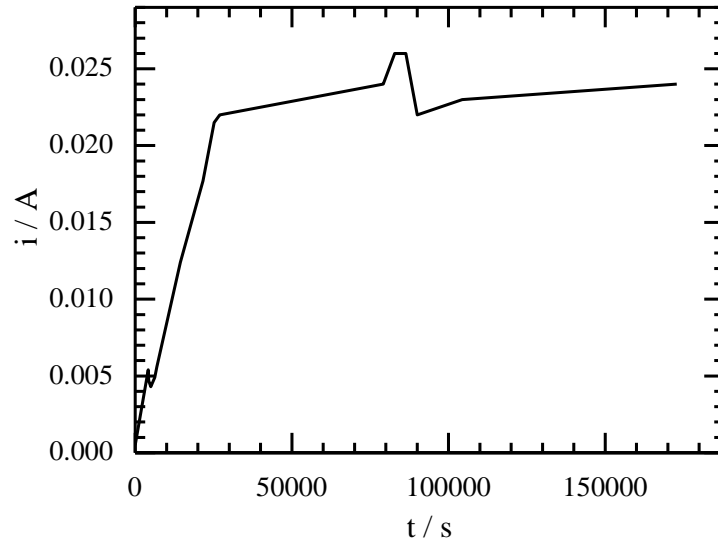


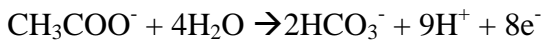
Figure-A1 The plot of current vs. time of SCMFC experiment

The charge, Q , as integrated using Origin Software = 3712.92

The mole electron can be calculated as

$$\text{mol } e = \frac{Q}{F} = \frac{3712.92}{96500} = 0.03848 \text{ mol}$$

According to the chemical equation of oxidation acetate



Therefore, the mol acetate real can be calculated as

$$\text{Mol CH}_3\text{COO} = 1/8 \times 0.03848 = 0.004809 \text{ mol}$$

From the experiment, the initial acetate concentration was 25.4 and the final acetate concentration (after 48 hours) was 19.

Therefore the consumed acetate = 25.4 - 19 = 6.4 mM

The consumed acetate (in mol) = 6.4 mM x 60 mL = 0.384 mmol = 0.000384 mol

Therefore efficiency of electron production can be calculated as

$$\text{Efficiency (\%)} = \frac{0.000384}{0.004809} \times 100\% = 7.98\%$$

Annex 2: Resume of SCMFC performance with various air-breathing cathode system

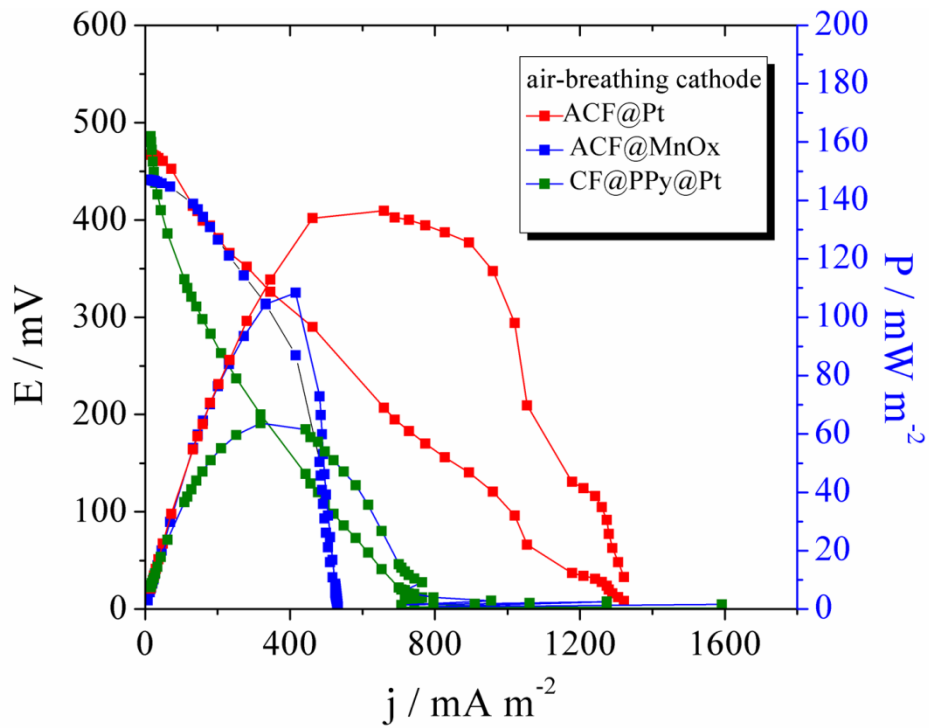


Figure-A2 Comparison of SCMFC performance with various air-breathing cathode systems

Annex 3: membrane fouling



Figure-A3 Fouling found on the membrane surface which faces cathodic solution (ferricyanide) at the end of DCMFC operation

Annex 4: membrane biofouling

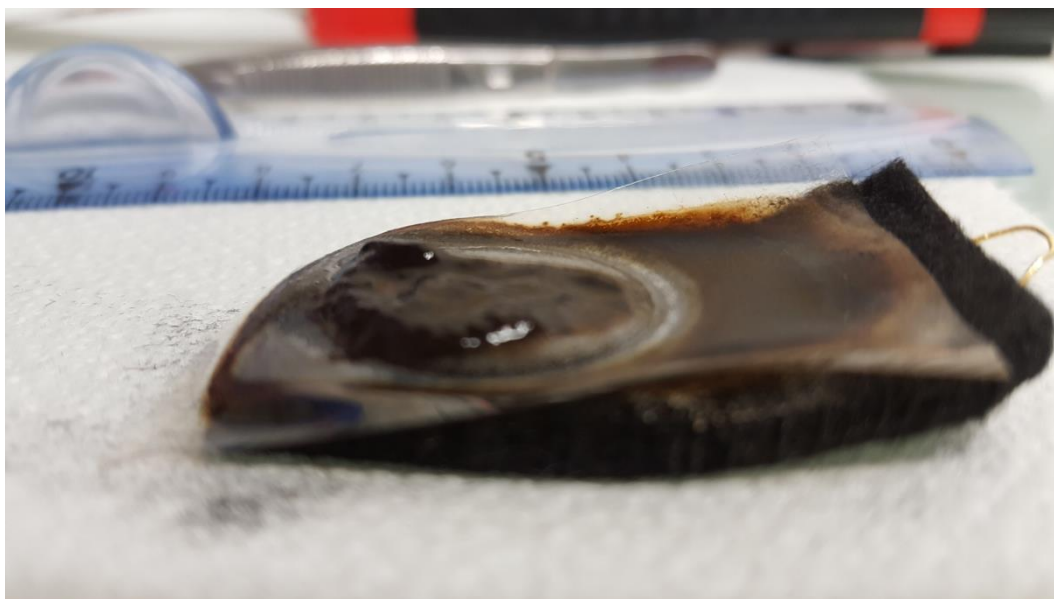


Figure-A4 Biofouling found on the membrane which faces the anodic solution at the end of SCMFC operation with ACF@MnO_x air-breathing cathode

Annex 5: MFC-electro-Fenton-like application prospect



Figure-A5.1 Coupling MFC with electro-Fenton like process for degradation azo dye compound

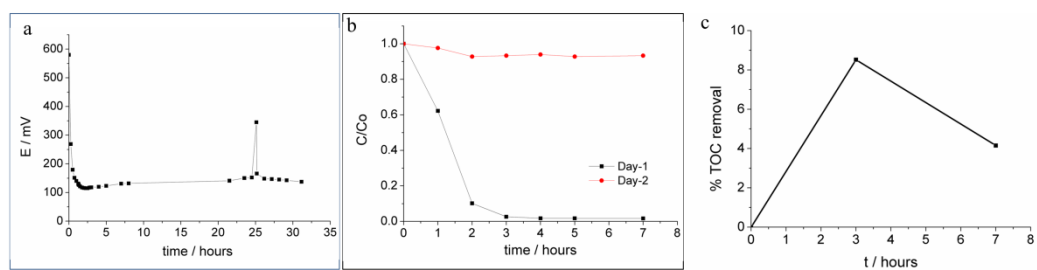


Figure-A5-2 a. Voltage evolution, b. decolorization, and c. demineralization of azo dye compound during the MFC-EF-like process

Abstract

MODIFICATION OF CARBON FELT FOR CONSTRUCTION OF AIR-BREATHING CATHODE AND ITS APPLICATION IN MICROBIAL FUEL CELL

Microbial fuel cell, MFC, is a bioengine that combine biochemical and electrochemical principle respectively, to extract the stored electrons in organic material and subsequently to turn them into electricity. In an MFC, living electroactive microbes, with its whole enzymatic system, are employed to biocatalyze the oxidation of organic fuel; an anode is artificially introduced to divert the electrons, as resulted in the bacterial respiratory system; and oppositely a cathode drives the electron flow that be switched further to electrical power. Electroactive microbes spread out in numerous sources such as soil, compost, sludge, waste water, and so on. The feed, organic fuel and/or other nutrient, also can abundantly be present in their matrix sources and in many other priceless sources, which commonly available in daily life. Bacterial abundance and unlimited organic fuel are the two attractive reasons for the development of sustainable energy source as such as MFC, which is also drawn our attention in this research. Herein, we developed MFC, double chamber (DCMFC) and single chamber (SCMFC), which powered by garden compost as electroactive source and acetate fuel. For sustainability reason and other advantages i.e. practicability and eco-friendly, we mainly focused on SCMFC with air-breathing cathode system. The common problematic of the SCMFC is the limited power production that mainly due to the slow kinetic of oxygen reduction reaction (ORR) in the cathodic part. Therefore, it is important to developed the material of air-breathing cathode which has a proper catalysis activity toward ORR to overcome this limitation. Carbon felt (CF) is the selected support material that suitable for air-breathing cathode fabrication. While, platinum (Pt) and manganese oxide (MnOx) respectively, as supreme and runner-up catalyst's class, has been grown on CF through a simple electrodeposition method. The resulting materials, named as ACF@Pt and ACF@MnOx, have been characterized comprehensively by electrochemical and physicochemical methods to determine their electrocatalytic performances, which support for air-breathing cathode application. Accordingly, we have developed two main types of air-breathing cathode, i.e. ACF@Pt and ACF@MnOx, which have been successfully applied in SCMFC powered by garden compost with generated power density respectively 140 mW m^{-2} and 110 mW m^{-2} . Moreover, the both developed material also reveal some promising applications. For instance, ACF@Pt has been applied as MFC's anode, both in DCMFC and SCMFC, and has improved the power density up to 300 mW m^{-2} . Interestingly, it is also shown as an excellent electrocatalyst in hydrogen evolution reaction, HER. While, the ACF@MnOx material shows a promising electrocatalyst in an electro-Fenton like system to mineralization of biorefractory material i.e. one of the hazardous pollutant constituent of waste water.

Key words: microbial fuel cell, air-breathing cathode, garden compost leachate, carbon felt, platinum, manganese oxide

Résumé

MODIFICATION DU FEUTRE DE CARBONE POUR LA CONSTRUCTION D'UNE CATHODE À RESPIRATION AÉRIENNE ET SON APPLICATION DANS UNE PILE A COMBUSTIBLE MICROBIENNE

La pile à combustible microbienne, MFC, est un bioengine qui associe respectivement le principe biochimique et le principe électrochimique pour extraire les électrons stockés dans la matière organique et les transformer en électricité. Dans un MFC, des microbes électroactifs vivants, avec son système enzymatique complet, sont utilisés pour biocatalyser l'oxydation du combustible organique; une anode est introduite artificiellement pour détourner les électrons, ce qui a eu pour résultat le système respiratoire bactérien; et à l'opposé, une cathode entraîne le flux d'électrons qui est ensuite commuté sur le courant électrique. Les microbes électroactifs se répandent dans de nombreuses sources telles que le sol, le compost, les boues, les eaux usées, etc. Les aliments pour animaux, les combustibles organiques et/ou d'autres nutriments peuvent également être abondamment présents dans leurs sources matricielles et dans de nombreuses autres sources inestimables, couramment disponibles dans la vie quotidienne. L'abondance bactérienne et le carburant organique illimité sont les deux raisons attrayantes pour le développement d'une source d'énergie durable telle que le MFC, qui attire également notre attention dans cette recherche. Ici, nous avons développé MFC, double chambre (DCMFC) et chambre unique (SCMFC), alimentés par compost de jardin comme source électroactive et acétate de carburant. Pour des raisons de durabilité et d'autres avantages, c'est-à-dire praticables et respectueux de l'environnement, nous nous sommes principalement concentrés sur le SCMFC avec un système de cathodes respiratoires. La problématique commune du SCMFC est la production d'énergie limitée due principalement à la cinétique lente de la réaction de réduction de l'oxygène (ORR) dans la partie cathodique. Par conséquent, il est important de mettre au point le matériau de la cathode respiratoire qui présente une activité de catalyse appropriée vis-à-vis de la perte de réponse optique pour surmonter cette limitation. Le feutre de carbone (CF) est le matériau de support choisi qui convient à la fabrication de cathodes à respiration aérienne. Alors que le platine (Pt) et l'oxyde de manganèse (MnOx), respectivement, en tant que classe de catalyseur suprême et de second rang, ont été développés sur CF grâce à une méthode simple d'électrodéposition. Les matériaux résultants, dénommés ACF@Pt et ACF@MnOx, ont été caractérisés de manière complète par des méthodes électrochimiques et physicochimiques afin de déterminer leurs performances électrocatalytiques, supportant ainsi l'application de cathodes respiratoires. En conséquence, nous avons développé deux principaux types de cathodes respiratoires, à savoir ACF@Pt et ACF@MnOx, appliquées avec succès dans le SCMFC alimenté par du compost de jardin avec une densité de puissance respective de 140 mW m^{-2} et 110 mW m^{-2} . De plus, les deux matériaux développés révèlent également des applications prometteuses. Par exemple, ACF@Pt a été utilisé comme anode de MFC, à la fois dans DCMFC et SCMFC, et a amélioré la densité de puissance jusqu'à 300 mW m^{-2} . Fait intéressant, il est également montré comme un excellent électrocatalyseur dans la réaction de dégagement d'hydrogène, HER. Alors que le matériau ACF@MnOx présente un électrocatalyseur prometteur dans un système de type électro-Fenton à la minéralisation d'un matériau biréfractif, c'est-à-dire l'un des constituants polluants dangereux des eaux usées.

Mots clés: pile à combustible microbienne, cathode respiratoire, lixiviat de compost de jardin, feutre de carbone, platine, oxyde de manganèse